

ON THE DYNAMICS OF PROTOPLANETARY DISKS

A Dissertation

Presented to the Faculty of the Graduate School

of Cornell University

in Partial Fulfillment of the Requirements for the Degree of

Doctor of Philosophy

by

J. J. Zanazzi

July 2018

© 2018 J. J. Zanazzi

ALL RIGHTS RESERVED

ON THE DYNAMICS OF PROTOPLANETARY DISKS

J. J. Zanazzi, Ph.D.

Cornell University 2018

Protoplanetary disks are disks of gas and dust orbiting young stars which form planetary systems. This thesis is devoted to understanding how gravitational interactions in different astrophysical situations effect the structure and dynamical evolution of protoplanetary disks, shaping the planetary systems the disks give birth to. Chapter 2 shows how disk warping in a hydrodynamical disk torqued by a spinning central star and inclined binary companion affects the disk's structure and drives its long-term evolution. Chapter 3 looks at how photoevaporation and the formation of a massive, short-period planet modifies the excitation between the spin-axis of a spinning oblate star and angular momentum axis of a protoplanetary disk generated by the gravitational torque from an inclined binary companion. Chapter 4 derives the conditions a protoplanetary disk must satisfy to undergo the Lidov-Kozai instability, where the disk's eccentricity grows from the gravitational torque exerted on the disk by an inclined binary companion. Chapter 5 derives the conditions a protoplanetary disk around an eccentric binary must satisfy to evolve into an orientation perpendicular to the binary's orbital plane (polar alignment). Chapter 6 shows an extended circumplanetary disk can remain stably tilted out of the planet's orbital plane, provided the torques from the oblate planet and disk self-gravity are sufficiently strong to resist the tidal torque from the planet's host star. The appendix derives a useful dispersion relation for density waves in a viscous, non-Keplarian disk.

BIOGRAPHICAL SKETCH

J.J. Zanazzi was born in the sprawling hot city of Phoenix, Arizona. His love for astronomy began while he was in high school, where he did an astronomy project with an astronomy graduate student at Arizona State University, looking for planets outside the solar system. He then continued his research and enrolled as an undergraduate at Northern Arizona University, a place whose hippy vibe matched perfectly with his then long hair and tattered flack jacket covered with punk rock patches. He spent his summers working as an undergraduate researcher at Wayne State University, Pennsylvania State University, and University of California Davis, and somehow convinced mathematicians at Pennsylvania State University and the Independent University of Moscow (in Russia) to let him into their intensive one-semester mathematics study abroad programs. After living like a pampered academic gypsy for four years, he graduated Northern Arizona University with degrees in physics, astronomy, and mathematics, and entered Cornell University's Ph.D. program in Astronomy and Space Sciences. There, he worked with Professor Dong Lai, who opened his eyes to the wonders of theoretical astrophysics. Now a short-haired recipient of a Ph.D., J. J. is ready to become a contributing member of society.

To my grandfather, whose attention and encouragement to pursue the sciences was a major part of me deciding to get a Ph.D. in Astrophysics. I wish he could be here to see the completion of this work.

ACKNOWLEDGEMENTS

First and foremost, I would like to thank my advisor, Dong Lai, for the tremendous amount of time and energy he put into advising me. I was truly fortunate to learn from someone with not only an incredibly deep knowledge of many fields in Astrophysics, but a pragmatic approach to research which leads to many significant results over a short period of time. It is no accident Dong is well known not only for his research, but also his many successful students, and I only hope I can continue this legacy. I would like to thank my committee members, Jim Cordes, Eanna Flannagan, and Phil Nicholson, for agreeing to serve on my thesis committee, and tolerating my radical shift of thesis topic in the middle of my Ph.D. I would also like to thank Amaury H.M.J. Triaud, Doug Lin, and Re'em Sari, for wonderful scientific collaborations, conversations, and great times.

My mother, Lorelei Wood, has been a tremendous source of support over the five years it took me to obtain my Ph.D. She is one of the main reasons I was driven to get a doctorate in Astrophysics, by encouraging my scientific pursuits while growing up, and giving me her insight on professional and personal matters. I could not have achieved what I did without her help. My late grandfather, Billy Wood, was also a source of gentle guidance and scientific inspiration. This thesis is dedicated to his memory. My father John Zanazzi, grandmother Ellen Wood, and grandfather John Zanazzi were also supportive when I found myself in a pinch. Some of the advise they gave me, which I dismissed as an angstty teenager, I have come to realize has been very insightful.

I would like to thank my friends Jeremy Hodis, Samuel Birch, Chelsea Sharon, Kassandra Anderson, Michael Lam, Tyler Pauly, Paul Corlies, Cristobal Caleidoscopico, Eamonn O'Shea, Dante Iozzo, Michael Matty, Abinov Jindal,

and Jean Teyssandier. You all have made the time I spent here in Ithaca some of the best years of my life.

And of course, thank to the National Aeronautics and Space Administration (NASA) for funding three years of my Ph.D. research through a NASA Earth and Space Sciences Fellowship (NESSF), and Cornell University for offering me a Teaching Assistantship to support my first two years. I would also like to thank the Exoplanet Summer Program at the University of California Santa Cruz, the 33rd Winter school in Theoretical Physics at Hebrew University, and the Sagan Summer Workshop at the California Institute of Technology, for funding me to visit their programs, as well as learn and collaborate with some of the best scientists in the field of exoplanetary science.

TABLE OF CONTENTS

Biographical Sketch	iii
Dedication	iv
Acknowledgements	v
Table of Contents	vii
List of Tables	x
List of Figures	xi
1 Introduction	1
2 Effects of Disk Warping on the Inclination Evolution of Star-Disk-Binary Systems	8
2.1 Introduction	8
2.2 Star-Disk-Binary System and Gravitational Torques	11
2.3 Disk Warping	13
2.3.1 Disk Warp Induced by Binary Companion	17
2.3.2 Disk Warp Induced by Oblate Star	20
2.3.3 Disk Warps Induced by Combined Torques	23
2.3.4 Disk Warp Profile: Summary	25
2.3.5 Viscous Evolution	27
2.4 Evolution of the Star-Disk-Binary System with Viscous Dissipation from Disk Warping	33
2.5 Discussion	38
2.5.1 Theoretical Uncertainties	38
2.5.2 Observational Implications	39
2.6 Conclusions	41
3 Planet Formation in Disks with Inclined Binary Companions: Can Primordial Spin-Orbit Misalignment be Produced?	43
3.1 Introduction	43
3.2 Spin-Disk Misalignment from Star-Disk-Binary Gravitational Interactions	46
3.2.1 Setup and Parameters	48
3.2.2 Gravitational Torques	49
3.2.3 System Evolution and Secular Resonance	52
3.3 Non-homologous Surface Density Evolution: Photoevaporation .	53
3.4 Planet-Star-Disk-Binary Interactions	57
3.4.1 Planet-Disk Interactions: Non-Gap Opening Planets	59
3.4.2 Planet-Disk Interactions: Gap Opening Planets	60
3.4.3 Planet Interactions with Outer Disk	62
3.4.4 Planet-Star and Planet-Binary Interactions	64
3.5 Inclination Evolution of Planet-Star-Disk-Binary Systems	67
3.5.1 Early In-Situ Formation of Hot-Jupiters	68

3.5.2	Late In-Situ Formation of Hot-Jupiters	71
3.5.3	Formation of Hot-Jupiters through Type-II Migration	75
3.5.4	Hot Jupiters left in disk cavity from photoevaporation	78
3.6	Discussion	83
3.6.1	Observational Implications	83
3.6.2	Theoretical Uncertainties	86
3.7	Conclusions	88
4	Lidov-Kozai Mechanism in Hydrodynamical Disks: Linear Stability Analysis	91
4.1	Introduction	91
4.2	Setup and Formalism	92
4.3	Results	98
4.3.1	Analytic Result for Thin Annulus	102
4.3.2	Inviscid Extended Disk	105
4.3.3	Effect of Viscosity	106
4.4	Summary and Discussion	108
4.4.1	Summary of Key Results	108
4.4.2	Discussion	110
5	Inclination Evolution of Protoplanetary Disks Around Eccentric Binaries	115
5.1	Introduction	115
5.2	Test Particle Dynamics	118
5.3	Circumbinary Disk Dynamics	122
5.3.1	Qualitative Discussion	123
5.3.2	Formalism	125
5.3.3	Disk Warp Profile	127
5.3.4	Viscous Torques	130
5.4	Secular Dynamics with Massive Inclined Outer Body	133
5.5	Torque on Binary and Effect of Accretion	136
5.6	Discussion	138
5.6.1	Theoretical Uncertainties	138
5.6.2	Observational Implications	139
5.7	Summary	141
6	Extended Transiting Disks and Rings Around Planets and Brown Dwarfs: Theoretical Constraints	148
6.1	External Torques and the Laplace Surface	151
6.2	Generalized Laplace Surface: Equilibrium with Self-Gravity	154
6.3	Time Evolution of Disk Warp	159
6.3.1	Stability of Generalized Laplace Equilibria	159
6.3.2	Coherent Disk Precession	162
6.3.3	Model for high σ disk	164

6.4	Summary and Discussion	166
6.4.1	Key Results	166
6.4.2	Hydrodynamical Effects	169
6.4.3	Implications	170
A	Chapter 1 of appendix	175
A.1	Density Wave Dispersion Relation	176
A.1.1	High k_z limit	177
A.1.2	Low k_z limit	179
A.2	Long-Wavelength Bending Wave Dispersion Relation	180

LIST OF TABLES

2.1	Dimensionless coefficients \mathcal{U}_b , \mathcal{V}_b , and \mathcal{W}_{bb} , tabulated for different p and q values	16
2.2	Dimensionless coefficients \mathcal{U}_s , \mathcal{V}_s , and \mathcal{W}_{ss} , for different values of p and q	20
2.3	Dimensionless coefficients \mathcal{W}_{bs} and \mathcal{W}_{sb} , for different values of p and q	23
2.4	Dimensionless viscosity coefficients Γ_b , Γ_s , and $\Gamma_{(bs)}$, for various p and q values	27
3.1	Definitions of relevant quantities in the star-disk-binary system	47
3.2	Definitions of quantities related to planet interactions with the star-disk-binary system	58
5.1	Binary eccentricities e_b , with their inclinations I_{crit} and I_{polar} , for the selected eccentric binaries with circumbinary disks	141

LIST OF FIGURES

2.1	Rescaled radial functions $\tilde{\tau}_b$, \tilde{V}_b , and \tilde{W}_{bb}	16
2.2	Rescaled radial functions $\tilde{\tau}_s$, \tilde{V}_s , and \tilde{W}_{ss}	20
2.3	Rescaled radial functions \tilde{W}_{bs} and \tilde{W}_{sb}	23
2.4	Disk misalignment angle β a function of radius r , for the h_{in} values indicated	25
2.5	Same as Fig. 2.4, except $a_b = 200$ au	26
2.6	The damping rate γ_b as a function of the binary semi-major axis a_b	28
2.7	The damping rate γ_{sd} as a function of the normalized stellar rotation frequency $\bar{\Omega}_*$	29
2.8	Inclination evolution of star-disk-binary systems	33
2.9	Total disk warp $\Delta\beta$ for the integrations of Fig. 2.8	34
2.10	Same as Figure 2.8, except $a_b = 200$ au	35
2.11	Same as Fig. 2.9, except for the examples considered in Fig. 2.10 .	36
3.1	Sample evolution of the star-disk-binary system	51
3.2	Evolution of surface density $\Sigma(r, t)$ undergoing photoionization .	54
3.3	Same as Fig. 3.1, except the disk surface density undergoes photoionization	55
3.4	Ratio of the precession frequency of the planet driven by the disk $\tilde{\omega}_{pd}$ to the precession frequency of the planet driven by the star ω_{ps} and binary ω_{pb} , for different planetary semi-major axis a_p . .	64
3.5	Evolution of the star-disk/star-planet angle $\theta_{sd} = \theta_{sp}$, modified star-disk precession frequency $\tilde{\omega}'_{sd}$, and modified disk-binary precession frequency $\tilde{\omega}'_{db}$, for different planetary semi-major axis a_p	68
3.6	Evolution of the star-planet/star-disk inclination $\theta_{sp} = \theta_{sd}$ in the late in-situ model, for different planetary mass growth timescales t_{grow} as indicated	72
3.7	Evolution of the planet's semi-major axis a_p with time, for different Λ_{mig} values	74
3.8	Evolution of the star-disk/star-planet angle $\theta_{sd} = \theta_{sp}$, and precession frequencies $\tilde{\omega}'_{sd}$ and $\tilde{\omega}'_{db}$ with time, for different Λ_{mig} values .	75
3.9	Evolution of the star-disk/star-planet angle $\theta_{sd} = \theta_{sp}$ and precession frequencies $\tilde{\omega}'_{sd}$ and $\tilde{\omega}'_{db}$, with different initial disk-binary inclinations $\theta_{db}(0)$	76
3.10	Star-disk-planet-binary evolution under a prescribed Σ depletion due to photoevaporation	79
3.11	Same as Fig. 3.10, except $a_p(t) = a_p(0) = 8 r_{in}$ and $t_p = 0.3$ Myr . .	80
4.1	Real and imaginary components of the Lidov-Kozai eigenvalue λ for a thin annulus, as functions of inclination $I = \cos^{-1}(\hat{l} \cdot \hat{i}_b)$. . .	100
4.2	Real and imaginary components of the Lidov-Kozai eigenvalue λ as functions of S	101

4.3	Real and imaginary components of the Lidov-Kozai eigenvalue λ for extended disks as a function of I	104
4.4	Real and imaginary components of the Lidov-Kozai eigenvalue λ for extended disks as a function of S	105
4.5	Real and imaginary components of the Lidov-Kozai eigenfunctions $E_+(r)$ and $E_-(r)$ for an extended disk	107
4.6	Real parts of the Lidov-Kozai eigenvalues λ for extended disks, plotted as functions of S , for different values of α_b	108
5.1	Test particle dynamics for positive and negative Λ	119
5.2	Test particle trajectories in the $I - \Omega$ and $I_e - \Omega_e$ planes	120
5.3	Circumbinary disk setup	122
5.4	Rescaled warp functions $\tilde{\tau}_b$, \tilde{V}_b , and \tilde{W}_{bb}	127
5.5	Time evolution of the disk orientation for different binary eccentricities e_b	131
5.6	Trajectories in the $I - \Omega$ and $e_b - \Omega$ planes for the J values indicated	133
5.7	Inclination I_{fp} as a function of J^{-1}	134
5.8	Contour plot of the probability of polar alignment P_{polar} as a function of disk inclination I and binary eccentricity e_b	139
5.9	Same as Fig. 5.5, except we neglect the disk's viscous torque, and include the disk's accretion torque	144
5.10	Same as Fig. 5.5, except we include the disk's viscous torque	147
6.1	Equilibrium disk inclination profile, or Laplace surface without self-gravity	154
6.2	Torques on the disk based on order-of-magnitude estimates, and normalized by $ T_*(r_{\text{out}}) $	157
6.3	Equilibrium disk inclination profile $\beta(r)$ including the effect of self gravity (the generalized Laplace surface), for different values of r_L/r_{out} and σ [see Eq. (6.20)] as indicated. The planetary obliquity is assumed to be $\beta_p = 60^\circ$. The $\sigma = 0$ curves correspond to the standard Laplace surface (without self-gravity). The solid lines are for the surface density power-law index $p = 1$, and dashed lines for $p = 1.5$	158
6.4	Equilibrium inclination of the disk at the outer radius, as a function of the disk mass parameter σ	160
6.5	Time evolution of the quantity j_{\max}	162
6.6	Evolution of the disk inclination $\beta(r, t)$ and twist angle $\phi(r, t)$ for different values of σ	164
6.7	Snapshots of the disk inclination profile $\beta(r, t)$ and twist profile $\phi(r, t)$ at different times	165
6.8	Evolution of the (flat) outer disk inclination β and twist angle ϕ using a simple disk model, for different σ values	167

6.9	The exact self-gravity integrand as a function of χ , for different values of α	173
6.10	Equilibrium disk inclination profile $\beta(r)$ including the effect of self-gravity for different values of r_L/r_{out} and σ	174

CHAPTER 1

INTRODUCTION

Protoplanetary disks are the disks of gas and dust orbiting young stars, and are the nurseries from which planets are born. By looking at the ages of stars in stellar clusters with disks, we know the typical lifetime of a protoplanetary disk is of order $\sim 1 - 10$ million years [Haisch, Lada & Lada, 2001]. Conveniently for the inhabitants of planets, the lifetime of protoplanetary disks is (slightly) longer than the time it takes to form a rocky core. When rocky cores/massive bodies grow to $\sim 0.01 - 10 M_{\oplus}$ by accreting small (\sim meter size) bodies in their local feeding zones (oligarchic growth), the massive bodies take $\sim 0.1 - 10$ million years to reach their respective isolation masses (no more small bodies may be accreted onto the massive body because the massive body's gravitational influence has cleared its feeding zone) [Goldreich, Lithwick & Sari, 2004]. When rocky cores grow to masses $\gtrsim 10 M_{\oplus}$ from the accretion of pebbles (\sim cm size bodies) in their local feeding zones (pebble accretion), the rocky cores take $\sim 10^{-3} - 1$ million years to grow to the body's isolation mass [Lambrechts & Johansen, 2012].

The idea that planets form from disks dates all the way back to the 18th century philosopher Immanuel Kant, whom argued a disk was a natural place to form our solar system, composed of planets on nearly circular and coplanar orbits. The nebular hypothesis was revitalized by Safronov [1972], who developed the Solar Nebula Disk Model (SNDM), where the planets in our solar system form from a disk of gas and dust orbiting our young sun. The SNDM nicely explained a number of features other solar system formation models had been struggling to explain for centuries (see Woolfson 1993 for a review) other planetary systems were expected to share:

1. Because disks have much more mass at their outer edges, low mass planets form close to their host stars, while massive planets form at larger semi-major axis.
2. Because interactions between planets and gaseous disks damp planetary eccentricities, planetary systems form with nearly circular orbits.
3. Since the disk forms from the same cloud of gas as the host star, the planetary systems produced have nearly coplanar orbits, which are also coplanar with the host star's equatorial plane.

Many of the first extra-solar planetary systems discovered did not have these predicted features. The first planet discovered (51 Pegasi b) orbited its host star at a distance of ~ 0.03 au [Mayor & Queloz, 1995], a distance ~ 10 times shorter than Mercury's semi-major axis. Many more gas giant planets with orbital periods between 1 – 10 days were discovered soon after, a class of planets which became known as "Hot Jupiters." Many massive exoplanets were shown to lie on extremely eccentric orbits, the highest being HD 80606b, which has an eccentricity of $e = 0.93$ [Naef, et al., 2001, Hébrard, et al., 2010]. And by using the Rossiter-McLaughlin effect [Rossiter, 1924, McLaughlin, 1924], many planets were shown to have their orbital angular momentum vectors highly misaligned with their host star's spin axis (e.g. Hébrard et al. 2008, Narita et al. 2009, Winn et al. 2009, Triaud et al. 2010; see Winn & Fabrycky 2015, Triaud 2017 for recent reviews).

Theoretical explanations for how these planetary systems form (especially hot Jupiters) typically fall into one of two categories (see Dawson & Johnson 2018 for a review). The first, called the "high-eccentricity channel," posits the massive planet forms far from its host star. Later in the planet's evolution, grav-

itational interactions from the torque by an inclined companion (either binary or planetary; Wu & Murray 2003, Fabrycky & Tremaine 2007, Nagasawa, Ida, & Bessho 2008, Wu & Lithwick 2011, Naoz, Farr & Rasio 2012, Beaugé & Nesvorný 2012, Petrovich 2015, Anderson et al. 2016, Muñoz, Lai & Liu 2016, Hamers & Portegies Zwart 2016), or strong encounters with other massive planets leading to planet-planet scattering [Rasio & Ford, 1996, Chatterjee, Ford, Matsumura & Rasio, 2008, Ford & Rasio, 2008, Jurić & Tremaine, 2008], places the soon to be formed hot Jupiter on an eccentric orbit misaligned with the planet's original orbital plane (and host star's equatorial plane). Tides then circularize the planet's orbit, forming a short-period Jovian planet on an orbit misaligned with the host star's equatorial plane. Although this is the favored formation pathway for hot Jupiters, it is unclear what fraction of HJs are formed through these high-eccentricity routes, and several observations remain difficult to explain, such as the lack of giant planets with high eccentricities [Dawson, Murray-Clay & Johnson, 2015], and the correlation between the spin-orbit misalignment and the effective temperature of the host star (e.g., Albrecht et al. 2012, Mazeh et al. 2015, Li & Winn 2016, Winn et al. 2017).

The second category of models argues these planetary architectures arose while the planet was still forming in its natal protoplanetary disk. A close-in hot Jupiter may follow the disk's viscous evolution, and migrate to an orbit close to the host star [Lin & Papaloizou, 1986, Lin, Bodenheimer & Richardson, 1996], or it can form at the location we observe it today [Batygin, Bodenheimer & Laughlin, 2016, Boley, Granados Contreras & Gladman, 2016]. The planet's eccentricity may in some circumstances be excited by interactions with the disk (e.g. Ogilvie & Lubow 2003, Goldreich & Sari 2003, Teyssandier & Ogilvie 2017, Rosotti, Booth, Clarke, Teyssandier, Facchini & Mustill 2017). And the disk it-

self may become misaligned with the equatorial plane of its host star, through magnetic interactions between the star and the disk [Lai et al., 2011, Spalding & Batygin, 2015], from accretion onto the disk by turbulent molecular clouds (Bate et al. 2010, Fielding et al. 2015; although see Spalding, Batygin & Adams 2014), or by the gravitational torque from an inclined binary companion [Batygin, 2012, Batygin & Adams, 2013, Lai, 2014, Spalding & Batygin, 2014].

Specifically, the torque from an inclined binary companion was shown to be a particularly robust way to generate large misalignments between the disk's orbital angular momentum vector and the host star's spin axis, which occurs when the system passes through a "secular resonance" [Batygin, 2012, Batygin & Adams, 2013, Lai, 2014, Spalding & Batygin, 2014]. The disk forms with a large amount of mass, and exerts a strong gravitational torque on the spinning host star. This torque causes the stellar spin axis to precess around the disk's orbital angular momentum, at a rate much faster than the frequency the disk is driven into precession around the binary's orbital angular momentum by the binary's gravitational torque. But as the disk loses mass, the star-disk precession frequency decreases, until it becomes comparable to the disk-binary precession frequency. When this occurs, a large amount of angular momentum is transferred from the binary to the mutual star-disk angular momenta, causing large inclinations to be excited between the stellar spin axis and the disk orbital angular momentum axis.

The bulk of this thesis is dedicated to understanding to what extent realistic star-disk-binary systems may suffer secular resonances, generating spin-orbit misalignments for the planetary systems forming within them (primordial misalignment). Chapter 2 uses the bending wave formalism developed by Lubow

& Ogilvie [2000] in the “resonant” regime (see Chapter A for details) to investigate how torques from the spinning host star and inclined binary companion twist and warp the disk. It also looks at the effect of viscous dissipation from disk warping to drive the star-disk-binary system’s dynamical evolution over the disk’s lifetime. Chapter 3 investigates how photoevaporation and the formation of a short-period gas giant may suppress the star-disk inclinations generated after the system passes through a secular resonance, or hinder the system from passing through a secular resonance in the first place. Chapter 4 looks at the conditions the disk no longer remains circular (a critical assumption of these models), but instead has its eccentricity excited by the binary’s gravitational torque, and undergoes eccentricity and inclination oscillations via the Lidov-Kozai effect.

The tools developed to tackle the problems mentioned above found applications to other types of protoplanetary disks besides star-disk-binary systems. One such problem is the dynamics of a protoplanetary disk around two binary stars in eccentric orbits. All circumbinary planets (planets orbiting two binary stars) lie on orbits nearly coplanar with the binary’s orbital plane [Doyle et al., 2011, Kostov et al., 2013, 2014, 2016, Orosz et al., 2012a,b, Schwamb et al., 2013, Welsh et al., 2012, 2015], an expected outcome if the planets formed in a disk with a low inclination to the binary’s orbital plane. In Foucart & Lai [2013, 2014], it was shown viscous dissipation from disk warping aligns the disk with the binary’s orbital plane over timescales much shorter than typical protoplanetary disk lifetimes. Most observations show circumbinary disks to be nearly aligned with their binary’s orbital plane within a few degrees (e.g. Andrews et al. 2010, Czekala et al. 2015, 2016, Kennedy et al. 2012b), supporting the picture of circumbinary planets forming coplanar to the binary’s orbital plane, but

some highly inclined circumbinary disks have been discovered (e.g. Chiang & Murray-Clay 2004, Marino et al. 2015, Brinch et al. 2016, Kennedy et al. 2012a). Specifically, the debris disk around 99 Herculis has a $\sim 90^\circ$ inclination with its binary orbital plane [Kennedy et al., 2012a].

Martin & Lubow [2017] provided a tentative theoretical explanation for the evolution of 99 Herculis B's debris disk to its polar orientation. Using Smoothed Particle Hydrodynamics simulations of a hydrodynamical disk around an eccentric ($e_b = 0.5$) binary, Martin & Lubow [2017] showed a protoplanetary disk with an initial disk-binary inclination of 60° will evolve to a polar state, due to the interplay of gravitational and viscous disk warping torques. But this was just one simulation of a gaseous circumbinary disk around an eccentric binary: a comprehensive theoretical study was lacking in the literature. Chapter 5 is such a comprehensive study. Generalizing the perturbative work of Foucart & Lai [2014] to arbitrary binary eccentricities and disk-binary inclinations, I provide a simple analytic criterion a circumbinary disk must satisfy to polar align with respect to the binary's orbital plane.

My expertise in protoplanetary disks also found applications to circumplanetary disks. By looking at archival light-curves from the K5 star 1 SWASP J140747-354542, Mamajek et al. [2012] made a tentative detection of an extended circumplanetary disk/ring system. Because the disk is so extended, to keep the disk stably tilted out of the planet's orbital plane, additional torques are required to resist the external torque exerted on the disk/ring system by tidal torques from the host star. Chapter 6 shows the combined influence of torques exerted on the rings by the oblate planet and torques between mutual ringlets from self-gravity are sufficient to stably tilt the disk/ring system out of the

planet's orbital plane.

The appendix derives a useful result related to how bending waves propagate across a hydrodynamical disk. Two different equations describe how bending waves and viscous torques resist external torques to keep a hydrodynamical disk rigid and drive the disk's dynamical evolution. When the Shakura-Sunyaev α parameter and epicyclic frequency $\kappa^2 = (2\Omega/r) d(r^2\Omega)/dr$ (where $\Omega^2 = r^{-1} \partial\Phi/\partial r|_{z=0}$ is the orbital frequency of the disk) satisfy

$$\max\left(\alpha, \left|\frac{\Omega^2 - \kappa^2}{2\Omega^2}\right|\right) \lesssim \frac{H}{r}, \quad (1.1)$$

where H is the disk's scale-height, the disk lies in the resonant bending wave regime, and warps propagate across the disk according to a wave-like equation [Papaloizou & Lin, 1995, Lubow & Ogilvie, 2000]. When condition (1.1) is violated, the disk lies in the viscous regime, and warps evolve according to a diffusion equation [Papaloizou & Pringle, 1983, Ogilvie, 1999]. Appendix A shows condition (1.1) may be understood using the dispersion relation for density waves propagating across a viscous, non-Keplarian disk.

CHAPTER 2

EFFECTS OF DISK WARPING ON THE INCLINATION EVOLUTION OF STAR-DISK-BINARY SYSTEMS

2.1 Introduction

Circumstellar disks in young protostellar binary systems are likely to form with an inclined orientation relative to the binary orbital plane, as a result of the complex star/binary/disc formation processes (e.g. Bate, Bonnell, & Bromm 2003, McKee & Ostriker 2007, Klessen 2011). Indeed, many misaligned circumstellar disks in protostellar binaries have been found in recent years (e.g. Stapelfeldt et al. 1998, 2003, Neuhäuser et al. 2009, Jensen & Akeson 2014, Williams et al. 2014, Brinch et al. 2016, Fernández-López, Zapata & Gabbasov 2017, Lee et al. 2017). Such misaligned disks experience differential gravitational torques from the binary companion, and are expected to be twisted/warped while undergoing damped precession around the binary (e.g. Lubow & Ogilvie 2000, Bate et al. 2000, Foucart & Lai 2014). On the other hand, a spinning protostar has a rotation-induced quadrupole, and thus exerts a torque on the disk (and also receives a back-reaction torque) when the stellar spin axis and the disk axis are misaligned. This torque tends to induce warping in the inner disk and drives mutual precession between the stellar spin and disk. In the presence of both torques on the disk, from the binary and from the central star, how does the disk warp and precess? What is the long-term evolution of the disk and stellar spin in such star-disk-binary systems? These are the questions we intend to address in this paper.

Several recent studies have examined the secular dynamics of the stellar spin

and circumstellar disk in the presence of an inclined binary companion [Batygin, 2012, Batygin & Adams, 2013, Lai, 2014, Spalding & Batygin, 2014, 2015]. These studies were motivated by the observations of spin-orbit misalignments in exoplanetary systems containing hot Jupiters, i.e., the planet's orbital plane is often misaligned with the stellar rotational equator (see Winn & Fabrycky 2015 and Triaud 2017 for recent reviews). It was shown that significant "primordial" misalignments may be generated while the planetary systems are still forming in their natal protoplanetary disks through secular star-disk-binary gravitational interactions [Batygin & Adams, 2013, Lai, 2014, Spalding & Batygin, 2014, 2015]. In these studies, various assumptions were made about the star-disk interactions, and uncertain physical processes such as star/disk winds, magnetic star-disk interactions, and accretion of disk angular momentum onto the star were incorporated in a parameterized manner. Nevertheless, the production of spin-orbit misalignments seems quite robust.

In Zanazzi & Lai [2017b], we showed that the formation of hot Jupiters in the protoplanetary disks can significantly suppress the excitation of spin-orbit misalignment in star-disk-binary systems. This is because the presence of such close-in giant planets lead to strong spin-orbit coupling between the planet and its host star, so that the spin-orbit misalignment angle is adiabatically maintained despite the gravitational perturbation from the binary companion. However, the formation of small planets or distant planets (e.g. warm Jupiters) do not affect the generation of primordial misalignments between the host star and the disk.

A key assumption made in all previous studies on misalignments in star-disk-binary systems [Batygin & Adams, 2013, Lai, 2014, Spalding & Batygin,

2015] is that the disk is nearly flat and behaves like a rigid plate in response to the external torques from the binary and from the host star. The rationale for this assumption is that different regions of the disk can efficiently communicate with each other through hydrodynamical forces and/or self-gravity, such that the disk stays nearly flat. However, to what extent this assumption is valid is uncertain, especially because in the star-disk-binary system the disk experiences two distinct torques from the oblate star and from the binary which tend to drive the disk toward different orientations (see Tremaine & Davis 2014 for examples of non-trivial disk warps when a disk is torqued by different forces). Moreover, the combined effects of disk warps/twists (even if small) and viscosity can lead to non-trivial long-term evolution of the star-disk-binary system. Previous works on warped disks in the bending wave regime have considered a single external torque, such as an ext binary companion [Lubow & Ogilvie, 2000, Bate et al., 2000, Foucart & Lai, 2014], an inner binary [Facchini, Lodato, & Price, 2013, Lodato & Facchini, 2013, Foucart & Lai, 2014, Zanazzi & Lai, 2018a], magnetic torques from the central star [Foucart & Lai, 2011], a central spinning black hole [Demianski & Ivanov, 1997, Lubow, Ogilvie, & Pringle, 2002, Franchini, Lodato, & Facchini, 2016, Chakraborty & Bhattacharyya, 2017], and a system of multiple planets on nearly coplanar orbits [Lubow & Ogilvie, 2001]. In this paper, we will focus on the hydrodynamics of warped disks in star-disk-binary systems, and will present analytical calculations for the warp amplitudes/profiles and the rate of evolution of disk inclinations due to viscous dissipation associated with these warps/twists.

This paper is organized as follows. Section 3.2.1 describes the setup and parameters of the star-disk-binary system we study. Section 2.3 presents all the technical calculations of our paper, including the disk warp/twist profile and

effect of viscous dissipation on the evolution of system. Section 2.4 examines how viscous dissipation from disk warps modifies the long-term evolution of star-disk-binary systems. Section 2.5 discusses theoretical uncertainties of our work. Section 3.7 contains our conclusions.

2.2 Star-Disk-Binary System and Gravitational Torques

Consider a central star of mass M_\star , radius R_\star , rotation rate Ω_\star , with a circumstellar disk of mass M_d , and inner and outer truncation radii of r_{in} and r_{out} , respectively. This star-disk system is in orbit with a distant binary companion of mass M_b and semimajor axis a_b . The binary companion exerts a torque on the disk, driving it into differential precession around the binary angular momentum axis \hat{l}_b . Averaging over the orbital period of the disk annulus and binary, the torque per unit mass is

$$\mathbf{T}_{\text{db}} = -r^2 \Omega \omega_{\text{db}} (\hat{l} \cdot \hat{l}_b) \hat{l}_b \times \hat{l}, \quad (2.1)$$

where $\Omega(r) \simeq \sqrt{GM_\star/r^3}$ is the disk angular frequency, $\hat{l} = \hat{l}(r, t)$ is the unit orbital angular momentum axis of a disk “ring” at radius r , and

$$\omega_{\text{db}}(r) = \frac{3GM_\star}{4a_b^3 \Omega} \quad (2.2)$$

is the characteristic precession frequency of the disk “ring” at radius r . Similarly, the rotation-induced stellar quadrupole drives the stellar spin axis \hat{s} and the disk onto mutual precession. The stellar rotation leads to a difference in the principal components of the star’s moment of inertia of $I_3 - I_1 = k_q M_\star R_\star^2 \bar{\Omega}_\star^2$, where $k_q \simeq 0.1$ for fully convective stars [Lai, Rasio & Shapiro, 1993]. Averaging over the orbital period of the disk annulus, the torque on the disk from the oblate star is

$$\mathbf{T}_{\text{ds}}(r, t) = -r^2 \Omega \omega_{\text{sd}} (\hat{s} \cdot \hat{l}) \hat{s} \times \hat{l}, \quad (2.3)$$

where

$$\omega_{\text{ds}}(r) = \frac{3G(I_3 - I_1)}{2r^5\Omega} = \frac{3Gk_{\text{q}}M_{\star}R_{\star}^2\bar{\Omega}_{\star}^2}{2r^5\Omega} \quad (2.4)$$

is the characteristic precession frequency of the disk ring at radius r . Since ω_{db} and ω_{ds} both depend on r , the disk would quickly lose coherence if there were no internal coupling between the different “rings.”

We introduce the following rescaled parameters typical of protostellar systems:

$$\begin{aligned} \bar{M}_{\star} &= \frac{M_{\star}}{1 M_{\odot}}, & \bar{R}_{\star} &= \frac{R_{\star}}{2 R_{\odot}}, & \bar{\Omega}_{\star} &= \frac{\Omega_{\star}}{\sqrt{GM_{\star}/R_{\star}^3}}, \\ \bar{M}_{\text{d}} &= \frac{M_{\text{d}}}{0.1 M_{\odot}}, & \bar{r}_{\text{in}} &= \frac{r_{\text{in}}}{8 R_{\odot}}, & \bar{r}_{\text{out}} &= \frac{r_{\text{out}}}{50 \text{ au}}, \\ \bar{M}_{\text{b}} &= \frac{M_{\text{b}}}{1 M_{\odot}}, & \bar{a}_{\text{b}} &= \frac{a_{\text{b}}}{300 \text{ au}}. \end{aligned} \quad (2.5)$$

The rotation periods of T Tauri stars vary from $P_{\star} \sim 1 - 10$ days [Bouvier, 2013], corresponding to $\bar{\Omega}_{\star} \sim 0.3 - 0.03$. We fix the canonical value of $\bar{\Omega}_{\star}$ to be 0.1, corresponding to a stellar rotation period of $P_{\star} = 3.3$ days. The other canonical values in Eq. (2.5) are unity, except the disk mass, which can change significantly during the disk lifetime. Our choice of r_{in} is motivated by typical values of a T Tauri star’s magnetospheric radius r_{m} , set by the balance of magnetic and plasma stresses (see Lai 2014b for review)

$$\begin{aligned} r_{\text{in}} \approx r_{\text{m}} &= \eta \left(\frac{\mu_{\star}^4}{GM_{\star}\dot{M}^2} \right)^{1/7} \\ &= 7.4 \eta \left(\frac{B_{\star}}{1 \text{ kG}} \right)^{4/7} \left(\frac{10^{-7} M_{\odot}/\text{yr}}{\dot{M}} \right)^{2/7} \frac{\bar{R}_{\star}^{12/7}}{\bar{M}_{\star}^{1/7}} R_{\odot}. \end{aligned} \quad (2.6)$$

Here, $\mu_{\star} = B_{\star}R_{\star}^3$ is the stellar dipole moment, B_{\star} is the stellar magnetic field, \dot{M} is the accretion rate onto the central star (e.g. Rafikov 2017), and η is a parameter of order unity. We note that we take the stellar radius to be fixed, in contrast to the models of Batygin & Adams [2013] and Spalding & Batygin [2014, 2015],

but we argue this will not change our results significantly. We are primarily concerned with the effects of viscous dissipation from disk warping, and a changing stellar radius will not affect the viscous torque calculations to follow.

We parameterize the disk surface density $\Sigma = \Sigma(r, t)$ as

$$\Sigma(r, t) = \Sigma_{\text{out}}(t) \left(\frac{r_{\text{out}}}{r} \right)^p. \quad (2.7)$$

We take $p = 1$ unless otherwise noted. The disk mass M_d is then (assuming $r_{\text{in}} \ll r_{\text{out}}$)

$$M_d = \int_{r_{\text{in}}}^{r_{\text{out}}} 2\pi \Sigma r dr \simeq \frac{2\pi \Sigma_{\text{out}} r_{\text{out}}^2}{2 - p}. \quad (2.8)$$

The disk angular momentum vector is $\mathbf{L}_d = L_d \hat{\mathbf{l}}_d$ (assuming a small disk warp), and stellar spin angular momentum vector is $\mathbf{S} = S \hat{\mathbf{s}}$, where $\hat{\mathbf{l}}_d$ and $\hat{\mathbf{s}}$ are unit vectors, and

$$L_d = \int_{r_{\text{in}}}^{r_{\text{out}}} 2\pi \Sigma r^3 \Omega dr \simeq \frac{2 - p}{5/2 - p} M_d \sqrt{GM_{\star} r_{\text{out}}}, \quad (2.9)$$

$$S = k_{\star} M_{\star} R_{\star}^2 \Omega_{\star}. \quad (2.10)$$

Here $k_{\star} \simeq 0.2$ for fully convective stars (e.g. Chandrasekhar 1939). The binary has orbital angular momentum $\mathbf{L}_b = L_b \hat{\mathbf{l}}_b$. Because typical star-disk-binary systems satisfy $L_b \gg L_d, S$, we take $\hat{\mathbf{l}}_b$ to be fixed for the remainder of this work.

2.3 Disk Warping

When $\alpha \lesssim H/r$ (α is the Shakura-Sunyaev viscosity parameter, H is the disk scaleheight), which is satisfied for protostellar disks (e.g. Rafikov 2017), the main internal torque enforcing disk rigidity and coherent precession comes from bending wave propagation [Papaloizou & Lin, 1995, Lubow & Ogilvie,

2000]. As bending waves travel at $1/2$ of the sound speed, the wave crossing time is of order $t_{\text{bw}} = 2(r/H)\Omega^{-1}$. When t_{bw} is longer than the characteristic precession times ω_{db}^{-1} or ω_{ds}^{-1} from an external torque, significant disk warps can be induced. In the extreme nonlinear regime, disk breaking may be possible [Larwood et al., 1996, Doğan et al., 2015]. To compare t_{bw} with ω_{sd}^{-1} and ω_{db}^{-1} , we adopt the disk sound speed profile

$$\begin{aligned} c_s(r) &= H(r)\Omega(r) = h_{\text{out}} \sqrt{\frac{GM_\star}{r_{\text{out}}}} \left(\frac{r_{\text{out}}}{r}\right)^q \\ &= h_{\text{in}} \sqrt{\frac{GM_\star}{r_{\text{in}}}} \left(\frac{r_{\text{in}}}{r}\right)^q, \end{aligned} \quad (2.11)$$

where $h_{\text{in}} = H(r_{\text{in}})/r_{\text{in}}$ and $h_{\text{out}} = H(r_{\text{out}})/r_{\text{out}}$. Passively heated disks have $q \approx 0.0 - 0.3$ [Chiang & Goldreich, 1997], while actively heated disks have $q \approx 3/8$ [Lynden-Bell & Pringle, 1974]. We find

$$t_{\text{bw}}\omega_{\text{sd}} = 4.7 \times 10^{-4} \left(\frac{0.1}{h_{\text{in}}}\right) \left(\frac{k_{\text{q}}}{0.1}\right) \frac{\bar{R}_\star^2}{\bar{r}_{\text{in}}^2} \left(\frac{r}{r_{\text{in}}}\right)^{q-7/2}, \quad (2.12)$$

$$t_{\text{bw}}\omega_{\text{db}} = 1.7 \times 10^{-2} \left(\frac{0.1}{h_{\text{out}}}\right) \frac{\bar{M}_\text{b}\bar{r}_{\text{out}}^3}{\bar{M}_\star\bar{a}_\text{b}^3} \left(\frac{r}{r_{\text{out}}}\right)^{q+3/2}. \quad (2.13)$$

Thus, we expect the small warp approximation to be valid everywhere in the disk. This expectation is confirmed by our detailed calculation of disk warps presented later in this section.

Although the disk is flat to a good approximation, the interplay between the disk warp/twist and viscous dissipation can lead to appreciable damping of the misalignment between the disk and the external perturber (i.e., the oblate star or the binary companion). In particular, when an external torque \mathbf{T}_{ext} (per unit mass) is applied to a disk in the bending wave regime (which could be either \mathbf{T}_{db} or \mathbf{T}_{ds}), the disk's viscosity causes the disk normal to develop a small twist, of order

$$\frac{\partial \hat{\mathbf{l}}}{\partial \ln r} \sim \frac{4\alpha}{c_s^2} \mathbf{T}_{\text{ext}}. \quad (2.14)$$

The detailed derivation of Eq. (2.14) is contained in Sections 2.3.1-2.3.3. Since $\mathbf{T}_{\text{ext}} \propto \hat{\mathbf{l}}_{\text{ext}} \times \hat{\mathbf{l}}$ ($\hat{\mathbf{l}}_{\text{ext}}$ is the axis around which $\hat{\mathbf{l}}$ precesses), where the viscous twist interacts with the external torque, effecting the evolution of $\hat{\mathbf{l}}$ over viscous timescales. To an order of magnitude, we have

$$\left| \frac{d\hat{\mathbf{l}}}{dt} \right|_{\text{visc}} \sim \left\langle \left(\frac{4\alpha}{c_s^2} \right) \frac{\mathbf{T}_{\text{ext}}^2}{r^2 \Omega} \right\rangle \sim \left\langle \frac{4\alpha}{c_s^2} (r^2 \Omega) \omega_{\text{ext}}^2 \right\rangle, \quad (2.15)$$

where ω_{ext} is either ω_{ds} or ω_{db} , and $\langle \dots \rangle$ implies proper average over r .

We now study the disk warp and viscous evolution quantitatively, using the formalism describing the structure and evolution of circular, weakly warped disks in the bending wave regime. The relevant equations have been derived by a number of authors [Papaloizou & Lin, 1995, Demianski & Ivanov, 1997, Lubow & Ogilvie, 2000]. We choose the formalism of Lubow & Ogilvie [2000] and Lubow, Ogilvie, & Pringle [2002] (see also Ogilvie 2006 when $|\partial\hat{\mathbf{l}}/\partial \ln r| \sim 1$), where the evolution of the disk is governed by

$$\Sigma r^2 \Omega \frac{\partial \hat{\mathbf{l}}}{\partial t} = \Sigma \mathbf{T}_{\text{ext}} + \frac{1}{r} \frac{\partial \mathbf{G}}{\partial r}, \quad (2.16)$$

$$\frac{\partial \mathbf{G}}{\partial t} = \left(\frac{\Omega^2 - \kappa^2}{2\Omega} \right) \hat{\mathbf{l}} \times \mathbf{G} - \alpha \Omega \mathbf{G} + \frac{\Sigma c_s^2 r^3 \Omega}{4} \frac{\partial \hat{\mathbf{l}}}{\partial r}, \quad (2.17)$$

where \mathbf{T}_{ext} is the external torque per unit mass acting on the disk, $\kappa = (2\Omega/r)\partial(r^2\Omega)/\partial r|_{z=0}$ is the epicyclic frequency, and \mathbf{G} is the internal torque, which arises from slightly eccentric fluid particles with velocities sheared around the disk mid-plane [Demianski & Ivanov, 1997]. Eq. (2.16) is the 2D momentum equation generalized to non-coplanar disks. Eq. (2.17) is related to how internal torques generated from disk warps are communicated across the disk under the influence of viscosity and precession from non-Keplarian epicyclic frequencies. See Nixon & King [2016] for a qualitative discussion and review of Eqs. (2.16)-(2.17).

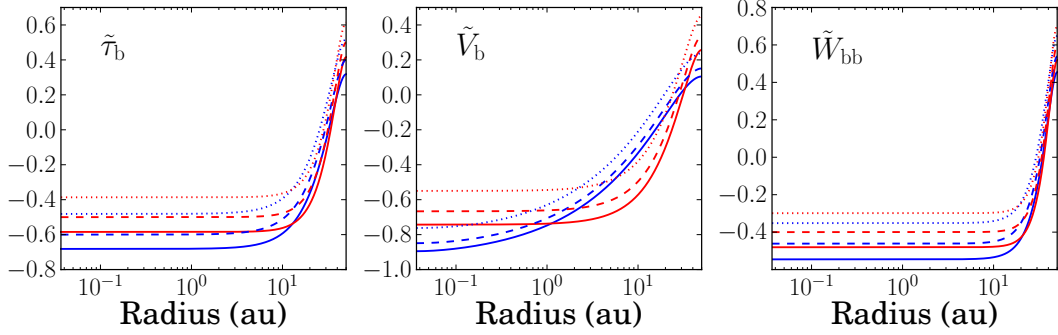


Figure 2.1: The rescaled radial functions [see Eq. (2.34) for rescaling] $\tilde{\tau}_b$ [Eq. (2.30)], \tilde{V}_b [Eq. (2.31)], and \tilde{W}_{bb} [Eq. (2.32)]. We take (p, q) values [Eq. (2.7) and (2.11)] of $p = 0.5$ (solid), $p = 1.0$ (dashed), and $p = 1.5$ (dotted) with $q = 0.0$ (blue) and $q = 0.5$ (red). All other parameters take their canonical values [Eq. (2.5)]. The re-scaled radial functions trace out the viscous twist (\tilde{V}_b) and warp ($\tilde{\tau}_b, \tilde{W}_{bb}$) profiles of the disk due to the gravitational torque from the binary companion.

p	q	\mathcal{U}_b	\mathcal{V}_b	\mathcal{W}_{bb}
0.5	0.5	0.857	0.857	0.857
1.0	0.5	1.00	1.00	1.00
1.5	0.5	1.20	1.20	1.20
0.5	0.0	1.65	3.67	1.32
1.0	0.0	1.93	4.26	1.54
1.5	0.0	2.31	5.02	1.85

Table 2.1: Dimensionless coefficients \mathcal{U}_b [Eq. (2.35)], \mathcal{V}_b [Eq. (2.36)], and \mathcal{W}_{bb} [Eq. (2.37)] tabulated for various p and q values [Eqs. (2.7) and (2.11)]. All the parameter values are canonical [Eq. (2.5)]. When varying q , we fix $h_{\text{out}} = 0.1$.

We are concerned with two external torques acting on different regions of the disk. For clarity, we break up our calculations into three subsections, considering disk warps produced by individual torques before examining the combined effects.

2.3.1 Disk Warp Induced by Binary Companion

The torque from an external binary companion is given by Eq. (2.1). The companion also gives rise to a non-Keplarian epicyclic frequency, given by

$$\frac{\Omega^2 - \kappa^2}{2\Omega} = \omega_{\text{db}} P_2(\hat{\mathbf{l}} \cdot \hat{\mathbf{l}}_b), \quad (2.18)$$

where P_l are Legendre polynomials.

To make analytic progress, we take advantage of our expectation that $|\partial \hat{\mathbf{l}} / \partial \ln r| \ll 1$ since $t_{\text{bw}} \omega_{\text{db}} \ll 1$ [see Eq. (2.13)]. Specifically, we take

$$\hat{\mathbf{l}}(r, t) = \hat{\mathbf{l}}_d(t) + \mathbf{l}_1(r, t) + \dots, \quad (2.19)$$

$$\mathbf{G}(r, t) = \mathbf{G}_0(r, t) + \mathbf{G}_1(r, t) + \dots, \quad (2.20)$$

where $|\mathbf{l}_1| \ll |\hat{\mathbf{l}}_d| = 1$. Here, $\mathbf{G}_0(r, t)$ is the internal torque maintaining coplanarity of $\hat{\mathbf{l}}_d(t)$, $\mathbf{G}_1(r, t)$ is the internal torque maintaining the leading order warp profile $\mathbf{l}_1(r, t)$, etc. To leading order, Eq. (2.16) becomes

$$\Sigma r^2 \Omega \frac{d\hat{\mathbf{l}}_d}{dt} = -\Sigma r^2 \Omega \omega_{\text{db}} (\hat{\mathbf{l}}_d \cdot \hat{\mathbf{l}}_b) \hat{\mathbf{l}}_b \times \hat{\mathbf{l}}_d + \frac{1}{r} \frac{\partial \mathbf{G}_0}{\partial r}. \quad (2.21)$$

Integrating (2.21) over $r dr$, and using the boundary condition

$$G_0(r_{\text{in}}, t) = G_0(r_{\text{out}}, t) = 0, \quad (2.22)$$

we obtain

$$\frac{d\hat{\mathbf{l}}_d}{dt} = -\tilde{\omega}_{\text{db}} (\hat{\mathbf{l}}_d \cdot \hat{\mathbf{l}}_b) \hat{\mathbf{l}}_b \times \hat{\mathbf{l}}_d, \quad (2.23)$$

where $\tilde{\omega}_{\text{db}}$ is given by

$$\begin{aligned} \tilde{\omega}_{\text{db}} &= \frac{2\pi}{L_d} \int_{r_{\text{in}}}^{r_{\text{out}}} \omega_{\text{db}} \Sigma r^3 \Omega dr \\ &\simeq \frac{3(5/2 - p)}{4(4 - p)} \left(\frac{M_b}{M_\star} \right) \left(\frac{a_b}{r_{\text{out}}} \right)^3 \sqrt{\frac{GM_\star}{r_{\text{out}}^3}}. \end{aligned} \quad (2.24)$$

The physical meaning of $\hat{\mathbf{l}}_d$ thus becomes clear: $\hat{\mathbf{l}}_d$ is the unit total angular momentum vector of the disk, or

$$\hat{\mathbf{l}}_d \equiv \frac{2\pi}{L_d} \int_{r_{in}}^{r_{out}} \Sigma r^3 \Omega \hat{\mathbf{l}}(r, t) dr. \quad (2.25)$$

Using Eqs. (2.22) and (2.23), we may solve Eq. (2.21) for $\mathbf{G}_0(r, t)$:

$$\mathbf{G}_0(r, t) = g_b(r)(\hat{\mathbf{l}}_d \cdot \hat{\mathbf{l}}_b)\hat{\mathbf{l}}_b \times \hat{\mathbf{l}}_d, \quad (2.26)$$

where

$$g_b(r) = \int_{r_{in}}^r (\omega_{db} - \tilde{\omega}_{db}) \Sigma r'^3 \Omega dr'. \quad (2.27)$$

Using Eqs. (2.26) and (2.17), and requiring that \mathbf{l}_1 not contribute to the total disk angular momentum vector, or

$$\int_{r_{in}}^{r_{out}} \Sigma r^3 \Omega \mathbf{l}_1(r, t) dr = 0, \quad (2.28)$$

we obtain the leading order warp $\mathbf{l}_1(r, t)$:

$$\begin{aligned} \mathbf{l}_1(r, t) = & -\tilde{\omega}_{db}\tau_b(\hat{\mathbf{l}}_d \cdot \hat{\mathbf{l}}_b)^2 \hat{\mathbf{l}}_b \times (\hat{\mathbf{l}}_b \times \hat{\mathbf{l}}_d) \\ & - W_{bb}(\hat{\mathbf{l}}_d \cdot \hat{\mathbf{l}}_b)P_2(\hat{\mathbf{l}}_d \cdot \hat{\mathbf{l}}_b)\hat{\mathbf{l}}_d \times (\hat{\mathbf{l}}_b \times \hat{\mathbf{l}}_d) \\ & + V_b(\hat{\mathbf{l}}_d \cdot \hat{\mathbf{l}}_b)\hat{\mathbf{l}}_b \times \hat{\mathbf{l}}_d, \end{aligned} \quad (2.29)$$

where

$$\tau_b(r) = \int_{r_{in}}^r \frac{4g_b}{\Sigma c_s^2 r'^3 \Omega} dr' - \tau_{b0}, \quad (2.30)$$

$$V_b(r) = \int_{r_{in}}^r \frac{4\alpha g_b}{\Sigma c_s^2 r'^3} dr' - V_{b0}, \quad (2.31)$$

$$W_{bb}(r) = \int_{r_{in}}^r \frac{4\omega_{db} g_b}{\Sigma c_s^2 r'^3 \Omega} dr' - W_{bb0}, \quad (2.32)$$

and the constants X_0 of the functions $X(r)$ (either $\tau_b(r)$, $V_b(r)$, or $W_{bb}(r)$) are determined by requiring

$$\int_{r_{in}}^{r_{out}} \Sigma r^3 \Omega X dr = 0. \quad (2.33)$$

Notice the radial functions τ_b , V_b , and W_{bb} trace out the disk's warp profile $|l_1(r)|$ due to the binary companion's gravitational torque. Because the magnitudes for the radial functions $(2\pi/\text{Myr})\tau_b$, V_b , and W_{bb} are much smaller than unity everywhere [see Eqs. (2.35)-(2.37)], we define the re-scaled radial function $\tilde{X}(r) = \tilde{\tau}_b$, \tilde{V}_b , and \tilde{W}_{bb} as

$$\tilde{X}(r) \equiv X(r)/[X(r_{\text{out}}) - X(r_{\text{in}})]. \quad (2.34)$$

Figure 2.1 plots the dimensionless radial functions $\tilde{\tau}_b$, \tilde{V}_b , and \tilde{W}_{bb} for the canonical parameters of the star-disk-binary system [Eq. (2.5)]. The scalings of the radial functions evaluated at the outer disk radius are

$$\begin{aligned} \tau_b(r_{\text{out}}) - \tau_b(r_{\text{in}}) &= -1.82 \times 10^{-5} \mathcal{U}_b \\ &\times \left(\frac{0.1}{h_{\text{out}}}\right)^2 \frac{\bar{M}_b \bar{r}_{\text{out}}^{9/2}}{\bar{M}_\star^{3/2} \bar{a}_b^6} \frac{\text{Myr}}{2\pi}, \end{aligned} \quad (2.35)$$

$$\begin{aligned} V_b(r_{\text{out}}) - V_b(r_{\text{in}}) &= -1.54 \times 10^{-3} \mathcal{V}_b \\ &\times \left(\frac{\alpha}{0.01}\right) \left(\frac{0.1}{h_{\text{out}}}\right)^2 \frac{\bar{M}_b \bar{r}_{\text{out}}^3}{\bar{M}_\star \bar{a}_b^3}, \end{aligned} \quad (2.36)$$

$$\begin{aligned} W_{bb}(r_{\text{out}}) - W_{bb}(r_{\text{in}}) &= -8.93 \times 10^{-5} \mathcal{W}_{bb} \\ &\times \left(\frac{0.1}{h_{\text{out}}}\right)^2 \frac{\bar{M}_b^2 \bar{r}_{\text{out}}^6}{\bar{M}_\star^2 \bar{a}_b^6}. \end{aligned} \quad (2.37)$$

Equations (2.35)-(2.37) provide an estimate for the misalignment angle between the disk's inner and outer orbital angular momentum vectors, or $|X(r_{\text{out}}) - X(r_{\text{in}})| \sim |\hat{l}(r_{\text{out}}, t) \times \hat{l}(r_{\text{in}}, t)|$, where $X = (2\pi/\text{Myr})\tau_b$, V_b , and W_{bb} . The dimensionless coefficients \mathcal{U}_b , \mathcal{V}_b , and \mathcal{W}_{bb} depend weakly on the parameters p , q , and $r_{\text{in}}/r_{\text{out}}$. Table 2.1 tabulates \mathcal{U}_b , \mathcal{V}_b , and \mathcal{W}_{bb} for values of p and q as indicated, with the canonical value of $r_{\text{in}}/r_{\text{out}}$ [Eq. (2.5)].

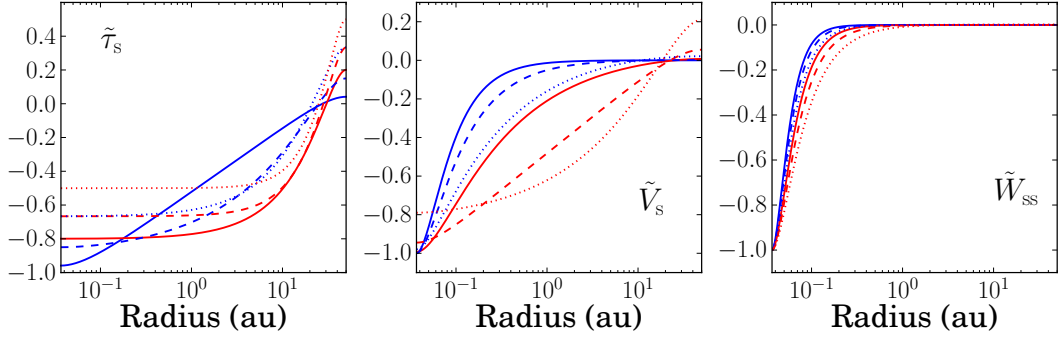


Figure 2.2: The rescaled radial functions [see Eq. (2.34) for rescaling] $\tilde{\tau}_s$ [Eq. (2.47)], \tilde{V}_s [Eq. (2.48)], and \tilde{W}_{ss} [Eq. (2.49)]. We take (p, q) values [Eq. (2.7) and (2.11)] of $p = 0.5$ (solid), $p = 1.0$ (dashed), and $p = 1.5$ (dotted) with $q = 0.0$ (blue) and $q = 0.5$ (red). Other parameters assume their canonical values [Eq. (2.5)]. The re-scaled radial functions trace out the viscous twist (\tilde{V}_s) and warp ($\tilde{\tau}_s, \tilde{W}_{ss}$) profiles of the disk due to the gravitational torque from the oblate star.

p	q	\mathcal{U}_s	\mathcal{V}_s	\mathcal{W}_{ss}
0.5	0.5	2.66	0.315	0.800
1.0	0.5	1.00	1.00	1.00
1.5	0.5	0.400	6.18	1.33
0.5	0.0	24.2	0.0735	0.457
1.0	0.0	4.28	0.110	0.533
1.5	0.0	1.20	0.207	0.639

Table 2.2: Dimensionless coefficients \mathcal{U}_s [Eq. (2.50)], \mathcal{V}_s [Eq. (2.51)], and \mathcal{W}_{ss} [Eq. (2.52)], for different values of p and q [Eqs. (2.7) and (2.11)]. All other parameter values are canonical [Eq. (2.5)]. When varying q , we fix $h_{\text{out}} = 0.1$.

2.3.2 Disk Warp Induced by Oblate Star

The torque on the disk from the oblate star is given by Eq. (2.3). The stellar quadrupole moment also gives rise to a non-Keplarian epicyclic frequency given by

$$\frac{\Omega^2 - \kappa^2}{2\Omega} = \omega_{\text{sd}} P_2(\hat{l} \cdot \hat{s}). \quad (2.38)$$

Equations (2.16)-(2.17) are coupled with the motion of the host star's spin axis:

$$S \frac{d\hat{s}}{dt} = - \int_{r_{\text{in}}}^{r_{\text{out}}} [2\pi \Sigma r^3 \Omega \omega_{\text{sd}} (\hat{s} \cdot \hat{l}) \hat{l} \times \hat{s}] dr, \quad (2.39)$$

Expanding $\hat{\mathbf{l}}$ and \mathbf{G} according to Eqs. (2.19) and (2.20), integrating Eq. (2.16) over $r dr$, and using the boundary condition (2.22), we obtain the leading order evolution equations

$$\frac{d\hat{\mathbf{s}}}{dt} = -\tilde{\omega}_{sd}(\hat{\mathbf{s}} \cdot \hat{\mathbf{l}}_d)\hat{\mathbf{l}}_d \times \hat{\mathbf{s}}, \quad (2.40)$$

$$\frac{d\hat{\mathbf{l}}_d}{dt} = -\omega_{sd}(\hat{\mathbf{l}}_d \cdot \hat{\mathbf{s}})\hat{\mathbf{s}} \times \hat{\mathbf{l}}_d, \quad (2.41)$$

where (assuming $r_{in} \ll r_{out}$)

$$\begin{aligned} \tilde{\omega}_{ds} &= \frac{2\pi}{L_d} \int_{r_{in}}^{r_{out}} \omega_{ds} \Sigma r^3 \Omega dr \\ &\simeq \frac{3(5/2-p)k_q}{2(1+p)} \frac{R_\star^2 \bar{\Omega}_\star^2}{r_{out}^{1-p} r_{in}^{1+p}} \sqrt{\frac{GM_\star}{r_{out}^3}}, \end{aligned} \quad (2.42)$$

$$\begin{aligned} \tilde{\omega}_{sd} &= (L_d/S)\tilde{\omega}_{ds} \\ &\simeq \frac{3(2-p)k_q}{2(1+p)k_\star} \left(\frac{M_d}{M_\star} \right) \bar{\Omega}_\star \frac{\sqrt{GM_\star R_\star^3}}{r_{out}^{2-p} r_{in}^{1+p}}. \end{aligned} \quad (2.43)$$

With $d\hat{\mathbf{l}}_d/dt$ and $d\hat{\mathbf{s}}/dt$ determined, Eq. (2.16) may be integrated to obtain the leading order internal torque:

$$\mathbf{G}_0(r, t) = g_s(r)(\hat{\mathbf{l}}_d \cdot \hat{\mathbf{s}})\hat{\mathbf{s}} \times \hat{\mathbf{l}}_d, \quad (2.44)$$

where

$$g_s(r) = \int_{r_{in}}^r (\omega_{sd} - \tilde{\omega}_s) \Sigma r'^3 \Omega dr'. \quad (2.45)$$

Similarly, the leading order warp profile is

$$\begin{aligned} \mathbf{l}_1(r, t) &= -\tilde{\omega}_{sd}\tau_s(\hat{\mathbf{l}}_d \cdot \hat{\mathbf{s}})^2(\hat{\mathbf{l}}_d \times \hat{\mathbf{s}}) \times \hat{\mathbf{l}}_d \\ &\quad - \omega_{sd}\tau_s(\hat{\mathbf{l}}_d \cdot \hat{\mathbf{s}})^2\hat{\mathbf{s}} \times (\hat{\mathbf{s}} \times \hat{\mathbf{l}}_d) \\ &\quad - W_{ss}(\hat{\mathbf{l}}_d \cdot \hat{\mathbf{s}})P_2(\hat{\mathbf{l}}_d \cdot \hat{\mathbf{s}})\hat{\mathbf{l}}_d \times (\hat{\mathbf{s}} \times \hat{\mathbf{l}}_d) \\ &\quad + V_s(\hat{\mathbf{l}}_d \cdot \hat{\mathbf{s}})\hat{\mathbf{s}} \times \hat{\mathbf{l}}_d, \end{aligned} \quad (2.46)$$

where

$$\tau_s(r) = \int_{r_{\text{in}}}^r \frac{4g_s}{\Sigma c_s^2 r'^3 \Omega} dr' - \tau_{s0}, \quad (2.47)$$

$$V_s(r) = \int_{r_{\text{in}}}^r \frac{4\alpha g_s}{\Sigma c_s^2 r'^3} dr' - V_{s0}, \quad (2.48)$$

$$W_{ss}(r) = \int_{r_{\text{in}}}^r \frac{4\omega_{sd} g_s}{\Sigma c_s^2 r'^3 \Omega} dr' - W_{ss0}. \quad (2.49)$$

In Figure 2.2, we plot the rescaled radial functions $\tilde{\tau}_s$, \tilde{V}_s , and \tilde{W}_{ss} for various p and q values, tracing out the re-scaled warp profile across the radial extent of the disk due to the oblate star's torque. The radial function differences evaluated at the disk's outer and inner truncation radii are

$$\begin{aligned} \tau_s(r_{\text{out}}) - \tau_s(r_{\text{in}}) &= 2.21 \times 10^{-6} \mathcal{U}_s \left(\frac{0.1}{h_{\text{out}}} \right)^2 \left(\frac{k_q}{0.1} \right) \\ &\times \left(\frac{1358 \bar{r}_{\text{out}}}{\bar{r}_{\text{in}}} \right)^{p-1} \frac{\bar{R}_\star^2 \bar{r}_{\text{out}}^{3/2}}{\bar{r}_{\text{in}}^2 \bar{M}_\star^{1/2}} \left(\frac{\bar{\Omega}_\star}{0.1} \right)^2 \frac{\text{Myr}}{2\pi}, \end{aligned} \quad (2.50)$$

$$\begin{aligned} V_s(r_{\text{out}}) - V_s(r_{\text{in}}) &= 1.13 \times 10^{-3} \mathcal{V}_s \\ &\times \left(\frac{\alpha}{0.01} \right) \left(\frac{0.1}{h_{\text{in}}} \right)^2 \left(\frac{k_q}{0.1} \right) \frac{\bar{R}_\star^2}{\bar{r}_{\text{in}}^2} \left(\frac{\bar{\Omega}_\star}{0.1} \right)^2, \end{aligned} \quad (2.51)$$

$$\begin{aligned} W_{ss}(r_{\text{out}}) - W_{ss}(r_{\text{in}}) &= 4.39 \times 10^{-7} \mathcal{W}_{ss} \\ &\times \left(\frac{k_q}{0.1} \right)^2 \left(\frac{0.1}{h_{\text{in}}} \right)^2 \frac{\bar{R}_\star^4}{\bar{r}_{\text{in}}^4} \left(\frac{\bar{\Omega}_\star}{0.1} \right)^2. \end{aligned} \quad (2.52)$$

Equations (2.50)-(2.52) provide an estimate for the misalignment angle between the disk's outer and inner orbital angular momentum unit vectors $|\hat{l}(r_{\text{out}}, t) \times \hat{l}(r_{\text{in}}, t)|$ due to the oblate star's torque. The dimensionless coefficients \mathcal{U}_s , \mathcal{V}_s , and \mathcal{W}_{ss} depend weakly on the parameters p , q , and $r_{\text{in}}/r_{\text{out}}$. In Table 2.2, we tabulate \mathcal{U}_s , \mathcal{V}_s , and \mathcal{W}_{ss} for the p and q values indicated, with $r_{\text{in}}/r_{\text{out}}$ taking the canonical value [Eq. (2.5)].

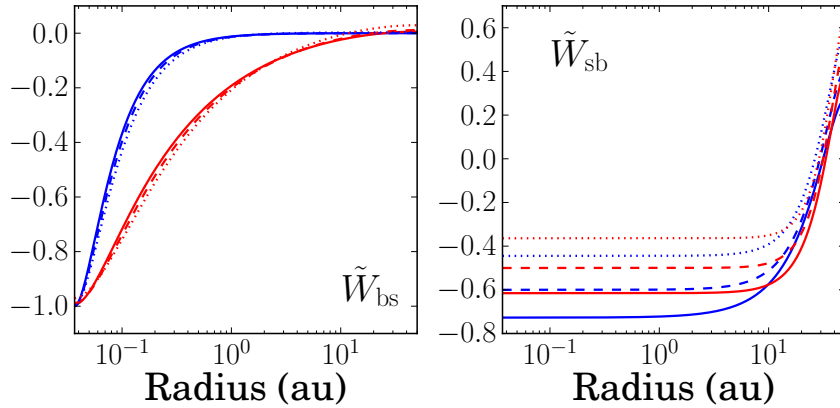


Figure 2.3: The rescaled radial functions [see Eq. (2.34) for rescaling] \tilde{W}_{bs} [Eq. (2.54)], and \tilde{W}_{sb} [Eq. (2.55)]. We take (p, q) values [Eq. (2.7) and (2.11)] of $p = 0.5$ (solid), $p = 1.0$ (dashed), and $p = 1.5$ (dotted) with $q = 0.0$ (blue) and $q = 0.5$ (red). We take all parameters to be canonical [Eq. (2.5)]. The re-scaled radial functions trace out the the warp ($\tilde{W}_{\text{bs}}, \tilde{W}_{\text{sb}}$) profiles of the disk due to the interaction between the binary companion and oblate star torques (see text for discussion).

p	q	\mathcal{W}_{bs}	\mathcal{W}_{sb}
0.5	0.5	2.13	0.917
1.0	0.5	1.00	1.00
1.5	0.5	0.457	1.06
0.5	0.0	4.57	312
1.0	0.0	1.93	319
1.5	0.0	0.823	307

Table 2.3: Dimensionless coefficients \mathcal{W}_{bs} [Eq. (2.56)] and \mathcal{W}_{sb} [Eq. (2.57)] for values of p and q as indicated [Eqs. (2.7) and (2.11)]. All parameter values are canonical [Eq. (2.5)]. When varying q , we fix $h_{\text{out}} = 0.1$.

2.3.3 Disk Warps Induced by Combined Torques

The combined torques from the distant binary and oblate star are given by Eqs. (2.1) and (2.3), and the non-Keplarian epicyclic frequencies are given by Eqs. (2.18) and (2.38). Using the same procedure as Sections 2.3.1-2.3.2, the leading order correction to the disk's warp is

$$\mathbf{l}_1(r, t) = (\mathbf{l}_1)_{\text{bin}} + (\mathbf{l}_1)_{\text{star}}$$

$$\begin{aligned}
& - \omega_{sd}\tau_b(\hat{l}_d \cdot \hat{s})[(\hat{s} \times \hat{l}_d) \cdot \hat{l}_b]\hat{l}_b \times \hat{l}_d \\
& - \omega_{sd}\tau_b(\hat{l}_d \cdot \hat{l}_b)(\hat{l}_d \cdot \hat{s})\hat{l}_b \times (\hat{s} \times \hat{l}_d) \\
& - \tilde{\omega}_{db}\tau_s(\hat{l}_d \cdot \hat{l}_b)[(\hat{l}_b \times \hat{l}_d) \cdot \hat{s}]\hat{s} \times \hat{l}_d \\
& - \tilde{\omega}_{db}\tau_s(\hat{l}_d \cdot \hat{s})(\hat{l}_d \cdot \hat{l}_b)\hat{s} \times (\hat{l}_b \times \hat{l}_d) \\
& - W_{sb}(\hat{l}_d \cdot \hat{l}_b)P_2(\hat{l}_d \cdot \hat{s})\hat{l}_d \times (\hat{l}_b \times \hat{l}_d) \\
& - W_{bs}(\hat{l}_d \cdot \hat{s})P_2(\hat{l}_d \cdot \hat{l}_b)\hat{l}_d \times (\hat{s} \times \hat{l}_d),
\end{aligned} \tag{2.53}$$

where $(l_1)_{\text{bin}}$ is Eq. (2.29), $(l_1)_{\text{star}}$ is Eq. (2.46), τ_b and τ_s are given in Eqs. (2.30) and (2.47), and

$$W_{bs}(r) = \int_{r_{in}}^r \frac{4\omega_{db}g_s}{\Sigma c_s^2 r'^3 \Omega} dr' - W_{bs0}, \tag{2.54}$$

$$W_{sb}(r) = \int_{r_{in}}^r \frac{4\omega_{sd}g_b}{\Sigma c_s^2 r'^3 \Omega} dr' - W_{sb0}. \tag{2.55}$$

Notice l_1 is not simply the sum $l_1 = (l_1)_{\text{bin}} + (l_1)_{\text{star}}$. The cross $\omega_{ds}\tau_b$ ($\omega_{db}\tau_s$) terms come from the motion of the internal torque resisting T_{ds} (T_{db}) induced by T_{db} (T_{ds}). The cross W_{bs} (W_{sb}) terms come from the internal torque resisting T_{ds} (T_{db}) twisted by the non-Keplarian epicyclic frequency induced by the binary [Eq. (2.18)] [star, Eq. (2.38)]. In Figure 2.3, we plot the re-scaled radial functions \tilde{W}_{bs} and \tilde{W}_{sb} for various p and q values, tracing out the warp profile across the radial extent of the disk due to the combined binary and stellar torques. The radial functions W_{bs} and W_{sb} evaluated at the disk's outer and inner truncation radii are

$$\begin{aligned}
W_{bs}(r_{out}) - W_{bs}(r_{in}) &= -7.23 \times 10^{-6} \mathcal{W}_{bs} \left(\frac{0.1}{h_{out}} \right)^2 \\
&\times \left(\frac{k_q}{0.1} \right) \left(\frac{1358 \bar{r}_{out}}{\bar{r}_{in}} \right)^{p-1} \frac{\bar{M}_b \bar{R}_\star^2 \bar{r}_{out}^3}{\bar{M}_\star \bar{a}_b^3 \bar{r}_{in}^2} \left(\frac{\bar{\Omega}_\star}{0.1} \right)^2,
\end{aligned} \tag{2.56}$$

$$\begin{aligned}
W_{sb}(r_{out}) - W_{sb}(r_{in}) &= 1.23 \times 10^{-9} \mathcal{W}_{sb} \\
&\times \left(\frac{0.1}{h_{out}} \right)^2 \left(\frac{k_q}{0.1} \right) \frac{\bar{M}_b \bar{R}_\star \bar{r}_{out}}{\bar{M}_\star \bar{a}_b^3} \left(\frac{\bar{\Omega}_\star}{0.1} \right)^2.
\end{aligned} \tag{2.57}$$

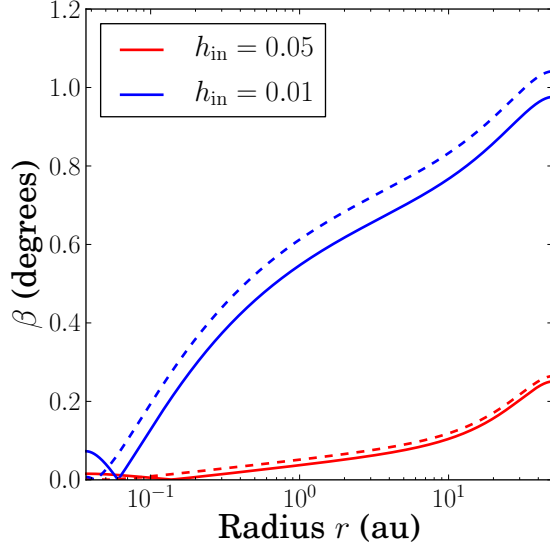


Figure 2.4: Disk misalignment angle β [Eq. (2.58)] as a function of radius r , for the h_{in} [Eq. (2.11)] values indicated, all for $h_{\text{out}} = 0.05$ [Eq. (2.11)]. The disk masses are $M_d = 0.1 M_\odot$ (solid) and $M_d = 0.01 M_\odot$ (dashed), with $p = 1$ [Eq. (2.7)], $\alpha = 0.01$, $a_b = 300 \text{ au}$, and \hat{s} , \hat{l}_d , and \hat{l}_b lying in the same plane with $\theta_{\text{sd}} = \theta_{\text{db}} = 30^\circ$.

These provide an estimate for the misalignment angle between the disk's outer and inner orbital angular momentum unit vectors $|\hat{l}(r_{\text{out}}, t) \times \hat{l}(r_{\text{in}}, t)|$ due to the binary and stellar torques. The dimensionless coefficients \mathcal{W}_{bs} and \mathcal{W}_{sb} depend on the parameters p , q , and $r_{\text{in}}/r_{\text{out}}$. Table 2.3 tabulates \mathcal{W}_{bs} and \mathcal{W}_{sb} for several p and q values, with $r_{\text{in}}/r_{\text{out}}$ taking the canonical value [Eq. (2.5)].

2.3.4 Disk Warp Profile: Summary

In the previous subsections, we have derived semi-analytic expressions for the disk warp profiles due to the combined torques from the oblate host star and the binary companion. Our general conclusion is that the warp is quite small across the whole disk. We illustrate this conclusion with a few examples (Figs. 2.4-2.5). We define the disk misalignment angle $\beta = \beta(r, t)$ as the misalignment of the

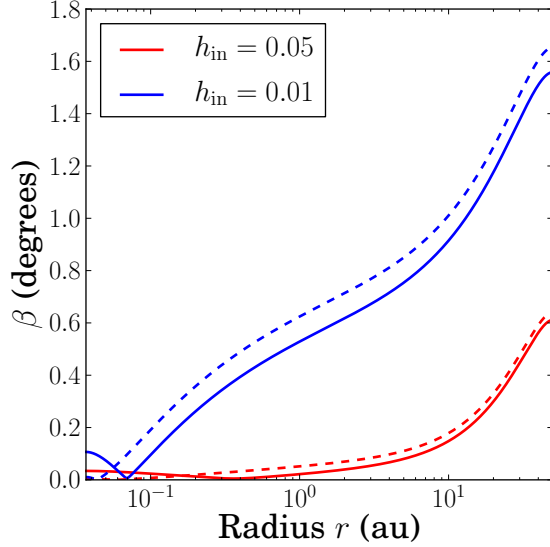


Figure 2.5: Same as Fig. 2.4, except $a_b = 200$ au.

disk's local angular momentum unit vector $\hat{l}(r, t)$ by

$$\sin \beta(r, t) \equiv |\hat{l}(r, t) \times \hat{l}_d(t)|, \quad (2.58)$$

where \hat{l}_d is unit vector along the total angular momentum of the disk [Eq. (2.25)].

Figures 2.4-2.5 that the disk warp angle is less than a few degrees for the range of parameters considered. When $h_{\text{in}} = 0.05$, the binary's torque has the strongest influence on the disk's warp profile. As a result, the disk warp ($\partial \beta / \partial \ln r$) is strongest near the disk's outer truncation radius ($r \gtrsim 10$ au). When $h_{\text{in}} = 0.01$, the spinning star's torque has a strong influence on the disk's warp profile, and the warp becomes large near the inner truncation radius ($r \lesssim 1$ au).

Notice that the differences between the high disk-mass ($M_d = 0.1 M_\odot$, solid lines) and low disk-mass ($M_d = 0.01 M_\odot$, dashed lines) are marginal. This is because only the precession rate of the star around the disk $\tilde{\omega}_{\text{sd}}$ [Eq. (2.43)] depends on the disk mass, and it enters the disk warp profile only through the term $\tilde{\omega}_{\text{sd}} \tau_s$ [see Eq. (2.46)]. Because the disk's internal torque from bending waves is purely

p	q	Γ_b	Γ_s	$\Gamma_{(bs)}$
0.5	0.5	0.698	0.522	1.70
1.0	0.5	1.00	1.00	1.00
1.5	0.5	1.41	2.86	0.527
0.5	0.0	1.44	0.0964	8.64
1.0	0.0	2.31	0.0970	5.38
1.5	0.0	3.82	0.108	3.05

Table 2.4: Dimensionless viscosity coefficients Γ_b [Eq. (5.47)], Γ_s [Eq. (2.70)], and $\Gamma_{(bs)}$ [Eq. (2.71)], for various p and q values. All other parameter values are canonical [Eq. (2.5)].

hydrodynamical, the other terms in the disk warp profile are independent of the disk mass.

2.3.5 Viscous Evolution

As noted above, when a hydrodynamical disk in the bending wave regime is torqued externally, viscosity causes the disk to develop a small twist, which exerts a back-reaction torque on the disk. When torqued by a central oblate star and a distant binary, the leading order viscous twist in the disk is

$$(\mathbf{l}_1)_{\text{visc}} = V_b(\hat{\mathbf{l}}_b \cdot \hat{\mathbf{l}}_d)\hat{\mathbf{l}}_b \times \hat{\mathbf{l}}_d + V_s(\hat{\mathbf{s}} \cdot \hat{\mathbf{l}}_d)\hat{\mathbf{s}} \times \hat{\mathbf{l}}_d, \quad (2.59)$$

where V_b and V_s are defined in Eqs. (2.31) and (2.48). All other terms in Eq. (2.53) are non-dissipative, and do not contribute to the alignment evolution of the disk. Inserting $(\mathbf{l}_1)_{\text{visc}}$ into Eqs. (2.16) and (2.39), and integrating over $2\pi r dr$, we obtain

$$\begin{aligned} \left(\frac{d\mathbf{L}_d}{dt} \right)_{\text{visc}} &= L_d \gamma_b (\hat{\mathbf{l}}_d \cdot \hat{\mathbf{l}}_b)^2 \hat{\mathbf{l}}_b \times (\hat{\mathbf{l}}_b \times \hat{\mathbf{l}}_d) \\ &\quad + L_d \gamma_s (\hat{\mathbf{l}}_d \cdot \hat{\mathbf{s}})^2 \hat{\mathbf{s}} \times (\hat{\mathbf{s}} \times \hat{\mathbf{l}}_d) \\ &\quad + L_d \gamma_{(bs)} (\hat{\mathbf{l}}_d \cdot \hat{\mathbf{l}}_b)(\hat{\mathbf{l}}_d \cdot \hat{\mathbf{s}}) \hat{\mathbf{l}}_b \times (\hat{\mathbf{s}} \times \hat{\mathbf{l}}_d) \end{aligned}$$

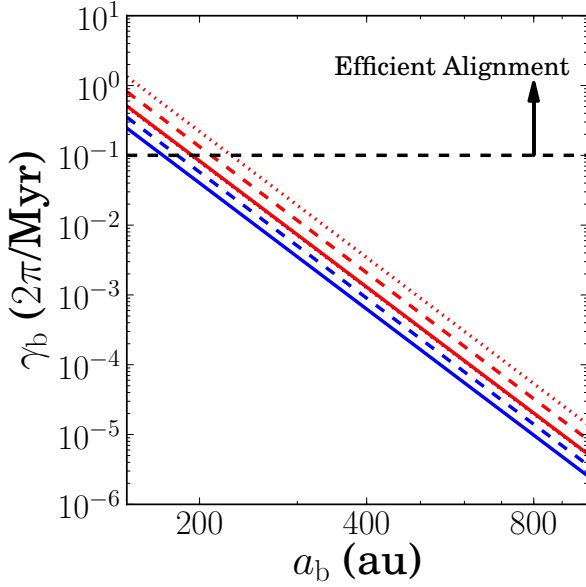


Figure 2.6: The damping rate γ_b [Eq. (5.47)] as a function of the binary semi-major axis a_b . We take the p [Eq. (2.7)] value to be $p = 0.5$ (solid), $p = 1.0$ (dashed), and $p = 1.5$ (dotted), with the q [Eq. (2.11)] value of $q = 0.0$ (blue) and $q = 0.5$ (red). We take all other parameter values to be canonical [Eq. (2.5)]. When varying q , we fix $h_{\text{out}} = 0.05$ [Eq. (2.11)]. When the damping rate $\gamma_b \gtrsim 0.1(2\pi/\text{Myr})$, viscous torques from disk warping may significantly decrease the mutual disk-binary inclination θ_{db} [Eq. (2.79)] over the disk's lifetime.

$$+ L_d \gamma_{(\text{bs})} (\hat{\mathbf{l}}_d \cdot \hat{\mathbf{s}}) (\hat{\mathbf{l}}_d \cdot \hat{\mathbf{l}}_b) \hat{\mathbf{s}} \times (\hat{\mathbf{l}}_b \times \hat{\mathbf{l}}_d), \quad (2.60)$$

$$\begin{aligned} \left(\frac{dS}{dt} \right)_{\text{visc}} &= -L_d \gamma_s (\hat{\mathbf{l}}_d \cdot \hat{\mathbf{s}})^2 \hat{\mathbf{s}} \times (\hat{\mathbf{s}} \times \hat{\mathbf{l}}_d) \\ &\quad - L_d \gamma_{(\text{bs})} (\hat{\mathbf{l}}_d \cdot \hat{\mathbf{s}}) (\hat{\mathbf{l}}_d \cdot \hat{\mathbf{l}}_b) \hat{\mathbf{s}} \times (\hat{\mathbf{l}}_b \times \hat{\mathbf{l}}_d), \end{aligned} \quad (2.61)$$

where

$$\begin{aligned} \gamma_b &\equiv \frac{2\pi}{L_d} \int_{r_{\text{in}}}^{r_{\text{out}}} \frac{4\alpha g_b^2}{\Sigma c_s^2 r^3} dr \\ &= -\frac{2\pi}{L_d} \int_{r_{\text{in}}}^{r_{\text{out}}} \Sigma r^3 \Omega (\omega_{\text{db}} - \tilde{\omega}_{\text{db}}) V_b dr, \end{aligned} \quad (2.62)$$

$$\begin{aligned} \gamma_s &\equiv \frac{2\pi}{L_d} \int_{r_{\text{in}}}^{r_{\text{out}}} \frac{4\alpha g_s^2}{\Sigma c_s^2 r^3} dr \\ &= -\frac{2\pi}{L_d} \int_{r_{\text{in}}}^{r_{\text{out}}} \Sigma r^3 \Omega (\omega_{\text{sd}} - \tilde{\omega}_{\text{sd}}) V_s dr, \end{aligned} \quad (2.63)$$

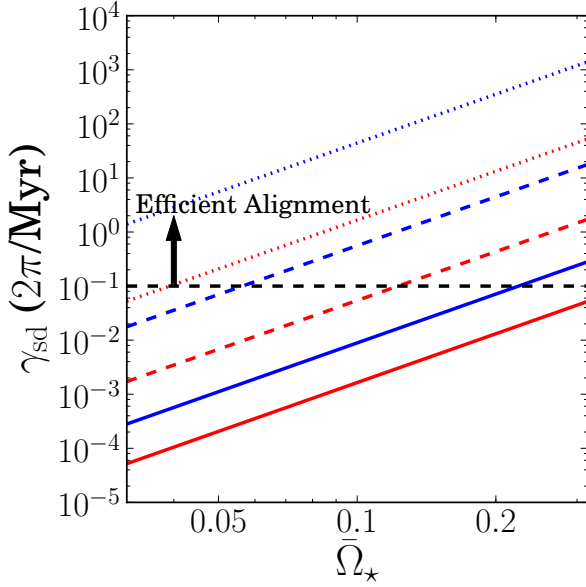


Figure 2.7: The damping rate γ_{sd} [Eq. (2.72)] as a function of the normalized stellar rotation frequency $\bar{\Omega}_\star$ [Eq. (2.5)]. We take the p [Eq. (2.7)] values to be $p = 0.5$ (solid), $p = 1.0$ (dashed), and $p = 1.5$ (dotted), with q [Eq. (2.11)] values of $q = 0.0$ (blue) and $q = 0.5$ (red). We take all other parameter values to be canonical [Eq. (2.5)]. When varying q , we fix $h_{\text{in}} = 0.03$ [Eq. (2.11)]. When the damping rate $\gamma_{\text{sd}} \gtrsim 0.1(2\pi/\text{Myr})$, viscous torques from disk warping may significantly decrease the mutual star-disk inclination θ_{sd} [Eq. (2.77)] over the disk's lifetime.

$$\begin{aligned} \gamma_{(\text{bs})} &\equiv \frac{2\pi}{L_d} \int_{r_{\text{in}}}^{r_{\text{out}}} \frac{4\alpha g_b g_s}{\Sigma c_s^2 r^3} dr \\ &= -\frac{2\pi}{L_d} \int_{r_{\text{in}}}^{r_{\text{out}}} \Sigma r^3 \Omega (\omega_{\text{sd}} - \tilde{\omega}_s) V_b dr \\ &= -\frac{2\pi}{L_d} \int_{r_{\text{in}}}^{r_{\text{out}}} \Sigma r^3 \Omega (\omega_{\text{db}} - \tilde{\omega}_{\text{db}}) V_s dr. \end{aligned} \quad (2.64)$$

When deriving Eqs. (2.60) and (2.61), we have neglected terms proportional to $\mathbf{l}_1 \cdot \hat{\mathbf{s}}$ or $\mathbf{l}_1 \cdot \hat{\mathbf{l}}_b$, as these only modify the dynamics by changing the star-disk and disk-binary precessional frequencies, respectively. Using

$$\frac{d\hat{\mathbf{l}}_d}{dt} = \frac{1}{L_d} \left(\frac{d\mathbf{L}_d}{dt} - \hat{\mathbf{l}}_d \frac{dL_d}{dt} \right), \quad (2.65)$$

$$\frac{d\hat{\mathbf{s}}}{dt} = \frac{1}{S} \left(\frac{d\mathbf{S}}{dt} - \hat{\mathbf{s}} \frac{dS}{dt} \right), \quad (2.66)$$

the leading order effect of viscous disk twisting on the time evolution of \hat{l}_d and \hat{s} is

$$\begin{aligned} \left(\frac{d\hat{l}_d}{dt} \right)_{\text{visc}} &= \gamma_b (\hat{l}_d \cdot \hat{l}_b)^3 \hat{l}_d \times (\hat{l}_b \times \hat{l}_d) \\ &\quad + \gamma_s (\hat{l}_d \cdot \hat{s})^3 \hat{l}_d \times (\hat{s} \times \hat{l}_d) \\ &\quad + \gamma_{(\text{bs})} (\hat{l}_d \cdot \hat{l}_b) (\hat{l}_d \cdot \hat{s})^2 \hat{l}_d \times (\hat{l}_b \times \hat{l}_d) \\ &\quad + \gamma_{(\text{bs})} (\hat{l}_d \cdot \hat{s}) (\hat{l}_d \cdot \hat{l}_b)^2 \hat{l}_d \times (\hat{s} \times \hat{l}_d), \end{aligned} \quad (2.67)$$

$$\begin{aligned} \left(\frac{d\hat{s}}{dt} \right)_{\text{visc}} &= - \frac{L_d}{S} \gamma_s (\hat{l}_d \cdot \hat{s})^2 \hat{s} \times (\hat{s} \times \hat{l}_d) \\ &\quad - \frac{L_d}{S} \gamma_{(\text{bs})} (\hat{l}_d \cdot \hat{s}) (\hat{l}_d \cdot \hat{l}_b) \hat{s} \times (\hat{l}_b \times \hat{l}_d). \end{aligned} \quad (2.68)$$

The four terms in $(d\hat{l}_d/dt)_{\text{visc}}$ [Eq. (2.67)] arises from four different back-reaction torques of the disk in response to \mathbf{T}_{ds} [Eq. (2.3)] and \mathbf{T}_{db} [Eq. (2.1)]. To resist the influence of the two external torques \mathbf{T}_{ds} and \mathbf{T}_{db} , the disk develops two twists $(\partial\hat{l}/\partial \ln r)_{ds}$ and $(\partial\hat{l}/\partial \ln r)_{db}$, given by Eqs. (2.46) and (2.29). The terms in Eqs. (2.67)-(2.68) proportional to γ_s arise from the back reaction of $(\partial\hat{l}/\partial \ln r)_{ds}$ to \mathbf{T}_{ds} , and works to align \hat{s} with \hat{l}_d . The term in Eq. (2.67) proportional to γ_b arises from the back reaction of \mathbf{T}_{db} to $(\partial\hat{l}/\partial \ln r)_{db}$, and works to align \hat{l}_d with \hat{l}_b . Because $\gamma_{(\text{bs})} < 0$, the terms in Eqs. (2.67)-(2.68) proportional to $\gamma_{(\text{bs})}$ have different effects than the terms proportional to γ_s and γ_b . One of the terms in Eqs. (2.67)-(2.68) proportional to $\gamma_{(\text{bs})}$ arises from the back reaction of \mathbf{T}_{ds} to $(\partial\hat{l}/\partial \ln r)_{db}$, and works to drive \hat{l}_d perpendicular to \hat{s} , while the other arises from the back-reaction of \mathbf{T}_{db} to $(\partial\hat{l}/\partial \ln r)_{ds}$, and works to drive \hat{l}_d perpendicular to \hat{l}_b . Although typically $|\gamma_s| > |\gamma_{(\text{bs})}|$ or $|\gamma_b| > |\gamma_{(\text{bs})}|$ (so the dynamical effect of $\gamma_{(\text{bs})}$ may be absorbed into γ_b and γ_s), the magnitude of $\gamma_{(\text{bs})}$ is not negligible compared to γ_s and γ_b . For completeness, we include the effects of the $\gamma_{(\text{bs})}$ terms in the analysis below.

The damping rates (2.62)-(2.64) may be evaluated and rescaled to give

$$\begin{aligned}\gamma_b &= 1.26 \times 10^{-9} \Gamma_b \left(\frac{\alpha}{0.01} \right) \left(\frac{0.1}{h_{\text{out}}} \right)^2 \\ &\times \frac{\bar{M}_b^2 \bar{r}_{\text{out}}^{9/2}}{\bar{a}_b^6 \bar{M}_\star^{3/2}} \left(\frac{2\pi}{\text{yr}} \right),\end{aligned}\quad (2.69)$$

$$\begin{aligned}\gamma_s &= 2.04 \times 10^{-10} \Gamma_s \left(\frac{\alpha}{0.01} \right) \left(\frac{0.1}{h_{\text{in}}} \right)^2 \left(\frac{1358 \bar{r}_{\text{out}}}{\bar{r}_{\text{in}}} \right)^{p-1} \\ &\times \left(\frac{k_q}{0.1} \right)^2 \frac{\bar{M}_\star^{1/2} \bar{R}_\star^4}{\bar{r}_{\text{in}}^4 \bar{r}_{\text{out}}^{3/2}} \left(\frac{\bar{\Omega}_\star}{0.1} \right)^4 \left(\frac{2\pi}{\text{yr}} \right),\end{aligned}\quad (2.70)$$

$$\begin{aligned}\gamma_{(\text{bs})} &= -2.04 \times 10^{-10} \Gamma_{(\text{bs})} \left(\frac{\alpha}{0.01} \right) \left(\frac{0.1}{h_{\text{out}}} \right)^2 \left(\frac{1358 \bar{r}_{\text{out}}}{\bar{r}_{\text{in}}} \right)^{p-1} \\ &\times \left(\frac{k_q}{0.1} \right) \frac{\bar{M}_b \bar{R}_\star^2 \bar{r}_{\text{out}}^{1/2}}{\bar{M}_\star^{1/2} \bar{a}_b^3 \bar{r}_{\text{in}}^2} \left(\frac{\bar{\Omega}_\star}{0.1} \right)^2 \left(\frac{2\pi}{\text{yr}} \right),\end{aligned}\quad (2.71)$$

where $h_{\text{in}} = (r_{\text{in}}/r_{\text{out}})^{q-1/2} h_{\text{out}}$. The rescaling above has removed the strongest dependencies of the damping rates on p , q , and $r_{\text{in}}/r_{\text{out}}$. Table 2.4 lists values of the dimensionless viscous coefficients Γ_b , Γ_s , and $\Gamma_{(\text{bs})}$, varying p and q .

Note that there are “mixed” terms in Eqs. (2.67)-(2.68): the counter-alignment rate of \hat{l}_d and \hat{l}_b depends on \hat{s} , while the counter-alignment rate of \hat{l}_d and \hat{s} depends on \hat{l}_b . Also note that net spin-disk alignment rate is given by

$$\gamma_{\text{sd}} = \left(1 + \frac{L_d}{S} \right) \gamma_s. \quad (2.72)$$

Assuming $L_d \gg S$, γ_{sd} evaluates to be

$$\begin{aligned}\gamma_{\text{sd}} &\simeq 7.52 \times 10^{-9} \frac{(2-p)\Gamma_s}{5/2-p} \left(\frac{\alpha}{0.01} \right) \left(\frac{0.1}{h_{\text{in}}} \right)^2 \left(\frac{1358 \bar{r}_{\text{out}}}{\bar{r}_{\text{in}}} \right)^{p-1} \\ &\times \left(\frac{2k_q}{k_\star} \right) \left(\frac{k_q}{0.1} \right) \frac{\bar{M}_d \bar{R}_\star^{7/2}}{\bar{M}_\star^{1/2} \bar{r}_{\text{in}}^4 \bar{r}_{\text{out}}} \left(\frac{\bar{\Omega}_\star}{0.1} \right)^3 \left(\frac{2\pi}{\text{yr}} \right).\end{aligned}\quad (2.73)$$

Figure 2.6 plots the disk-binary damping rate γ_b as a function of the binary semi-major axis a_b . In agreement with Foucart & Lai [2014], we find the damping rate to be small, and weakly dependent on the power-law surface density

and sound-speed indices p and q . This is because the torque from the binary companion is strongest around $r \sim r_{\text{out}}$. The properties of the disk near r_{out} are “global,” since the amount of inertia of disk annuli near r_{out} is set mainly by the total disk mass rather than the surface density profile, and the disk sound-speed does not vary greatly around $r \sim r_{\text{out}}$. We conclude that viscous torques from disk warping are unlikely to significantly decrease the mutual disk-binary inclination θ_{db} unless $a_{\text{b}} \lesssim 200$ au.

Figure 2.7 plots the star-disk alignment rate γ_{sd} as a function of the normalized stellar rotation frequency $\bar{\Omega}_{\star}$. Unlike the disk-binary alignment rate γ_{b} (Fig. 2.6), γ_{sd} depends strongly on the surface density and sound-speed power-law indices p and q . The alignment rate of a circumbinary disk with its binary orbital plane has a similarly strong dependence on p and q [Foucart & Lai, 2013, 2014, Lubow & Martin, 2018]. This strong dependence arises because the torque on the inner part of a disk from an oblate star or binary is strongest near r_{in} . The disk properties near $r \sim r_{\text{in}}$ are very local (both the amount of inertia for disk annuli and disk sound-speed), and hence will depend heavily on p and q . Despite this uncertainty, Figure 2.7 shows that there are reasonable parameters for which viscous torques from disk warping can significantly reduce the star-disk inclination θ_{sd} [when $\gamma_{\text{sd}} \gtrsim 0.1(2\pi/\text{Myr})$], especially when the stellar rotation rate is sufficiently high ($\bar{\Omega}_{\star} \gtrsim 0.2$).

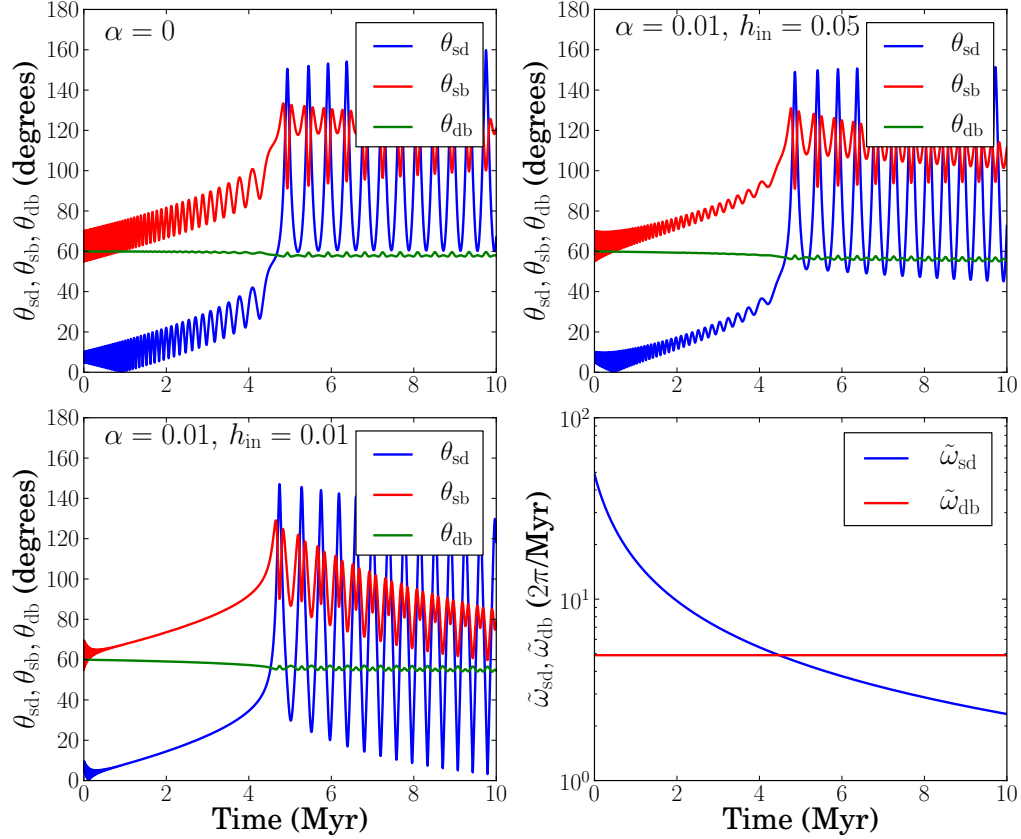


Figure 2.8: Inclination evolution of star-disk-binary systems. The top panels and bottom left panel plot the time evolution of the angles θ_{sd} [Eq. (2.77)], θ_{sb} [Eq. (2.78)], and θ_{db} [Eq. (2.79)], integrated using Eqs. (2.74) and (5.22), with values of α and h_{in} [Eq. (2.11)] as indicated. The bottom right panel shows the precession frequencies $\tilde{\omega}_{\text{sd}}$ [Eq. (2.43)] and $\tilde{\omega}_{\text{db}}$ [Eq. (2.24)]. We take $\theta_{\text{db}}(0) = 60^\circ$, $\theta_{\text{sd}}(0) = 5^\circ$, and $h_{\text{out}} = 0.05$ [Eq. (2.11)]. The damping rates are $\gamma_b = 5.05 \times 10^{-9}(2\pi/\text{yr})$ [Eq. (2.69)], $\gamma_{\text{sd}}(0) = 2.00 \times 10^{-7}(2\pi/\text{yr})$ [Eq. (2.72)], and $\gamma_{\text{bs}} = -8.18 \times 10^{-10}(2\pi/\text{yr})$ [Eq. (2.71)] for $h_{\text{in}} = 0.05$, and $\gamma_b = 7.12 \times 10^{-9}(2\pi/\text{yr})$, $\gamma_{\text{sd}}(0) = 1.37 \times 10^{-6}(2\pi/\text{yr})$, and $\gamma_{\text{bs}} = -1.51 \times 10^{-9}(2\pi/\text{yr})$ for $h_{\text{in}} = 0.01$.

2.4 Evolution of the Star-Disk-Binary System with Viscous Dissipation from Disk Warping

This section investigates the evolution of star-disk-binary systems under gravitational and viscous torques:

$$\frac{d\hat{s}}{dt} = -\tilde{\omega}_{\text{sd}}(\hat{s} \cdot \hat{l}_d)\hat{l}_d \times \hat{s} + \left(\frac{d\hat{s}}{dt} \right)_{\text{visc}}, \quad (2.74)$$

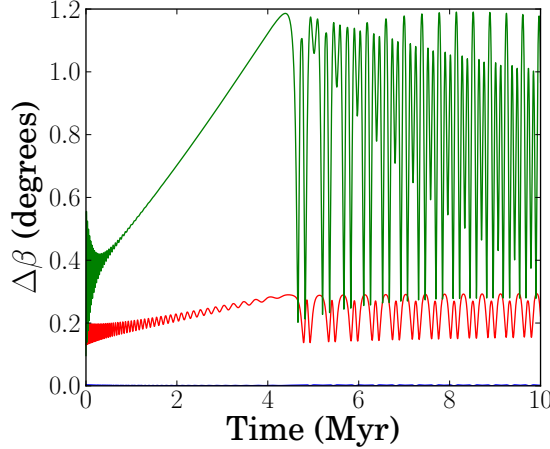


Figure 2.9: Total disk warp $\Delta\beta$ [Eq. (2.80)] for the integrations of Fig. 2.8. The blue curve denotes the integration where $(h_{\text{in}}, \alpha) = (0.05, 0.0)$, the red is $(h_{\text{in}}, \alpha) = (0.05, 0.01)$, and the green is $(h_{\text{in}}, \alpha) = (0.01, 0.01)$. All other parameters are listed in Fig. 2.8. All examples considered have $\Delta\beta < 1.2^\circ$, indicating the disk remains highly coplanar throughout the system's evolution. Notice $\Delta\beta \ll 1^\circ$ when $\alpha = 0$ (blue, hugs the x-axis).

$$\begin{aligned} \frac{d\hat{l}_d}{dt} = & -\tilde{\omega}_{ds}(\hat{l}_d \cdot \hat{s})\hat{s} \times \hat{l}_d \\ & -\tilde{\omega}_{db}(\hat{l}_d \cdot \hat{l}_b)\hat{l}_b \times \hat{l}_d + \left(\frac{d\hat{l}_d}{dt} \right)_{\text{visc}}. \end{aligned} \quad (2.75)$$

The viscous terms are given by Eqs. (2.67)-(2.68). As in Batygin & Adams [2013] and Lai [2014], we assume the disk's mass is depleted according to

$$M_d(t) = \frac{M_{d0}}{1 + t/t_v}, \quad (2.76)$$

where $M_{d0} = 0.1 M_\odot$ and $t_v = 0.5$ Myr. See Lai [2014] and Zanazzi & Lai [2017b] for discussions on the dynamical evolution of \hat{s} and \hat{l}_d and secular resonance ($\tilde{\omega}_{sd} \sim \tilde{\omega}_{db}$) when viscous dissipation from disk warping is neglected.

The effect of the γ_s term on the dynamical evolution of \hat{s} over viscous timescales depends on the precessional dynamics of the star-disk-binary system. If $\tilde{\omega}_{sd} \gg \tilde{\omega}_{db}$, \hat{s} rapidly precesses around \hat{l}_d , and the γ_s term works to align \hat{s} with \hat{l}_d . If $\tilde{\omega}_{sd} \ll \tilde{\omega}_{db}$, \hat{s} cannot “follow” the rapidly varying \hat{l}_d , and effectively

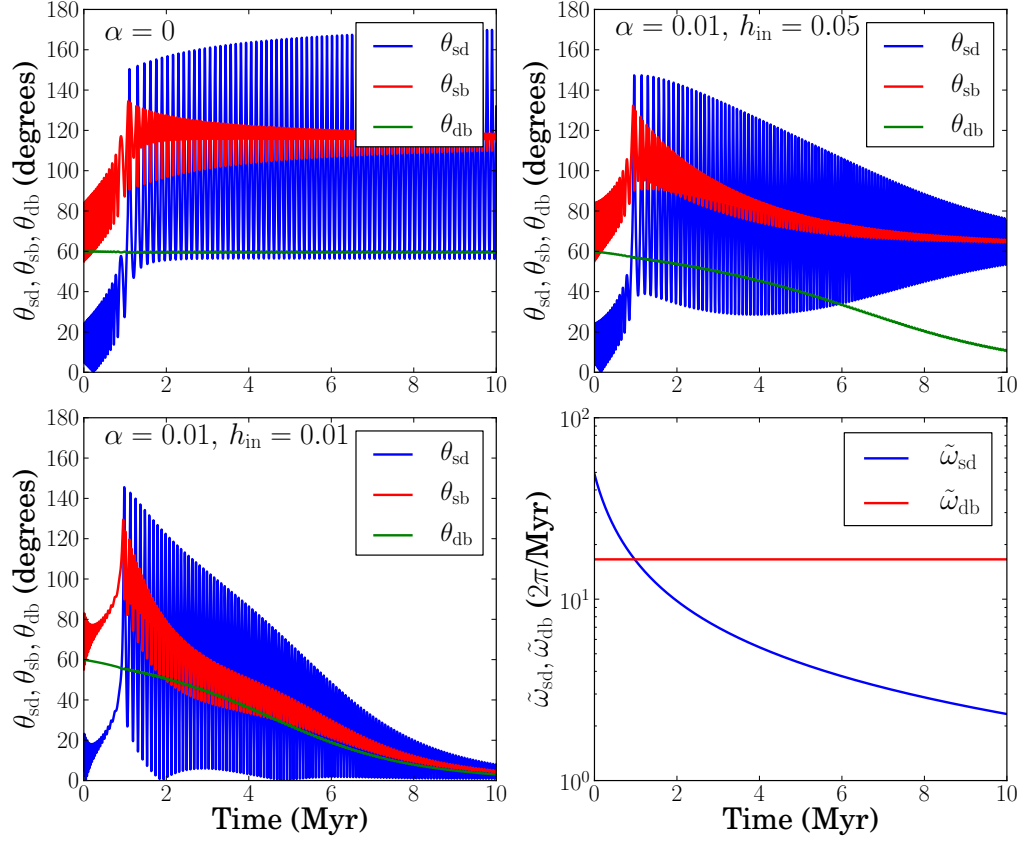


Figure 2.10: Same as Figure 2.8, except $a_b = 200$ AU. The damping rates are $\gamma_b = 5.75 \times 10^{-8}(2\pi/\text{yr})$, $\gamma_{sd}(0) = 2.00 \times 10^{-7}(2\pi/\text{yr})$, and $\gamma_{(bs)} = -2.76 \times 10^{-9}(2\pi/\text{yr})$ for $h_{in} = 0.05$, and $\gamma_b = 8.11 \times 10^{-8}(2\pi/\text{yr})$, $\gamma_{sd}(0) = 1.37 \times 10^{-6}(2\pi/\text{yr})$, and $\gamma_{(bs)} = -5.10 \times 10^{-9}(2\pi/\text{yr})$ for $h_{in} = 0.01$.

precesses around \hat{l}_b . In the latter case, because of the rapid variation of \hat{l}_d around \hat{l}_b , \hat{s} is only effected by the secular \hat{l}_d . As a result, γ_s works to drive θ_{sb} to θ_{db} . The effect of the γ_b term is simpler: it always works to align \hat{l}_d with \hat{l}_b .

Figure 2.8 shows several examples of the evolution of star-disk-binary systems. The top panels and bottom left panel of Fig. 2.8 show the time evolution of the angles

$$\theta_{sd} = \cos^{-1}(\hat{s} \cdot \hat{l}_d), \quad (2.77)$$

$$\theta_{sb} = \cos^{-1}(\hat{s} \cdot \hat{l}_b), \quad (2.78)$$

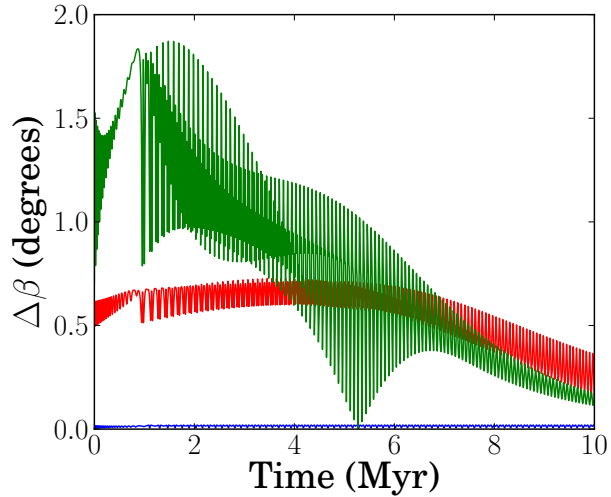


Figure 2.11: Same as Fig. 2.9, except for the examples considered in Fig. 2.10. All examples considered have $\Delta\beta < 1.9^\circ$, indicating the disk remains highly coplanar throughout the disk's lifetime.

$$\theta_{\text{db}} = \cos^{-1}(\hat{\mathbf{l}}_{\text{d}} \cdot \hat{\mathbf{l}}_{\text{b}}), \quad (2.79)$$

from integrating Eqs. (2.74)-(2.75), while the bottom right panel plots the characteristic precession frequencies $\tilde{\omega}_{\text{sd}}$ and $\tilde{\omega}_{\text{db}}$. The top left panel of Fig. 2.8 does not include viscous torques ($\alpha = 0$). Because the damping rates γ_{b} [Eq. (2.69)] and γ_{sd} [Eq. (2.72)] are much less than $0.1(2\pi/\text{Myr})$ over most of the system's lifetime (10 Myr), viscous torques have a negligible effect on the evolution of θ_{sd} , θ_{sb} , and θ_{db} . The bottom left panel of Fig. 2.8 shows the evolution of θ_{sd} , θ_{sb} , and θ_{db} with $\alpha = 0.01$ and $h_{\text{in}} = 0.01$. Because the inner edge of the disc has a much smaller scaleheight, the oblate star warps the inner edge of the disk more [Eq. (2.14)], resulting in γ_{sd} taking a value larger than $0.1(2\pi/\text{Myr})$. This increase in γ_{sd} causes a much tighter coupling of $\hat{\mathbf{s}}$ to $\hat{\mathbf{l}}_{\text{d}}$ before secular resonance ($\tilde{\omega}_{\text{sd}} \gtrsim \tilde{\omega}_{\text{db}}$), evidenced by the damped oscillations in θ_{sd} . After secular resonance ($\tilde{\omega}_{\text{sd}} \lesssim \tilde{\omega}_{\text{db}}$), the γ_s term damps $\hat{\mathbf{s}}$ toward $\hat{\mathbf{l}}_{\text{b}}$. Notice θ_{sb} approaches θ_{db} because of the rapid precession of $\hat{\mathbf{l}}_{\text{d}}$ around $\hat{\mathbf{l}}_{\text{b}}$ after secular resonance, not $\theta_{\text{sb}} \rightarrow 0$.

To gain insight to how the disk warp evolves during the star-disk-binary system's evolution, we introduce the misalignment angle $\Delta\beta$ between the disk's outer and inner orbital angular momentum unit vectors:

$$\begin{aligned}\sin \Delta\beta(t) &= |\hat{\mathbf{l}}(r_{\text{out}}, t) \times \hat{\mathbf{l}}(r_{\text{in}}, t)| \\ &\simeq |[\mathbf{l}_1(r_{\text{out}}, t) - \mathbf{l}_1(r_{\text{in}}, t)] \times \hat{\mathbf{l}}_d(t)|\end{aligned}\quad (2.80)$$

Figure 2.9 plots $\Delta\beta$ as a function of time, for the examples considered in Fig. 2.8. We see even when viscous torques from disk warping significantly alter the star-disk-binary system dynamics (e.g. $\alpha = 0.01$ and $h_{\text{in}} = 0.01$), $\Delta\beta < 1.2^\circ$ over the disk's lifetime, indicating a high degree of disk coplanarity throughout the system's evolution.

Figure 2.10 is identical to Fig. 2.8, except we take $a_b = 200 \text{ au}$ instead of $a_b = 300 \text{ au}$. Since γ_b is greater than $0.1(2\pi/\text{Myr})$, $\hat{\mathbf{l}}_d$ aligns with γ_b over the disk's lifetime. In the top right panel of Fig. 2.10, γ_{sd} is less than $0.1(2\pi/\text{Myr})$ for most of the disk's lifetime, so $\hat{\mathbf{s}}$ stays misaligned with both $\hat{\mathbf{l}}_d$ and $\hat{\mathbf{l}}_b$. At the end of the disk's lifetime, $\hat{\mathbf{s}}$ precesses around $\hat{\mathbf{l}}_b$, which is aligned with $\hat{\mathbf{l}}_d$. In the bottom left panel, both γ_b and γ_{sd} are greater than $0.1(2\pi/\text{Myr})$ for most of the disk's lifetime. This results in alignment of $\hat{\mathbf{l}}_d$, $\hat{\mathbf{s}}$, and $\hat{\mathbf{l}}_b$ over 10 Myr. Figure 2.11 shows the evolution of disk misalignment angles for the examples considered in Fig. 2.10. We see $\Delta\beta < 1.9^\circ$ for all examples considered, indicating the disk remains highly co-planar throughout the system's evolution.

2.5 Discussion

2.5.1 Theoretical Uncertainties

Our study of warped disks in star-disk-binary systems relies critically on the warp evolution equations derived in Lubow & Ogilvie [2000] for disks in the bending wave regime ($\alpha \lesssim H/r$), assuming a small disk warp ($|\partial \hat{l}/\partial \ln r| \ll 1$). A non-linear disk warp will change the surface density evolution of the disk through advection and viscosity where the warp is strongest (e.g. Ogilvie 1999, Tremaine & Davis 2014). In addition, even a small warp may interact resonantly with inertial waves, resulting in a parametric instability which enhances the disk’s dissipation rate [Gammie, Goodman, & Ogilvie, 2000, Ogilvie & Latter, 2013]. Because we have found for typical parameters, the warp in the disk torqued externally by a central oblate star and distant binary is small [see Eqs. (2.35)-(2.37), (2.50)-(2.52), and (2.54)-(2.55)], such effects are unlikely to change the main results of this paper.

In this study, we have assumed that the circumstellar disk in a binary system is circular. This may not be a valid assumption, as the disk may undergo eccentricity growth through resonant Lindblad torques [Lubow, 1991] or the Lidov-Kozai effect [Martin et al., 2014, Fu et al., 2015a, Zanazzi & Lai, 2017a, Lubow & Ogilvie, 2017]. Lindblad torques only cause eccentricity growth where the binary orbital frequency is commensurate with the disk orbital frequency, so they are unlikely to be relevant unless the outer edge of the disk is close to tidal truncation by the binary companion. Lidov-Kozai oscillations are a much more likely culprit for causing eccentricity growth of circumstellar disks in binaries when $\theta_{\text{db}} \gtrsim 40^\circ$. Lidov-Kozai oscillations may be suppressed by the disk’s self-

gravity when [Fu et al., 2015b]

$$M_d \gtrsim 0.04 M_b \left(\frac{3r_{\text{out}}}{a_b} \right)^3, \quad (2.81)$$

and by the disk's pressure gradients when [Zanazzi & Lai, 2017a, Lubow & Ogilvie, 2017]

$$a_b \gtrsim 4.2 r_{\text{out}} \left(\frac{M_b}{M_\star} \right)^{1/3} \left(\frac{h_{\text{out}}}{0.1} \right)^{-2/3}. \quad (2.82)$$

For our canonical parameters [Eq. (2.5)], the Lidov-Kozai effect is unlikely to be relevant unless $a_b \lesssim 4r_{\text{out}}$.

2.5.2 Observational Implications

In our companion work [Zanazzi & Lai, 2017b], we show that the formation of a short-period (orbital periods less than 10 days) massive planet in many instances significantly reduces or completely suppresses primordial misalignments generated by the gravitational torque from an inclined binary companion. Primordial misalignments are still robustly generated in protostellar systems forming low-mass ($\sim 1 M_\oplus$) multiple planets, and systems with cold (orbital periods greater than one year) Jupiters. On the other hand, observations suggest that most Kepler compact multi-planet systems have small stellar obliquities (e.g. Albrecht et al. 2013, Winn et al. 2017). A major goal of this work was to examine if viscous torques from disk warping may reduce or suppress the generation of primordial misalignments in star-disk-binary systems. We find that for some parameters, the star-disk inclination damping rate can be significant (see Fig. 2.7); in particular, the star-disk misalignment may be reduced when the disk is sufficiently cold with strong external torques (Figs. 2.8 & 2.10).

Observational evidence is mounting which suggests hot stars (effective temperatures $\gtrsim 6000^\circ \text{ K}$) have higher obliquities than cold stars [Winn et al., 2010, Albrecht et al., 2012, Mazeh et al., 2015, Li & Winn, 2016]. Since all damping rates from viscous disk-warping torques in star-disk-binary systems are inversely proportional to the disk's sound-speed squared [see Eqs. (2.69)-(2.72)], a tempting explanation for this correlation is that hot stars have hot disks with low damping rates which remain misaligned, while cold stars have cold disks with high damping rates which have star-disk misalignments significantly reduced over the disk's lifetime. However, we do not believe this is a likely explanation, since the protostellar disk's temperature should not vary strongly with the T-Tauri stellar mass. If a disk is passively heated from irradiation by its young host star [Chiang & Goldreich, 1997], low mass ($\lesssim 3 M_\odot$) pre-main sequence stars have effective temperatures which are not strongly correlated with their masses [Hayashi, 1961]. If the disk is actively heated by turbulent viscosity [Lynden-Bell & Pringle, 1974], the disk's accretion rate does not vary enough between different host star masses to create a difference in disk temperature [Rafikov, 2017].

Even in systems where viscous torques from disk warping alter the dynamics of the star-disk-binary system over the disk's lifetime (Figs. 2.8 & 2.10), we find the misalignment angle between the outer and inner disk orbital angular momentum unit vectors to not exceed a few degrees (Figs. 2.9 & 2.11). Therefore, it is unlikely that the disk warp profile plays a role in setting the mutual inclinations of forming exoplanetary systems with inclined binary companions.

2.6 Conclusions

We have studied how disk warps and the associated viscous dissipation affect the evolution of star-disk inclinations in binary systems. Our calculation of the disk warp profile shows that when the circumstellar disk is torqued by both the exterior companion and the central oblate star, the deviation of the disk angular momentum unit vector from coplanarity is less than a few degrees for the entire parameter space considered (Figs. 2.9 & 2.11). This indicates that disk warping in star-disk-binary systems does not alter exoplanetary architectures while the planets are forming in the disk. We have derived analytical expressions for the viscous damping rates of relative inclinations (Sec. 2.3.5), and have examined how viscous dissipation affects the inclination evolution of star-disk-binary systems. Because the star-disk [Eq. (2.72), Fig. 2.7] and disk-binary [Eq. (2.69), Fig. 2.6] alignment timescales are typically longer than the protoplanetary disk's lifetime ($\lesssim 10$ Myrs), viscous dissipation from disk warping does not significantly modify the long-term inclination evolution of most star-disk-binary systems (Fig. 2.8, top left panel). However, in sufficiently cold disks (small H/r) with strong external torques from the oblate star or inclined binary companion, the star-disk-binary evolution may be altered by viscous dissipation from disk warping, reducing the star-disk misalignment generated by star-disk-binary interactions (Figs. 2.8 & 2.10). In particular, we find when the stellar rotation rate is sufficiently high (rotation periods $\lesssim 2$ days), the star-disk damping is particularly efficient (Fig. 2.7). This viscous damping may explain the observed spin-orbit alignment in some multiplanetary systems (e.g. Albrecht et al. 2013, Winn et al. 2017) in the presence of inclined binary companions.

Acknowledgements

We thank the referee, Christopher Spalding, for many comments which improved the presentation and clarity of this work. JZ thanks Re'em Sari and Yoram Lithwick for helpful discussions. This work has been supported in part by NASA grants NNX14AG94G and NNX14AP31G, and NSF grant AST-1715246. JZ is supported by a NASA Earth and Space Sciences Fellowship in Astrophysics.

CHAPTER 3

**PLANET FORMATION IN DISKS WITH INCLINED BINARY
COMPANIONS: CAN PRIMORDIAL SPIN-ORBIT MISALIGNMENT BE
PRODUCED?**

3.1 Introduction

Many exoplanetary systems containing hot Jupiters (HJs, giant planets with periods of order a few days) have been found to have their orbital angular momentum axis significantly misaligned with the spin axis of the host star (e.g. Hébrard et al. 2008, Narita et al. 2009, Winn et al. 2009, Triaud et al. 2010; see Winn & Fabrycky 2015, Triaud 2017 for recent reviews). This “spin-orbit misalignment” is unexpected for a planet formed in a protoplanetary disk, as a young star’s spin axis is expected to be aligned with the disk’s angular momentum vector. One explanation is HJs are formed through high-eccentricity channels, in which the planet is pumped into a very eccentric orbit as a result of gravitational interactions with other planets or with a distant stellar companion, followed by tidal dissipation which circularizes the planet’s orbit (e.g., Wu & Murray 2003, Fabrycky & Tremaine 2007, Nagasawa, Ida, & Bessho 2008, Wu & Lithwick 2011, Naoz, Farr & Rasio 2012, Beaugé & Nesvorný 2012, Petrovich 2015, Anderson et al. 2016, Muñoz, Lai & Liu 2016, Hamers & Portegies Zwart 2016). In this “high-eccentricity migration” scenario, the chaotic spin evolution of the parent star driven by the changing orbit of the planet (even for planets which do not suffer “orbit flips”) plays the dominant role in setting the final spin-orbit misalignment [Storch, Anderson & Lai, 2014, Storch & Lai, 2015, Storch, Lai & Anderson, 2017]. Currently, it is unclear what fraction of

HJs are formed through these high-eccentricity routes, and several observations remain difficult to explain, such as the lack of giant planets with high eccentricities [Dawson, Murray-Clay & Johnson, 2015], and the correlation between the spin-orbit misalignment and the effective temperature of the host star (e.g., Albrecht et al. 2012, Mazeh et al. 2015, Li & Winn 2016, Winn et al. 2017).

Other mechanisms have been proposed to explain spin-orbit misalignments of HJ systems. One idea is that the misalignment is indicative of stellar astrophysics rather than planetary formation. In Rogers, Lin, & Lau [2012], it was suggested that internal gravity waves in massive stars may transport angular momentum in the radiative envelope, altering the star's surface rotation direction in a quasi-periodic manner.

There is observational evidence that a non-negligible fraction of HJs may be formed in protoplanetary disks in-situ or through disk-driven migration. For example, HJs (or hot Neptunes) around young T Tauri stars have recently been detected [Donati et al., 2016, David et al., 2016]; such young HJs can only form in protoplanetary disks or through disk-driven migration. The HJ WASP-47b has two low-mass neighbors [Becker et al., 2015], and thus cannot be formed through high-eccentricity migration. Boley, Granados Contreras & Gladman [2016] and Batygin, Bodenheimer & Laughlin [2016] have advocated in-situ formation for such systems. Schlaufman & Winn [2016] found that HJs are equally likely to have exterior giant planet companions inside the ice line compared to longer-period giant planets, and argued against the high- e migration scenario for HJ formation. For HJs formed in-situ or through disk-driven migration, the observed stellar obliquities may result from "primordial misalignment," where spin-orbit misalignments are produced while the planets are embedded in the

protoplanetary disk. Ways of generating primordially misaligned disks include chaotic star formation [Bate et al., 2010, Fielding et al., 2015], dynamical encounters with other proto-stellar systems [Thies et al., 2011], magnetic star - disk interactions [Lai et al., 2011, Foucart & Lai, 2011], and gravitational interactions with inclined planets [Matsakos & Königl, 2017].

Batygin [2012] first suggested that the gravitational torque from an inclined binary companion can change the orientation of a protoplanetary disk with respect to its host star. Batygin & Adams [2013], Lai [2014] and Spalding & Batygin [2014] included the gravitational coupling between the host star and the disk, and showed that a secular resonance occurs during the disk evolution, leading to a robust excitation of misalignment between the stellar spin axis and the disk axis. Although these works incorporated various effects such as stellar winds, stellar contraction, accretion and magnetic star-disk interactions, the disk physics included was highly idealized. In particular, these previous works assumed a flat disk with homologous surface density evolution (i.e. the disk density profile remains constant in shape but decreases in magnitude during the disk evolution). Moreover, although these works aimed at explaining the misalignment between the planet's orbit and the spin of the host star, the gravitational influence of a massive planet on the dynamics of the star-disk-binary system was neglected.

In this paper we study how the non-homologous surface density evolution of disks due to photoevaporation and the formation/migration of a planet orbiting close to its host star influence the generation of spin-orbit misalignments in star-disk-binary systems. In a companion paper [Zanazzi & Lai, 2017b] we consider non-flat (warped) disks and examine the effect of viscous dissipation

from disk warping on the spin-disk misalignments. Our paper is organized as follows. Section 3.2 reviews the physics of stellar obliquity excitation through star-disk-binary interactions. Section 3.3 introduces a prescription parameterizing how photoevaporation affects the disk’s surface density evolution, and studies how such evolution affects the inclination excitation in star-disk-binary systems. Section 3.4 presents an overview of how an inclined planet interacts with the disk, the central oblate star, and the distant binary companion. Section 3.5 investigates how the formation/migration of a short-period, massive planet affects the inclination evolution of star-disk-binary systems. We discuss the theoretical uncertainties and observational implications in Section 3.6, and provide a summary of our key results in Section 3.7.

3.2 Spin-Disk Misalignment from Star-Disk-Binary Gravitational Interactions

Previous works [Batygin & Adams, 2013, Lai, 2014, Spalding & Batygin, 2014] have shown that secular resonance can generate misalignment between the stellar spin and protoplanetary disk in star-disk-binary systems. In this section, we set up the problem and review the main physics behind this mechanism. We assume the disk is flat with orbital angular momentum unit vector \hat{l}_d , justified in a companion paper [Zanazzi & Lai, 2017b]. Our treatment follows Lai [2014] (hereafter L14) based on the dynamics of angular momentum vectors. For clarity, we display all quantities defined in Sections 3.2-3.3 in Table 3.1.

Symbol	Meaning	Eq.
M_\star	central star mass	-
R_\star	central star radius	-
Ω_\star	central star's rotation rate	-
P_\star	central star's rotation period	-
M_d	disk mass	(3.3)
r_{in}	disk inner truncation radius	-
r_{out}	disk outer truncation radius	-
M_b	binary mass	-
a_b	binary semi-major axis	-
\bar{X}	normalized quantity X	(3.1)
Σ	disk surface density	-
Σ_{out}	disk surface density at $r = r_{\text{out}}$	(3.2)
p	power-law surface density index	(3.2)
L_d	disk total orbital angular momentum	(3.4)
S	stellar spin angular momentum	(3.5)
k_\star	stellar spin normalization	(3.5)
k_q	stellar quadrupole moment normalization	-
\hat{s}	stellar spin unit vector	-
\hat{l}_d	disk orbital angular momentum unit vector	-
$\tilde{\omega}_{ds}$	precession rate of disk around star	(3.7)
$\tilde{\omega}_{sd}$	precession rate of star around disk	(3.8)
$\tilde{\omega}_{db}$	precession rate of disk around binary	(3.10)
M_{d0}	disk initial mass	-
t_v	disk viscous timescale	(3.16)
\tilde{M}_{d0}	normalized disk initial mass	-
θ_{sd}	mutual star-disk inclination	(3.17)
θ_{sb}	mutual star-binary inclination	(3.18)
θ_{db}	mutual disk-binary inclination	(3.19)
r_c	critical photoevaporation radius	-
t_w	critical photoevaporation time	-
$t_{v,\text{out}}$	outer disk's viscous time	-
$t_{v,\text{in}}$	inner disk's viscous time	-
Σ_c	disk surface density at $r = r_c$	-
$\tilde{\omega}_{sd>}$	precession rate of star around disk exterior to r_c	(3.25)
$\tilde{\omega}_{sd<}$	precession rate of star around disk interior to r_c	(3.26)
$\tilde{\omega}_{d>s}$	precession rate of disk interior to r_c around star	(3.27)
$\tilde{\omega}_{d<s}$	precession rate of disk exterior to r_c around star	(3.28)

Table 3.1: Definitions of relevant quantities in the star-disk-binary system.

3.2.1 Setup and Parameters

Consider a central star of mass M_\star , radius R_\star , rotation rate Ω_\star , with a circumstellar disk of mass M_d , and inner and outer truncation radii of r_{in} and r_{out} , respectively. This star-disk system is in orbit with a distant binary companion of mass M_b and semimajor axis a_b . We introduce the following rescaled parameters typical of protostellar systems:

$$\begin{aligned}\bar{M}_\star &= \frac{M_\star}{1 M_\odot}, & \bar{R}_\star &= \frac{R_\star}{2 R_\odot}, & \bar{\Omega}_\star &= \frac{\Omega_\star}{\sqrt{GM_\star/R_\star^3}}, \\ \bar{M}_d &= \frac{M_d}{0.01 M_\odot}, & \bar{r}_{\text{in}} &= \frac{r_{\text{in}}}{8 R_\odot}, & \bar{r}_{\text{out}} &= \frac{r_{\text{out}}}{50 \text{ au}}, \\ \bar{M}_b &= \frac{M_b}{1 M_\odot}, & \bar{a}_b &= \frac{a_b}{300 \text{ au}}.\end{aligned}\quad (3.1)$$

The canonical value of $\bar{\Omega}_\star$ is 0.1, corresponding to a stellar rotation period of $P_\star = 3.3$ days. The other canonical values in Eq. (3.1) are unity, except the disk mass, which can change significantly during the disk lifetime.

In the simplest model, we parameterize the disk surface density $\Sigma = \Sigma(r, t)$ as

$$\Sigma(r, t) = \Sigma_{\text{out}}(t) \left(\frac{r_{\text{out}}}{r} \right)^p. \quad (3.2)$$

L14 used $p = 1$. We will introduce a more complex parameterization of $\Sigma(r, t)$ in Section 3.3 to account for the effect of photoevaporation. We choose p between 1 and 3/2. This choice is motivated by various observations. In the outer regions of disks around YSO's ($r \gtrsim$ few au), p is constrained to lie in between $\sim 0.5 - 1$ [Williams & Cieza, 2011]. For the inner regions ($r \lesssim$ few au), direct observational constraints are lacking. The Minimum Mass Solar Nebulae has $p = 3/2$ [Weidenschilling, 1977], and the Minimum Mass Extra-Solar Nebulae (assuming the planets discovered by *Kepler* formed in-situ; Chiang & Laughlin 2013) have $p \simeq 1.6$. The main effect of increasing p is to increase the amount of mass

available to form a short-period gas-giant planet [see Eq. (3.63)], and increase the mutual star-disk precession frequencies [see Eqs. (3.7)-(3.8)]. We will always assume $p < 2$ when calculating global disk properties (mass, angular momentum, precession frequencies, etc.), the expressions for many of these quantities will differ when $p \geq 2$ in the limit $r_{\text{in}} \ll r_{\text{out}}$.

The disk mass M_d is then (assuming $r_{\text{in}} \ll r_{\text{out}}$)

$$M_d = \int_{r_{\text{in}}}^{r_{\text{out}}} 2\pi\Sigma r dr \simeq \frac{2\pi\Sigma_{\text{out}} r_{\text{out}}^2}{2-p}. \quad (3.3)$$

The disk angular momentum vector is $\mathbf{L}_d = L_d \hat{\mathbf{l}}_d$, and the stellar spin angular momentum vector is $\mathbf{S} = S \hat{\mathbf{s}}$, where $\hat{\mathbf{l}}_d$ and $\hat{\mathbf{s}}$ are unit vectors, and

$$\mathbf{L}_d = \int_{r_{\text{in}}}^{r_{\text{out}}} 2\pi\Sigma r^3 \Omega dr \simeq \frac{2-p}{5/2-p} M_d \sqrt{GM_\star r_{\text{out}}}, \quad (3.4)$$

$$S = k_\star M_\star R_\star^2 \Omega_\star, \quad (3.5)$$

with $\Omega(r) \simeq \sqrt{GM_\star/r^3}$ and $k_\star \simeq 0.2$.

3.2.2 Gravitational Torques

The stellar rotation leads to a difference in the principal components of the star's moment of inertia of $I_3 - I_1 = k_q M_\star R_\star^2 \bar{\Omega}_\star^2$, where $k_q \simeq 0.1$ for fully convective stars [Lai, Rasio & Shapiro, 1993]. The gravitational torque on the disk from the star is¹

$$\begin{aligned} \tilde{\mathbf{T}}_{\text{ds}} &= - \int_{r_{\text{in}}}^{r_{\text{out}}} \frac{3G(I_3 - I_1)}{2r^3} (\hat{\mathbf{l}}_d \cdot \hat{\mathbf{s}})(\hat{\mathbf{s}} \times \hat{\mathbf{l}}_d) 2\pi\Sigma r^3 \Omega dr \\ &= -L_d \tilde{\omega}_{\text{ds}} (\hat{\mathbf{l}}_d \cdot \hat{\mathbf{s}}) \hat{\mathbf{s}} \times \hat{\mathbf{l}}_d, \end{aligned} \quad (3.6)$$

¹Throughout this paper, quantities with a tilde ($\tilde{\cdot}$) imply an average or integration over the disk

where (assuming $r_{\text{in}} \ll r_{\text{out}}$)

$$\tilde{\omega}_{\text{ds}} \simeq \frac{3(5/2 - p)k_q}{2(1 + p)} \frac{R_\star^2 \bar{\Omega}_\star^2}{r_{\text{out}}^{1-p} r_{\text{in}}^{1+p}} \sqrt{\frac{GM_\star}{r_{\text{out}}^3}} \quad (3.7)$$

characterizes the precession frequency of the disk around the star. The back-reaction torque on the star from the disk is $\tilde{\mathbf{T}}_{\text{sd}} = -\tilde{\mathbf{T}}_{\text{ds}}$, and causes the star to precess around the disk at a characteristic frequency

$$\begin{aligned} \tilde{\omega}_{\text{sd}} &= (L_d/S)\tilde{\omega}_{\text{ds}} \\ &\simeq \frac{3(2 - p)k_q}{2(1 + p)k_\star} \left(\frac{M_d}{M_\star} \right) \bar{\Omega}_\star \frac{\sqrt{GM_\star R_\star^3}}{r_{\text{out}}^{2-p} r_{\text{in}}^{1+p}}. \end{aligned} \quad (3.8)$$

The torque on the disk from the inclined binary companion is (assuming $r_{\text{out}} \ll a_b$)

$$\begin{aligned} \tilde{\mathbf{T}}_{\text{db}} &\simeq - \int_{r_{\text{in}}}^{r_{\text{out}}} \left(\frac{3GM_b r^2}{4a_b^3} \right) (\hat{\mathbf{l}}_d \cdot \hat{\mathbf{l}}_b) (\hat{\mathbf{l}}_b \times \hat{\mathbf{l}}_d) 2\pi \Sigma r^3 \Omega dr \\ &= -L_d \tilde{\omega}_{\text{db}} (\hat{\mathbf{l}}_d \cdot \hat{\mathbf{l}}_b) \hat{\mathbf{l}}_b \times \hat{\mathbf{l}}_d, \end{aligned} \quad (3.9)$$

where

$$\tilde{\omega}_{\text{db}} \simeq \frac{3(5/2 - p)}{4(4 - p)} \left(\frac{M_b}{M_\star} \right) \left(\frac{r_{\text{out}}}{a_b} \right)^3 \sqrt{\frac{GM_\star}{r_{\text{out}}^3}} \quad (3.10)$$

characterizes the precession frequency of the disk around the binary.

Taking $p = 1$, the precession frequencies (3.7), (3.8), and (3.10) evaluate to

$$\omega_{\text{sd}} = 2.0 \times 10^{-7} \left(\frac{k_q}{0.1} \right) \frac{\bar{R}_\star^2 \bar{M}_\star^{1/2}}{\bar{r}_{\text{in}}^2 \bar{r}_{\text{out}}^{3/2}} \left(\frac{\bar{\Omega}_\star}{0.1} \right)^2 \left(\frac{2\pi}{\text{yr}} \right), \quad (3.11)$$

$$\tilde{\omega}_{\text{db}} = 4.9 \times 10^{-6} \frac{\bar{M}_b \bar{r}_{\text{out}}^{3/2}}{\bar{M}_\star^{1/2} \bar{a}_b^3} \left(\frac{2\pi}{\text{yr}} \right), \quad (3.12)$$

$$\tilde{\omega}_{\text{sd}} = 4.9 \times 10^{-5} \left(\frac{2k_q}{k_\star} \right) \frac{\bar{M}_d}{\bar{M}_\star^{1/2} \bar{R}_\star^{1/2} \bar{r}_{\text{in}}^2 \bar{r}_{\text{out}}} \left(\frac{\bar{\Omega}_\star}{0.1} \right) \left(\frac{2\pi}{\text{yr}} \right). \quad (3.13)$$

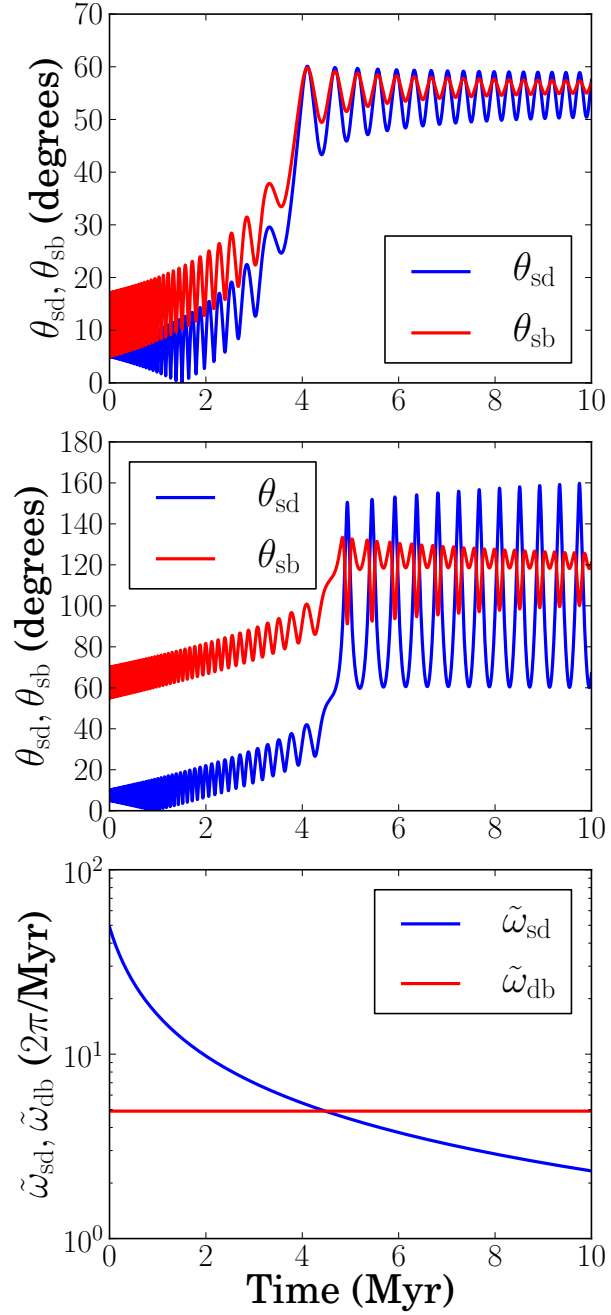


Figure 3.1: Sample evolution of the star-disk-binary system. The top and middle panels plot the evolution of the star-disk inclination θ_{sd} [Eq. (3.17)] and star-binary inclination θ_{sb} [Eq. (3.18)]. We take the initial disk-binary inclination θ_{db} to be $\theta_{\text{db}}(0) = 10^\circ$ (top panel) and $\theta_{\text{db}}(0) = 60^\circ$ (middle panel) with $\theta_{\text{sd}}(0) = 5^\circ$ for both panels. The bottom panel plots the time evolution of the precession rates $\tilde{\omega}_{\text{sd}}$ [Eq. (3.8)] and $\tilde{\omega}_{\text{db}}$ [Eq. (3.10)]. We take all parameter values to be canonical [Eq. (3.1)].

3.2.3 System Evolution and Secular Resonance

The time evolution of the star-disk-binary system is given by

$$\frac{d\hat{s}}{dt} = -\tilde{\omega}_{sd}(\hat{s} \cdot \hat{l}_d)\hat{l}_d \times \hat{s}, \quad (3.14)$$

$$\frac{d\hat{l}_d}{dt} = -\tilde{\omega}_{ds}(\hat{l}_d \cdot \hat{s})\hat{s} \times \hat{l}_d - \tilde{\omega}_{db}(\hat{l}_d \cdot \hat{l}_b)\hat{l}_b \times \hat{l}_d. \quad (3.15)$$

As in Batygin & Adams [2013] and Lai [2014], we assume the disk mass evolves according to

$$M_d = \frac{M_{d0}}{1 + t/t_v}. \quad (3.16)$$

For our canonical parameters, we choose $M_{d0} = 0.1 M_\odot$ and $t_v = 0.5$ Myr. We define $\bar{M}_{d0} = M_{d0}/0.1 M_\odot$.

Figure 3.1 shows an example of the star-disk-binary system evolution. We define the angles

$$\theta_{sd} = \cos^{-1}(\hat{s} \cdot \hat{l}_d), \quad (3.17)$$

$$\theta_{sb} = \cos^{-1}(\hat{s} \cdot \hat{l}_b), \quad (3.18)$$

$$\theta_{db} = \cos^{-1}(\hat{l}_d \cdot \hat{l}_b). \quad (3.19)$$

The angles θ_{sd} , θ_{sb} , and θ_{db} denote the mutual star-disk, star-binary, and disk-binary inclinations, respectively. We take \hat{s} , \hat{l} , and \hat{l}_b to initially all lie in the same plane, with $\theta_{sd}(0) = 5^\circ$ and two different values of $\theta_{db}(0)$. We choose our initial value of θ_{sd} to be $\theta_{sd}(0) \ll 1$. The dynamics of the star-disk-binary system remain qualitatively unchanged as long as $\theta_{sd}(0)$ is much smaller than unity [Spalding & Batygin, 2014].

When $\tilde{\omega}_{db} \ll \tilde{\omega}_{sd}$ early in the disk's lifetime, \hat{s} adiabatically tracks \hat{l}_d , and $\theta_{sd} \sim \text{constant}$. When $\tilde{\omega}_{db} \gg \tilde{\omega}_{sd}$ later in the disk's lifetime, \hat{s} tracks \hat{l}_b with

$\theta_{\text{sb}} \sim \text{constant}$. A secular resonance occurs when $\tilde{\omega}_{\text{db}} \sim \tilde{\omega}_{\text{sd}}$, and large θ_{sd} can be generated due to the change in the dynamical behavior of the stellar spin axis (see L14 for discussion). This resonant excitation of θ_{sd} is prominent when $L_{\text{d}} \gtrsim S$ at the resonance crossing.

3.3 Non-homologous Surface Density Evolution: Photoevaporation

Section 3.2 assumes (as in previous works) the disk surface density evolves homologously, maintaining the power-law r^{-p} profile while decreasing in the overall magnitude. Realistic protostellar disks do not evolve in such a homogeneous way. This section explores an alternate prescription for the surface density evolution that captures the essential physics of photoevaporation (e.g. Clarke et al. 2001, Alexander et al. 2014).

As described in Clarke et al. [2001], the combined influence of photoevaporation and viscous accretion dramatically influence the surface density evolution of disks around T-Tauri stars (see Alexander et al. 2014, Owen 2016 for recent reviews). The surface density Σ has distinct behaviors before and after the characteristic time t_w , when the viscous accretion rate and photo-evaporative mass loss rate become comparable at the critical photoevaporation radius $r_c \sim$ a few au (the maximal radius where photoionized gas remains bound to the central star; Hollenbach et al. 1994, Alexander, Clarke & Pringle 2006). Before t_w , viscous accretion drives the disk's mass depletion, and the surface density evolves over the outer disk's viscous time $t_{v,\text{out}} = t_v$. After t_w , Σ at $r > r_c$ continues to evolve viscously over the timescale $t_{v,\text{out}} = t_v$ [see Eq. (3.16)]; interior to r_c , photoevapo-

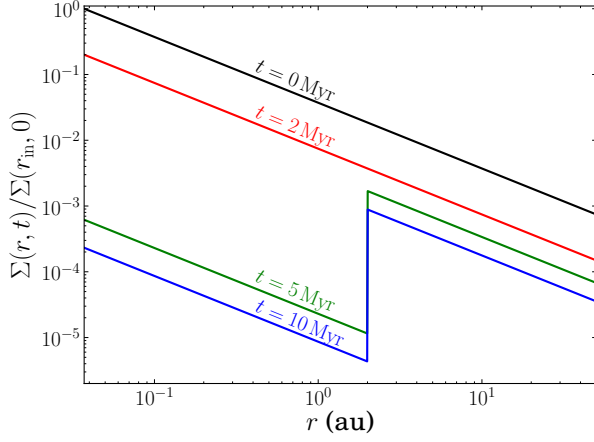


Figure 3.2: Evolution of the disk surface density $\Sigma(r, t)$, given by Eq. (3.20). We take the disk's outer viscous timescale to be $t_v = 0.5$ Myr, the time when the disk's photo-ionization rate is comparable to viscous depletion rate $t_w = 2$ Myr, the disk's inner viscous time $t_{v,in} = 0.02$ Myr, and the critical radius separating the inner and outer regions of the disk $r_c = 2$ au.

ration starves the inner disk from resupply by the outer disk's viscous evolution, and the inner disk is drained over the inner disk's viscous time $t_{v,in} \ll t_{v,out}$.

To capture the main effect of photoevaporation, we parameterize the disk's surface density evolution as

$$\Sigma(r, t) = \begin{cases} \Sigma_c(t)(r_c/r)^p & r_{in} \leq r \leq r_c \\ \Sigma_{out}(t)(r_{out}/r)^p & r_c < r \leq r_{out} \end{cases}, \quad (3.20)$$

where $\Sigma_{out}(t) = \Sigma_{out}(0)/(1 + t/t_v)$ [see Eq. (3.16)], while

$$\Sigma_c(t) = \begin{cases} \Sigma_c(0)(1 + t/t_v)^{-1} & t \leq t_w \\ \Sigma_c(t_w)[1 + (t - t_w)/t_{v,in}]^{-1} & t > t_w \end{cases}, \quad (3.21)$$

and

$$\Sigma_c(0) = \Sigma_{out}(0)(r_c/r_{out})^p. \quad (3.22)$$

Figure 3.2 shows a sample evolution of $\Sigma(r, t)$. Our prescription of $\Sigma(r, t)$ introduces three new parameters: t_w (when the inner disk begins to be rapidly depleted), $t_{v,in}$ (the timescale over which the inner disk is depleted), and r_c (the

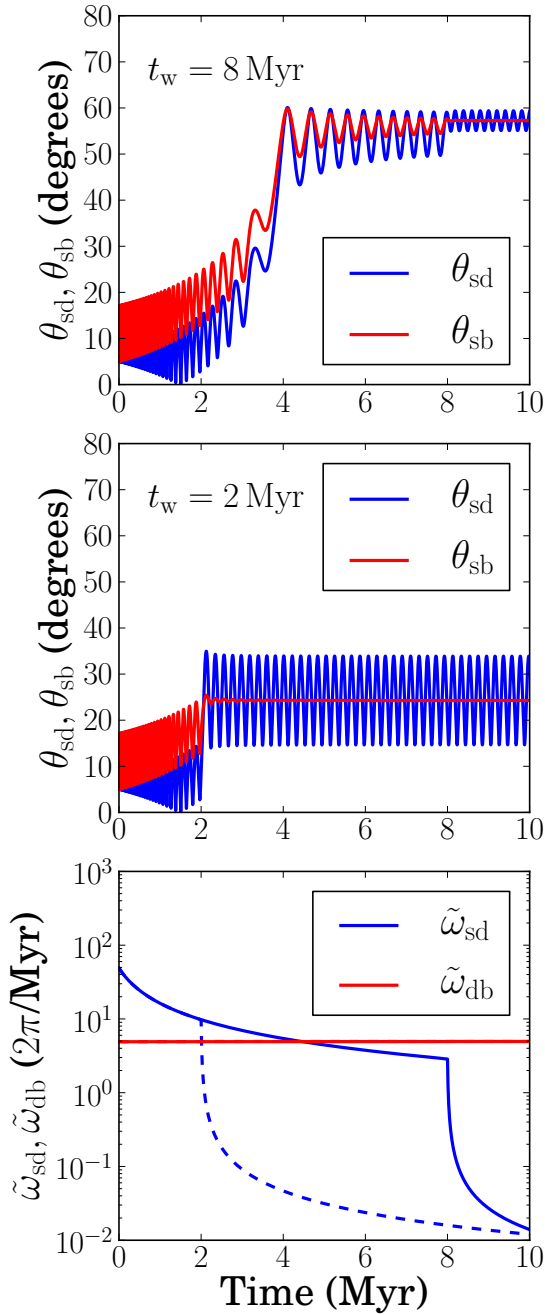


Figure 3.3: Same as Fig. 3.1, except the disk surface density $\Sigma(r, t)$ evolves according to the prescription (3.20), with values of t_w as indicated. The bottom panel shows the disk-binary precession rate $\tilde{\omega}_{\text{db}}$ [Eq. (3.10)] and the star-disk precession rate $\tilde{\omega}_{\text{sd}}$ [Eq. (3.23)], with $t_w = 8$ Myr (solid), and $t_w = 2$ Myr (dashed). We take $r_c = 2$ AU, $t_v = 0.5$ Myr, $t_{v,\text{in}} = 0.02$ Myr. All other parameters canonical, with the initial star-disk inclination $\theta_{\text{sd}}(0) = 5^\circ$ and disk-binary inclination $\theta_{\text{db}}(0) = 10^\circ$.

critical radius separating the inner and outer disks). Observations constrain $t_w \sim 10^6 - 10^7$ years, $t_{v,in} \sim 10^2 - 10^5$ years, and $r_c \sim \text{few} \times \text{au}$ [Alexander et al., 2014, Owen, 2016]. We choose $r_c = 2 \text{ au}$ throughout this paper, varying t_w and $t_{v,in}$ for different disk models.

To model the dynamics of the star-disk-binary system, we neglect any misalignments which may develop between the inner and outer disk planes, since the gravitational influence of the inner disk quickly becomes irrelevant to the dynamics of the star-disk-binary system. Coplanarity between these two disk planes is maintained via bending waves [Papaloizou & Lin, 1995, Lubow & Ogilvie, 2000, Zanazzi & Lai, 2017b] and disk self-gravity [Batygin, 2012, Batygin & Adams, 2013, Zanazzi & Lai, 2017a].

The modified surface density evolution alters the mutual star-disk precession frequencies:

$$\tilde{\omega}_{sd} = \tilde{\omega}_{sd<} + \tilde{\omega}_{sd>}, \quad (3.23)$$

$$\tilde{\omega}_{ds} = \tilde{\omega}_{d<s} + \tilde{\omega}_{d>s}. \quad (3.24)$$

Here, $d <$ ($d >$) denotes the disk interior (exterior) to r_c . In terms of model parameters, the frequencies in Eqs. (3.23)-(3.24) evaluate to be (assuming $r_{in} \ll r_c \ll r_{out}$)

$$\tilde{\omega}_{sd>} \simeq \frac{3k_q}{(1+p)k_\star} \bar{\Omega}_\star \left(\frac{\pi \Sigma_{out} r_{out}^2}{M_\star} \right) \frac{\sqrt{GM_\star R_\star^3}}{r_c^{1+p} r_{out}^{2-p}}, \quad (3.25)$$

$$\tilde{\omega}_{sd<} \simeq \frac{3k_q}{(1+p)k_\star} \bar{\Omega}_\star \left(\frac{\pi \Sigma_c r_c^2}{M_\star} \right) \frac{\sqrt{GM_\star R_\star^3}}{r_{in}^{1+p} r_c^{2-p}}, \quad (3.26)$$

$$\tilde{\omega}_{d>s} \simeq \frac{3(5/2-p)k_q}{2(1+p)} \bar{\Omega}_\star^2 \frac{R_\star^2}{r_c^{1+p} r_{out}^{1-p}} \sqrt{\frac{GM_\star}{r_{out}^3}}, \quad (3.27)$$

$$\tilde{\omega}_{d<s} \simeq \frac{3(5/2-p)k_q}{2(1+p)} \bar{\Omega}_\star^2 \frac{\Sigma_c r_c^p R_\star^2}{\Sigma_{out} r_{in}^{1+p} r_{out}} \sqrt{\frac{GM_\star}{r_{out}^3}}. \quad (3.28)$$

The disk-binary precession frequency [$\tilde{\omega}_{\text{db}}$, Eq. (3.10)] is unchanged (assuming $r_c \ll r_{\text{out}}$). The frequency $\tilde{\omega}_{\text{sd}>}$ ($\tilde{\omega}_{\text{sd}<}$) denotes the precession frequency of the star around the disk exterior (interior) to r_c , while $\tilde{\omega}_{\text{d}>s}$ ($\tilde{\omega}_{\text{d}<s}$) denotes the precession frequency of the disk exterior (interior) to r_c around the star.

Figure 3.3 shows examples of the star-disk-binary evolution under the $\Sigma(r, t)$ prescription (3.20), for two values of t_w . We see that the main effect of photo-evaporation is a potential change in resonance crossing time. If the resonance ($\tilde{\omega}_{\text{sd}} \sim \tilde{\omega}_{\text{db}}$) occurs before t_w , the excitation of θ_{sd} is more or less unaffected. If the resonance occurs after t_w , the rapid depletion of the inner disk causes $\tilde{\omega}_{\text{sd}}$ to rapidly approach zero over the time $t_{v,\text{in}}$, and $\tilde{\omega}_{\text{sd}} \sim \tilde{\omega}_{\text{db}}$ at $t \approx t_w + t_{v,\text{in}}$. The resulting θ_{sd} excitation is smaller because the resonance crossing is fast. In either case, after t_w , the spin-binary misalignment angle θ_{sb} freezes to a constant value because of the greatly diminished inner disk mass.

3.4 Planet-Star-Disk-Binary Interactions

We now add a planet in our star-disk-binary system. This section examines how the planet interacts with the protoplanetary disk, the host star, and the inclined binary. We take the planet to lie on a circular orbit, with mass M_p , semi-major axis a_p , and orbital angular momentum $\mathbf{L}_p = M_p \sqrt{GM_\star a_p} \hat{\mathbf{l}}_p$. For clarity, we display all quantities defined in Sections 3.4-3.5 in Table 3.2.

Symbol	Meaning	Eq.
M_p	planet mass	-
a_p	planet semi-major axis	-
\hat{l}_p	planet orbital angular momentum unit vector	-
h	disk aspect ratio	-
Δ_p	gap width	-
$\bar{\Sigma}$	average disk surface density at gap edges	-
h_p	maximum of $h(a_p)$ and Δ_p/a_p	-
$\tilde{\omega}_{pd}$	precession rate of planet around disk	(3.34)
$\tilde{\omega}_{db}$	precession rate of disk around planet	(3.35)
Λ_{mig}	Migration rate free parameter	(3.39)
t_{mig}	type II migration timescale	(3.39)
$\tilde{\omega}_{pd<}$	precession rate of planet around disk interior to r_c	(3.40)
$\tilde{\omega}_{pd>}$	precession rate of planet around disk exterior to r_c	(3.42)
$\tilde{\omega}_{d<p}$	precession rate of disk interior to r_c around planet	(3.44)
$\tilde{\omega}_{d>p}$	precession rate of disk exterior to r_c around planet	(3.43)
ω_{ps}	precession rate of planet around star	(3.48)
ω_{sp}	precession rate of star around planet	(3.49)
ω_{pb}	precession rate of planet around binary	(3.51)
ξ	feeding zone free parameter	(3.62)
θ_{ps}	mutual planet-star inclination	(3.58)
θ_{pd}	mutual planet-disk inclination	(3.59)
θ_{pb}	mutual planet-binary inclination	(3.60)
$\tilde{\omega}'_{sd}$	modified precession frequency of star around disk	(3.67)
$\tilde{\omega}'_{ds}$	modified precession frequency of disk around star	(3.68)
$\tilde{\omega}'_{db}$	modified precession frequency of disk around binary	(3.69)

Table 3.2: Definitions of quantities related to planet interactions with the star-disk-binary system.

3.4.1 Planet-Disk Interactions: Non-Gap Opening Planets

When the planet has a mass insufficient to open a gap in the disk, the gravitational torque on the planet from the disk causes $\hat{\mathbf{l}}_p$ to precess around $\hat{\mathbf{l}}_d$ at a rate [Ward, 1981, Hahn, 2003]

$$\tilde{\omega}_{pd, \text{no gap}} \simeq \frac{\pi \Sigma(a_p, t) a_p^2}{M_\star h(a_p)} \sqrt{\frac{GM_\star}{a_p^3}} \quad (3.29)$$

where $\Sigma(a_p, t)$ is the disk surface density at $r = a_p$, and $h(a_p)$ is the disk aspect ratio $h = H/r$ (H is the disk scaleheight) evaluated at $r = a_p$. Equation (3.29) was derived assuming $|\hat{\mathbf{l}}_p \times \hat{\mathbf{l}}_d| \ll h(a_p) \ll 1$, using a disk potential with softening length H .

In addition to the direct gravitational torque, when $\hat{\mathbf{l}}_p$ is misaligned with $\hat{\mathbf{l}}_d$, the planet drives bending waves which propagate through the disk, working to cause $\hat{\mathbf{l}}_p$ to precess and align with $\hat{\mathbf{l}}_d$ on a characteristic timescale [Tanaka & Ward, 2004, Cresswell et al., 2007, Kley & Nelson, 2012]

$$t_{bw} = \frac{M_\star}{\Sigma(a_p, t) a_p^2} \left(\frac{M_\star}{M_p} \right) h^4(a_p) \sqrt{\frac{a_p^3}{GM_\star}}. \quad (3.30)$$

Since

$$t_{bw} \tilde{\omega}_{pd, \text{no gap}} = 1.05 \times 10^3 \left(\frac{M_p}{1 M_\oplus} \right)^{-1} \bar{M}_\star \left(\frac{h(a_p)}{0.1} \right)^3, \quad (3.31)$$

we expect $\hat{\mathbf{l}}_p$ to precess around $\hat{\mathbf{l}}_d$ mainly due to the gravitational torque, with the bending waves aligning $\hat{\mathbf{l}}_p$ with $\hat{\mathbf{l}}_d$ over a longer time-scale.

The planet also drives density waves in the disk, leading to its radial migration [Goldreich & Tremaine, 1979, Tanaka, Takeuchi, & Ward, 2002, Kley & Nelson, 2012]. The characteristic migration time is

$$t_{mig, \text{no gap}} = \frac{t_{bw}}{h^2(a_p)}$$

$$= \frac{M_\star}{\Sigma(a_p, t)a_p^2} \left(\frac{M_\star}{M_p} \right) h^2(a_p) \sqrt{\frac{a_p^3}{GM_\star}}. \quad (3.32)$$

The migration rate depends on the detailed local properties of the disk, such as if the disk lies in a dead zone (e.g. McNally et al. 2017), the local temperature gradient (e.g. Jiménez & Masset 2017), and the disk’s thermal diffusivity and planet’s accretion rate [Benítez-Llambay et al., 2015, Masset & Velasco Romero, 2017, Masset, 2017]. These effects may drive a_p to increase or decrease with time. Because the planet becomes dynamically important only when its mass becomes sufficiently large to open a gap, we will neglect its orbital evolution, and fix a_p in time before a gap is opened.

3.4.2 Planet-Disk Interactions: Gap Opening Planets

When the planet has sufficient mass $M_p \gtrsim 40M_\star ah^2(a_p)$ (e.g. Lin & Papaloizou 1993), it can open a gap in the disk, with a width $\Delta_p = \xi a_p (M_p/3M_\star)^{1/3}$ (ξ is a free parameter). The disk surface density around the gap is clearly complex. In our calculation, we adopt the simple prescription that $\Sigma(r, t) \simeq 0$ for $|r - a_p| < \Delta_p/2$, and $\Sigma(r, t)$ obeys Eqs. (3.2) or (3.20) otherwise. The mutual planet-disk interactions are modified from the non-gap opening planet case. When the planet opens a gap, because we expect the disk gravitational potential Φ_d to not exceed $2\pi G \bar{\Sigma}(a_p, t) a_p^2 / \Delta_p$, where $\bar{\Sigma}(a_p, t) = \frac{1}{2}[\Sigma(a_p - \Delta_p/2, t) + \Sigma(a_p + \Delta_p/2, t)]$, we may replace the softening length in the disk potential Φ_d by Δ_p . The characteristic precession frequency of the planet around the disk is then modified to become [cf. Eq. (3.29)]

$$\tilde{\omega}_{pd, \text{gap}} \simeq \frac{\pi \bar{\Sigma}(a_p, t) a_p^3}{M_\star \Delta_p} \sqrt{\frac{GM_\star}{a_p^3}}. \quad (3.33)$$

From now on, we define

$$\tilde{\omega}_{\text{pd}} = \frac{\pi \bar{\Sigma}(a_{\text{p}}, t) a_{\text{p}}^2}{M_{\star} h_{\text{p}}} \sqrt{\frac{GM_{\star}}{a_{\text{p}}^3}}, \quad (3.34)$$

where $h_{\text{p}} = \max[h(a_{\text{p}}), \Delta_{\text{p}}/a_{\text{p}}]$. The planet exerts a back-reaction torque on the disk, causing \hat{l}_{d} to precess around \hat{l}_{p} at a characteristic rate

$$\begin{aligned} \tilde{\omega}_{\text{dp}} &= (L_{\text{p}}/L_{\text{d}})\tilde{\omega}_{\text{pd}} \\ &\simeq \frac{5/2 - p}{2h_{\text{p}}} \left(\frac{a_{\text{p}}}{r_{\text{out}}} \right)^{1-p} \left(\frac{M_{\text{p}}}{M_{\star}} \right) \sqrt{\frac{GM_{\star}}{r_{\text{out}}^3}}. \end{aligned} \quad (3.35)$$

Because bending waves propagate through the disk as a result of resonant Lindblad and co-rotational torques, a gap Δ_{p} lengthens t_{bw} to be [c.f. Eq. (3.31)]

$$t_{\text{bw}} = \Lambda_{\text{gap}} \frac{M_{\star}}{\bar{\Sigma}(a_{\text{p}})a_{\text{p}}^2} \left(\frac{M_{\star}}{M_{\text{p}}} \right) h^4(a_{\text{p}}) \sqrt{\frac{a_{\text{p}}^3}{GM_{\star}}}. \quad (3.36)$$

The numerical value of Λ_{gap} must be obtained via hydrodynamical simulations to account for non-linear effects. No simulations have carefully calculated Λ_{gap} as a function of the planet's parameters and local disk properties, but simulations suggest $\Lambda_{\text{gap}} \gg 1$ (e.g. Xiang-Gruess & Papaloizou 2013, Bitsch et al. 2013, Chametla et al. 2017). Comparing $\tilde{\omega}_{\text{pd}}$ to t_{bw} ,

$$\begin{aligned} \tilde{\omega}_{\text{pd, gap}} t_{\text{bw}} &= 3.29 \times 10^2 \left(\frac{\Lambda_{\text{gap}}}{100} \right) \left(\frac{M_{\text{p}}}{1 M_{\text{J}}} \right)^{-1} \\ &\quad \times \bar{M}_{\star} \left(\frac{h(a_{\text{p}})}{0.1} \right)^4 \left(\frac{\Delta_{\text{p}}/a_{\text{p}}}{0.1} \right)^{-1}. \end{aligned} \quad (3.37)$$

From this, we see a gap-opening planet should interact with a disk mainly through gravitational torques.

When a planet opens a gap in the disk, a_{p} evolves due to the disk's viscous evolution (Type II migration). If $M_{\text{p}} \lesssim 2\pi \bar{\Sigma}(a_{\text{p}})a_{\text{p}}^2$, the planet follows the viscous evolution of the disk, and a_{p} decreases over the disk's viscous time t_{v}

[Lin & Papaloizou, 1985, Lin, Bodenheimer & Richardson, 1996, Kley & Nelson, 2012]. When $M_p \gtrsim 2\pi\bar{\Sigma}(a_p)a_p^2$, the planet's gravitational torque balances the disk's viscous torque, and migrates inward over a timescale longer than t_v [Lin & Papaloizou, 1985, Ida & Lin, 2004, Kley & Nelson, 2012]. Motivated by simulations of gap-opening planets migrating through viscous disks (e.g. Duffell et al. 2014, Dürmann & Kley 2015), we assume a_p evolves in time according to

$$\frac{da_p}{dt} = -\frac{a_p}{t_{\text{mig}}}, \quad (3.38)$$

where

$$t_{\text{mig}} = \Lambda_{\text{mig}} \max\left(1, \frac{M_p}{2\pi\bar{\Sigma}(a_p)a_p^2}\right) t_v, \quad (3.39)$$

and $\Lambda_{\text{mig}} \sim 1$ is a factor parameterizing the uncertainty in t_{mig} . When $M_p < 2\pi\bar{\Sigma}(a_p, t)a_p^2$, a smaller (larger) Λ_{mig} value corresponds to a migration timescale t_{mig} shorter (longer) than the disk's viscous timescale t_v , parameterizing the effects seen in Duffell et al. [2014].

For photo-ionized disks (Sec. 3.3), Eq. (3.38) applies to planets in the outer disk ($r > r_c$). We neglect the migration of planets in the inner depleted disk ($r < r_c$).

3.4.3 Planet Interactions with Outer Disk

As discussed in Section 3.3, photoevaporation may deplete the inner disk ($r < r_c$) on a very short timescale. If the planet's semi-major axis a_p lies inside r_c , the mutual gravitational torques between the planet and the disk are modified. As noted in Section 3.3, we neglect any misalignment between the inner ($r < r_c$) and outer ($r > r_c$) disks, since the timescale over which the inner disk is depleted is

much shorter than the age of the system. The precession rate of \hat{l}_p around \hat{l}_d due to the mass of the inner disk,

$$\tilde{\omega}_{pd<} \simeq \frac{\pi\bar{\Sigma}(a_p, t)a_p^2}{M_\star h_p} \sqrt{\frac{GM_\star}{a_p^3}}, \quad (3.40)$$

is diminished due to the inner disk's rapid depletion from photoevaporation (see Sec. 3.3). Instead, the precession of \hat{l}_p around \hat{l}_d is mainly governed by the torque on the planet from the outer disk ($r > r_c$):

$$\begin{aligned} \tilde{T}_{pd>} &\simeq - \int_{r_c}^{r_{out}} \left(\frac{3GM_p a_p^2}{4r^3} \right) (\hat{l}_p \cdot \hat{l}_d) (\hat{l}_d \times \hat{l}_p) 2\pi \Sigma r dr \\ &= -L_p \tilde{\omega}_{pd>} (\hat{l}_p \cdot \hat{l}_d) \hat{l}_d \times \hat{l}_p, \end{aligned} \quad (3.41)$$

where

$$\tilde{\omega}_{pd>} \simeq \frac{3\pi G \Sigma(r_c, t)}{2(1+p)r_c} \sqrt{\frac{a_p^3}{GM_\star}} \quad (3.42)$$

characterizes the precession frequency of the planet around the outer disk (assuming $a_p \ll r_c \ll r_{out}$).

The planet also exerts a back-reaction torque on the disk, causing the outer/inner disk to precess around the planet at the characteristic rates

$$\tilde{\omega}_{d>p} \simeq \frac{3(5/2-p)}{4(1+p)} \left(\frac{M_p}{M_\star} \right) \frac{a_p^2}{r_c^{1+p} r_{out}^{1-p}} \sqrt{\frac{GM_\star}{r_{out}^3}}, \quad (3.43)$$

$$\tilde{\omega}_{d<p} \simeq \frac{5/2-p}{2\Delta_p/a_p} \left(\frac{\Sigma_c r_c^p a_p^{1-p}}{\Sigma_{out} r_{out}} \right) \left(\frac{M_p}{M_\star} \right) \sqrt{\frac{GM_\star}{r_{out}^3}}. \quad (3.44)$$

[Compare the scaling of Eq. (3.43) to (3.7), and (3.44) to (3.35)] The total planet-disk mutual precession rates are then

$$\tilde{\omega}_{pd} = \tilde{\omega}_{pd>} + \tilde{\omega}_{pd<}, \quad (3.45)$$

$$\tilde{\omega}_{dp} = \tilde{\omega}_{d>p} + \tilde{\omega}_{d<p}. \quad (3.46)$$

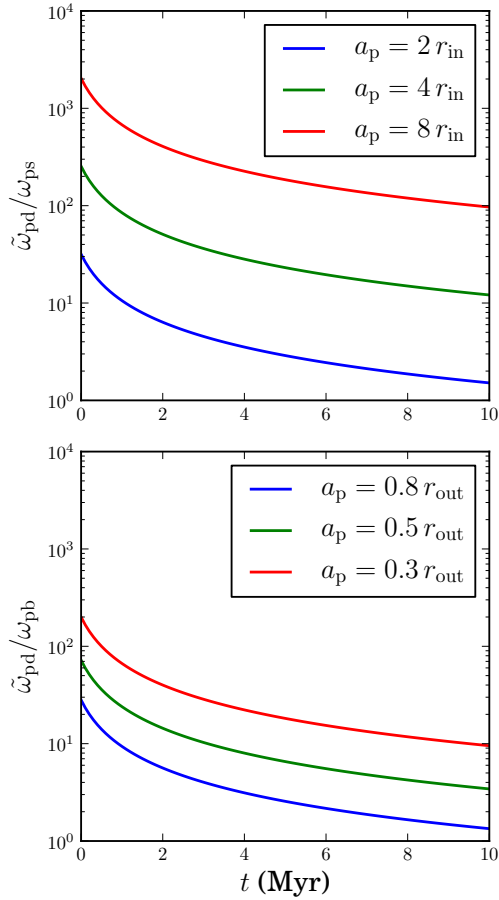


Figure 3.4: Ratio of the precession frequency of the planet driven by the disk $\tilde{\omega}_{pd}$ [Eq. (3.34)] to the precession frequency of the planet driven by the star ω_{ps} [Eq. (3.48)] and binary ω_{pb} [Eq. (3.51)] for different planetary semi-major axis a_p , with $p = 3/2$ and all other parameters canonical. This plot shows the planet is tightly coupled to the disk, so we may approximate $\hat{l}_p \simeq \hat{l}_d$. We assume $h_p = 0.1$.

3.4.4 Planet-Star and Planet-Binary Interactions

The oblate central star exerts a torque on the planet, given by

$$\mathbf{T}_{ps} = -L_p \omega_{ps} (\hat{l}_p \cdot \hat{s}) \hat{s} \times \hat{l}_p, \quad (3.47)$$

where

$$\omega_{ps} = \frac{3k_q}{2} \bar{\Omega}_\star^2 \left(\frac{R_\star}{a_p} \right)^2 \sqrt{\frac{GM_\star}{a_p^3}} \quad (3.48)$$

characterizes the precession frequency of \hat{l}_p around \hat{s} . The back-reaction torque on the star from the planet causes \hat{s} to precess around \hat{l}_p at a characteristic rate

$$\begin{aligned}\omega_{\text{sp}} &= (L_p/S)\omega_{\text{ps}} \\ &= \frac{3k_q}{2k_\star} \bar{\Omega}_\star \left(\frac{M_p}{M_\star} \right) \frac{\sqrt{GM_\star R_\star^3}}{a_p^3}.\end{aligned}\quad (3.49)$$

The binary companion also exerts torque on the planet:

$$\mathbf{T}_{\text{pb}} = -L_p \omega_{\text{pb}} (\hat{l}_p \cdot \hat{l}_b) \hat{l}_b \times \hat{l}_p,\quad (3.50)$$

where

$$\omega_{\text{pb}} = \frac{3M_b}{4M_\star} \left(\frac{a_p}{a_b} \right)^3 \sqrt{\frac{GM_\star}{a_p^3}}\quad (3.51)$$

characterizes the precession frequency of \hat{l}_p around \hat{l}_b . Because the binary has orbital angular momentum $L_b \gg L_p$, the back reaction torque on the binary from the planet is neglected.

As discussed in Sections 3.4.1-3.4.3, the dominant planet-disk coupling involves mutual precession, with characteristic frequency $\tilde{\omega}_{\text{pd}}$. For homologously evolving disks, comparing $\tilde{\omega}_{\text{pd}}$ [Eq. (3.34)] to ω_{ps} and ω_{pb} , we see (assuming $p = 3/2$)

$$\begin{aligned}\frac{\tilde{\omega}_{\text{pd}}}{\omega_{\text{ps}}} &= 7.27 \left(\frac{k_q}{0.1} \right)^{-1} \left(\frac{h_p}{0.1} \right)^{-1} \frac{\bar{M}_d}{\bar{M}_\star} \\ &\times \left(\frac{\bar{\Omega}_\star}{0.1} \right)^{-2} \frac{\bar{r}_{\text{in}}^{5/2}}{\bar{r}_{\text{out}}^{1/2} \bar{R}_\star^2} \left(\frac{a_p}{r_{\text{in}}} \right)^{5/2},\end{aligned}\quad (3.52)$$

$$\frac{\tilde{\omega}_{\text{pd}}}{\omega_{\text{pb}}} = 7.20 \left(\frac{h_p}{0.1} \right)^{-1} \frac{\bar{M}_d \bar{a}_b^3}{\bar{M}_b \bar{r}_{\text{out}}^3} \left(\frac{r_{\text{out}}}{a_p} \right)^{5/2},\quad (3.53)$$

where we have used Eqs. (3.2) and (3.3) to relate $\bar{\Sigma}(a_p, t)$ to M_d . Figure 3.4 plots the ratios (3.52) and (3.53) for a standard disk model. We see for most values of a_p (with $a_p \gtrsim$ a few r_{in} and $a_p \ll r_{\text{out}}$), $\tilde{\omega}_{\text{pd}} \gg \omega_{\text{ps}}, \omega_{\text{pb}}$ over the disk's lifetime.

This allows us to make the simplifying assumption $\hat{l}_p(t) \simeq \hat{l}_d(t)$ when Σ evolves homologously. We note that in certain situations, a secular resonance between a planet, disk, and binary may greatly increase the planet-disk inclination [Lubow & Martin, 2016, Martin et al., 2016], breaking the assumption that $\hat{l}_p \simeq \hat{l}_d$.

When the planet lies in the inner region ($a_p < r_c$) of a photo-ionized disk, we have (assuming $p = 3/2$)

$$\frac{\tilde{\omega}_{pd>}}{\omega_{ps}} = 2.1 \times 10^{-5} \left(\frac{k_q}{0.1} \right)^{-1} \left(\frac{\bar{\Omega}_\star}{0.1} \right)^{-2} \left(\frac{r_{out}}{25 r_c} \right)^{5/2} \times \frac{\bar{r}_{in}^5 \bar{M}_d}{\bar{R}_\star^2 \bar{r}_{out}^3 \bar{M}_\star} \left(\frac{a_p}{r_{in}} \right)^5, \quad (3.54)$$

$$\frac{\tilde{\omega}_{pd>}}{\omega_{pb}} = 1.3 \times 10^3 \frac{\bar{M}_d \bar{a}_b^3}{\bar{M}_b \bar{r}_{out}^3} \left(\frac{r_{out}}{25 r_c} \right)^{5/2}. \quad (3.55)$$

Clearly, the planet-outer disk precession frequency greatly exceeds the planet-binary precession frequency when $a_p < r_c$. However, the ratio $\tilde{\omega}_{pd>}/\omega_{ps}$ depends sensitively on the distance of the planet from the star. The planet's full response to the star, disk and binary will need to be taken into account when the inner disk is depleted.

The star's response to the planet is important in the context of planet-star-disk-binary dynamics. Comparing ω_{sp} [Eq. (3.49)] to $\tilde{\omega}_{sd}$ [Eq. (3.8)], we have (assuming $p = 3/2$)

$$\frac{\omega_{sp}}{\tilde{\omega}_{sd}} = 3.5 \left(\frac{M_p}{1 M_J} \right) \frac{\bar{r}_{out}^{1/2}}{\bar{M}_d \bar{r}_{in}^{1/2}} \left(\frac{r_{in}}{a_p} \right)^3. \quad (3.56)$$

Equation (3.56) shows $\omega_{sp} \gtrsim \tilde{\omega}_{sd}$ near the end of the disk's lifetime ($\bar{M}_d \ll 1$), when the planet lies close to the disk's inner truncation radius. More interesting is the magnitude of ω_{sp} compared to $\tilde{\omega}_{db}$ [Eq. (3.10)] (assuming $p = 3/2$):

$$\frac{\omega_{sp}}{\tilde{\omega}_{db}} = 333 \left(\frac{2k_q}{k_\star} \right) \left(\frac{\bar{\Omega}_\star}{0.1} \right) \left(\frac{M_p}{1 M_J} \right) \frac{\bar{a}_b^3 \bar{R}_\star^{3/2}}{\bar{M}_b \bar{r}_{in}^3 \bar{r}_{out}^{3/2}} \left(\frac{r_{in}}{a_p} \right)^3. \quad (3.57)$$

Equation (3.57) shows for a substantial region of parameter space, $\omega_{sp} \gtrsim \tilde{\omega}_{db}$. This implies that *a close-in massive planet can suppress secular resonance*. The next

section explores different formation scenarios of close-in massive planets (hot Jupiters), and their implications to spin-orbit misalignments generated via star-disk-binary interactions.

3.5 Inclination Evolution of Planet-Star-Disk-Binary Systems

This section explores how the formation and migration of a gas giant in protoplanetary disks affects the generation of primordial spin-orbit misalignments through star-disk-binary interactions. The core-accretion scenario assumes a gas giant forms following the run-away accretion of protoplanetary disk gas onto a $\sim 10 M_{\oplus}$ core (e.g. Pollack et al. 1996). After the formation of the massive planet, we consider three different models for its evolution through the disk. The first assumes the planet forms in-situ, with the planet's semi-major axis a_p fixed in time (Secs. 3.5.1-3.5.2), the second models the formation of a hot Jupiter via Type II migration (Sec. 3.5.3), while the last considers the system's dynamics after the hot Jupiter is left in a photo-ionized disk cavity (Sec. 3.5.4).

We will frequently refer to the angles θ_{ps} , θ_{pd} , and θ_{pb} throughout this section, defined as

$$\theta_{ps} = \cos^{-1}(\hat{\mathbf{l}}_p \cdot \hat{\mathbf{s}}), \quad (3.58)$$

$$\theta_{pd} = \cos^{-1}(\hat{\mathbf{l}}_p \cdot \hat{\mathbf{l}}_d), \quad (3.59)$$

$$\theta_{pb} = \cos^{-1}(\hat{\mathbf{l}}_p \cdot \hat{\mathbf{l}}_b), \quad (3.60)$$

which define the mutual planet-star, planet-disk, and planet-binary inclinations, respectively.

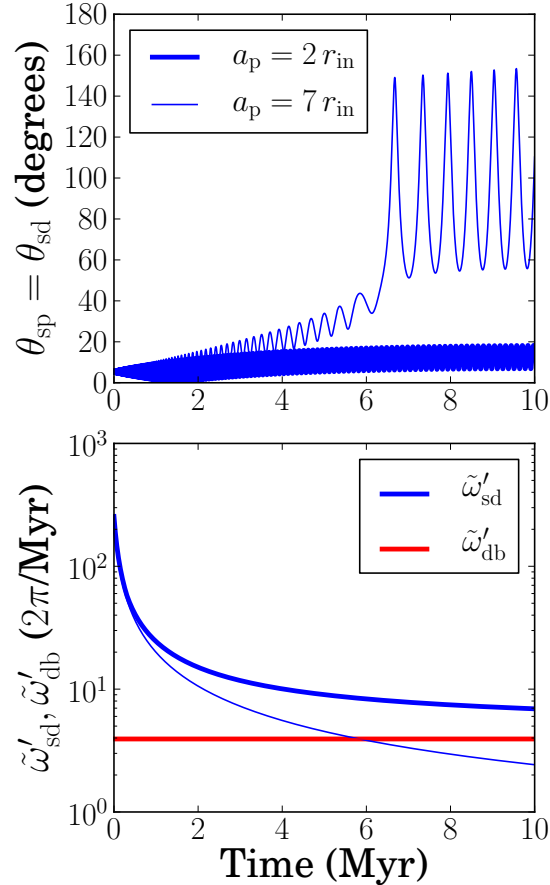


Figure 3.5: Evolution of the star-disk/star-planet angle $\theta_{sd} = \theta_{sp}$ (top panel), modified star-disk precession frequency $\tilde{\omega}'_{sd}$ [Eq. (3.67)] and modified disk-binary precession frequency $\tilde{\omega}'_{db}$ [Eq. (3.69)] (bottom panel) for planetary semi-major axis of $a_p = 2 r_{in} = 0.0736$ au (thick lines) and $a_p = 7 r_{in} = 0.258$ au (thin lines). We take all parameters to be canonical except $\bar{\Omega}_\star = 0.03$, $p = 3/2$, $t_v = 0.1$ Myr, with $t_p = 0.3$ Myr and $\xi = 10$. Here, the planet's mass $M_p = 0.201 M_J$ when $a_p = 2 r_{in}$ and $M_p = 0.514 M_J$ when $a_p = 7 r_{in}$. We take the initial star-disk inclination $\theta_{sd}(0) = 5^\circ$ and disk-binary inclination $\theta_{db}(0) = 60^\circ$ for all integrations. The hot Jupiter formed in-situ (thick lines) does not experience appreciable excitations of spin-orbit misalignment.

3.5.1 Early In-Situ Formation of Hot-Jupiters

Batygin, Bodenheimer & Laughlin [2016] proposed Hot-Jupiters form in-situ in their protoplanetary disks over timescales shorter than 1 million years. They argued that a $10 M_\oplus$ core with $a_p \lesssim 0.1$ au may undergo run-away accretion

early in the disk's lifetime. This scenario may explain why hot Jupiters do not have close, low-mass planetary companions [Batygin, Bodenheimer & Laughlin, 2016, Spalding & Batygin, 2017]. Here we explore how in-situ formation affects the star-disk-binary system dynamics.

For early formation of a gas giant, we assume the planet's mass is accreted from the disk within the planet's feeding zone. Specifically, we take the time-dependent planetary mass to be

$$M_p(t) = \begin{cases} 2\pi\Sigma(a_p, t)a_p\Delta a_p, & t < t_p \\ 2\pi\Sigma(a_p, t_p)a_p\Delta a_p & t \geq t_p \end{cases} \quad (3.61)$$

where t_p is the formation time,

$$\Delta a_p = \xi a_p (M_p/3M_\star)^{1/3} \quad (3.62)$$

is the width of the planet's feeding zone, and ξ is a free parameter. This yields a final ($t \geq t_p$) planetary mass of

$$\frac{M_p}{M_\star} = \frac{\xi^{3/2}}{3^{1/2}} \left[\frac{2\pi\Sigma(a_p, t_p)a_p^2}{M_\star} \right]^{3/2}. \quad (3.63)$$

This model neglects accretion of gas onto the planet due to the viscous transport of disk material across the planet's gap. This is a reasonable approximation, since simulations show the accretion rate onto a planet undergoing run-away gas accretion is typically much greater than the global accretion rate of the disk onto the host star (e.g. Papaloizou & Nelson 2005, D'Angelo & Lubow 2008, Ayliffe & Bate 2009a, Tanigawa & Tanaka 2016)

Equation (3.63) with $p = 3/2$ gives a final planetary mass for a hot Jupiter formed in-situ of

$$\frac{M_p}{M_\star} = \frac{1.93 \times 10^{-3}}{(1 + t_p/t_v)^{3/2}} \left(\frac{\xi}{10} \right)^{3/2} \frac{\bar{M}_{d0}^{3/2}}{\bar{M}_\star^{3/2} \bar{r}_{\text{out}}^{3/4}} \left(\frac{a_p}{0.1 \text{ au}} \right)^{3/4}. \quad (3.64)$$

Even with a large feeding zone ($\xi = 10$), we see that the hot Jupiter must form at a time $t_p \lesssim \text{few} \times t_v \sim 1 \text{ Myr}$ to attain mass $M_p \sim 1 M_J$.

We assume in this subsection that $\hat{\mathbf{l}}_p(t) \simeq \hat{\mathbf{l}}_d(t)$, since $\tilde{\omega}_{pd} \gg \omega_{ps}, \omega_{pb}$ when the planet is embedded in the disk (see Fig. 3.4). The evolution equations for $\hat{\mathbf{s}}$ and $\hat{\mathbf{l}}_d = \hat{\mathbf{l}}_p$ become

$$\frac{d\hat{\mathbf{s}}}{dt} = -\tilde{\omega}'_{sd}(\hat{\mathbf{s}} \cdot \hat{\mathbf{l}}_d)\hat{\mathbf{l}}_d \times \hat{\mathbf{s}}, \quad (3.65)$$

$$\frac{d\hat{\mathbf{l}}_d}{dt} = -\tilde{\omega}'_{ds}(\hat{\mathbf{l}}_d \cdot \hat{\mathbf{s}})\hat{\mathbf{s}} \times \hat{\mathbf{l}}_d - \tilde{\omega}'_{db}(\hat{\mathbf{l}}_d \cdot \hat{\mathbf{l}}_b)\hat{\mathbf{l}}_b \times \hat{\mathbf{l}}_d, \quad (3.66)$$

where

$$\tilde{\omega}'_{sd} = \tilde{\omega}_{sd} + \omega_{sp}, \quad (3.67)$$

$$\tilde{\omega}'_{ds} = \tilde{\omega}_{ds} + (L_p/L_d)\omega_{ps}, \quad (3.68)$$

$$\tilde{\omega}'_{db} = \tilde{\omega}_{db} + (L_p/L_d)\omega_{pb}, \quad (3.69)$$

are the mutual star-disk-binary precession frequencies modified by the presence of a massive planet.

Figure 3.5 shows the evolution of $\theta_{sd} = \theta_{sp}$ (top panel) and precession frequencies $\tilde{\omega}'_{sd}$ and $\tilde{\omega}'_{db}$ (bottom panel). We see when the planet forms too close to its host star ($a_p = 2 r_{in}$), $\tilde{\omega}'_{sd}$ is always larger than $\tilde{\omega}'_{db}$ throughout the disk evolution, the system averts secular resonance, and no significant spin-orbit misalignment is generated. In other words, a close-in giant planet makes $\hat{\mathbf{s}}$ closely follow $\hat{\mathbf{l}}_d \simeq \hat{\mathbf{l}}_p$. When the planet forms further from its host star ($a_p = 7 r_{in}$), ω_{sp} is reduced, and the system goes through secular resonance, and significant θ_{sp} is achieved. The star-planet-disk-binary system may undergo secular resonance when the planet forms at a sufficiently large a_p , so that $\omega_{sp} \lesssim \tilde{\omega}_{db}$. This inequality gives a lower bound for a_p :

$$a_p \gtrsim \left[\frac{2(4-p)k_q}{(5/2-p)k_\star} \right]^{1/3} \bar{\Omega}_\star^{1/3} \left(\frac{M_p}{M_b} \right)^{1/3} \left(\frac{R_\star}{r_{out}} \right)^{1/2} a_b. \quad (3.70)$$

Taking $p = 3/2$, we have

$$a_p \gtrsim 0.23 \left(\frac{2k_q}{\bar{k}_\star} \right)^{1/3} \left(\frac{\bar{\Omega}_\star}{0.1} \right)^{1/3} \left(\frac{M_p}{1 M_J} \right)^{1/3} \frac{\bar{R}_\star^{1/2} \bar{a}_b}{\bar{M}_b^{1/3} \bar{r}_{\text{out}}^{1/2}} \text{ au.} \quad (3.71)$$

Thus, only giant planets formed at large distances ($a_p \gtrsim 0.2$ au) have any chance of experiencing excitation of spin-orbit misalignment from star-disk-binary interactions. Lower mass planets ($M_p \lesssim 0.1 M_J$) formed around slowly-spinning stars ($\bar{\Omega}_\star \lesssim 0.03$) with close binary companions ($a_b \lesssim 200$ au) may experience excitation of spin-orbit misalignments when $a_p \gtrsim 0.04$ au, but this is a very limited region of the parameter space of observed star-disk-binary systems. We conclude significant θ_{sp} is unlikely to be excited when a HJ forms in-situ early ($t_p \lesssim 1$ Myr).

3.5.2 Late In-Situ Formation of Hot-Jupiters

Boley, Granados Contreras & Gladman [2016] proposed that a $\sim 10 M_\oplus$ core may form at orbital periods $\lesssim 10$ days after a phase of dynamical instability in a short-period ($\lesssim 200$ days) multi-planet system. If this critical core forms late in the disk's lifetime ($t_p \gtrsim 1$ Myr), the planet cannot accrete much of the disk's mass locally [Eq. (3.64)]. Therefore, we assume a hot Jupiter formed late ($t_p \gtrsim 1$ Myr) in the disk's lifetime grows primarily from disk mass advected through the planets gap. Simulations show the accretion rate of viscously advected disk-mass onto a gap-opening planet may be written as

$$\frac{dM_p}{dt} = -\eta \frac{dM_d}{dt}, \quad (3.72)$$

where $\eta \sim 0.7 - 0.9$ depending on the planet's mass and local disk properties (e.g. Lubow & D'Angelo 2006). The accretion rate (3.72) will cause the planet's

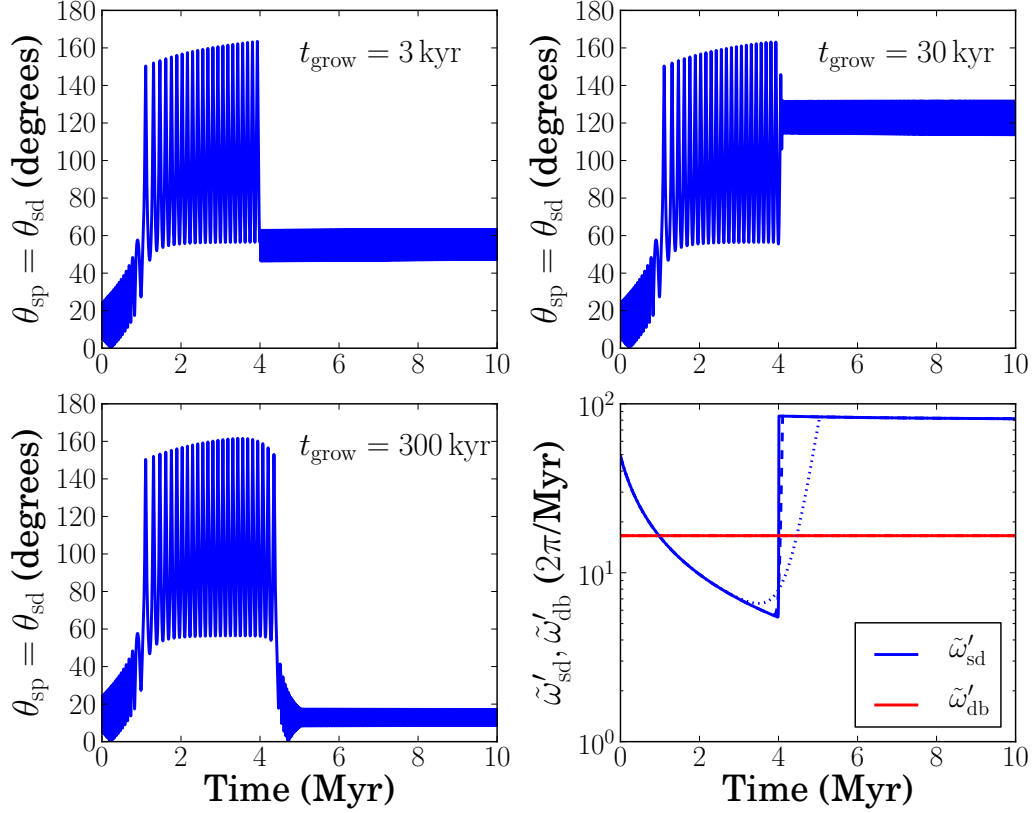


Figure 3.6: Evolution of the star-planet/star-disk inclination $\theta_{\text{sp}} = \theta_{\text{sd}}$ in the late in-situ model, for different planet mass growth timescale t_{grow} [Eq. (3.73)] as indicated (top and bottom left panels). The bottom right panel shows the modified star-disk precession frequency $\tilde{\omega}'_{\text{sd}}$ [Eq. (3.67)] and modified disk-binary precession frequency $\tilde{\omega}'_{\text{db}}$ [Eq. (3.69)] for $t_{\text{grow}} = 3$ kyr (solid), $t_{\text{grow}} = 30$ kyr (dashed), and $t_{\text{grow}} = 300$ kyr (dotted). All parameter values are canonical [Eq. (3.1)] except the binary's semi-major axis $a_b = 200$ au. The planet has a semi-major axis of $a_p = 2 r_{\text{in}} = 0.0736$ au, and forms at time $t_p = 4$ Myr. The adiabatic parameter A [Eq. (3.75)] takes values of $A = 0.312$ ($t_{\text{grow}} = 3$ kyr), $A = 3.12$ ($t_{\text{grow}} = 30$ kyr), and $A = 31.2$ ($t_{\text{grow}} = 300$ kyr). Large star-planet/disk inclinations are maintained only when $A \lesssim$ a few.

mass M_p to grow on a timescale

$$\begin{aligned} t_{\text{grow}} &\equiv \frac{M_p}{dM_p/dt} \sim \frac{t_v}{\eta} \left(\frac{M_p}{M_d} \right) \\ &= 2.15 \text{ kyr} \left(\frac{t_v}{0.5 \text{ Myr}} \right) \left(\frac{0.7}{\eta} \right) \left(\frac{M_p}{10 M_\oplus} \right) \bar{M}_d^{-1}. \end{aligned} \quad (3.73)$$

Because in this model the planet's mass is accreted globally from the disk, we assume that M_p remains independent of the local disk properties (most notably the disk surface density near $r = a_p$), and prescribe $M_p = M_p(t)$ as

$$M_p(t) = \min \left[10 M_\oplus \exp \left(\frac{t - t_p}{t_{\text{grow}}} \right), 1 M_J \right]. \quad (3.74)$$

Notice our early in-situ formation model for hot Jupiters [Eq. (3.63)] fixes $\omega_{\text{sp}} = \text{constant}$ when $t \geq t_p$, while our late in-situ formation model [Eq. (3.74)] causes ω_{sp} to grow until $M_p = 1 M_J$.

Because the late in-situ formation of a hot Jupiter causes an increase of $\tilde{\omega}'_{\text{sd}}$ after formation, we expect the system to encounter a second secular resonance (when $\omega_{\text{sp}} \sim \tilde{\omega}_{\text{db}}$) if the system undergoes an initial secular resonance (when $\tilde{\omega}_{\text{sd}} \sim \tilde{\omega}_{\text{db}}$) before the planet forms. The timescale of this second resonance crossing is of order t_{grow} . If t_{grow} is sufficiently long compared to $(\tilde{\omega}_{\text{db}})^{-1}$, a large amount of angular momentum may be exchanged throughout the planet-star-disk-binary system during the resonance crossing, significantly influencing the final star-planet/disk inclinations $\theta_{\text{sp}} = \theta_{\text{sd}}$. If t_{grow} is comparable or shorter than $(\tilde{\omega}_{\text{db}})^{-1}$, the system cannot exchange much angular momentum during its period of secular resonance, effectively freezing the star-planet/disk inclination at the time the planet forms ($\theta_{\text{sp}}(t) \approx \theta_{\text{sp}}(t_p)$ when $t \geq t_p$). We introduce the adiabaticity parameter

$$A = t_{\text{grow}} \tilde{\omega}_{\text{db}}. \quad (3.75)$$

When $A \gg 1$, we expect a large amount of angular momentum to be exchanged between the stellar spin and the planet/disk orbital angular momenta.

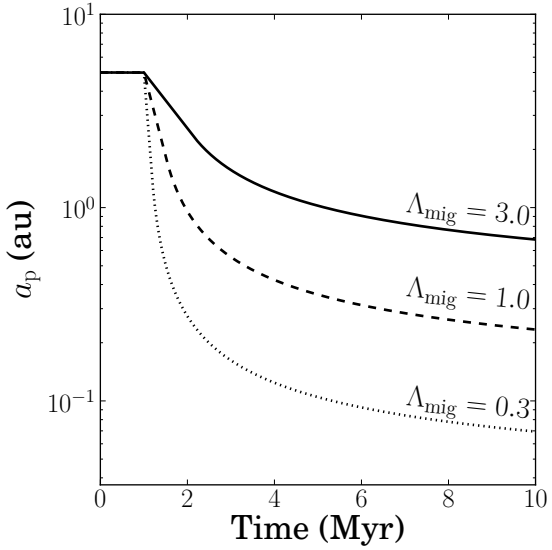


Figure 3.7: Evolution of the planet’s semi-major axis a_p with time, for different Λ_{mig} values as indicated [see Eq. (3.39)]. We assume the planet forms at $t_p = 1$ Myr and $a_p = 5$ au with $M_p = 0.93 M_J$, assuming $\xi = 4$ (assuming $p = 1$, and canonical disk parameters). The planet migrates to $a_p = 0.07$ au ($\Lambda_{\text{mig}} = 0.3$, fast migration), $a_p = 0.23$ au ($\Lambda_{\text{mig}} = 1.0$, moderate migration), and $a_p = 0.68$ au ($\Lambda_{\text{mig}} = 3.0$, slow migration).

Figure 3.6 shows the evolution of $\theta_{\text{sp}} = \theta_{\text{sd}}$ (top and bottom left panels) and precession frequencies $\tilde{\omega}'_{\text{sd}}$ and $\tilde{\omega}'_{\text{db}}$ (bottom right panel) using our late in-situ hot Jupiter formation model, with t_{grow} indicated. In the top two panels, $A \lesssim$ a few, so the system’s second secular resonance does not allow a significant amount of angular momentum to be transferred from the stellar spin to the planet/disk angular momenta. As a result, the star-planet/disk inclinations freeze to $\theta_{\text{sp}} \approx 60^\circ$ (top left) and $\theta_{\text{sp}} \approx 120^\circ$ (top right) after the planet forms ($t_p = 4$ Myr). In the bottom left panel, $A = 31.2 \gg 1$, so the star-planet/disk inclination settles down to $\theta_{\text{sp}} \approx 10^\circ$ after the second resonance crossing.

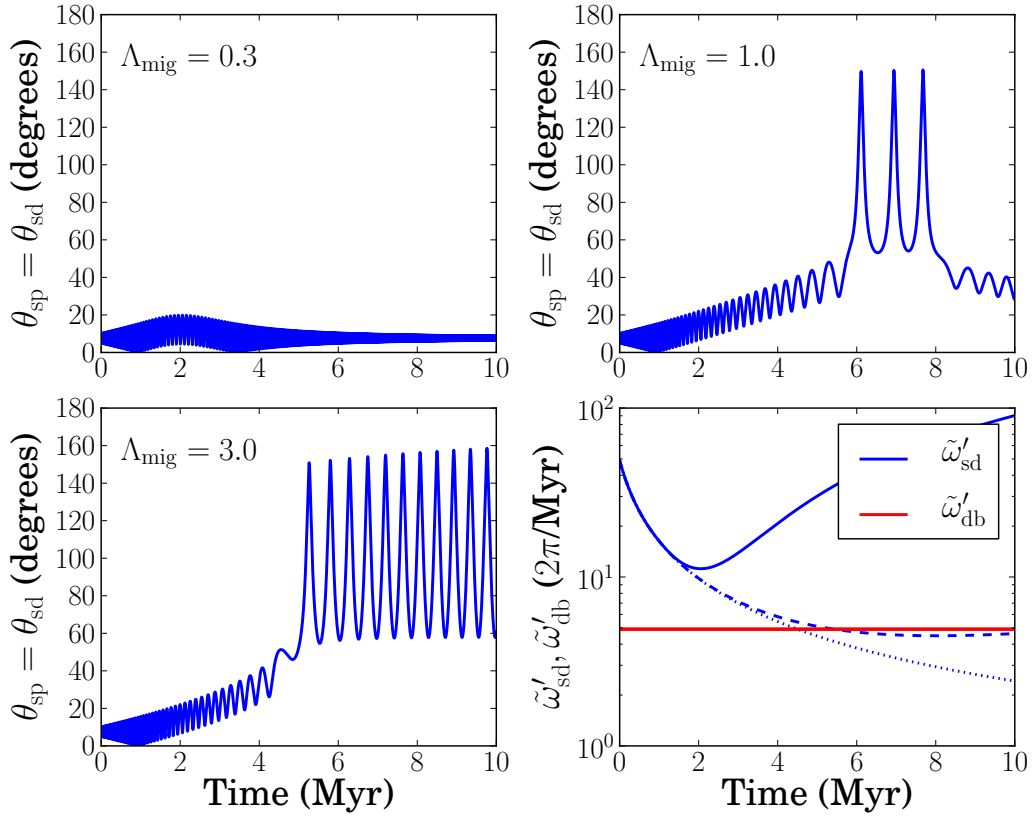


Figure 3.8: Evolution of the star-disk/star-planet angle $\theta_{\text{sd}} = \theta_{\text{sp}}$ (top and bottom left panels) and precession frequencies $\tilde{\omega}'_{\text{sd}}$ [Eq. (3.67)] and $\tilde{\omega}'_{\text{db}}$ [Eq. (3.69)] (bottom right panel) with time, for the Λ_{mig} values indicated. In the bottom right panel, the different lines correspond to fast migration ($\Lambda_{\text{mig}} = 0.3$, dotted), moderate migration ($\Lambda_{\text{mig}} = 1.0$, dashed), and slow migration ($\Lambda_{\text{mig}} = 3.0$, solid). We take all parameters to be canonical with $p = 1$ and $t_v = 0.5$ Myr. The planet forms at $t_p = 1$ Myr and $a_p = 5$ au with $M_p = 0.931 M_J$ [assuming $\xi = 4$ in Eq. (3.63)]. We take $\theta_{\text{sd}}(0) = 5^\circ$ and $\theta_{\text{db}}(0) = 60^\circ$ in all integrations. See Fig. 3.7 for the a_p evolution. No appreciable θ_{sp} is generated when a hot Jupiter is produced (see the $\Lambda_{\text{mig}} = 0.3$ case).

3.5.3 Formation of Hot-Jupiters through Type-II Migration

We now consider the scenario where the giant planet forms at a large semi-major axis and subsequently undergoes Type-II migration. The planet forms with a mass M_p given by Eq. (3.61), where a_p is fixed when $t \leq t_p$, afterwards it

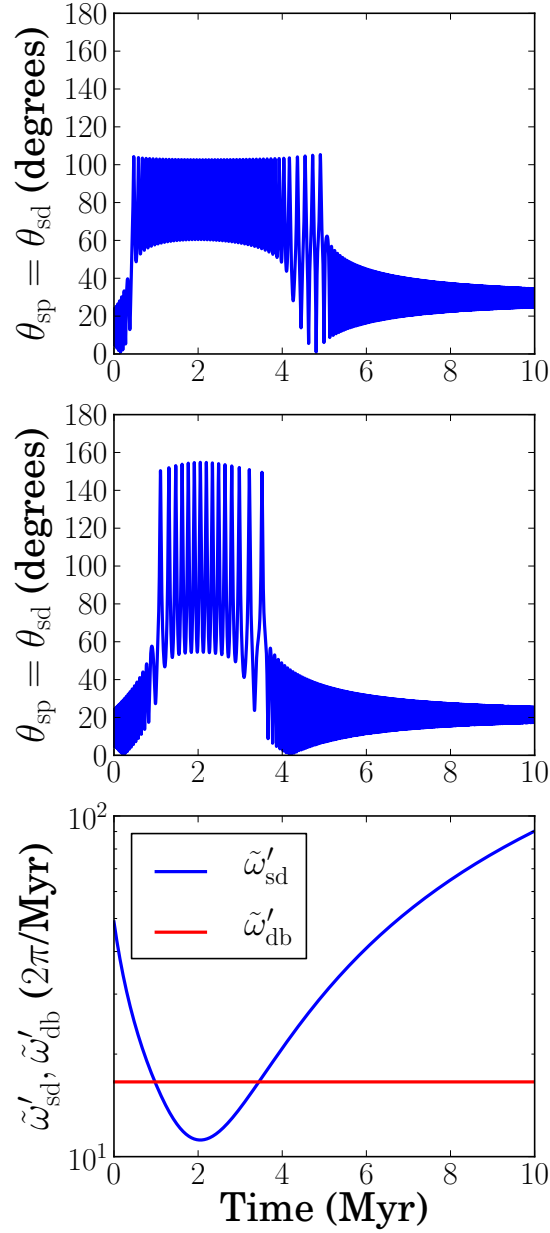


Figure 3.9: Evolution of the star-disk/star-planet angle $\theta_{\text{sd}} = \theta_{\text{sp}}$ (top and middle panels) and precession frequencies $\tilde{\omega}'_{\text{sd}}$ [Eq. (3.67)] and $\tilde{\omega}'_{\text{db}}$ [Eq. (3.69)] (bottom panel) with $\theta_{\text{db}}(t)$ approximately equal to $\theta_{\text{db}}(0) = 20^\circ$ (top) and $\theta_{\text{db}}(0) = 60^\circ$ (middle), for $\Lambda_{\text{mig}} = 0.3$ and $\theta_{\text{sd}}(0) = 5^\circ$ in all integrations. We take all parameters to be canonical except $a_b = 200$ au with $p = 1$ and $t_v = 0.5$ Myr. The planet forms at $t_p = 1$ Myr and $a_p = 5$ au with $M_p = 0.931 M_J$ [assuming $\xi = 4$ in Eq. (3.63)]. See Fig. 3.7 for the a_p evolution. Significant ($\theta_{\text{sp}} \gtrsim 30$) spin-orbit misalignments are not sustained when a Jovian planet migrates close to its host star after the star-disk-binary system experiences secular resonance ($\tilde{\omega}_{\text{sd}} \sim \tilde{\omega}_{\text{db}}$).

migrates inwards according to Eqs. (3.38) and (3.39). For $p = 1$, Eq. (3.63) gives

$$\frac{M_p}{M_\star} = \frac{1.63 \times 10^{-3}}{(1 + t_p/t_v)^{3/2}} \left(\frac{\xi}{4}\right)^{3/2} \frac{\bar{M}_{d0}^{3/2}}{\bar{M}_\star^{3/2} \bar{r}_{\text{out}}^{3/2}} \left(\frac{a_p(t_p)}{5 \text{ au}}\right)^{3/2}. \quad (3.76)$$

Figure 3.7 shows the semi-major axis evolution of a planet formed at $t_p = 1 \text{ Myr}$ with $a_p(t_p) = 5 \text{ au}$. The shortest migration time parameter ($\Lambda_{\text{mig}} = 0.3$) leads to a hot Jupiter at the end of the disk's lifetime ($a_p \lesssim 0.1 \text{ au}$ at $t = 10 \text{ Myr}$), while longer migration time parameters allow a_p to decrease and stop at a value $\gtrsim 0.1 \text{ au}$. Fig. 3.7 also shows that most of the planet's migration occurs when the disk is young ($t \lesssim \text{few} \times t_v$), since the reduction of disk mass lengthens t_{mig} significantly [see Eq. (3.39)].

Figure 3.8 plots $\theta_{\text{sp}} = \theta_{\text{sd}}$ (top and bottom left panels), $\tilde{\omega}'_{\text{sd}}$, and $\tilde{\omega}'_{\text{db}}$ (bottom right panel) with time, for the Λ_{mig} values indicated. When $\Lambda_{\text{mig}} = 0.3$, the planet quickly migrates close to its host star within the first few Myr's (see Fig. 3.7). This causes $\tilde{\omega}'_{\text{sd}}$ to increase in time after a few Myr's, ensuring that the secular resonance is never achieved (bottom right panel of Fig. 3.8). As a result, θ_{sp} is not excited by star-disk-binary interactions (top left panel of Fig. 3.8), and the hot Jupiter forms without spin-orbit misalignment. When $\Lambda_{\text{mig}} = 1.0$, the planet migrates to an a_p value so that $\tilde{\omega}'_{\text{sd}} \sim \tilde{\omega}'_{\text{db}}$ after a few Myr's. The star-disk-binary system proceeds to pass into and out of secular resonance, generating a planet with spin-orbit misalignment (top right panel of Fig. 3.8). However, this planet has become a warm Jupiter, with a final semi-major axis $a_p = 0.234 \text{ au}$ at $t = 10 \text{ Myr}$ (see Fig. 3.7). When $\Lambda_{\text{mig}} = 3.0$, the planet stays sufficiently far from its host star so that secular resonance may occur without modification by ω_{sp} , allowing θ_{sp} to be excited by star-disk-binary interactions (bottom left panel of Fig. 3.8). The $\Lambda_{\text{mig}} = 3.0$ planet ends at a semi-major axis of $a_p = 0.683 \text{ au}$, far too large to be considered a hot Jupiter.

Figure 3.9 shows another example of the evolution of star-disk-binary system, in which a hot Jupiter forms via Type-II migration after secular resonance (when $\tilde{\omega}'_{\text{sd}} \sim \tilde{\omega}'_{\text{db}}$). A large θ_{sp} is achieved while $\tilde{\omega}'_{\text{sd}} \lesssim \tilde{\omega}'_{\text{db}}$. However, once the planet migrates close enough to its host star so that $\omega_{\text{sp}} \gtrsim \tilde{\omega}_{\text{db}}$, the system passes through secular resonance again, and \hat{s} switches from precessing around \hat{l}_b to precessing around $\hat{l}_d \simeq \hat{l}_p$. Although θ_{sd} evolves to values significantly larger than the initial $\theta_{\text{sd}}(0) = 5^\circ$, the final stellar obliquity is modest, and border on being considered coplanar ($\theta_{\text{sp}} \lesssim 20^\circ$). We see that even when the star-disk-planet-binary system does undergo secular resonance, the star-planet interaction significantly reduces spin-orbit misalignment after the planet has migrated near the vicinity of the host star.

3.5.4 Hot Jupiters left in disk cavity from photoevaporation

This section examines the fate of hot Jupiters in star-disk-binary systems when the disk's inner cavity is rapidly cleared by photoevaporation. We adopt the $\Sigma(r, t)$ prescription of Section 3.3. For simplicity, we assume the hot Jupiters form in-situ, although they could have undergone Type-II migration before the inner disk is depleted at $t \approx t_w$. Note that when the planet lies in the inner disk depleted by photoevaporation [see Eq. (3.39)], radial migration is negligible, halting the hot Jupiter at $a_p \approx a_p(t_w)$. We assume the planet forms at $t = t_p < t_w$ with mass M_p given by Eq. (3.63).

The evolution of the planet-star-disk-binary system proceeds in two stages. For $t \leq t_w$, the planet is embedded in the “full” disk, so $\hat{l}_p \simeq \hat{l}_d$ and Eqs. (3.65)-(3.66) apply. For $t > t_w$, the planet resides in a depleted disk cavity and $\tilde{\omega}_{\text{pd}} \lesssim$

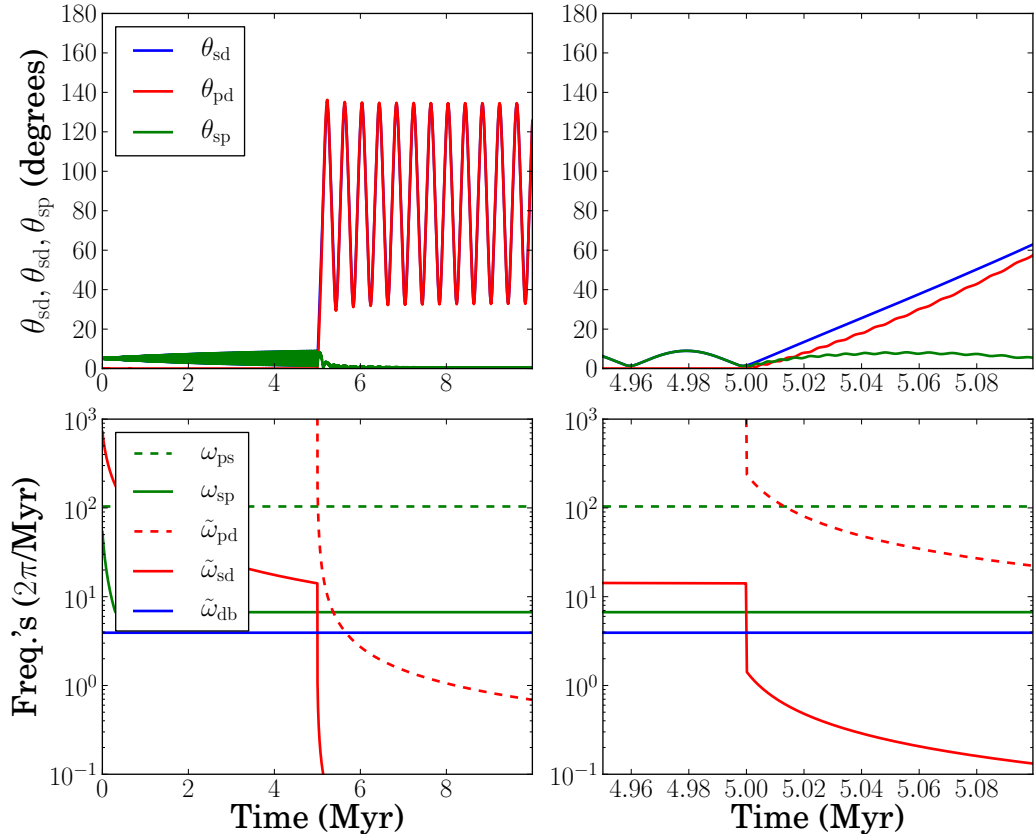


Figure 3.10: Star-disk-planet-binary evolution under a prescribed Σ depletion due to photoevaporation (see Sec. 3.3). Top panels display θ_{sd} , θ_{pd} , and θ_{ps} with time, bottom panels display numerous characteristic precession frequencies with time. Left panels show the system's entire dynamical evolution over 10 Myr, right panels show the system's dynamics near $t \approx t_w = 5$ Myr. All parameters are canonical except $p = 3/2$ and $t_v = 0.1$ Myr, with $t_w = 5$ Myr, $t_{v,in} = 0.01$ Myr, $r_c = 2$ au, $h_p = 0.2$, $a_p(t) = a_p(0) = 4 r_{in} = 0.147$ au, $t_p = 0.3$ Myr, and $M_p = 0.338 M_J$ (assuming $\xi = 10$). We take $\theta_{sd}(0) = 5^\circ$ and $\theta_{db}(t) \approx \theta_{db}(0) = 60^\circ$ for all integrations. Because $\tilde{\omega}'_{sd} \gtrsim \tilde{\omega}'_{db}$ at $t \approx t_w$, the star-planet inclination θ_{sp} stays negligible.

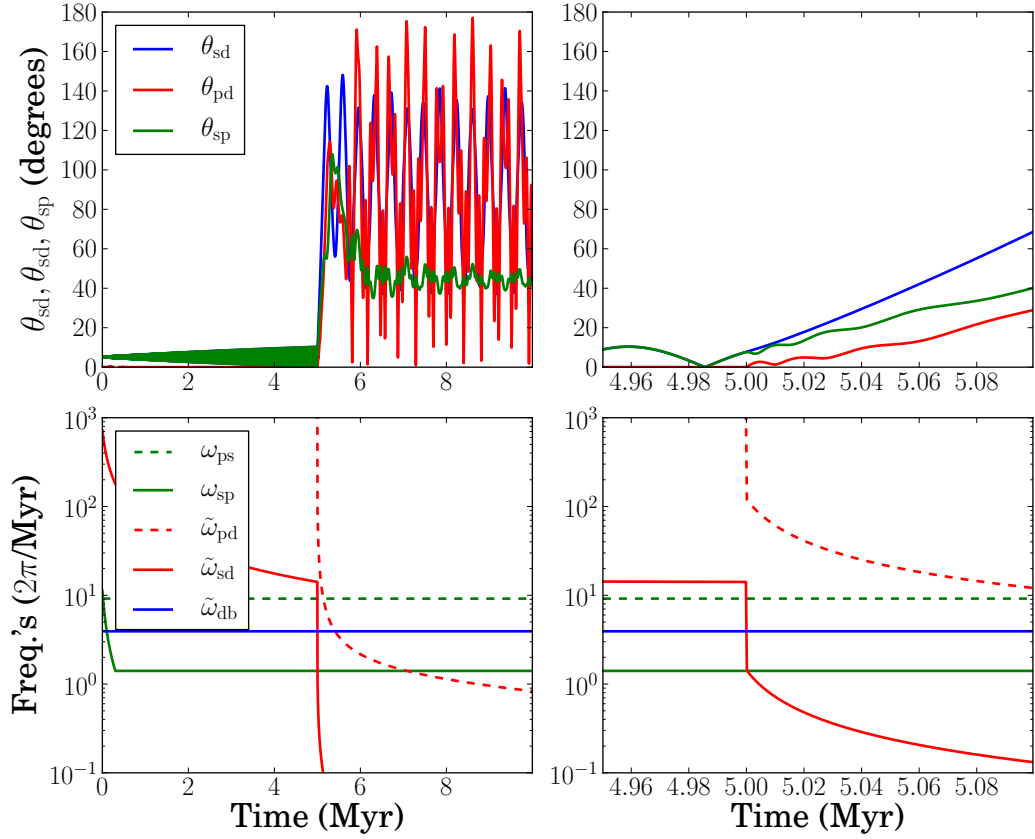


Figure 3.11: Same as Fig. 3.10 except $a_p(t) = a_p(0) = 8 r_{\text{in}} = 0.294 \text{ au}$, $t_p = 0.3 \text{ Myr}$ with $M_p = 0.568 M_J$ (assuming $\xi = 10$). Because $\tilde{\omega}'_{\text{sd}} \lesssim \tilde{\omega}'_{\text{db}}$ at $t \approx t_w$, the star-planet inclination θ_{sp} is excited after t_w .

$\omega_{\text{ps}}, \omega_{\text{pb}}$ [see Eqs. (3.54)-(3.55)], so \hat{l}_p and \hat{l}_d decouple and evolve separately. The evolution equations for $t > t_w$ are

$$\frac{d\hat{s}}{dt} = -\tilde{\omega}_{\text{sd}}(\hat{s} \cdot \hat{l}_d)\hat{l}_d \times \hat{s} - \omega_{\text{sp}}(\hat{s} \cdot \hat{l}_p)\hat{l}_p \times \hat{s}, \quad (3.77)$$

$$\begin{aligned} \frac{d\hat{l}_d}{dt} = & -\tilde{\omega}_{\text{ds}}(\hat{l}_d \cdot \hat{s})\hat{s} \times \hat{l}_d - \tilde{\omega}_{\text{dp}}(\hat{l}_d \cdot \hat{l}_p)\hat{l}_p \times \hat{l}_d \\ & - \tilde{\omega}_{\text{db}}(\hat{l}_d \cdot \hat{l}_b)\hat{l}_b \times \hat{l}_d, \end{aligned} \quad (3.78)$$

$$\begin{aligned} \frac{d\hat{l}_p}{dt} = & -\tilde{\omega}_{\text{pd}}(\hat{l}_p \cdot \hat{l}_d)\hat{l}_d \times \hat{l}_p - \omega_{\text{ps}}(\hat{l}_p \cdot \hat{s})\hat{s} \times \hat{l}_p \\ & - \omega_{\text{pb}}(\hat{l}_p \cdot \hat{l}_b)\hat{l}_b \times \hat{l}_p, \end{aligned} \quad (3.79)$$

where $\tilde{\omega}_{\text{pd}}$ and $\tilde{\omega}_{\text{dp}}$ are given by Eqs. (3.45) and (3.46).

Before t_w , the disk/planet is strongly coupled to the star ($\tilde{\omega}'_{\text{sd}} \gg \tilde{\omega}'_{\text{db}}$). Immediately following t_w , the inner disk's rapid depletion causes $\tilde{\omega}_{\text{sd}}$ to fall well below ω_{sp} . The main coupling allowing \hat{s} to track \hat{l}_p and \hat{l}_d is ω_{sp} , while the main external forcing trying to disrupt the mutual planet-star-disk coupling is $\tilde{\omega}_{\text{db}}$. Since $\tilde{\omega}_{\text{pd}}$ is typically much larger than the other frequencies during this time, \hat{l}_p and \hat{l}_d are coupled. Whether \hat{s} is allowed to become significantly misaligned with \hat{l}_p and \hat{l}_d after t_w depends on the magnitude of ω_{sp} compared to $\tilde{\omega}_{\text{db}}$:

1. If $\omega_{\text{sp}} \gtrsim \tilde{\omega}_{\text{db}}$, the planet star-disk coupling is stronger than the disk-binary coupling working to misalign the planet-star-disk system. The stellar spin \hat{s} stays aligned with \hat{l}_p and \hat{l}_d , and stellar obliquity is not excited at $t \approx t_w$.
2. If $\omega_{\text{sp}} \lesssim \tilde{\omega}_{\text{db}}$, the planet star-disk coupling is weaker than the disk-binary coupling. The stellar spin \hat{s} decouples from \hat{l}_p and \hat{l}_d , and stellar obliquities are excited at $t \approx t_w$.

Soon after t_w , $\tilde{\omega}_{\text{pd}} \approx \tilde{\omega}_{\text{pd},>}$ falls well below ω_{ps} , and \hat{l}_p decouples from \hat{l}_d but remains strongly coupled to \hat{s} . The stellar obliquities excited in planet-star-disk-binary systems over the disk's lifetime depends on the magnitude of ω_{sp} compared to $\tilde{\omega}_{\text{db}}$.

Figure 3.10 displays the evolution of the star-disk-planet-binary system for $a_p = 4 r_{\text{in}} = 0.147$ au, which implies $\omega_{\text{sp}} \gtrsim \tilde{\omega}_{\text{db}}$. We assume $\Sigma(r, t)$ evolves under prescription (3.20) with $t_{v,\text{in}} = 0.01$ Myr and $t_w = 5$ Myr. The left panels of Fig. 3.10 show the evolution of various angles and frequencies over the disk's lifetime, while the right panels zoom in around $t \approx t_w$. The top right panel shows \hat{s} and \hat{l}_d decouple first, since $\theta_{\text{sd}} > \theta_{\text{pd}}, \theta_{\text{sp}}$ after t_w . The bottom panel of Fig. 3.10 shows that because $\tilde{\omega}_{\text{pd}} \gtrsim \omega_{\text{ps}}$ directly after t_w , \hat{l}_p remains strongly coupled to \hat{l}_d ,

while $\tilde{\omega}_{\text{sd}}$ has fallen well below ω_{sp} and $\tilde{\omega}_{\text{db}}$ in magnitude. Because $\omega_{\text{sp}} \gtrsim \tilde{\omega}_{\text{db}}$, \hat{s} decouples from \hat{l}_d and begins to adiabatically follow \hat{l}_p . The adiabatic trailing of \hat{s} around \hat{l}_p directly following t_w suppresses any θ_{sp} excitation (top right panel of Fig. 3.10). The top left panel shows by the end of the disk's lifetime, θ_{sp} is not excited, the expected outcome since $\omega_{\text{sp}} \gtrsim \tilde{\omega}_{\text{db}}$ (bottom left panel of Fig. 3.10). The star-planet system ends up decoupled from the disk, which continues to precess around the binary's orbital angular momentum vector \hat{l}_b .

Figure 3.11 is identical to Fig. 3.10, except $a_p = 8 r_{\text{in}} = 0.294$ au so the system falls into the $\omega_{\text{sp}} \lesssim \tilde{\omega}_{\text{db}}$ regime. The bottom right panel of Fig. 3.11 shows for a brief amount of time following t_w , \hat{l}_p is still strongly coupled to \hat{l}_d but not to \hat{s} ($\tilde{\omega}_{\text{pd}} \gtrsim \omega_{\text{ps}}$), while \hat{s} quickly decouples from \hat{l}_d and couples to \hat{l}_p ($\omega_{\text{sp}} \gtrsim \tilde{\omega}_{\text{sd}}$). Because $\omega_{\text{sp}} \lesssim \tilde{\omega}_{\text{db}}$, \hat{s} cannot adiabatically track \hat{l}_p due to its rapid precession around \hat{l}_b through the strong coupling of \hat{l}_p to \hat{l}_d , explaining why $\theta_{\text{sd}} > \theta_{\text{pd}}, \theta_{\text{sp}}$ when $t > t_w$ (top right panel of Fig. 3.11). Some time after t_w , θ_{sp} is excited to large values (top left panel of Fig. 3.11). After $t \gtrsim t_w + \text{few} \times t_v$, $\tilde{\omega}_{\text{pd}}$ falls well below ω_{ps} (bottom left panel of Fig. 3.11), causing \hat{l}_p to couple strongly with \hat{s} , explaining why $\theta_{\text{sp}} \sim \text{constant}$ soon after its excitation at $t \approx t_w$.

These two examples show that although the planet-star-disk-binary system's dynamics following t_w is complex, the key criterion for exciting stellar obliquities is $\omega_{\text{sp}} \lesssim \tilde{\omega}_{\text{db}}$ at $t \approx t_w$. This is similar to the criterion discussed in Section 3.5.1 [see Eqs. (3.70)-(3.71)].

3.6 Discussion

3.6.1 Observational Implications

Due to the prevalence of circumstellar disks in binary systems misaligned with the binary’s orbital plane (e.g. Stapelfeldt et al. 1998, Jensen & Akeson 2014), star-disk-binary interactions have been suggested to generate primordial spin-orbit misalignments in exoplanetary systems [Batygin, 2012, Batygin & Adams, 2013, Lai, 2014, Spalding & Batygin, 2014]. For a wide range of disk/binary parameters, the star-disk-binary system naturally passes through a secular resonance during the disk’s evolution, in which the precession rate of the stellar spin driven by the disk ($\tilde{\omega}_{\text{sd}}$) matches the precession rate of the disk driven by the binary companion ($\tilde{\omega}_{\text{db}}$). When the system passes through this secular resonance, a significant misalignment between the stellar spin and disk axis is generated, even for systems with low disk-binary inclinations (see Fig. 3.1). Because this mechanism is so robust, the effects of accretion and magnetic interactions have been invoked to damp the spin-disk misalignment [Lai, 2014, Spalding & Batygin, 2015], and to explain the observed correlation between stellar effective temperatures and obliquities [Winn et al., 2010, Albrecht et al., 2012, Mazeh et al., 2015, Li & Winn, 2016, Winn et al., 2017].

We have shown that when a giant planet forms or migrates to a semi-major axis a_p where the precession rate of the spinning star around the planet exceeds the precession rate of the disk around the binary companion [$\omega_{\text{sp}} \gtrsim \tilde{\omega}_{\text{db}}$, see Eqs. (3.49) and (3.10)], stellar obliquity excitation may be reduced or completely suppressed. The excitation is reduced when the planet-star-disk-binary system undergoes secular resonance before the planet migrates near the inner edge of

the protoplanetary disk (Fig. 3.9). The obliquity excitation is completely suppressed when the planet forms or migrates to a semi-major axis too close to its host star before the system has a chance to experience secular resonance (Figs. 3.5 and 3.8). The obliquity excitation may be maintained if the planet accretes a significant amount of mass non-locally over sufficiently short timescales (Fig. 3.6). We find in order for star-disk-binary interactions to generate significant misalignment between a planet and its host star ($\theta_{\text{sp}} \gtrsim 30^\circ$), the planet must lie on an orbit where the disk-binary precession frequency exceeds the star-planet precession frequency ($\tilde{\omega}_{\text{db}} \gtrsim \omega_{\text{sp}}$), or the system's second secular resonance (when $\omega_{\text{sp}} \sim \tilde{\omega}_{\text{db}}$) must be crossed quickly. Rapidly clearing the protoplanetary disk's inner region via photoionization does not modify this criterion (Sec. 3.5.4). Assuming the gas-giant's growth is sufficiently slow, a lower bound may be placed on the semi-major axis a_p of a planet [see Eqs. (3.70)-(3.71)] which may have primordial spin-orbit misalignment generated via star-disk-binary interactions (assuming $p = 1$):

$$a_p \gtrsim 0.24 \left(\frac{2k_q}{k_\star} \right)^{1/3} \left(\frac{M_p}{1 M_J} \right)^{1/3} \left(\frac{\bar{\Omega}_\star}{0.1} \right)^{1/3} \frac{\bar{R}_\star^{1/2} \bar{a}_b}{\bar{M}_b^{1/3} \bar{r}_{\text{out}}^{1/2}} \text{ au.} \quad (3.80)$$

Eq. (3.80) depends very weakly on the surface density power-law index p [Eq. (3.70)].

Misalignments of Hot Jupiter Systems

Equation (3.80) [see also Eqs. (3.70)-(3.71)] shows that while “cold” Jupiters (planets with mass $M_p \sim 1 M_J$ and semi-major axis $a_p \gtrsim 1 \text{ au}$) and close-in earth-mass planets can experience primordial misalignment excitations from binary companions, hot Jupiters (HJ) may have this primordial misalignment reduced or completely suppressed. Most systems with significant stellar obliqu-

uities detected via the Rossiter-McLaughlin effect are HJs with semi-major axis $a_p \lesssim 0.1$ au [Winn & Fabrycky, 2015, Triaud, 2017]. Thus our work shows that HJs with star-planet inclinations $\theta_{sp} \gtrsim 30^\circ$ are unlikely to have developed these misalignments through planet-star-disk-binary interactions.

Other ways to primordially misalign the stellar spin axis with the planet's orbital angular momentum include molecular cloud turbulence during the formation of circumstellar disks [Bate et al., 2000, 2010, Fielding et al., 2015] and magnetic star-disk interactions [Lai et al., 2011, Foucart & Lai, 2011]. For molecular cloud turbulence to generate spin-orbit misalignment primordially, the infalling cloud material must cause the disk's orbital angular momentum vector to vary on timescales less than the precession period of the stellar spin around the disk [Spalding, Batygin & Adams, 2014]. Our work shows that the location and time of massive planet formation is also relevant for how efficiently molecular cloud turbulence may generate primordial spin-orbit misalignments.

Kepler Multi-planet Systems

Observational evidence suggesting multi-planet systems discovered by *Kepler* have low stellar obliquities is beginning to mount [Albrecht et al., 2013, Winn et al., 2017]. Equation (3.80) shows that such systems may experience primordial obliquity excitation by inclined binary companions, depending on the mass of the planet and the semi-major axis of the companion. If HJs form in multi-planetary systems, but are subsequently disrupted or engulfed by the host star (e.g. by stellar tides), the hot Jupiter's presence before the protoplanetary disk dissipates may "protect" multi-planet systems from primordial spin-orbit misalignment excitation in the presence of an inclined binary companion. The oc-

currence rate of HJs is $\lesssim 1\%$ (e.g. Marcy et al. 2005, Gould et al. 2006, Cumming et al. 2008, Howard et al. 2010, 2012, Bayliss & Sackett 2011, Wright et al. 2012), the occurrence rates of Jovian-mass planets orbiting interior to \sim few au is $\sim 5 - 10\%$ (e.g. Cumming et al. 2008, Clanton & Gaudi 2016), and potentially as high as $\sim 50\%$ for long-period (semi-major axis \sim few – 100 au) giant planets (e.g. Clanton & Gaudi 2016, Foreman-Mackey et al. 2016, Vigan et al. 2017). If the population of “destroyed” HJs is comparable to the fraction of long-period massive planets, a significant fraction of low-obliquity ($\theta_{\text{sp}} \approx 0^\circ$) exoplanetary systems may be explained through this mechanism. The multi-planet system WASP-47, containing a HJ with two low-mass planet “neighbors” [Becker et al., 2015] and a stellar obliquity $\theta_{\text{sp}} = 0 \pm 24^\circ$ consistent with 0 [Sanchis-Ojeda et al., 2015], may be an example of a multi-planet system with a HJ “protector” which has survived to the present day.

3.6.2 Theoretical Uncertainties

In Section 3.3, we considered a simple model for non-homologous surface density evolution, parameterizing the UV-switch model of photoevaporation [Clarke et al., 2001]. Our model assumes the critical radius r_c (where the disk’s photo-ionization rate is comparable to the disk’s viscous depletion rate) is fixed in time. In reality, photoevaporation forces r_c to expand in time shortly ($\lesssim 10^5$ years) after the inner disk is viscously depleted onto the central star, and expands outward over a timescale of $\sim 10^5$ years [Alexander, Clarke & Pringle, 2006, Owen et al., 2010]. There is not a simple way to relate this timescale to t_w (when the inner disk begins to clear) and $t_{v,\text{in}}$ (the timescale over which the inner disk is depleted). In addition, the expansion of r_c may accelerate due to

a dynamical instability termed “thermal sweeping” [Owen, Clarke & Ercolano, 2012, Haworth, Clarke & Owen, 2016]. Including the expansion of r_c will work to reduce the magnitudes of the precession rate of the stellar spin around the outer disk [$\tilde{\omega}_{sd}$, Eq. (3.25)] and the precession rate of the planet about the outer disk [$\tilde{\omega}_{pd}$, Eq. (3.42)], which already become insignificant shortly after the inner disk is viscously drained ($t \gtrsim t_w + \text{few} \times t_v$, see Figs. 3.10-3.11). Since the excitation of stellar obliquities with a planet inside the disk’s inner cavity depends mainly on the planet-star-disk-binary properties when the inner disk is drained ($t \approx t_w$), inclusion of an expanding r_c will not change the main results of this paper.

Other models exist which cause the disk surface density to evolve non-homologously. For instance, Russo & Thompson [2015a,b] considered the evolution of protoplanetary disks through magnetorotational instability [Balbus & Hawley, 1991] driven turbulence, seeded by magnetized stellar winds. Because the magnetic field from the star is larger near the inner truncation radius, the inner region of the disk is more turbulent than the outer region. This model for turbulence in disks around T-Tauri stars results in the inner ($r \lesssim \text{few au}$) disk accreting in less than a few Myr. Investigating the effect of such non-homologous disk evolution models is outside the scope of this paper.

In this work, we have assumed that the disk is flat (i.e. \hat{l}_d is independent of radius). Disk warping may change the mutual inclinations of planets formed in star-disk-binary systems, and align the stellar spin, disk, and binary orbital angular momentum axis over viscous timescales. These issues are addressed in a companion work [Zanazzi & Lai, 2017b]. Disk warping may also affect the planet-disk interaction of massive planets, explored in Lubow & Ogilvie [2001].

3.7 Conclusions

In this work, we have studied how the formation of a massive planet orbiting close to its host star affects the generation of primordial misalignment between the stellar spin and the orbital angular momentum axes of the planet and disk in the presence of an inclined external binary companion. We find that when a protoplanetary disk's inner cavity is rapidly cleared by photoevaporation before secular resonance occurs, the star-disk misalignment is reduced (Sec. 3.3, Fig. 3.3). More importantly, when a giant planet (hot Jupiter) forms or migrates early to the near vicinity of the host star, it becomes strongly coupled to the star, preventing any significant excitation of spin-orbit misalignment. Specifically, we find (Sec. 3.5):

1. If a hot Jupiter forms early in-situ, spin-orbit misalignment is *completely suppressed* since the star-planet precession frequency ω_{sp} [Eq. (3.49)] always exceeds the disk-binary precession frequency $\tilde{\omega}_{\text{db}}$ [Eq. (3.10)].
2. If a hot Jupiter forms late in-situ and accretes most of its mass from viscously advected disk gas, spin-orbit misalignment is *significantly reduced* when the planet's mass grows over a timescale sufficiently longer than the disk-binary precession period (Fig. 3.6). Spin-orbit misalignment can be maintained if the planet's mass growth timescale [Eq. (3.73)] is shorter than the disk-binary precession period (Fig. 3.6).
3. If a giant planet forms in the outer region of the protoplanetary disk, and migrates in via Type-II migration, the excitation of spin-orbit misalignments depends on the migration history of the planet relative to the time of the secular resonance. If the planet migrates to a semi-major axis a_p such

that the star-planet precession frequency exceeds the disk-binary precession frequency ($\omega_{\text{sp}} \gtrsim \tilde{\omega}_{\text{db}}$) *before* secular resonance, spin-orbit misalignment is *completely suppressed* (Fig. 3.8, top left panel). If the planet migration occurs after secular resonance, the stellar obliquity is significantly reduced when the planet migrates to a close-in orbit which satisfies $\omega_{\text{sp}} \gtrsim \tilde{\omega}_{\text{db}}$ (Fig. 3.9).

4. If the giant planet is left in the photoevaporated inner disk cavity before secular resonance occurs in the star-disk-binary system, spin-orbit misalignment is *completely suppressed*, unless the star-planet precession frequency is less than the disk-binary precession frequency ($\omega_{\text{sp}} \lesssim \tilde{\omega}_{\text{db}}$) when the inner disk is cleared (Figs. 3.10-3.11).

Overall, our work shows that regardless of the complication of disk evolution, significant stellar obliquities can be generated only when the planet forms at an orbital separation where the star-planet precession frequency exceeds the disk-binary precession frequency ($\omega_{\text{sp}} \gtrsim \tilde{\omega}_{\text{db}}$), or the planet forms quickly after the system undergoes secular resonance. This places a lower bound on a slowly forming planet’s semi-major axis such that primordial spin-orbit misalignment can be generated via star-disk-binary interactions [Eqs. (3.70),(3.71) or (3.80)]. Hot Jupiters do not satisfy this bound, and thus may not acquire significant spin-orbit misalignment through this mechanism, depending on how the planet accreted its mass (Sec. 3.6.1). On the other hand, “cold Jupiters” and close-in earth-mass planets may experience excitation of spin-orbit misalignments under appropriate conditions. If hot Jupiters form in multi-planet systems, they may protect the system from suffering primordial spin-orbit misalignments in the presence of an inclined binary companion (Sec. 3.6.1).

Acknowledgements

JZ thanks Doug Lin, Christopher Spalding, Konstantin Batygin, and Eve Lee for helpful discussions. This work has been supported in part by NASA grants NNX14AG94G and NNX14AP31G, and NSF grant AST- 1715246. JZ is supported by a NASA Earth and Space Sciences Fellowship in Astrophysics.

CHAPTER 4

LIDOV-KOZAI MECHANISM IN HYDRODYNAMICAL DISKS: LINEAR STABILITY ANALYSIS

4.1 Introduction

When a test particle orbiting a central mass has a distant binary companion, it can undergo eccentricity and inclination oscillations if the initial inclination I between the orbital planes of the test mass and the binary is sufficiently large. This is termed Lidov-Kozai (LK) oscillation, and was originally invoked to explain the dynamics of artificial satellites [Lidov, 1962] and asteroids [Kozai, 1962]. Since then, the LK effect has found a plethora of applications in astrophysics (e.g. Tremaine & Yavetz 2014, Naoz 2016), such as the formation of the Jovian irregular satellites [Carruba et al., 2002, Nesvorný et al., 2003], mergers of massive black hole binaries [Blaes et al., 2002], formation of short-period stellar binaries [Eggleton & Kiseleva-Eggleton, 2001] and hot Jupiters [Wu & Murray, 2003, Fabrycky & Tremaine, 2007, Petrovich, 2015, Anderson et al., 2016], and Type Ia supernovae from white dwarf binary mergers [Katz & Dong, 2012].

The simplest LK oscillation involves only the quadrupole potential from the companion. It has been recognized that the high-order perturbation (e.g., Ford et al. 2000, Naoz et al. 2011, Katz et al. 2011) and short-range forces (e.g., Holman et al. 1997, Wu & Murray 2003, Liu, Muñoz, & Lai 2015) can significantly influence the LK oscillation dynamics. Thus, one may expect that any eccentricity/inclination oscillations of a gaseous disk inside a stellar binary, if occur at all, may be modified or suppressed by hydrodynamic forces.

Recently Martin et al. [2014] used SPH simulations to show that LK oscillations may be excited in circumstellar disks with distant, inclined binary companions (see also Fu et al. 2015a). Fu et al. [2015b] showed that these disk oscillations can be suppressed by the disk self-gravity when the disk mass is sufficiently large (Batygin et al. 2011; see discussion in Sec. 4). If real, this may have interesting astrophysical implications due to the ubiquity of misaligned circumstellar accretion disks in binary systems.

In this paper we use linear theory of eccentric disks[Goodchild & Ogilvie, 2006, Ogilvie, 2008, Teyssandier & Ogilvie, 2016] to study the possibility of coherent LK oscillations of circumstellar disks in binaries. Section 4.2 gives the set-up and formalism of this work. Section 4.3 contains our results. Section 4.4 presents the summary and discussion of our work.

4.2 Setup and Formalism

Consider a circumstellar disk around a host star of mass M . The disk has an inner radius $r = r_{\text{in}}$, outer radius $r = r_{\text{out}}$, and surface density $\Sigma = \Sigma(r)$. The disk warp and eccentricity are specified by the unit angular momentum vector $\hat{\mathbf{l}} = \hat{\mathbf{l}}(r, t)$ and eccentricity vector $\mathbf{e} = \mathbf{e}(r, t)$. We take the disk to be nearly circular, so $e \ll 1$ everywhere. We adopt a locally isothermal equation of state, so that the height-integrated pressure at any location in the disk is given by $P = c_s^2 \Sigma$, where $c_s = c_s(r)$ is the sound speed. For a thin disk with mass much less than M , the orbital frequency of the disk is given by $n(r) \simeq \sqrt{GM/r^3}$. The host star has a distant external binary companion with semimajor axis $a_b \gtrsim 3r_{\text{out}}^1$, mass M_b ,

¹The upper bound on the outer disk radius is set by tidal truncation [Artymowicz & Lubow, 1994, Miranda & Lai, 2015]

and orbital angular momentum unit vector $\hat{\mathbf{l}}_b$. We take the binary's orbit to be circular. Because the angular momentum of the binary is much larger than that of the circumstellar disk, we take $\hat{\mathbf{l}}_b$ to be fixed in time.

The gravitational force of the binary companion drives the eccentricity and angular momentum unit vectors of disk annuli according to [Tremaine et al., 2009, Tremaine & Yavetz, 2014]

$$\left(\frac{\partial \hat{\mathbf{l}}}{\partial t}\right)_{\text{bin}} = \omega_b(\hat{\mathbf{l}} \cdot \hat{\mathbf{l}}_b)\hat{\mathbf{l}} \times \hat{\mathbf{l}}_b + O(e^2) \quad (4.1)$$

$$\left(\frac{\partial \mathbf{e}}{\partial t}\right)_{\text{bin}} = \omega_b[(\hat{\mathbf{l}} \cdot \hat{\mathbf{l}}_b)\mathbf{e} \times \hat{\mathbf{l}}_b - 5(\mathbf{e} \cdot \hat{\mathbf{l}}_b)\hat{\mathbf{l}} \times \hat{\mathbf{l}}_b + 2\hat{\mathbf{l}} \times \mathbf{e}] + O(e^3), \quad (4.2)$$

where

$$\omega_b(r) = \frac{3GM_b}{4a_b^3n} \quad (4.3)$$

characterizes the precession frequency of a disk annulus around the external binary. Equations (4.1) and (4.2) include the effect of the quadrupole potential from the binary and are averaged over the binary period.

Internal hydrodynamical forces work to resist the differential nodal precession of the disk annuli, either in the form of bending waves [Papaloizou & Lin, 1995, Lubow & Ogilvie, 2000] or viscosity [Papaloizou & Pringle, 1983, Ogilvie, 1999], and enforce both coplanarity ($|\partial \hat{\mathbf{l}} / \partial \ln r| \ll 1$) and rigid body precession [Larwood et al., 1996, Xiang-Gruess & Papaloizou, 2014]. Under their influence, the time evolution of the disk's unit angular momentum vector is given by

$$\left(\frac{\partial \hat{\mathbf{l}}}{\partial t}\right)_{\text{int}} + \left(\frac{\partial \hat{\mathbf{l}}}{\partial t}\right)_{\text{bin}} = \tilde{\omega}_{\text{db}}(\hat{\mathbf{l}} \cdot \hat{\mathbf{l}}_b)\hat{\mathbf{l}} \times \hat{\mathbf{l}}_b + O(e^2) \quad (4.4)$$

$$\Rightarrow \left(\frac{\partial \hat{\mathbf{l}}}{\partial t}\right)_{\text{int}} = (\tilde{\omega}_b - \omega_b)(\hat{\mathbf{l}} \cdot \hat{\mathbf{l}}_b)\hat{\mathbf{l}} \times \hat{\mathbf{l}}_b + O(e^2), \quad (4.5)$$

where $\hat{\mathbf{l}}$ is (nearly) independent of r , and

$$\tilde{\omega}_b = \frac{\int_{r_{\text{in}}}^{r_{\text{out}}} \Sigma r^3 n \omega_b dr}{\int_{r_{\text{in}}}^{r_{\text{out}}} \Sigma r^3 n dr} \quad (4.6)$$

characterizes the precession frequency of the rigid disk around the binary. The internal force that enforces rigid disk nodal precession must also act on \mathbf{e} , so that \mathbf{e} remains perpendicular to $\hat{\mathbf{l}}$, i.e.,

$$\left[\frac{\partial(\mathbf{e} \cdot \hat{\mathbf{l}})}{\partial t} \right]_{\text{int}} = 0. \quad (4.7)$$

This requirement, together with the assumption that the internal force responsible for Eq. (4.5) is perpendicular to the disk, imply that the time evolution of the disk's eccentricity vector is

$$\left(\frac{\partial \mathbf{e}}{\partial t} \right)_{\text{int}} = (\tilde{\omega}_b - \omega_b)(\hat{\mathbf{l}} \cdot \hat{\mathbf{l}}_b)[\hat{\mathbf{l}} \cdot (\mathbf{e} \times \hat{\mathbf{l}}_b)]\hat{\mathbf{l}} + O(e^3). \quad (4.8)$$

We justify Eq. (4.8) in the appendix.

Before we proceed, we comment on the validity of the assumption of coplanarity and rigid-body precession. When the dimensionless Shakura-Sunyaev viscosity parameter α satisfies $\alpha \lesssim H/r$ (H is the disk scaleheight), bending waves keep the disk coherent [Papaloizou & Lin, 1995, Lubow & Ogilvie, 2000]. The amount of disk warp in this bending wave regime has been calculated in Foucart & Lai [2014], and assuming $p = 1$ and $q = 1/2$ [see Eqs. (4.19)-(4.20) in next section], is

$$\begin{aligned} \hat{\mathbf{l}}(r_{\text{out}}, t) - \hat{\mathbf{l}}(r_{\text{in}}, t) \approx \\ 0.01 \left(\frac{\alpha}{0.01} \right) \left(\frac{H(r_{\text{out}})}{0.1 r_{\text{out}}} \right)^{-2} \left(\frac{M_b}{M} \right) \left(\frac{3r_{\text{out}}}{a_b} \right)^3 \frac{\hat{\mathbf{l}}_b \times \hat{\mathbf{l}}(r_{\text{out}}, t)}{\sin I} \\ - 0.01 \left(\frac{H(r_{\text{out}})}{0.1 r_{\text{out}}} \right)^{-2} \left(\frac{M_b}{M} \right)^2 \left(\frac{3r_{\text{out}}}{a_b} \right)^6 \frac{[\hat{\mathbf{l}}_b \times \hat{\mathbf{l}}(r_{\text{out}}, t)] \times \hat{\mathbf{l}}_b}{\sin I}. \end{aligned} \quad (4.9)$$

Numerical simulations give a similar result (e.g. Larwood et al. 1996, Xiang-Gruess & Papaloizou 2014, Picogna & Marzari 2015). On the other hand, when $\alpha \gtrsim H/r$, viscous torques keep the disk coherent [Papaloizou & Pringle, 1983, Ogilvie, 1999], and the disk diffusively damps to its steady-state equilibrium

warp profile over the timescale $t_{\text{visc}} \sim 2\alpha r^2/(H^2 n)$ [Lodato & Pringle, 2007, Lodato & Price, 2010, Foucart & Lai, 2011]. Large warping and sometimes disk breaking is observed when the disk's viscous torque is comparable to or less than the torque exerted on the disk by the distant binary (e.g. Larwood et al. 1996, Doğan et al. 2015). Thus, the following derivation of the LK disk instability will be restricted to the $\alpha \lesssim H/r$ regime, which is applicable to protoplanetary disks.

For a flat disk, the effect of pressure on the time evolution of the disk's eccentricity is described by [Teyssandier & Ogilvie, 2016]

$$\begin{aligned} \left(\frac{\partial \mathbf{e}}{\partial t} \right)_{\text{press}} &= \hat{\mathbf{l}} \times \left[\frac{1}{\Sigma r^3 n} \frac{\partial}{\partial r} \left(\frac{\Sigma c_s^2 r^3}{2} \frac{\partial \mathbf{e}}{\partial r} \right) \right] \\ &+ \frac{1}{2\Sigma r n} \frac{d(\Sigma c_s^2)}{dr} \hat{\mathbf{l}} \times \mathbf{e} - \hat{\mathbf{l}} \times \left[\frac{1}{2\Sigma r^3 n} \frac{\partial}{\partial r} \left(\Sigma \frac{dc_s^2}{dr} r^3 \mathbf{e} \right) \right] \\ &+ \frac{3}{2r^3 n} \frac{d(c_s^2 r^2)}{dr} \hat{\mathbf{l}} \times \mathbf{e} + O(e^2). \end{aligned} \quad (4.10)$$

The last term in Eq. (4.10) arises from the disk's "breathing mode," where the fluid displacements are proportional to z^2 , where z is the vertical coordinate of the disk [Ogilvie, 2008]. Earlier theories of eccentric disks do not include this term [Goodchild & Ogilvie, 2006].

Following Teyssandier & Ogilvie [2016], we also include the effect of bulk viscosity on the disk eccentricity evolution:

$$\left(\frac{\partial \mathbf{e}}{\partial t} \right)_{\text{visc}} = \frac{1}{2\Sigma r^3 n} \frac{\partial}{\partial r} \left(\alpha_b \Sigma c_s^2 r^3 \frac{\partial \mathbf{e}}{\partial r} \right) + O(e^2), \quad (4.11)$$

small kinematic viscosity leads to over-stability, and a small bulk viscosity is needed to stabilize the eccentric disturbance [Ogilvie, 2001, Latter & Ogilvie, 2006].

From Equation (5.22), we see that the disk's unit angular momentum vector

$\hat{l}(t)$ precesses uniformly around \hat{l}_b with frequency $\omega_{\text{prec}} = -\tilde{\omega}_b \cos I$, where I is the inclination angle ($\cos I = \hat{l} \cdot \hat{l}_b$). Indeed, in the linear theory of LK oscillation of a test mass, the inclination stays constant while the eccentricity grows in time [Tremaine & Yavetz, 2014]. To determine the stability of $e(r, t)$, it is necessary to consider the evolution equation of e in the frame co-rotating with $\hat{l}(t)$ [Tremaine & Yavetz, 2014]. Including the gravitational perturbations and hydrodynamical effects, the time evolution of the disk's eccentricity vector e is given by

$$\begin{aligned} \left(\frac{\partial e}{\partial t} \right)_{\text{rot}} = & \left(\frac{\partial e}{\partial t} \right)_{\text{bin}} + \left(\frac{\partial e}{\partial t} \right)_{\text{int}} + \left(\frac{\partial e}{\partial t} \right)_{\text{press}} \\ & + \left(\frac{\partial e}{\partial t} \right)_{\text{visc}} + (\tilde{\omega}_b \cos I) \hat{l}_b \times e. \end{aligned} \quad (4.12)$$

We will work in this frame for the rest of the paper, and drop the subscript “rot.”

Define the complex eccentricity $E(r, t) \equiv e(r, t) \cdot (\hat{x} + i\hat{y})$, where $\hat{y} = \hat{l} \times \hat{l}_b / \sin I$ and $\hat{x} = \hat{y} \times \hat{l}$ are unit vectors, constant in the rotating frame. Then Equation (4.12) becomes

$$\begin{aligned} \frac{\partial E}{\partial t} = & i\omega_b \left[2E - \frac{5 \sin^2 I}{2} (E + E^*) \right] \\ & + i(\tilde{\omega}_b - \omega_b) \cos^2 I E + \frac{i}{\Sigma r^3 n} \frac{\partial}{\partial r} \left(\frac{\Sigma c_s^2 r^3}{2} \frac{\partial E}{\partial r} \right) \\ & + \frac{i}{2\Sigma r n} \frac{d(\Sigma c_s^2)}{dr} E - \frac{i}{2\Sigma r^3 n} \frac{\partial}{\partial r} \left(\Sigma \frac{dc_s^2}{dr} r^3 E \right) \\ & + \frac{3i}{2r^3 n} \frac{d(c_s^2 r^2)}{dr} E + \frac{1}{2\Sigma r^3 n} \frac{\partial}{\partial r} \left(\alpha_b \Sigma c_s^2 r^3 \frac{\partial E}{\partial r} \right), \end{aligned} \quad (4.13)$$

where E^* denotes the complex conjugate to E . To find the eigenmodes of Eq. (4.13), we separate E into two “polarizations”:

$$E(r, t) = E_+(r) \exp(\lambda t) + E_-^*(r) \exp(\lambda^* t). \quad (4.14)$$

Here, E_+ and E_- are two complex functions, while λ is a complex eigenvalue. Substituting Eq. (4.14) into Eq. (4.13), we obtain the coupled eigenvalue equa-

tions

$$\begin{aligned} \lambda E_+ &= i\omega_b \left[2E_+ - \frac{5 \sin^2 I}{2} (E_+ + E_-) \right] \\ &\quad + i(\tilde{\omega}_b - \omega_b) \cos^2 I E_+ + \frac{i}{\Sigma r^3 n} \frac{d}{dr} \left(\frac{\Sigma c_s^2 r^3}{2} \frac{dE_+}{dr} \right) \\ &\quad + \frac{i}{2\Sigma rn} \frac{d(\Sigma c_s^2)}{dr} E_+ - \frac{i}{2\Sigma r^3 n} \frac{d}{dr} \left(\Sigma \frac{dc_s^2}{dr} r^3 E_+ \right) \\ &\quad + \frac{3i}{2r^3 n} \frac{d(c_s^2 r^2)}{dr} E_+ + \frac{1}{2\Sigma r^3 n} \frac{d}{dr} \left(\alpha_b \Sigma c_s^2 r^3 \frac{dE_+}{dr} \right), \end{aligned} \quad (4.15)$$

$$\begin{aligned} \lambda E_- &= -i\omega_b \left[2E_- - \frac{5 \sin^2 I}{2} (E_+ + E_-) \right] \\ &\quad - i(\tilde{\omega}_b - \omega_b) \cos^2 I E_- - \frac{i}{\Sigma r^3 n} \frac{d}{dr} \left(\frac{\Sigma c_s^2 r^3}{2} \frac{dE_-}{dr} \right) \\ &\quad - \frac{i}{2\Sigma rn} \frac{d(\Sigma c_s^2)}{dr} E_- + \frac{i}{2\Sigma r^3 n} \frac{d}{dr} \left(\Sigma \frac{dc_s^2}{dr} r^3 E_- \right) \\ &\quad - \frac{3i}{2r^3 n} \frac{d(c_s^2 r^2)}{dr} E_- + \frac{1}{2\Sigma r^3 n} \frac{d}{dr} \left(\alpha_b \Sigma c_s^2 r^3 \frac{dE_-}{dr} \right). \end{aligned} \quad (4.16)$$

When $\alpha_b = 0$, the eigenvalue λ is either real or imaginary. Imaginary eigenvalues imply the eccentricity vector e is precessing or librating around \hat{l} , while real eigenvalues imply an exponentially growing or damping eccentricity.

For a thin ring ($r_{\text{in}} \simeq r_{\text{out}}$) of pressure-less particles ($c_s = 0$), Eqs. (4.15)-(4.16) can be easily solved, giving

$$\lambda^2 = -2\omega_b^2(2 - 5 \sin^2 I). \quad (4.17)$$

This recovers the standard results: eccentricity grows when $I_{\text{LK}} < I < 180^\circ - I_{\text{LK}}$ [Tremaine & Yavetz, 2014], where

$$I_{\text{LK}} \equiv \sin^{-1} \sqrt{2/5} \simeq 39^\circ. \quad (4.18)$$

4.3 Results

To analyze the solutions of Eqs. (4.15) and (4.16), we assume the disk surface density and sound-speed profiles of

$$\Sigma(r) = \Sigma(r_{\text{out}}) \left(\frac{r_{\text{out}}}{r} \right)^p \quad (4.19)$$

and

$$c_s(r) = c_s(r_{\text{out}}) \left(\frac{r_{\text{out}}}{r} \right)^q. \quad (4.20)$$

A key dimensionless parameter in our analysis is the ratio

$$\begin{aligned} S &\equiv \frac{c_s^2(r_{\text{out}})}{r_{\text{out}}^2 n(r_{\text{out}}) \omega_b(r_{\text{out}})} \\ &\simeq 0.36 \left(\frac{a_b}{3 r_{\text{out}}} \right)^3 \left(\frac{M}{M_b} \right) \left(\frac{H(r_{\text{out}})}{0.1 r_{\text{out}}} \right)^2, \end{aligned} \quad (4.21)$$

where we have approximated $c_s \simeq Hn$ (where H is the disk scale-height), and ω_b is defined in Eq. (4.3). Physically, S^{-1} measures the strength of the tidal torque (per unit mass) acting on the outer disc from the external companion ($r^2 n \omega_b$) relative to the torque associated with gas pressure (c_s^2).

Define the dimensionless radial coordinate $x \equiv r/r_{\text{out}}$, inner radius parameter $x_{\text{in}} \equiv r_{\text{in}}/r_{\text{out}}$, and dimensionless eigenvalue

$$\bar{\lambda} \equiv \lambda/\omega_b(r_{\text{out}}). \quad (4.22)$$

We assume that $\alpha_b = \text{constant}$. In terms of these parameters, Equations (4.15) and (4.16) become

$$\begin{aligned} \bar{\lambda} E_+ &= ix^{3/2} \left[2E_+ - \frac{5 \sin^2 I}{2} (E_+ + E_-) \right] \\ &+ i \left[\frac{5/2 - p}{4 - p} \left(\frac{1 - x_{\text{in}}^{4-p}}{1 - x_{\text{in}}^{5/2-p}} \right) - x^{3/2} \right] \cos^2 IE_+ \end{aligned}$$

$$\begin{aligned}
& + i \frac{S x^{3/2-2q}}{2} \left[\frac{d^2}{dx^2} + \left(\frac{3-p}{x} \right) \frac{d}{dx} + \frac{A(p,q)}{x^2} \right] E_+ \\
& + \alpha_b \frac{S x^{3/2-2q}}{2} \left[\frac{d^2}{dx^2} + \left(\frac{3-p-2q}{x} \right) \frac{d}{dx} \right] E_+, \tag{4.23}
\end{aligned}$$

$$\begin{aligned}
\bar{\lambda} E_- = & -ix^{3/2} \left[2E_- - \frac{5 \sin^2 I}{2} (E_+ + E_-) \right] \\
& - i \left[\frac{5/2-p}{4-p} \left(\frac{1-x_{in}^{4-p}}{1-x_{in}^{5/2-p}} \right) - x^{3/2} \right] \cos^2 I E_- \\
& - i \frac{S x^{3/2-2q}}{2} \left[\frac{d^2}{dx^2} + \left(\frac{3-p}{x} \right) \frac{d}{dx} + \frac{A(p,q)}{x^2} \right] E_- \\
& + \alpha_b \frac{S x^{3/2-2q}}{2} \left[\frac{d^2}{dx^2} + \left(\frac{3-p-2q}{x} \right) \frac{d}{dx} \right] E_-, \tag{4.24}
\end{aligned}$$

where²

$$A(p,q) = 6 - 4q - p - 2pq - 4q^2. \tag{4.25}$$

We adopt a free boundary condition, where the eccentricity gradient vanishes on the disk's boundaries:

$$\frac{dE_\pm}{dr} \Big|_{r=r_{in}} = \frac{dE_\pm}{dr} \Big|_{r=r_{out}} = 0. \tag{4.26}$$

In the following subsections, we calculate the eigenvalues and eigenmodes to Eqs. (4.23) and (4.24). In Section 4.3.1, we investigate the limit $|r_{out} - r_{in}| \ll r_{out}$, where λ , $E_+(r)$, and $E_-(r)$ may be found analytically. In Section 4.3.2, we calculate numerically λ , $E_+(r)$, and $E_-(r)$ for an inviscid ($\alpha_b = 0$) extended ($|r_{out} - r_{in}| \sim r_{out}$) disk. In Section 4.3.3, we investigate the effect of a non-zero bulk viscosity α_b on the eigenvalues λ .

²If the breathing mode term is not included [last term in Eq. (4.10)], $A(p,q) = 2q - p - 2pq - 4q^2$. Equations (4.23)-(4.24) otherwise remain unchanged.

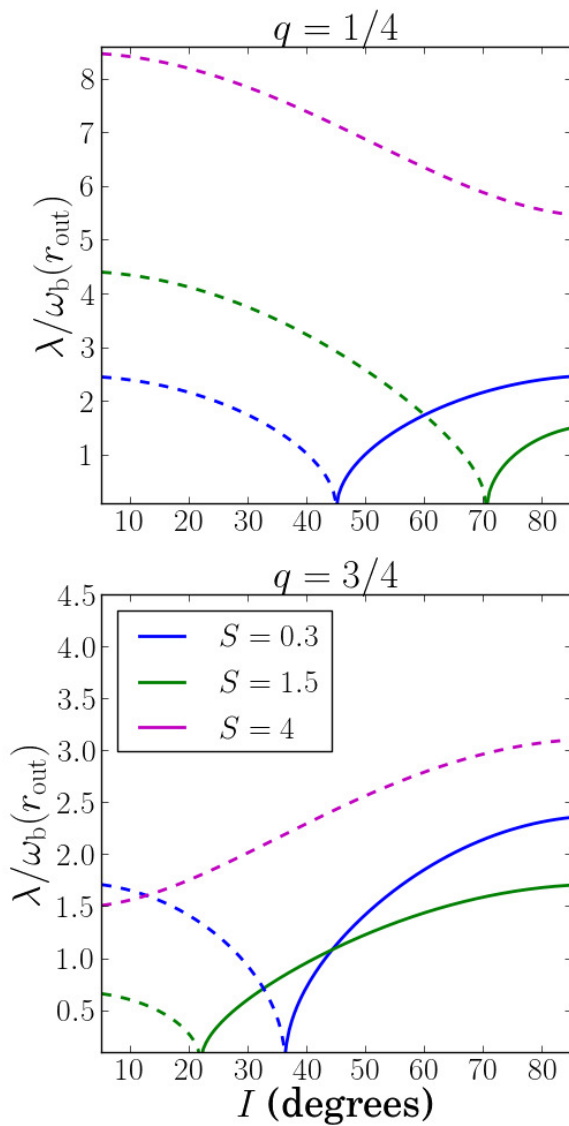


Figure 4.1: Real (solid) and imaginary (dotted) components of eigenvalue λ for a thin annulus [see Eqs. (4.29) and (4.14)] as functions of inclination $I = \cos^{-1}(\hat{l} \cdot \hat{l}_b)$, for values of S [Eq. (4.21)] and q [Eq. (4.20)] as indicated. We take $p = 1$ [Eq. (4.19)].

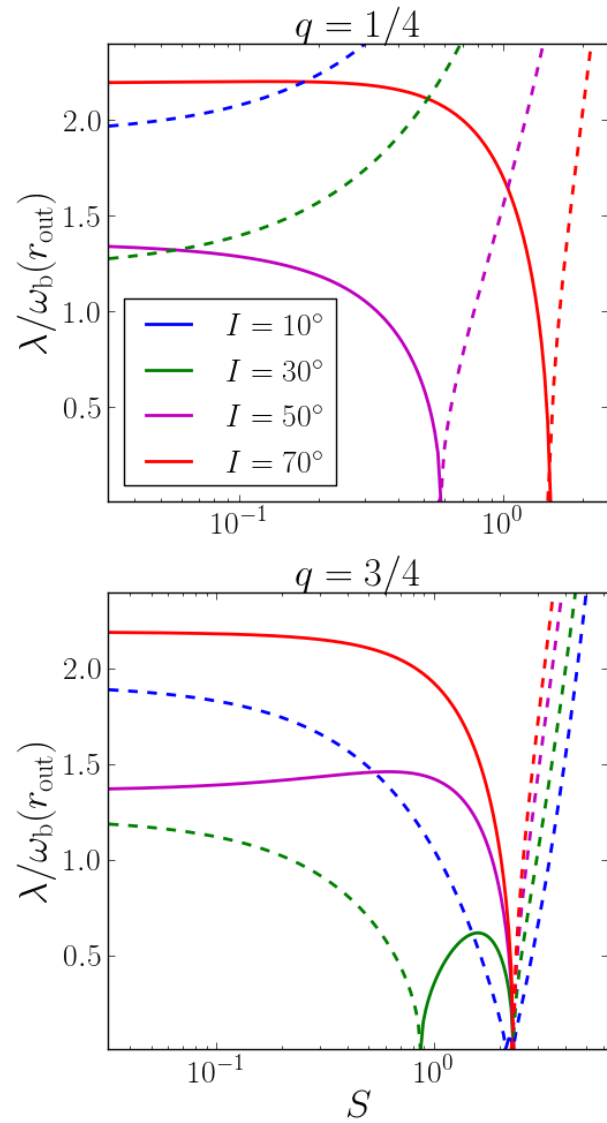


Figure 4.2: Real (solid) and imaginary (dotted) components of the eigenvalue λ [see Eqs. (4.29) and (4.14)] as functions of S [Eq. (4.21)], for values of inclination $I = \cos^{-1}(\hat{\mathbf{l}} \cdot \hat{\mathbf{l}}_b)$ and q [Eq. (4.20)] as indicated. We take $p = 1$ [Eq. (4.19)].

4.3.1 Analytic Result for Thin Annulus

When $r_{\text{out}} - r_{\text{in}} \ll r_{\text{out}}$, we may expand all quantities in Equations (4.15) and (4.16) in terms of the small parameter $(r_{\text{out}} - r)/r_{\text{out}} = 1 - x$. The boundary condition (4.26) and normalization condition $E_+(r_{\text{out}}) = 1$ imply

$$E_+(r) = 1 + O[(1 - x)^3] \quad (4.27)$$

and

$$E_-(r) = E_-(r_{\text{out}}) + O[(1 - x)^3]. \quad (4.28)$$

Using the form of solutions (4.27) and (4.28), we may solve for the eigenvalue $\bar{\lambda}$ [Eq. (4.22)] to lowest order in $(r_{\text{out}} - r_{\text{in}})/r_{\text{out}} = 1 - x_{\text{in}}$:

$$\bar{\lambda}^2 = -[2 + SA(p, q)/2][(2 - 5 \sin^2 I) + SA(p, q)/2]. \quad (4.29)$$

The polynomial $A(p, q)$ is defined in Eq. (4.25), and S in Eq. (4.21).

Plotted in Figure 4.1 are the real (solid) and imaginary (dashed) components of the eigenvalue λ given by Equation (4.29), as functions of inclination I with values of S as indicated. We always show the solutions with $\text{Re}(\lambda) > 0$ and $\text{Im}(\lambda) > 0$. When $S \ll 1$, we recover the classic LK result for a test particle, with $\lambda^2 > 0$ when I exceeds the critical inclination angle I_{LK} [Eq. (4.18)]. When $S \gg 1$, the Lidov-Kozai effect is suppressed by pressure gradients even when $I > I_{\text{LK}}$. In general, the critical inclination angle for eccentricity growth increases with increasing S . However, we see from Fig. 4.1 that for $S = 1.5$ and $q = 3/4$, the instability sets in when $I \gtrsim 22^\circ$.

Figure 4.2 further illustrates the difference in behavior between $q = 1/4$ (top panel) and $q = 3/4$ (bottom panel). For $q = 1/4$, the real growth rate for inclinations $I > I_{\text{LK}}$ [Eq. (4.18)] monotonically decreases with increasing S , until λ

becomes imaginary. But for $q = 3/4$, a “window of instability” opens for inclinations $I < I_{\text{LK}}$ when $S \sim 1$.

To understand the difference between these two models, consider the test particle limit ($c_s = 0$) and some additional pericenter precession ω_{ext} from a source other than the binary companion. In the frame co-rotating with the test particle’s orbit normal, the time evolution of the eccentricity vector is given by

$$\frac{d\mathbf{e}}{dt} = \omega_b [2\hat{\mathbf{l}} \times \mathbf{e} - 5(\mathbf{e} \cdot \hat{\mathbf{l}}_b) \hat{\mathbf{l}} \times \hat{\mathbf{l}}_b] + \omega_{\text{ext}} \hat{\mathbf{l}} \times \mathbf{e}. \quad (4.30)$$

Assuming $\mathbf{e} \propto \exp(\lambda t)$, we find the eigenvalue

$$\lambda^2 = -(2\omega_b + \omega_{\text{ext}})(2\omega_b + \omega_{\text{ext}} - 5\omega_b \sin^2 I). \quad (4.31)$$

When $\omega_{\text{ext}} \geq 0$, the extra pericenter precession works to suppress the LK instability, decreasing the range of I values for eccentricity growth ($\lambda^2 > 0$). When $\omega_{\text{ext}} \leq -2\omega_b$ or $\omega_{\text{ext}} \geq 3\omega_b$, no value of I is capable of exciting eccentricity growth. But when $-2\omega_b < \omega_{\text{ext}} < 0$, the extra precession works to cancel the pericenter precession induced on the test particle by the distant binary ($2\omega_b$), thus increases the range of I values for eccentricity growth.

Comparing Eq. (4.31) to Eq. (4.29) shows the pressure force in a disk annulus induces precession $\omega_{\text{ext}} = \omega_b S A(p, q)/2$. Since $A(1, 1/4) > 0$, the pressure force in the $p = 1$ and $q = 1/4$ disk tends to suppress eccentricity growth (Figs. 4.1-4.2, top). But because $A(1, 3/4) < 0$, the pressure force in the $p = 1$ and $q = 3/4$ disk can lead to eccentricity growth even when $I < I_{\text{LK}}$ (Figs. 4.1-4.2, bottom).

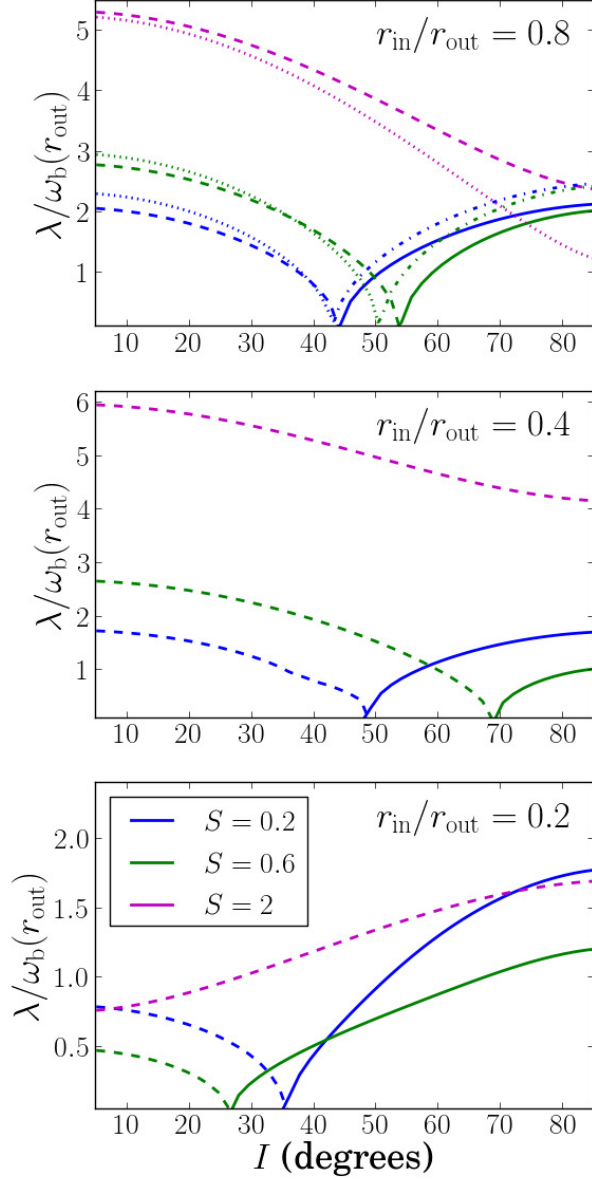


Figure 4.3: Real (solid lines) and imaginary (dashed lines) components of the eigenvalue λ for extended disks as a function of I . We take $\alpha_b = 0$, $p = 1$ [Eq. (4.19)], $q = 1/4$ [Eq. (4.20)], with values of S [Eq. (4.21)] and $r_{\text{in}}/r_{\text{out}}$ as indicated. In the top panel, we also plot the real (dot-dashed lines) and imaginary (dotted lines) components of the eigenvalue in the thin annulus limit [Eq. (4.29)].

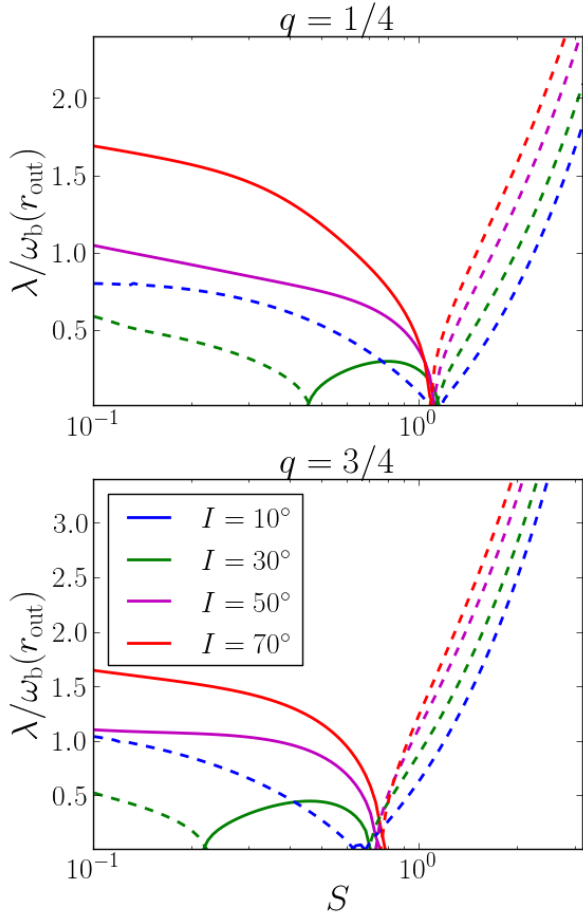


Figure 4.4: Real (solid lines) and imaginary (dashed lines) components of the eigenvalue for extended disks as a function of S . We take $\alpha_b = 0$, $p = 1$ [Eq. (4.19)], $r_{\text{in}}/r_{\text{out}} = 0.2$, and values of q [Eq. (4.20)] and inclination I as indicated.

4.3.2 Inviscid Extended Disk

We solve eigenvalue equations (4.23) and (4.24) using the shooting method [Press et al., 2002] for an inviscid ($\alpha_b = 0$) extended ($|r_{\text{out}} - r_{\text{in}}| \sim r_{\text{out}}$) disk. In Figure 4.3, we plot the real (solid) and imaginary (dashed) components of the eigenvalues $\lambda = \bar{\lambda}\omega_b$ as functions of inclination I . For $r_{\text{in}}/r_{\text{out}}$ close to unity, our numerical result agrees with the analytic expression for a thin annulus [Eq. (4.29)]. In general, when $S \gg 1$, the pressure force suppresses the eccentricity growth for all values of I . When $S \sim 1$, Fig. 4.3 displays the importance of the disk's

radial extent on the eigenvalues λ . For example, when $S = 0.6$ and $x_{\text{in}} = 0.4$, eccentricity growth is achieved for $I \gtrsim 69^\circ$, while for $x_{\text{in}} = 0.2$ the LK instability occurs for $I \gtrsim 27^\circ$.

In Figure 4.4, we plot the eigenvalue $\lambda = \bar{\lambda}\omega_b(r_{\text{out}})$ as a function of S , for $r_{\text{in}}/r_{\text{out}} = 0.2$, $p = 1$, and values of q and I as indicated. Both models ($q = 1/4$ and $q = 3/4$) exhibit the suppression of eccentricity growth for $S \gtrsim 1$, and both models have a window of instability open when $S \sim (\text{few}) \times 0.1$. This window of instability is similar to that seen in Figure 4.2.

Figure 4.5 depicts some examples of the eigenfunctions $E_+(r)$ and $E_-(r)$ for disk models with $S = 0.03, 0.3$, and 3 . We see that for small S (top panel), the amplitudes $|E_+|$ and $|E_-|$ are largest at $r = r_{\text{out}}$ and decreases rapidly as $r \rightarrow r_{\text{in}}$. For larger S (middle and lower panels), the variations of $|E_+|$ and $|E_-|$ across the disk become smaller as the larger sound speed “smooths out” the disk. The bottom panel of Fig. 4.5 shows that when $S = 3$ (for which the disk is stable since λ is imaginary), the eigenfunctions E_+ and E_- are both real and satisfy $E_- > E_+$, implying retrograde precession of the disk’s eccentricity.

4.3.3 Effect of Viscosity

We solve the eigenvalue equations (4.15)-(4.16) including the viscosity term. In Figure 4.6, we plot the real parts of the eigenvalues λ for $\alpha_b = 0, 0.03$, and 0.1 . When $S \lesssim 1$, we see for a range of inclinations, the growth rates are only slightly modified by viscosity. When $S \gtrsim 1$, the addition of a small viscosity begins to be important. However, in this regime, the instability is already suppressed by the disk’s pressure, so the additional damping from α_b when $S \gtrsim 1$ is not relevant

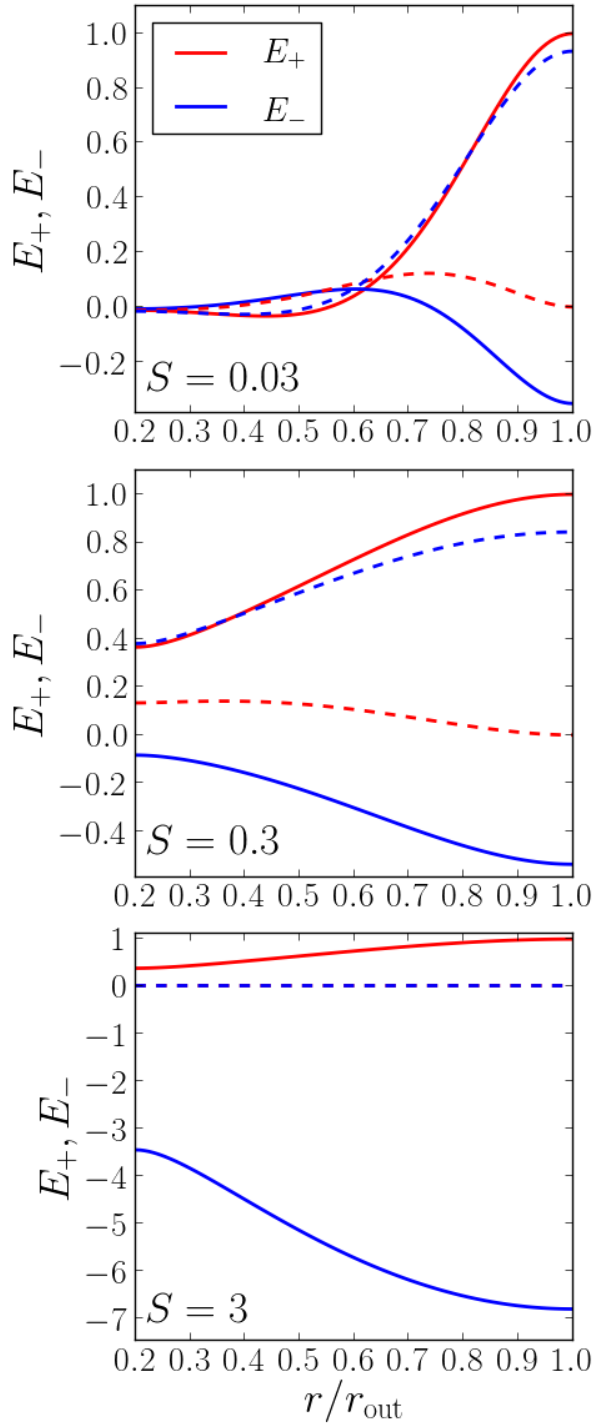


Figure 4.5: Real (solid lines) and imaginary (dashed lines) components of the eigenfunctions $E_+(r)$ and $E_-(r)$ for an extended disk. The normalization condition is $E_+(r_{\text{out}}) = 1$. The disk parameters are $\alpha_b = 0$, $p = 1$, $q = 3/4$, $r_{\text{in}}/r_{\text{out}} = 0.2$, inclination $I = 70^\circ$, and values of S [Eq. (4.21)] as indicated. The corresponding eigenvalues are $\bar{\lambda} = 1.84$ (top), $\bar{\lambda} = 1.44$ (middle), and $\bar{\lambda} = 5.57i$ (bottom).

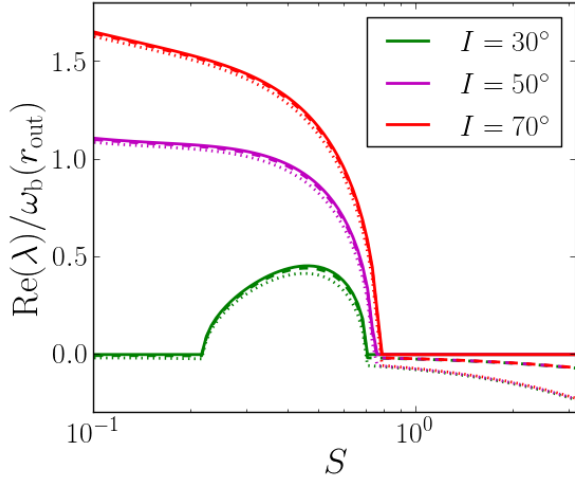


Figure 4.6: Real parts of the eigenvalues λ for extended disks, plotted as a function of S , with $\alpha_b = 0$ (solid), $\alpha_b = 0.03$ (dashed), and $\alpha_b = 0.1$ (dotted). The other disk parameters are $p = 1$, $q = 3/4$, $r_{\text{in}}/r_{\text{out}} = 0.2$, and the values of I are as indicated.

for the LK effect. We conclude that a small bulk viscosity does little to quench the LK instability.

4.4 Summary and Discussion

4.4.1 Summary of Key Results

Using linear theory of eccentric disturbances in hydrodynamical disks, we have shown that circumstellar disks in binary systems may undergo coherent eccentricity growth when the disk is significantly inclined with respect to binary orbital plane. We consider the regime where the disk remains approximately flat and undergoes rigid-body nodal precession around the binary; this requires that bending waves efficiently communicate warps in different regions of the disk

within the precession period. We find that the disk's eccentricity response to the secular tidal forcing from the binary companion depends crucially on the dimensionless ratio [see Eq. (4.21)],

$$S = \left(\frac{c_s^2}{3GM_b r^2 / 4a_b^3} \right)_{r=r_{\text{out}}} , \quad (4.32)$$

where c_s^2 (disk sound speed squared) measures the characteristic torque (per unit mass) associated with gas pressure, $3GM_b r^2 / 4a_b^3$ (with M_b and a_b the companion mass and semi-major axis) measures the tidal torque from the companion. The eccentricity response also depends on the disk's radial extent ($r_{\text{out}}/r_{\text{in}}$) and density and sound speed profiles [Eqs. (4.19) and (4.20)].

1. When $S \ll 1$, the “standard” Lidov-Kozai effect is reproduced for a thin disk annulus ($r_{\text{out}}/r_{\text{in}} \rightarrow 1$), with exponential eccentricity growth occurring for disk inclination I (with respect to the binary orbital plane) between 39° and 141° .
2. As S increases, the inclination window for disk eccentricity growth generally decreases. When $S \gg 1$, eccentricity growth is completely quenched for all disk inclinations.
3. When $S \sim 1$, a new “window of instability” opens up for certain disk parameters, where coherent disk eccentricity growth is observed for inclinations I outside the standard ($39^\circ, 141^\circ$) window.

These conclusions are qualitatively robust, shown through both analytic calculations when the disk's radial extent is negligible (thin annulus; Sec. 4.3.1) and numerical eigenmode analyses when the disk has a significant radial extent (Sec. 4.3.2). We find that viscosity does little to quench the Lidov-Kozai instability of the disk (Sec. 4.3.3).

The different disk eccentricity responses to the secular tidal forcing can be understood in terms of the apsidal precession produced by gas pressure (i.e. Papaloizou 2002, Goodchild & Ogilvie 2006, Teyssandier & Ogilvie 2016). This precession depends on the S and the disk density/pressure profiles. Unlike the other short-range forces, such as those due to General Relativity and tidal interaction in hierarchical triple systems (e.g. Liu et al. 2015), the pressure-induced precession can be either prograde or retrograde, depending on the disk profiles [see Eq. (4.29); see also Teyssandier & Ogilvie 2016]. This gives rise to the non-trivial behavior of the disk's eccentricity response for $S \sim 1$.

4.4.2 Discussion

In this paper we have focused on the linear regime of the disk Lidov-Kozai instability, which manifests as the coherent growth of disk eccentricity, with no change in the disk inclination (which enters at the order e^2). Numerical simulations are necessary to fully understand the nonlinear development of the disk eccentricity-inclination oscillations [Martin et al., 2014, Fu et al., 2015a,b]. Nevertheless, our analytic results can be used to determine under what conditions a hydrodynamical circumstellar disk is susceptible to Lidov-Kozai oscillations, without resorting to full 3D numerical simulations.

We note that the dynamical behavior of eccentric disturbances in a hydrodynamical disk depends on the disk's equation of state and vertical structure [Goodchild & Ogilvie, 2006, Ogilvie, 2008, Teyssandier & Ogilvie, 2016]. We have adopted the eccentric disk models with locally isothermal equation of state, including the 3D breathing mode term from the disk's vertical structure

(see Ogilvie 2008 for discussion). Using different models can change the details of our results, but not the general conclusions summarized in Section 4.4.1.

The disk eccentricity excitation mechanism studied in this paper is distinct from the mechanism that relies on eccentric Lindblad resonance [Lubow, 1991]. The latter operates on the dynamical timescale and requires that the disk be sufficiently extended relative to the binary separation (i.e., r_{out}/a is sufficiently larger) so that the resonance resides in the disk. By contrast, the disk Lidov-Kozai mechanism for eccentricity excitation requires an inclined binary companion, and operates on a secular timescale [Eq. (4.3)]

$$t_{\text{LK}} \sim \omega_b(r_{\text{out}})^{-1} = 5.7 \times 10^3 \text{ years} \left(\frac{M}{M_b} \right) \left(\frac{a_b}{3r_{\text{out}}} \right)^3 \times \left(\frac{M}{1M_\odot} \right)^{-1/2} \left(\frac{r_{\text{out}}}{100 \text{ AU}} \right)^{3/2}. \quad (4.33)$$

For protoplanetary disks, this timescale is much less than the disk lifetime (a few Myrs). To avoid suppression of the instability by the gas pressure, we also require

$$S = 0.36 \left(\frac{a_b}{3r_{\text{out}}} \right)^3 \left(\frac{M}{M_b} \right) \left(\frac{H(r_{\text{out}})}{0.1r_{\text{out}}} \right)^2 \lesssim 1. \quad (4.34)$$

Thus, a “weaker” companion (large a_b and small M_b) would not excite eccentricity in a thick (large H/R) disk. Condition (4.34) is consistent with the SPH simulations of Martin et al. [2014] and Fu et al. [2015a], where S values in the range 8.5×10^{-3} to 0.11 were used.

Finally, for a massive disk, the LK instability can be suppressed due to apsidal precession generated by disk self-gravity [Batygin et al., 2011, Fu et al., 2015b]. The apsidal precession rate from the disk’s self gravity is roughly

$$\omega_{\text{sg}}(r) \sim \frac{\pi G \Sigma}{rn}. \quad (4.35)$$

Crudely, to avoid suppression of the LK instability, we require $\omega_{\text{sg}}(r_{\text{out}}) \lesssim \omega_b(r_{\text{out}})$, or the disk mass

$$M_d \lesssim M_b \left(\frac{r_{\text{out}}}{a_b} \right)^3 \sim 0.04 M_b \left(\frac{3r_{\text{out}}}{a_b} \right)^3. \quad (4.36)$$

Acknowledgments

We thank the anonymous referee for his or her valuable comments. This work has been supported in part by NASA grants NNX14AG94G and NNX14AP31G, and a Simons Fellowship from the Simons Foundation. JZ is supported by a NASA Earth and Space Sciences Fellowship in Astrophysics.

Appendix

This appendix is devoted to the derivation of Eqs. (4.5) and (4.8). Our key assumption is that the internal force in the disk acts to enforce coplanarity and rigid body precession of the disk.

Consider a disk particle (test mass) with the position vector \mathbf{r} and velocity \mathbf{v} relative to the central star. Its angular momentum is $\mathbf{L} = \mathbf{r} \times \mathbf{v}$, and its eccentricity vector is

$$\mathbf{e} = \frac{1}{GM} \mathbf{v} \times (\mathbf{r} \times \mathbf{v}) - \frac{\mathbf{r}}{r}. \quad (4.37)$$

Under the action of a perturbing force \mathbf{f} , the vectors \mathbf{L} and \mathbf{e} evolve according to

$$\frac{\partial \mathbf{L}}{\partial t} = \mathbf{r} \times \mathbf{f}, \quad (4.38)$$

$$\frac{\partial \mathbf{e}}{\partial t} = \frac{1}{GM} \mathbf{f} \times (\mathbf{r} \times \mathbf{v}) + \frac{1}{GM} \mathbf{v} \times (\mathbf{r} \times \mathbf{f}). \quad (4.39)$$

The perturbing force $\mathbf{f} = \mathbf{f}_b + \mathbf{f}_{\text{int}}$ consists of the tidal force from the binary companion \mathbf{f}_b and the internal pressure force \mathbf{f}_{int} . To quadrupole order, the tidal force is given by

$$\mathbf{f}_b = \frac{GM_b}{|\mathbf{r}_b|^3} \left[\mathbf{r} - 3 \frac{\mathbf{r}_b(\mathbf{r} \cdot \mathbf{r}_b)}{|\mathbf{r}_b|^2} \right], \quad (4.40)$$

where M_b and \mathbf{r}_b are the mass and position vectors of the companion. Take the binary to be on a circular orbit with semi-major axis a_b and mean anomaly ϕ_b , and let $\hat{\mathbf{r}}, \hat{\boldsymbol{\varphi}} = \hat{\mathbf{l}} \times \hat{\mathbf{r}}$, and $\hat{\mathbf{l}}$ be the radial, azimuthal, and angular momentum unit vectors of the test mass, respectively. Averaging over the binary's orbital motion, we obtain the averaged tidal force

$$\bar{\mathbf{f}}_b \equiv \frac{1}{2\pi} \int_0^{2\pi} \mathbf{f}_b d\phi_b \quad (4.41)$$

$$\begin{aligned} &= \frac{2}{3} rn\omega_b (1 - 3 \sin^2 \varphi \sin^2 I) \hat{\mathbf{r}} \\ &\quad - 2rn\omega_b (\sin \varphi \cos \varphi \sin^2 I) \hat{\boldsymbol{\varphi}} \\ &\quad - 2rn\omega_b (\sin \varphi \sin I \cos I) \hat{\mathbf{l}}, \end{aligned} \quad (4.42)$$

where ω_b is defined in Eq. (4.3), and $\varphi = \omega + f$ is the azimuthal angle of the test mass measured from the ascending node (ω and f are the argument of pericenter and true anomaly). The $\hat{\mathbf{r}}$ and $\hat{\boldsymbol{\varphi}}$ components of $\bar{\mathbf{f}}_b$ do not change \mathbf{L} , and the $\hat{\mathbf{l}}$ component induces precession at a rate $-\omega_b \cos I \hat{\mathbf{l}}$ [see Eq. (4.1)]. To ensure coplanarity and rigid-body precession of test particles at different radii, we assume that the internal force from disk pressure has the form

$$\mathbf{f}_{\text{int}} = -2rn(\tilde{\omega}_b - \omega_b)(\sin \varphi \sin I \cos I) \hat{\mathbf{l}}, \quad (4.43)$$

where $\tilde{\omega}_b$ is given in Eq. (5.28).

We now substitute Eq. (4.43) into Eqs. (4.38) and (4.39) to obtain the effect of \mathbf{f}_{int} on $\hat{\mathbf{l}}$ and \mathbf{e} . For a disk particle on an eccentric orbit $e \ll 1$, we can expand

r and f in powers of e [Murray & Dermott, 1999]. Averaging over the mean anomaly of the test particle, we obtain Eqs. (4.5) and (4.8).

CHAPTER 5

INCLINATION EVOLUTION OF PROTOPLANETARY DISKS AROUND ECCENTRIC BINARIES

5.1 Introduction

To date, 11 transiting circumbinary planets have been detected around 9 binary star systems [Doyle et al., 2011, Kostov et al., 2013, 2014, 2016, Orosz et al., 2012a,b, Schwamb et al., 2013, Welsh et al., 2012, 2015]. All planets detected have orbital planes very well aligned with their binary orbital planes, with mutual binary-planet inclinations not exceeding 3° . The circumbinary planet detectability is a very sensitive function of the binary-planet inclination [Martin & Triaud, 2015, Li, Holman, & Tao, 2016]. If the mutual inclination is always small ($\lesssim 5^\circ$), then the occurrence rate of circumbinary planets is comparable to that of planets around single stars, but if modest inclinations ($\gtrsim 5^\circ$) are common, the circumbinary planet occurrence rate may be much larger [Armstrong et al., 2014]. For these reasons, it is important to understand if and how a binary aligns with its circumbinary disk from which these planets form.

Observations show that most circumbinary disks tend to be aligned with their host binary orbital planes. The gas rich circumbinary disks HD 98800 B [Andrews et al., 2010], AK Sco [Czekala et al., 2015], DQ Tau [Czekala et al., 2016], and the debris circumbinary disks α CrB and β Tri [Kennedy et al., 2012b] all have mutual disk-binary inclinations not exceeding 3° . However, there are some notable exceptions. The circumbinary disk around KH 15D is mildly misaligned with the binary orbital plane by $\sim 10^\circ$ - 20° [Winn et al., 2004, Chiang & Murray-Clay, 2004, Capelo et al., 2012]. Shadows [Marino et al., 2015] and gas

kinematics [Casassus et al., 2015] of the disks in HD 142527 are consistent with a misalignment of $\sim 70^\circ$ between the outer circumbinary disk and binary orbital plane [Lacour et al., 2016]. The disks (circumbinary and two circumstellar) in the binary protostar IRS 43 are misaligned with each other and with the binary [Brinch et al., 2016]. Most intriguingly, the debris disk around the eccentric ($e_b = 0.77$) binary 99 Herculis may be highly inclined: By modeling the resolved images from *Hershel*, Kennedy et al. [2012a] strongly favor a disk orientation where the disk angular momentum vector is inclined to the binary orbital angular momentum vector by 90° (polar alignment). Kennedy et al. [2012a] also produced a model with a disk-binary inclination of 30° which fits the observations, but this configuration is unlikely, since differential precession of dust due to the gravitational influence of the binary would rapidly destroy the disk.

Since star/binary formation takes place in turbulent molecular clouds [McKee & Ostriker, 2007], the gas that falls onto the central protostellar core/binary and assembles onto the disk at different times may rotate in different directions (e.g. Bate, Bonnell, & Bromm 2003, see also Bate et al. 2010, Fielding et al. 2015). In this scenario, it is reasonable to expect a newly formed binary to be surrounded by a highly misaligned circumbinary disk which forms as a result of continued gas accretion [Foucart & Lai, 2013]. The observed orientations of circumbinary disks then depend on the long-term inclination evolution driven by binary-disk interactions.

Foucart & Lai [2013, 2014] studied the warping and the dissipative torque driving the inclination evolution of a circumbinary disk, assuming a circular binary. Foucart & Lai [2013] considered an infinite disk and included the effect of accretion onto the binary, while Foucart & Lai [2014] considered a more re-

alistic disk of finite size and angular momentum, which can precess coherently around the binary. It was shown that under typical protoplanetary conditions, both viscous torque associated with disk warping and accretion torque tend to damp the mutual disk-binary inclination on timescale much shorter than the disk lifetime (a few Myr). By contrast, a circumstellar disc inside a binary can maintain large misalignment with respect to the binary orbital plane over its entire lifetime [Lubow & Ogilvie, 2000, Foucart & Lai, 2014]. This is consistent with the observations that most circumbinary disks are nearly coplanar with their host binaries. On the other hand, the observed circumbinary disk misalignment (such as in KH 15D and IRS 43) can provide useful constraints on the uncertain aspects of the disc warp theory, such as non-linear effects [Ogilvie, 2006] and parametric instabilities due to disk warping [Gammie, Goodman, & Ogilvie, 2000, Ogilvie & Latter, 2013]

However, several recent numerical studies using smoothed particle hydrodynamics (SPH) suggest that other outcomes may be possible for disks around *eccentric* binaries. Aly et al. [2015] showed that disks around binary black holes (which typically lie in the “viscous regime” of disk warps, with the viscosity parameter α larger than the disk aspect ratio H/r ; Papaloizou & Pringle 1983, Ogilvie 1999; see Sec. 5.3) around eccentric binaries may be driven into polar alignment. Martin & Lubow [2017] found numerically that a circumbinary protoplanetary disk (typically in the bending wave regime, with $\alpha \lesssim H/r$ Papaloizou & Lin 1995, Lubow & Ogilvie 2000), inclined to an eccentric ($e_b = 0.5$) binary by 60° will evolve to a polar configuration. They suggested that this dynamical outcome arises from the combined influence of the gravitational torque on the disk from the binary and viscous torques from disk warping. They also proposed that 99 Herculis (with $e_b = 0.77$) followed such an evolution to end in

the orbital configuration (polar alignment) observed today.

In this paper, we provide a theoretical analysis to the above numerical results. In particular, we generalize the study of Foucart & Lai [2014] to apply to circumbinary disks with arbitrary disk-binary inclinations and binary eccentricities. We derive the critical condition and calculate the timescale for the disk to evolve toward polar alignment with the binary. In Section 5.2, we review the secular dynamics of a test particle around an eccentric binary. In Section 5.3, we calculate the disk warp profile and dissipative disk torques acting on the disk, and derive the requirements for the disk to evolve into polar alignment with the binary. Section 5.4 considers the situation when the circumbinary disk has a non-negligible angular momentum compared to the inner binary. In Section 5.5, we examine the back-reaction torque from the disk on the binary and the effect of gas accretion. We discuss our results in Section 5.6, and summarize in Section 5.7.

5.2 Test Particle Dynamics

In preparation for later sections, we review the secular dynamics of a test particle surrounding an eccentric binary [Farago & Laskar, 2010, Li, Zhou, & Zhang, 2014, Naoz et al., 2017]. Consider a circular test mass with semimajor axis r and orbital angular momentum unit vector \hat{l} , surrounding an eccentric binary with orbital angular momentum vector \hat{l}_b , eccentricity vector e_b , semimajor axis a_b , total mass $M_b = M_1 + M_2$ (where M_1, M_2 are individual masses), and reduced mass $\mu_b = M_1 M_2 / M_b$. The orbit-averaged torque per unit mass on the test parti-

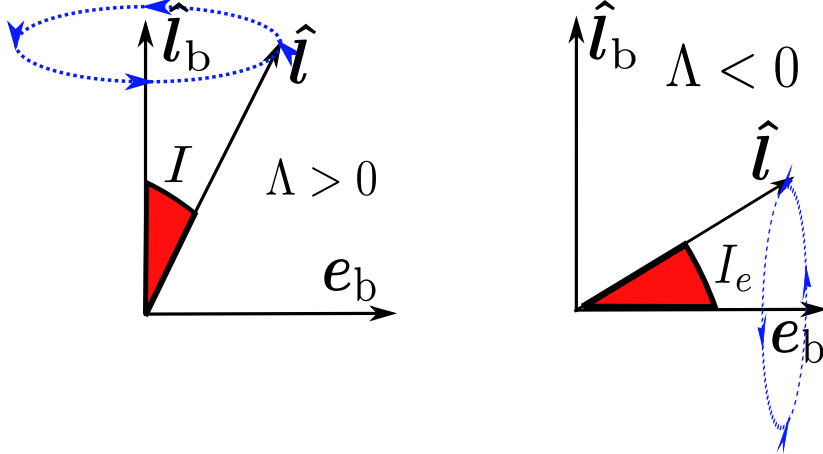


Figure 5.1: Test particle dynamics. When $\Lambda > 0$, \hat{l} precesses around \hat{l}_b , with $I \sim \text{constant}$ and Ω circulating. When $\Lambda < 0$, \hat{l} precesses around e_b , with $I_e \sim \text{constant}$ and Ω_e circulating. See Eq. (5.6) for definitions of I_e and Ω_e .

cle is (e.g. Liu, Muñoz, & Lai 2015, Petrovich 2015)

$$\mathbf{T}_{\text{db}} = -r^2 n \omega_b \left[(1 - e_b^2) (\hat{l} \cdot \hat{l}_b) \hat{l}_b \times \hat{l} - 5 (\hat{l} \cdot e_b) e_b \times \hat{l} \right], \quad (5.1)$$

where $n \simeq \sqrt{GM_b/r^3}$ is the test particle orbital frequency (mean-motion), and

$$\omega_b = \frac{3G\mu_b a_b^2}{4r^5 n} \quad (5.2)$$

characterizes the precession frequency of the test particle around the binary. The torque \mathbf{T}_{db} in Eq. (5.1) is evaluated to the lowest order in a_b/r .

The time evolution of the test particle's orbital angular momentum vector is given by

$$\frac{d\hat{l}}{dt} = -\omega_b \left[(1 - e_b^2) (\hat{l} \cdot \hat{l}_b) \hat{l}_b \times \hat{l} - 5 (\hat{l} \cdot e_b) e_b \times \hat{l} \right]. \quad (5.3)$$

Equation (5.3) can be solved analytically [Landau & Lifshitz, 1969, Farago & Laskar, 2010, Li, Zhou, & Zhang, 2014], but the dynamics may be easily understood by analyzing the energy curves. Equation (5.3) has an integral of motion

$$\Lambda = (1 - e_b^2) (\hat{l} \cdot \hat{l}_b)^2 - 5 (\hat{l} \cdot e_b)^2, \quad (5.4)$$

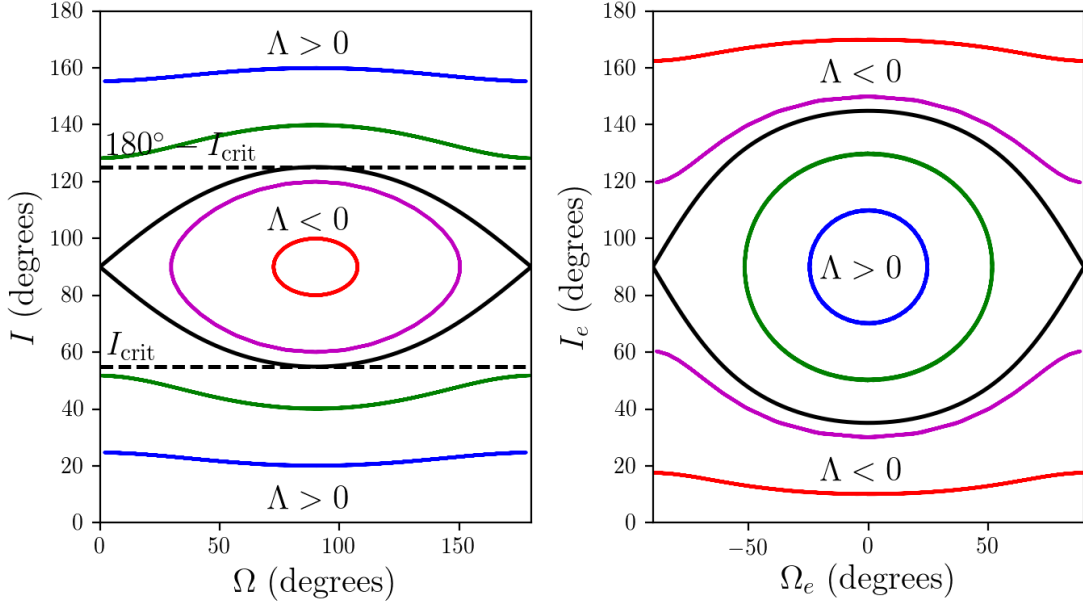


Figure 5.2: Test particle trajectories in the $I - \Omega$ and $I_e - \Omega_e$ planes [see Eq. (5.6)], with binary eccentricity $e_b = 0.3$. When $\Lambda > 0$, \hat{l} precesses around \hat{l}_b , with $I \sim \text{constant}$ and Ω circulating its full range of values (0° - 360°), while Ω_e librates around 0° . When $\Lambda < 0$, \hat{l} precesses around e_b , with $I_e \sim \text{constant}$ and Ω_e circulating its full range of values (-180° - 180°), while Ω librating around 90° (see Fig. 5.1). Black lines denote the $\Lambda = 0$ separatrix. The other curves have $\Lambda = 0.751$ (blue), $\Lambda = 0.348$ (green), $\Lambda = -0.110$ (magenta), $\Lambda = -0.409$ (red). Only Ω and Ω_e in the range $[0^\circ, 180^\circ]$ and $[-90^\circ, 90^\circ]$ are shown. The energy curves for Ω in $[180^\circ, 360^\circ]$ duplicate those of $[0^\circ, 180^\circ]$, and the energy curves for Ω_e in $[90^\circ, 270^\circ]$ duplicate those of $[-90^\circ, 90^\circ]$.

which is simply related to the quadrupole interaction energy (double-averaged over the two orbits) by (e.g. Tremaine et al. 2009, Tremaine & Yavetz 2014, Liu, Muñoz, & Lai 2015)

$$\Phi_{\text{quad}} = \frac{G\mu_b a_b^2}{8r^3} (1 - 6e_b^2 - 3\Lambda). \quad (5.5)$$

To plot the energy curves, we set up the Cartesian coordinate system (x, y, z) , where $\hat{l}_b = \hat{z}$ and $e_b = e_b \hat{x}$. We may write

$$\begin{aligned} \hat{l} &= (\sin I \sin \Omega, -\sin I \cos \Omega, \cos I) \\ &= (\cos I_e, \sin I_e \sin \Omega_e, \sin I_e \cos \Omega_e), \end{aligned} \quad (5.6)$$

where I is the angle between \hat{l} and \hat{l}_b , Ω is the test particle's longitude of the ascending node (measured in the xy plane from the x -axis); similarly I_e is the angle between \hat{l} and e_b , and Ω_e measures the longitude of the node in the yz plane (see Fig. 5.1). In terms of I and Ω , we have

$$\Lambda = (1 - e_b^2) \cos^2 I - 5e_b^2 \sin^2 I \sin^2 \Omega. \quad (5.7)$$

In Figure 5.2, we plot the test particle trajectories in the $I - \Omega$ (left panel) and $I_e - \Omega_e$ (right panel) planes for the binary eccentricity $e_b = 0.3$. The critical separatrix $\Lambda = 0$ is displayed in black in both plots. When $\Lambda > 0$, \hat{l} precesses around \hat{l}_b with $I \sim \text{constant}$ and Ω circulating the full range ($0 - 360^\circ$), while Ω_e librates around 0° . When $\Lambda < 0$, \hat{l} precesses around e_b with $I_e \sim \text{constant}$ and Ω_e circulating the full range ($0 - 360^\circ$), while Ω librates around 90° (see Fig. 5.1).

Thus, the test particle angular momentum axis \hat{l} transitions from precession around \hat{l}_b for $\Lambda > 0$ to precession around e_b for $\Lambda < 0$. Because the $\Lambda = 0$ separatrix has $\Omega \in [0^\circ, 360^\circ]$ (Fig. 5.2), a necessary condition for \hat{l} to precess around e_b is $I_{\text{crit}} < I < 180^\circ - I_{\text{crit}}$, where

$$I_{\text{crit}} = \cos^{-1} \sqrt{\frac{5e_b^2}{1 + 4e_b^2}} = \tan^{-1} \sqrt{\frac{1 - e_b^2}{5e_b^2}}. \quad (5.8)$$

Figure 5.2 clearly reveals the stable fixed points of the system. In terms of the variables (Ω, I) , the stable fixed points (where $dI/dt = d\Omega/dt = 0$) are $I = \pi/2$ and $\Omega = \pi/2, 3\pi/2$, corresponding to $\hat{l} = \pm e_b/e_b$. In terms of the variables (Ω_e, I_e) , the fixed points are $I_e = \pi/2$ and $\Omega_e = 0, \pi$, corresponding to $\hat{l} = \pm \hat{l}_b$. We will see in Section 3 that in the presence of dissipation, the disk may be driven toward one of these fixed points.

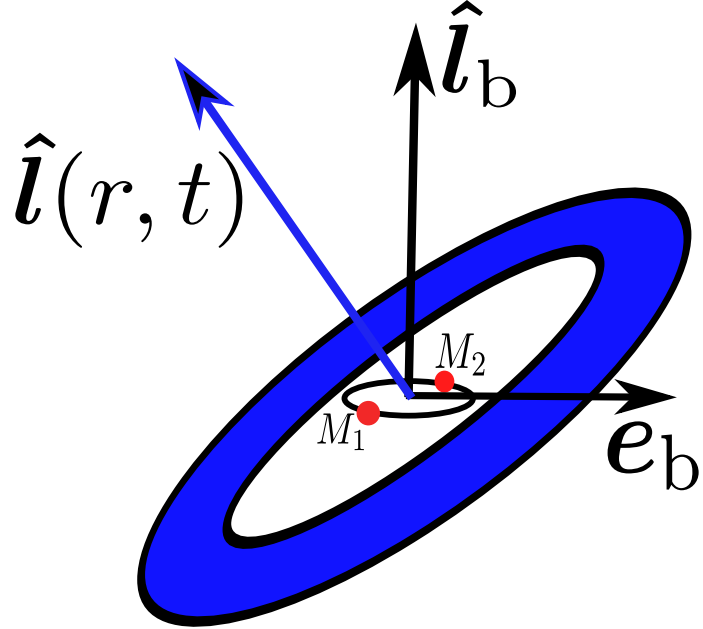


Figure 5.3: Circumbinary disk setup. The binary has individual masses M_1 and M_2 , with total mass $M_b = M_1 + M_2$ and reduced mass $\mu_b = M_1 M_2 / M_b$, with orbital angular momentum vector \hat{l}_b and eccentricity vector e_b . The binary is surrounded by a circular circumbinary disk with unit orbital angular momentum $\hat{l} = \hat{l}(r, t)$, surface density $\Sigma = \Sigma(r)$ [Eq. (6.12)], and inner (outer) truncation radii r_{in} (r_{out}).

5.3 Circumbinary Disk Dynamics

We now consider a binary (with the same parameters as in Section 5.2, see also Fig. 5.3) surrounded by a circular circumbinary disk with inner truncation radius r_{in} , outer truncation radius r_{out} , with unit angular momentum vector $\hat{l} = \hat{l}(r, t)$, and surface density $\Sigma = \Sigma(r)$. For concreteness, we adopt the surface density profile

$$\Sigma(r) = \Sigma_{\text{in}} \left(\frac{r_{\text{in}}}{r} \right). \quad (5.9)$$

We assume $r_{\text{in}} \ll r_{\text{out}}$ throughout this work. We could assume a more general surface density profile $\Sigma \propto r^{-p}$, with p observationally constrained to lie in the range 0.5 – 1.5 (e.g. Weidenschilling 1977, Williams & Cieza 2011, Chiang &

Laughlin 2013). A more general p will effect the disk mass [Eq. (5.11)] and angular momentum [Eq. (5.12)], as well as the precession [Eq. (5.28)] and viscous [Eq. (5.47)] rates, by factors of order unity.

The binary has orbital angular momentum

$$L_b = \mu_b \sqrt{(1 - e_b^2)GM_b a_b}, \quad (5.10)$$

while the disk has mass

$$M_d = 2\pi \int_{r_{in}}^{r_{out}} \Sigma r dr \simeq 2\pi \Sigma_{in} r_{in} r_{out} \quad (5.11)$$

and angular momentum (assuming a small disk warp; see below)

$$L_d = 2\pi \int_{r_{in}}^{r_{out}} \Sigma r^3 n dr \simeq \frac{2}{3} M_d \sqrt{GM_b r_{out}}, \quad (5.12)$$

where $n(r) \simeq \sqrt{GM_b/r^3}$. Comparing L_b to L_d , we have

$$\frac{L_d}{L_b} \simeq 0.067 (1 - e_b^2)^{-1/2} \left(\frac{M_d}{0.01 \mu_b} \right) \left(\frac{r_{out}}{100 a_b} \right)^{1/2}. \quad (5.13)$$

Because $L_b \gg L_d$ for typical circumbinary disk parameters, in this section we assume \hat{l}_b and e_b are fixed in time, neglecting the back-reaction torque on the binary from the disk. We discuss the system's dynamics when L_d is non-negligible compared to L_b in Section 5.4, and the effects of the back-reaction torque on the binary from the disk in Section 5.5.

5.3.1 Qualitative Discussion

Assuming the disk to be nearly flat, the time evolution of the disk unit angular momentum vector is given by

$$\frac{d\hat{l}_d}{dt} = \left\langle \frac{\mathbf{T}_{db}}{r^2 n} \right\rangle, \quad (5.14)$$

where T_{db} is given in Eq. (5.1), $\hat{\mathbf{l}}_{\text{d}}(t)$ is a suitably averaged unit angular momentum of the disk [see Eq. (5.24)], and $\langle \dots \rangle$ implies a proper average over r [see Eq. (5.27)]. When the disk is flat, the time evolution of $\hat{\mathbf{l}}_{\text{d}}$ is identical to that of a test particle (see discussion at the end of Sec. 5.3.2).

When $\alpha \lesssim H/r$ (H is the disk scaleheight, α is the viscosity parameter), the main internal torque enforcing disk rigidity and coherent precession comes from bending wave propagation [Papaloizou & Lin, 1995, Lubow & Ogilvie, 2000]. As bending waves travel at 1/2 the sound speed, the wave crossing time is of order $t_{\text{bw}} = 2r/c_s$. When t_{bw} is longer than the characteristic precession time ω_b^{-1} [see Eq. (5.2)], strong disk warps can be induced. In the extreme nonlinear regime, disk breaking may be possible in circumbinary disks [Larwood & Papaloizou, 1997, Facchini, Lodato, & Price, 2013, Nixon, King, & Price, 2013]. To compare t_{bw} with ω_b^{-1} , we adopt the disk sound speed profile

$$c_s(r) = H(r)n(r) = h \sqrt{\frac{GM_b}{r_{\text{in}}}} \left(\frac{r_{\text{in}}}{r}\right)^{1/2}, \quad (5.15)$$

where $h = H/r$. We find

$$t_{\text{bw}}\omega_b = 0.94 \left(\frac{0.1}{h}\right) \left(\frac{4\mu_b}{M_b}\right) \left(\frac{2a_b}{r_{\text{in}}}\right)^2 \left(\frac{r_{\text{in}}}{r}\right)^2 \quad (5.16)$$

Thus, we expect that the small warp approximation should be valid everywhere in the disk except the inner-most region. Throughout this paper, we scale our results to $h = 0.1$. Real protoplanetary disks can have aspect ratios in the range $h \sim 0.03 - 0.2$ (e.g. Lynden-Bell & Pringle 1974, Chiang & Goldreich 1997, Williams & Cieza 2011). We normalize r_{in} to $2a_b$, but note that the inner truncation radius of the disk depends non-trivially on the binary's eccentricity [Miranda, Muñoz, & Lai, 2017].

Although the disk is flat to a good approximation, the interplay between disk twist/warp and viscous dissipation may modify the disk's dynamics over

timescales much longer than ω_b^{-1} . When the external torque \mathbf{T}_{db} is applied to the disk in the bending wave regime, the disk's viscosity causes the disk to develop a small twist of order

$$\frac{\partial \hat{\mathbf{l}}_d}{\partial \ln r} \Big|_{twist} \sim -\frac{4\alpha}{c_s^2} \mathbf{T}_{db}, \quad (5.17)$$

while the precession of bending waves from a non-Keplarian epicyclic frequency κ causes the disk to develop a small warp, of order

$$\frac{\partial \hat{\mathbf{l}}_d}{\partial \ln r} \Big|_{warp} \sim -\frac{4}{c_s^2} \left(\frac{\kappa^2 - n^2}{2n^2} \right) \hat{\mathbf{l}}_d \times \mathbf{T}_{db}. \quad (5.18)$$

The viscous twist [Eq. (5.17)] interacts with the external torque, effecting the evolution of $\hat{\mathbf{l}}$ over the viscous timescale. To an order of magnitude, we have

$$\left| \frac{d\hat{\mathbf{l}}_d}{dt} \right|_{visc} \sim \left\langle \frac{\mathbf{T}_{db}}{r^2 n} \cdot \frac{\partial \hat{\mathbf{l}}}{\partial \ln r} \Big|_{twist} \right\rangle \sim \left\langle \frac{4\alpha}{c_s^2} (r^2 n) \omega_b^2 \right\rangle. \quad (5.19)$$

In the above estimate, we have assumed the relevant misalignment angles (between $\hat{\mathbf{l}}_d$ and $\hat{\mathbf{l}}_b$, or between $\hat{\mathbf{l}}_d$ and \mathbf{e}_b) is of order unity.

5.3.2 Formalism

The torque per unit mass on the disk from the inner binary is given by Eq. (5.1), with $\mathbf{T}_{db} = \mathbf{T}_{db}(r, t)$. In addition, the gravitational potential from the binary induces a non-Keplarian angular frequency [Miranda & Lai, 2015], with

$$\kappa^2 - n^2 = -2\omega_b n f_b, \quad (5.20)$$

where

$$f_b = \frac{1}{2} \left\{ \left[3(\hat{\mathbf{l}} \cdot \hat{\mathbf{l}}_b)^2 - 1 \right] \left(1 + \frac{3}{2} e_b^2 \right) - 15 e_b^2 (\hat{\mathbf{l}} \times \hat{\mathbf{l}}_b)^2 \right\}. \quad (5.21)$$

When the Shakura-Sunaev α -viscosity parameter satisfies $\alpha \lesssim H/r$, the disk lies in the bending wave regime [Papaloizou & Lin, 1995, Lubow & Ogilvie,

2000]. Any warp induced by an external torque is smoothed by bending waves passing through the disk. Protoplanetary disks typically lie in the bending wave regime. The time evolution of $\hat{\mathbf{l}}(r, t)$ is governed by the equations (Lubow & Ogilvie 2000; see also Lubow, Ogilvie, & Pringle 2002)

$$\Sigma r^2 n \frac{\partial \hat{\mathbf{l}}}{\partial t} = \frac{1}{r} \frac{\partial \mathbf{G}}{\partial r} + \Sigma \mathbf{T}_{\text{db}}, \quad (5.22)$$

$$\frac{\partial \mathbf{G}}{\partial t} - \omega_b f_b \hat{\mathbf{l}} \times \mathbf{G} + \alpha \Omega \mathbf{G} = \frac{\Sigma c_s^2 r^3 n}{4} \frac{\partial \hat{\mathbf{l}}}{\partial r}, \quad (5.23)$$

where \mathbf{G} is the internal torque.

From equation (5.16), we see that $t_{\text{bw}} < \omega_b^{-1}$ for standard circumbinary disk parameters, so the disk should be only mildly warped. We may therefore expand

$$\hat{\mathbf{l}}(r, t) = \hat{\mathbf{l}}_d(t) + \mathbf{l}_1(r, t) + \dots, \quad (5.24)$$

$$\mathbf{G}(r, t) = \mathbf{G}_0(r, t) + \mathbf{G}_1(r, t) + \dots \quad (5.25)$$

where $\hat{\mathbf{l}}_d$ is the unit vector along the total angular momentum of the disk, $|\mathbf{l}_1| \ll |\hat{\mathbf{l}}_d| = 1$ [see Eqs. (5.31)-(5.32) below]. As we will see, the internal torque $\mathbf{G}_0(r, t)$ maintains the rigid body dynamical evolution of $\hat{\mathbf{l}}_d$, while $\mathbf{G}_1(r, t)$ maintains the warp profile \mathbf{l}_1 . Perturbative expansions to study warped disk structure and time evolution have been taken by Lubow & Ogilvie [2000, 2001] and Foucart & Lai [2014]. Inserting (5.24) into Eq. (5.22), integrating over $r dr$, and using the zero torque boundary condition

$$\mathbf{G}_0(r_{\text{in}}, t) = \mathbf{G}_0(r_{\text{out}}, t) = 0, \quad (5.26)$$

we find the leading order time evolution of $\hat{\mathbf{l}}$ is given by

$$\frac{d\hat{\mathbf{l}}_d}{dt} = -\tilde{\omega}_b \left[(1 - e_b^2)(\hat{\mathbf{l}}_d \cdot \hat{\mathbf{l}}_b) \hat{\mathbf{l}}_b \times \hat{\mathbf{l}}_d - 5(\hat{\mathbf{l}}_d \cdot \mathbf{e}_b) \mathbf{e}_b \times \hat{\mathbf{l}}_d \right]. \quad (5.27)$$

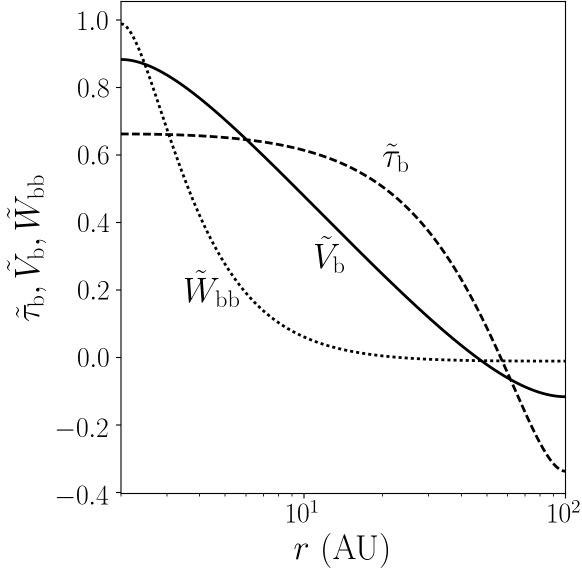


Figure 5.4: Rescaled warp functions $\tilde{\tau}_b = \tau_b/[\tau_b(r_{\text{in}}) - \tau_b(r_{\text{out}})]$ [Eq. (5.36)], $\tilde{V}_b = V_b/[V_b(r_{\text{in}}) - V_b(r_{\text{out}})]$ [Eq. (5.37)], and $\tilde{W}_{bb} = W_{bb}/[W_{bb}(r_{\text{in}}) - W_{bb}(r_{\text{out}})]$ [Eq. (5.38)] as a function of radius. We take $r_{\text{in}} = 2$ AU and $r_{\text{out}} = 100$ AU.

Here,

$$\begin{aligned}\tilde{\omega}_b &= \frac{2\pi}{L_d} \int_{r_{\text{in}}}^{r_{\text{out}}} \Sigma r^3 \Omega \omega_b dr \simeq \frac{9G\mu_b a_b^2}{16r_{\text{in}}^2 r_{\text{out}} \sqrt{GM_b r_{\text{out}}}} \\ &= 4.97 \times 10^{-5} \left(\frac{2a_b}{r_{\text{in}}} \right)^2 \left(\frac{4\mu_b}{M_b} \right) \\ &\quad \times \left(\frac{M_b}{2M_\odot} \right)^{1/2} \left(\frac{r_{\text{out}}}{100 \text{ AU}} \right)^{-3/2} \left(\frac{2\pi}{\text{yr}} \right)\end{aligned}\quad (5.28)$$

is the characteristic precession frequency of the rigid disk. Equation (5.27) is equivalent to Equation (5.3) if one replaces $\tilde{\omega}_b$ with ω_b , and the disk dynamics reduce to those of a test particle with $\hat{l} = \hat{l}_d$ when $c_s \rightarrow \infty$.

5.3.3 Disk Warp Profile

With \hat{l}_d determined with boundary condition (5.26), we may solve for $\mathbf{G}_0(r, t)$:

$$\mathbf{G}_0(r, t) = g_b \left[(1 - e_b^2)(\hat{l}_d \cdot \hat{l}_b) \hat{l}_b \times \hat{l}_d - 5(\hat{l}_d \cdot \mathbf{e}_b) \mathbf{e}_b \times \hat{l}_d \right], \quad (5.29)$$

where

$$g_b(r) = \int_{r_{in}}^r \Sigma r'^3 n(\omega_b - \tilde{\omega}_b) dr'. \quad (5.30)$$

With the leading order terms for \hat{l} and G , we may solve for \mathbf{l}_1 . We impose the normalization condition

$$\int_{r_{in}}^{r_{out}} \Sigma r^3 \Omega \mathbf{l}_1(r, t) dr = 0, \quad (5.31)$$

so that \hat{l}_d is the unit vector along the *total* angular momentum of the disk, or

$$\hat{l}_d(t) = \frac{2\pi}{L_d} \int_{r_{in}}^{r_{out}} \Sigma r^3 \Omega \hat{l}(r, t) dr. \quad (5.32)$$

Inserting Eq. (5.29) into Eq. (5.23) and integrating, we obtain

$$\begin{aligned} \mathbf{l}_1(r, t) &= (\mathbf{l}_1)_{twist} + (\mathbf{l}_1)_{warp} \\ &+ 5\tilde{\omega}_b g_b (1 - e_b^2) \hat{l}_d \cdot (\hat{l}_b \times \mathbf{e}_b) [(\hat{l}_d \cdot \mathbf{e}_b) \hat{l}_b \times \hat{l}_d - (\hat{l}_d \cdot \hat{l}_b) \mathbf{e}_b \times \hat{l}_d], \end{aligned} \quad (5.33)$$

where

$$(\mathbf{l}_1)_{twist} = V_b [(1 - e_b^2) (\hat{l}_d \cdot \hat{l}_b) \hat{l}_b \times \hat{l}_d - 5(\hat{l}_d \cdot \mathbf{e}_b) \mathbf{e}_b \times \hat{l}_d], \quad (5.34)$$

and

$$\begin{aligned} (\mathbf{l}_1)_{warp} &= \\ &- \tilde{\omega}_b \tau_b (1 - e_b^2) (\hat{l}_d \cdot \hat{l}_b) \\ &\times [(1 - e_b^2) (\hat{l}_d \cdot \hat{l}_b) \hat{l}_b \times (\hat{l}_b \times \hat{l}_d) - 5(\mathbf{e}_b \cdot \hat{l}_d) \hat{l}_b \times (\mathbf{e}_b \times \hat{l}_d)] \\ &+ 5\tilde{\omega}_b \tau_b (\hat{l}_d \cdot \mathbf{e}_b) \\ &\times [(1 - e_b^2) (\hat{l}_d \cdot \hat{l}_b) \mathbf{e}_b \times (\hat{l}_b \times \hat{l}_d) - 5(\mathbf{e}_b \cdot \hat{l}_d) \mathbf{e}_b \times (\mathbf{e}_b \times \hat{l}_d)] \\ &- W_{bb} f_b \\ &\times [(1 - e_b^2) (\hat{l}_d \cdot \hat{l}_b) \hat{l}_d \times (\hat{l}_b \times \hat{l}_d) - 5(\mathbf{e}_b \cdot \hat{l}_d) \hat{l}_d \times (\mathbf{e}_b \times \hat{l}_d)]. \end{aligned} \quad (5.35)$$

Here,

$$\tau_b(r) = \int_{r_{in}}^r \frac{g_b}{\Sigma c_s^2 r'^3 n} dr' - \tau_{b0}, \quad (5.36)$$

$$V_b(r) = \int_{r_{in}}^r \frac{\alpha g_b}{\Sigma c_s^2 r'^3} dr' - V_{b0}, \quad (5.37)$$

$$W_{bb}(r) = \int_{r_{in}}^r \frac{\omega_b g_b}{\Sigma c_s^2 r'^3 n} dr' - W_{bb0}, \quad (5.38)$$

and

$$\tau_{b0} = \frac{2\pi}{L_d} \int_{r_{in}}^{r_{out}} \Sigma r^3 n \left(\int_{r_{in}}^r \frac{g_b}{\Sigma c_s^2 r'^3 n} dr' \right) dr, \quad (5.39)$$

$$V_{b0} = \frac{2\pi}{L_d} \int_{r_{in}}^{r_{out}} \Sigma r^3 n \left(\int_{r_{in}}^r \frac{\alpha g_b}{\Sigma c_s^2 r'^3} dr' \right) dr, \quad (5.40)$$

$$W_{bb0} = \frac{2\pi}{L_d} \int_{r_{in}}^{r_{out}} \Sigma r^3 n \left(\int_{r_{in}}^r \frac{\omega_b g_b}{\Sigma c_s^2 r'^3 n} dr' \right) dr. \quad (5.41)$$

The third term in Eq. (5.33) arises from the fact that $\hat{l}_d \cdot \mathbf{e}_b$ and $\hat{l}_d \cdot \hat{l}_b$ are not constant in time, and is dynamically unimportant. Although it is strait-forward to compute the integrals in Eqs. (5.36)-(5.38), this calculation is tedious and unilluminating. Instead, we notice that over most of the region in the integrals, the internal torque radial function $g_b(r)$ is of order

$$g_b(r) \sim \Sigma r^4 n \omega_b. \quad (5.42)$$

Evaluating the warp functions and using the fact that $r_{in} \ll r_{out}$, we obtain the approximate expressions

$$\begin{aligned} \tilde{\omega}_b [\tau_b(r_{in}) - \tau_b(r_{out})] &\approx -0.108 \\ &\times \left(\frac{0.1}{h} \right)^2 \left(\frac{4\mu_b}{M_b} \right)^2 \left(\frac{2a_b}{r_{in}} \right)^4 \left(\frac{50 r_{in}}{r_{out}} \right)^{3/2}, \end{aligned} \quad (5.43)$$

$$\begin{aligned} V_b(r_{in}) - V_b(r_{out}) &\approx -0.258 \\ &\times \left(\frac{\alpha}{0.01} \right) \left(\frac{0.1}{h} \right)^2 \left(\frac{4\mu_b}{M_b} \right) \left(\frac{2a_b}{r_{in}} \right)^2, \end{aligned} \quad (5.44)$$

$$\begin{aligned} W_{bb}(r_{in}) - W_{bb}(r_{out}) &\approx -0.108 \\ &\times \left(\frac{0.1}{h} \right)^2 \left(\frac{4\mu_b}{M_b} \right)^2 \left(\frac{2a_b}{r_{in}} \right)^4. \end{aligned} \quad (5.45)$$

In Figure 5.4, we plot the rescaled warp functions $\tilde{\tau}_b = \tau_b / [\tau_b(r_{in}) - \tau_b(r_{out})]$, $\tilde{V}_b = V_b / [V_b(r_{in}) - V_b(r_{out})]$, and $\tilde{W}_{bb} = W_{bb} / [W_{bb}(r_{in}) - W_{bb}(r_{out})]$.

5.3.4 Viscous Torques

The disk twisting due to viscosity (\mathbf{l}_1)_{twist} [Eq. (5.34)] interacts with \mathbf{T}_{db} [Eq. (5.1)], effecting the evolution of $\hat{\mathbf{l}}_{\text{d}}$ over viscous timescales. Inserting $\hat{\mathbf{l}} = \hat{\mathbf{l}}_{\text{d}} + (\mathbf{l}_1)_{\text{twist}}$ into Equation (5.22), integrating over $2\pi r dr$, and using the boundary condition (5.26), we obtain

$$\begin{aligned} \left(\frac{d\mathbf{L}_{\text{d}}}{dt} \right)_{\text{visc}} &= L_{\text{d}}\gamma_{\text{b}} \left[(1 - e_{\text{b}}^2)(\hat{\mathbf{l}}_{\text{d}} \cdot \hat{\mathbf{l}}_{\text{b}})^2 \hat{\mathbf{l}}_{\text{b}} \times (\hat{\mathbf{l}}_{\text{b}} \times \hat{\mathbf{l}}_{\text{d}}) \right. \\ &\quad + 25(\hat{\mathbf{l}}_{\text{d}} \cdot \mathbf{e}_{\text{b}})^2 \mathbf{e}_{\text{b}} \times (\mathbf{e}_{\text{b}} \times \hat{\mathbf{l}}_{\text{d}}) \\ &\quad - 5(1 - e_{\text{b}}^2)(\hat{\mathbf{l}}_{\text{d}} \cdot \mathbf{e}_{\text{b}})(\hat{\mathbf{l}}_{\text{d}} \cdot \hat{\mathbf{l}}_{\text{b}}) \hat{\mathbf{l}}_{\text{b}} \times (\mathbf{e}_{\text{b}} \times \hat{\mathbf{l}}_{\text{d}}) \\ &\quad \left. - 5(1 - e_{\text{b}}^2)(\hat{\mathbf{l}}_{\text{d}} \cdot \mathbf{e}_{\text{b}})(\hat{\mathbf{l}}_{\text{d}} \cdot \hat{\mathbf{l}}_{\text{b}}) \mathbf{e}_{\text{b}} \times (\hat{\mathbf{l}}_{\text{b}} \times \hat{\mathbf{l}}_{\text{d}}) \right]. \end{aligned} \quad (5.46)$$

Here,

$$\gamma_{\text{b}} = \frac{2\pi}{L_{\text{d}}} \int_{r_{\text{in}}}^{r_{\text{out}}} \frac{4\alpha g_{\text{b}}^2}{\Sigma c_s^2 r^3} dr. \quad (5.47)$$

Using the approximate expression of g_{b} [Eq. (5.42)], one may easily reproduce Eq. (5.19). The same argument used in the calculation of Eqs. (5.43)-(5.45) may be used to calculate the approximate expression of the viscous rate γ_{b} :

$$\begin{aligned} \gamma_{\text{b}} &\approx 1.02 \times 10^{-5} \left(\frac{\alpha}{0.01} \right) \left(\frac{0.1}{h} \right)^2 \left(\frac{2a_{\text{b}}}{r_{\text{in}}} \right)^4 \\ &\quad \times \left(\frac{4\mu_{\text{b}}}{M_{\text{b}}} \right)^2 \left(\frac{M_{\text{b}}}{2M_{\odot}} \right)^{1/2} \left(\frac{100 \text{ AU}}{r_{\text{out}}} \right)^{3/2} \left(\frac{2\pi}{\text{yr}} \right). \end{aligned} \quad (5.48)$$

We choose to normalize γ_{b} by $\alpha = 0.01$; real protoplanetary disks may have α in the range $10^{-1} - 10^{-5}$ [Rafikov, 2017]. Since

$$\frac{d\hat{\mathbf{l}}_{\text{d}}}{dt} = \frac{1}{L_{\text{d}}} \left(\frac{d\mathbf{L}_{\text{d}}}{dt} - \frac{dL_{\text{d}}}{dt} \hat{\mathbf{l}}_{\text{d}} \right), \quad (5.49)$$

the viscous dissipation from disk twisting effects the evolution of $\hat{\mathbf{l}}_{\text{d}}$ according to

$$\left(\frac{d\hat{\mathbf{l}}_{\text{d}}}{dt} \right)_{\text{visc}} = \gamma_{\text{b}} \Lambda [(1 - e_{\text{b}}^2)(\hat{\mathbf{l}}_{\text{d}} \cdot \hat{\mathbf{l}}_{\text{b}}) \hat{\mathbf{l}}_{\text{d}} \times (\hat{\mathbf{l}}_{\text{b}} \times \hat{\mathbf{l}}_{\text{d}})]$$

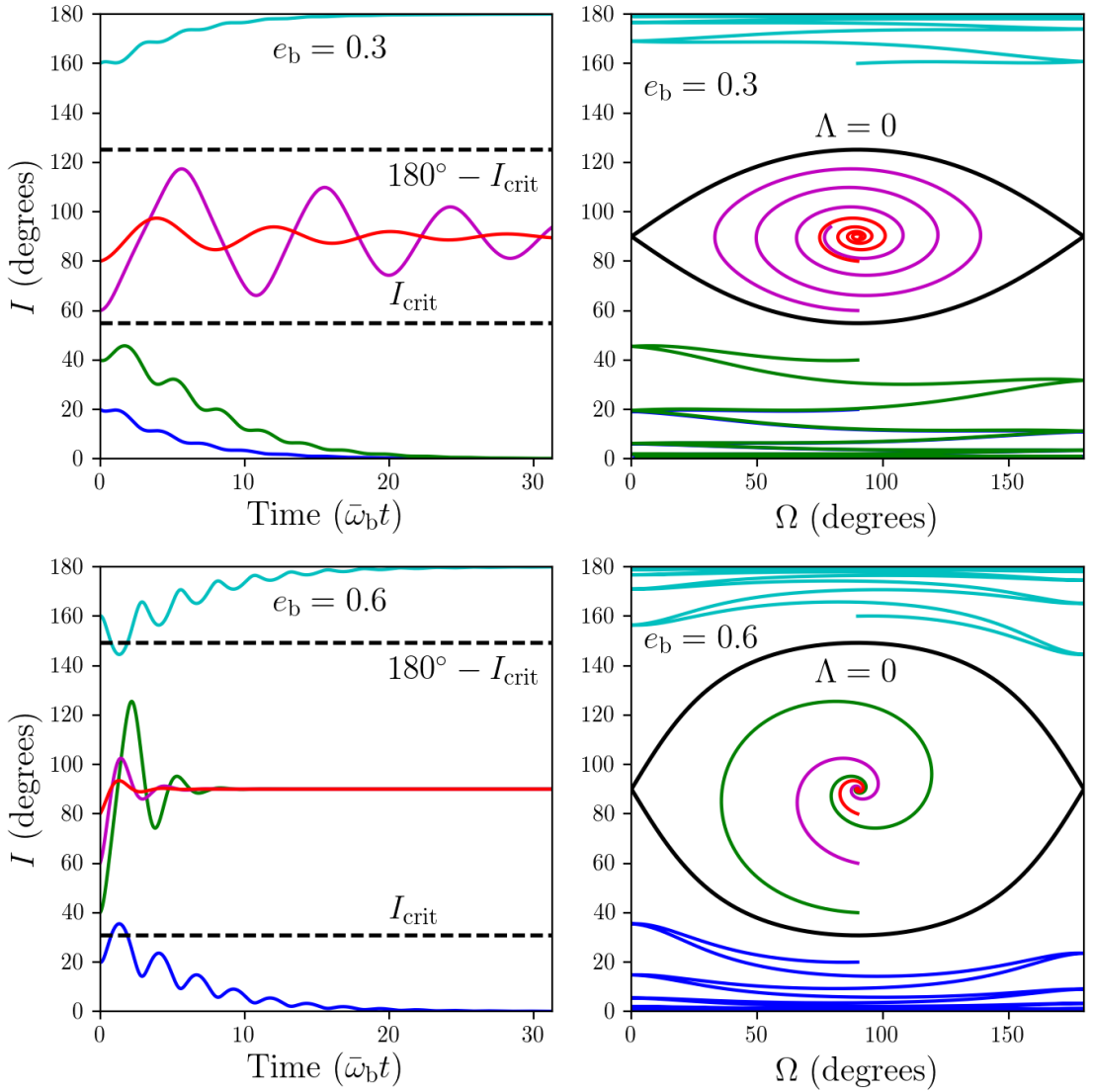


Figure 5.5: Time evolution of the disk orientation for two binary eccentricities e_b as indicated. **Left Panels:** Disk inclination I (the angle between \hat{l}_d and \hat{l}_b) as a function of time. The black dashed lines mark I_{crit} (55° for $e_b = 0.3$ and 31° for $e_b = 0.6$) and $180^\circ - I_{\text{crit}}$. **Right Panels:** Disk trajectories on the $I - \Omega$ plane (where Ω is the longitude of the ascending node of the disk). The black solid curves mark the $\Lambda = 0$ separatrix. Initial values are $I(0) = 20^\circ$ (blue), $I(0) = 40^\circ$ (green), $I(0) = 60^\circ$ (magenta), $I(0) = 80^\circ$ (red), and $I(0) = 160^\circ$ (cyan), with $\Omega(0) = 90^\circ$ for all trajectories. The other parameters are $M_b = 2 M_\odot$, $\mu_b = 0.5 M_\odot$, $a_b = 1 \text{ AU}$, $r_{\text{in}} = 2 \text{ AU}$, $r_{\text{out}} = 100 \text{ AU}$, $\alpha = 0.01$, and $h = 0.1$.

$$- 5(\hat{\mathbf{l}}_d \cdot \mathbf{e}_b) \hat{\mathbf{l}}_d \times (\mathbf{e}_b \times \hat{\mathbf{l}}_d)], \quad (5.50)$$

where Λ is given by Eq. (5.4), except we replace $\hat{\mathbf{l}}$ by $\hat{\mathbf{l}}_d$:

$$\Lambda = (1 - e_b^2)(\hat{\mathbf{l}}_d \cdot \hat{\mathbf{l}}_b)^2 - 5(\hat{\mathbf{l}}_d \cdot \mathbf{e}_b)^2. \quad (5.51)$$

Equation (5.50) is the main result of our technical calculation. We see

$$\frac{d}{dt}(\hat{\mathbf{l}}_b \cdot \hat{\mathbf{l}}_d) \Big|_{\text{visc}} = \gamma_b \Lambda (\hat{\mathbf{l}}_d \cdot \hat{\mathbf{l}}_b)[(1 - e_b^2) - \Lambda], \quad (5.52)$$

$$\frac{d}{dt}(\mathbf{e}_b \cdot \hat{\mathbf{l}}_d) \Big|_{\text{visc}} = -\gamma_b \Lambda (\hat{\mathbf{l}}_d \cdot \mathbf{e}_b)[\Lambda + 5e_b^2], \quad (5.53)$$

Because $-5e_b^2 < \Lambda < (1 - e_b^2)$ [Eq. (5.51)], Equations (5.52)-(5.53) show the system has two different end-states depending on the initial value for Λ :

1. $\Lambda > 0$: The viscous torque (5.50) pushes $\hat{\mathbf{l}}_d$ towards $\hat{\mathbf{l}}_b$. The final state of $\hat{\mathbf{l}}_d$ is alignment (if $\hat{\mathbf{l}}_b \cdot \hat{\mathbf{l}}_d > 0$ initially) or anti-alignment (if $\hat{\mathbf{l}}_b \cdot \hat{\mathbf{l}}_d < 0$ initially) with $\hat{\mathbf{l}}_b$.
2. $\Lambda < 0$: The viscous torque (5.50) pushes $\hat{\mathbf{l}}_d$ towards \mathbf{e}_b . The final state of $\hat{\mathbf{l}}_d$ is alignment (or anti-alignment) with \mathbf{e}_b .

Figure 5.5 shows several examples of the results for the evolution of disk orientation, obtained by integrating the time evolution of $\hat{\mathbf{l}}_d$, including gravitational [Eq. (5.27)] and viscous [Eq. (5.50)] torques. On the left panels, we plot the disk inclination I with time, for the binary eccentricities indicated. We choose the initial $\Omega(0) = 90^\circ$ for all cases, so that $I < I_{\text{crit}}$ ($I > I_{\text{crit}}$) corresponds exactly to $\Lambda > 0$ ($\Lambda < 0$) (see Eqs. (5.4) and (5.8)). Thus we expect $I \rightarrow 0^\circ$ when $I < I_{\text{crit}}$, $I \rightarrow 90^\circ$ when $I_{\text{crit}} < I < 180^\circ - I_{\text{crit}}$, and $I \rightarrow 180^\circ$ when $I > 180^\circ - I_{\text{crit}}$. On the right panels of Figure 5.5, we plot the disk trajectories on the $I - \Omega$ plane [Eq. (5.6) with $\hat{\mathbf{l}} \rightarrow \hat{\mathbf{l}}_d$]. Again, we see when $I < I_{\text{crit}}$ ($\Lambda > 0$), $\hat{\mathbf{l}}_d$ aligns with $\hat{\mathbf{l}}_b$, while when $I > I_{\text{crit}}$ ($\Lambda < 0$), $\hat{\mathbf{l}}_d$ aligns with \mathbf{e}_b , as expected.

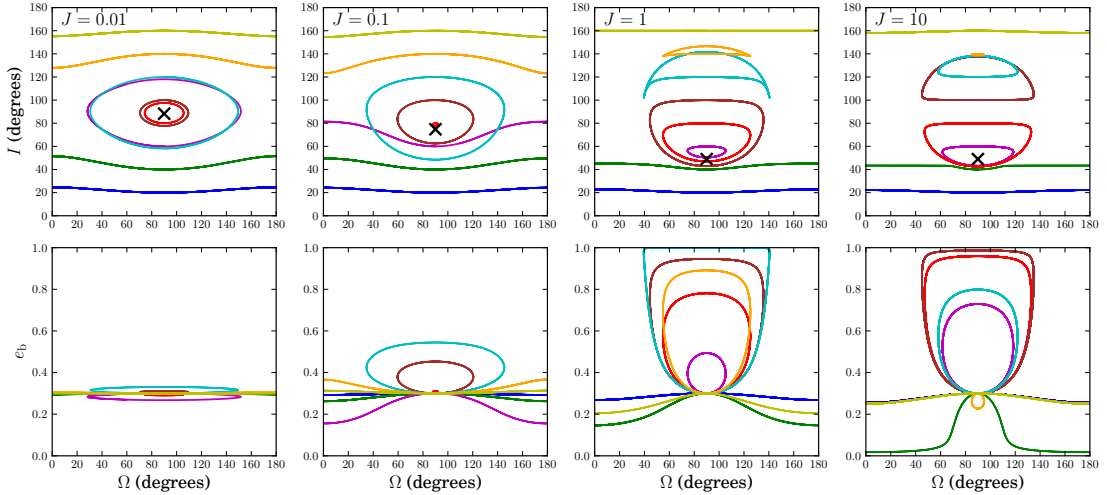


Figure 5.6: Trajectories in the $I - \Omega$ (top panels) and $e_b - \Omega$ (bottom panels) planes for the J values indicated, with fixed points $(I, \Omega) = (I_{fp}, 90^\circ)$ computed with Eq. (5.64) marked with black x's. Initial values for the trajectories are $I(0) = 20^\circ$ (blue), $I(0) = 40^\circ$ (green), $I(0) = 60^\circ$ (magenta), $I(0) = 80^\circ$ (red), $I(0) = 100^\circ$ (brown), $I(0) = 120^\circ$ (cyan), $I(0) = 140^\circ$ (orange), and $I(0) = 160^\circ$ (yellow), with $\Omega(0) = 90^\circ$ and $e_b(0) = 0.3$ for all trajectories.

5.4 Secular Dynamics with Massive Inclined Outer Body

Sections 5.2-5.3 neglected the circumbinary disk's angular momentum, a valid assumption as long as $L_d \ll L_b$ [Eq. (5.13)]. When $L_d \gtrsim L_b$, the non-zero disk angular momentum will change the locations of the fixed points of the system, and hence may effect its dynamical evolution over viscous timescales.

Consider the setup of Section 5.2, except we now include the outer body's mass m and angular momentum $\mathbf{L} = m\sqrt{GM_b r}\hat{\mathbf{l}}$. The evolution equations for $\hat{\mathbf{l}}$, $\mathbf{j}_b = \sqrt{1 - e_b^2}\hat{\mathbf{j}}_b$, and \mathbf{e}_b are [Liu, Muñoz, & Lai 2015; Eqs. (17)-(19)]

$$\frac{d\hat{\mathbf{l}}}{dt} = -\omega_b [(j_b \cdot \hat{\mathbf{l}}) j_b \times \hat{\mathbf{l}} - 5(e_b \cdot \hat{\mathbf{l}}) e_b \times \hat{\mathbf{l}}], \quad (5.54)$$

$$\frac{d\mathbf{j}_b}{dt} = J\omega_b [(j_b \cdot \hat{\mathbf{l}}) j_b \times \hat{\mathbf{l}} - 5(e_b \cdot \hat{\mathbf{l}}) e_b \times \hat{\mathbf{l}}], \quad (5.55)$$

$$\frac{d\mathbf{e}_b}{dt} = J\omega_b [(j_b \cdot \hat{\mathbf{l}}) e_b \times \hat{\mathbf{l}} + 2\mathbf{j}_b \times \mathbf{e}_b - 5(e_b \cdot \hat{\mathbf{l}}) j_b \times \hat{\mathbf{l}}], \quad (5.56)$$

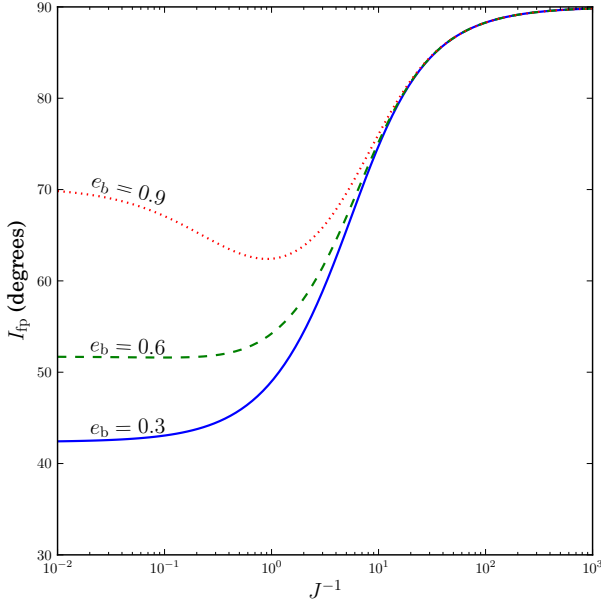


Figure 5.7: Inclination I_{fp} as a function of J^{-1} , computed with Eq. (5.64) with $\Omega = \pi/2$. The binary eccentricity $e_b = e_b(0)$ takes values as indicated.

where

$$J = \frac{L}{L_b / \sqrt{1 - e_b^2}} = \frac{\mu}{\mu_b} \left(\frac{M_b + m}{M_b} \right)^{1/2} \left(\frac{r}{a_b} \right)^{1/2}, \quad (5.57)$$

$$\omega_b = \frac{3}{4} \left(\frac{m}{\mu} \right) \left(\frac{\mu_b}{M_b} \right) \left(\frac{M_b}{M_b + m} \right)^{1/2} \left(\frac{a_b}{r} \right)^{7/2} \sqrt{\frac{GM_b}{a_b^3}}, \quad (5.58)$$

and $\mu = mM_b/(m + M_b)$. Equation (5.58) reduces to Eq. (5.2) when $m \rightarrow 0$. The conservations of total quadrupole potential energy [see Eq. (5.5)] and total angular momentum yield two constants of motion (e.g. Liu, Muñoz, & Lai 2015, Anderson, Lai, & Storch 2017)

$$\Psi = 1 - 6e_b^2 - 3(1 - e_b^2) \cos^2 I + 15e_b^2 \sin^2 I \sin^2 \Omega, \quad (5.59)$$

$$K = \sqrt{1 - e_b^2} \cos I - \frac{e_b^2}{2J}. \quad (5.60)$$

For a given K , one may solve Eq. (5.60) to get $e_b^2 = e_b^2(I)$. Assuming $0 \leq I \leq \pi/2$

and requiring $0 \leq e_b < 1$, we obtain

$$e_b^2 = 2J^2 \left[\cos I \sqrt{\left(\frac{2K}{J} + \frac{1}{J^2} \right) + \cos^2 I} - \left(\frac{K}{J} + \cos^2 I \right) \right]. \quad (5.61)$$

Equation (5.59) then gives $\Psi = \Psi(I, \Omega)$. When $J \sim K^{-1} \ll 1$, Eq. (5.61) reduces to

$$e_b^2 \simeq -2KJ = \text{constant}, \quad (5.62)$$

while when $J \gg 1$, Eq. (5.61) becomes

$$e_b^2 \simeq 1 - \frac{K^2}{\cos^2 I}. \quad (5.63)$$

The fixed points of the system in the $I - \Omega$ plane are determined by

$$\frac{\partial \Psi}{\partial I} = \frac{\partial \Psi}{\partial \Omega} = 0. \quad (5.64)$$

The condition $\partial \Psi / \partial \Omega = 0$ gives $\Omega = \pi/2$ and $\Omega = 3\pi/2$, as before (see Sec. 5.2). For arbitrary J , one must numerically solve $\partial \Psi / \partial I|_{\Omega=\pi/2,3\pi/2} = 0$ to calculate the fixed points $I = I_{fp} > 0$ ($I = 0$ is always a fixed point of the system). However, when $J \ll 1$, one may show analytically that (as found in Sec. 5.2)

$$I_{fp} \simeq \pi/2, \quad (5.65)$$

while when $J \gg 1$,

$$I_{fp} \simeq \cos^{-1} \sqrt{\frac{3(1 - e_b^2)}{5}}, \quad (5.66)$$

where $e_b^2 = e_b^2(0)$. Notice I_{fp} is the Lidov-Kozai critical inclination when $J \gg 1$ and $e_b(0) = 0$ [Lidov, 1962, Kozai, 1962].

Figure 5.6 plots trajectories of the system in the $I - \Omega$ and $e_b - \Omega$ planes. When $J \ll 1$, the system's dynamics reduce to that discussed in Section 5.2, with $I_{fp} \simeq 90^\circ$ (black x's), $e_b \simeq e_b(0)$, and trajectories above and below $I = 90^\circ$ are symmetric. As J increases in magnitude, I_{fp} decreases, e_b begins to oscillate, and the

inclination symmetry above and below $I = 90^\circ$ is lost. Although different trajectories may cross in the $I - \Omega$ plane, each still has a unique Ψ value [Eq. (5.59)], since the binary's e_b value differs from Eq. (5.61) when $I > \pi/2$. When $J \gg 1$, the system's dynamics approaches the classic Lidov-Kozai regime [Lidov, 1962, Kozai, 1962]. The fixed point I_{fp} of the system approaches Eq. (5.66), with e_b reaching large values when $I(0) > I_{fp}$, and with trajectories symmetric above and below $I = 90^\circ$.

Figure 5.7 plots I_{fp} as a function of J^{-1} , computed for $\Omega = \pi/2$ with the $e_b = e_b(0)$ values as indicated. The two limiting cases given by Eqs. (5.65) and (5.66) are achieved when $J \ll 1$ and $J \gg 1$, respectively, and I_{fp} generally varies non-monotonically with increasing J . Since e_b should evolve in time under the influence of viscous dissipation from disk warping, one cannot determine the final value of I_{fp} the system may evolve into starting from initial $I(0)$ and $e_b(0)$ values without a detailed calculation similar to Section 5.3. Nevertheless, Figures 5.6 and 5.7 show there exist highly inclined fixed points for any value of J . For $J \lesssim 0.1$, the system may evolve into near polar alignment, with I_{fp} somewhat less than 90° .

5.5 Torque on Binary and Effect of Accretion

In the previous sections, we have studied the evolution of the disk around a binary with fixed $\hat{\mathbf{l}}_b$ and \mathbf{e}_b . Here we study the back-reaction torque on the binary from the disk. First consider a circular binary. The viscous back reaction torque on the binary from the disk is [Eq. (5.46)]

$$\left(\frac{d\mathbf{L}_b}{dt} \right)_{visc} = - \left(\frac{d\mathbf{L}_d}{dt} \right)_{visc}$$

$$= -L_d \gamma_b (\hat{l}_d \cdot \hat{l}_b)^2 \hat{l}_b \times (\hat{l}_b \times \hat{l}_d). \quad (5.67)$$

In addition, accretion onto the binary from the disk adds angular momentum to the binary's orbit:

$$\left(\frac{dL_b}{dt} \right)_{\text{acc}} \simeq \lambda \dot{M} \sqrt{GM_b r_{\text{in}}} \hat{l}_d. \quad (5.68)$$

Here, \dot{M} is the mass accretion rate onto the binary, $\lambda \sim 1$ (e.g. Miranda, Muñoz, & Lai 2017), and we have assumed $\hat{l}(r_{\text{in}}, t) \simeq \hat{l}_d(t)$ (see below). The torques (5.67) and (5.68) are equivalent to those considered in Foucart & Lai [2013], except we give different power-law prescriptions for $\Sigma = \Sigma(r)$ and $H = H(r)$. For disks in steady state, we have

$$\dot{M} \simeq 3\pi\alpha h^2 \Sigma_{\text{in}} r_{\text{in}}^2 n(r_{\text{in}}), \quad (5.69)$$

Using Eqs. (5.46) (with $e_b = 0$), (5.67) and (5.68), we obtain the net disk-binary alignment timescale for small angle between \hat{l}_d and \hat{l}_b :

$$t_{\text{align}} = \gamma_b^{-1} \left[1 + (1 + \eta) \frac{L_d}{L_b} \right]^{-1}, \quad (5.70)$$

where

$$\begin{aligned} \eta &\equiv \frac{\lambda \dot{M} \sqrt{GM_b r_{\text{in}}}}{L_d \gamma_b} \\ &\approx 0.031 \lambda \left(\frac{h}{0.1} \right)^4 \left(\frac{r_{\text{in}}}{2a_b} \right)^4 \left(\frac{M_b}{4\mu_b} \right)^2 \end{aligned} \quad (5.71)$$

measures the strength of the accretion torque to the viscous torque on the binary ($\eta/\lambda = f^{-1}$, $\lambda = g$ in the notation of Foucart & Lai 2013).

Since $\hat{l}(r_{\text{in}}, t) \neq \hat{l}(r_{\text{out}}, t)$, the disk angular momentum loss through accretion causes \hat{l}_d to change with time:

$$\left(\frac{d\hat{l}_d}{dt} \right)_{\text{acc}} \sim -\frac{\lambda \dot{M} \sqrt{GM_b r_{\text{in}}}}{L_d} \{ \hat{l}(r_{\text{in}}, t) - \hat{l}_d [\hat{l}_d \cdot \hat{l}(r_{\text{in}}, t)] \}. \quad (5.72)$$

Because the magnitude of the tilt of $\hat{l}(r_{\text{in}}, t)$ from \hat{l}_d is of order

$$[\hat{l}(r_{\text{in}}, t) - \hat{l}_d] \sim -\frac{\partial \hat{l}}{\partial \ln r} \Big|_{\text{warp}}, \quad (5.73)$$

we find

$$\left(\frac{d\hat{\mathbf{l}}_d}{dt}\right)_{acc} \sim -\frac{4\lambda\dot{M}\sqrt{GM_b r_{in}}}{c_s^2 L_d} \left(\frac{\kappa^2 - n^2}{2n^2}\right) \hat{\mathbf{l}}_d \times \mathbf{T}_{db}. \quad (5.74)$$

Detailed calculation shows that the accretion torque (5.74) is always much less than the viscous torque (5.19) on the disk. We relegate the calculation and discussion of the accretion torque (5.74) to the Appendix.

For eccentric binaries, the back-reaction torque from the disk is $d\mathbf{L}_b/dt = -d\mathbf{L}_d/dt$ [Eq. (5.46)]. But this is not sufficient for determining the evolution of \mathbf{e}_b and $\hat{\mathbf{l}}_b$. In addition, how accretion affects the binary eccentricity is also uncertain (e.g. Rafikov 2016, Miranda, Muñoz, & Lai 2017). Nevertheless, as long as $L_b \gtrsim L_d$, the timescale for the disk-binary inclination evolution should be of order γ_b^{-1} , with an estimate given by Eq. (5.48).

5.6 Discussion

5.6.1 Theoretical Uncertainties

Our theoretical analysis of disks around binaries assumes a linear disk warp. However, we find that at the inner disk region, $|\partial\hat{\mathbf{l}}/\partial\ln r|$ reaches ~ 0.1 for a wide range of binary and disk parameters. Inclusion of weakly non-linear warps in Equations (5.22)-(5.23) may introduce new features in the disk warp profile [Ogilvie, 2006]. In addition, disk warps of this magnitude may interact resonantly with inertial waves in the disk, leading to a parametric instability which may excite turbulence in the disk [Gammie, Goodman, & Ogilvie, 2000, Ogilvie & Latter, 2013]. An investigation of these effects is outside the scope of this

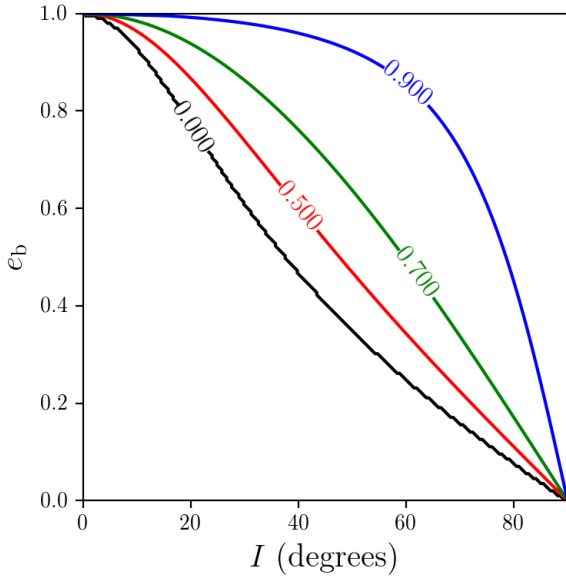


Figure 5.8: Contour plot of the probability of polar alignment P_{polar} [Eq. (5.76)] as a function of disk inclination I and binary eccentricity e_b . Contours of constant P_{polar} are labeled as indicated. The $P_{\text{polar}} = 0$ line (black) traces out I_{crit} [Eq. (5.8)], while the $P_{\text{polar}} = 0.5$ line (red) traces out I_{polar} [Eq. (5.78)].

paper, but their inclusion is unlikely to change the direction of disk-binary inclination evolution (alignment vs polar alignment).

5.6.2 Observational Implications

In Section 5.3.4, we showed that the viscous torque associated with disk twist/warp tends to drive the circumbinary disk axis \hat{l}_d toward $\pm \hat{l}_b$ (alignment or anti-alignment) when $\Lambda > 0$, and toward $\pm e_b$ (polar alignment) when $\Lambda < 0$. Note that $I_{\text{crit}} < I < 180^\circ - I_{\text{crit}}$ is a necessary, but not sufficient condition for polar alignment of the disk [Eq. (5.8)]. An extreme example is when $\Omega = 0^\circ$, since $\Lambda \geq 0$ for all inclinations I . Because the circumbinary disk probably formed in a turbulent molecular cloud, the disk is unlikely to have a preferred Ω when it

forms. The condition for polar alignment ($\Lambda < 0$) requires Ω to satisfy

$$\sin^2 \Omega > \left(\frac{1 - e_b^2}{5e_b^2} \right) \frac{1}{\tan^2 I} = \frac{\tan^2 I_{\text{crit}}}{\tan^2 I}. \quad (5.75)$$

Assuming a uniform distribution of Ω -values from 0 to 2π , the probability of the disk to polar align is (for given I, e_b)

$$P_{\text{polar}}(I, e_b) = 1 - 2\Omega_{\min}/\pi. \quad (5.76)$$

where

$$\Omega_{\min}(I, e_b) = \begin{cases} \pi/2 & |\sin I| \leq |\sin I_{\text{crit}}| \\ \sin^{-1} \left(\frac{\tan I_{\text{crit}}}{|\tan I|} \right) & \text{otherwise} \end{cases} \quad (5.77)$$

We define the inclination I_{polar} through $P_{\text{polar}}(I_{\text{polar}}, e_b) = 0.5$. Solving for I_{polar} , we obtain

$$I_{\text{polar}} = \tan^{-1} \sqrt{2(1 - e_b^2)/5e_b^2} \quad (5.78)$$

In Figure 5.8, we plot contours of constant P_{polar} in the $I - e_b$ space. The $P_{\text{polar}} = 0$ curve (black) traces out I_{crit} [Eq. (5.8)], while the $P_{\text{polar}} = 0.5$ curve (red) traces out I_{polar} [Eq. (5.78)]. When $I < I_{\text{crit}}$, alignment of \hat{l} with \hat{l}_b is inevitable. When $I > I_{\text{polar}}$, alignment of \hat{l} with e_b is probable.

Table 5.1 lists a number of circumbinary systems with highly eccentric binaries. With the exception of 99 Herculis, all the binaries listed have disks coplanar with the binary orbital plane within a few degrees. We also list I_{crit} [Eq. (5.8)] and I_{polar} [Eq. (5.78)] for these systems. We do not list the binaries KH 15D [Winn et al., 2004, Chiang & Murray-Clay, 2004, Capelo et al., 2012] and HD 142527B [Marino et al., 2015, Casassus et al., 2015, Lacour et al., 2016] since the orbital elements of these binaries are not well constrained. However, both binaries ap-

Binary	e_b	I_{crit}	I_{polar}
99 Herculis	0.77	20°	28°
α CrB	0.37	48°	58°
β Tri	0.43	43°	53°
DQ Tau	0.57	33°	42°
AK Sco	0.47	40°	50°
HD 98800 B	0.78	20°	27°

Table 5.1: Binary eccentricities e_b , with their inclinations I_{crit} [Eq. (5.8)] and I_{polar} [Eq. (5.78)], for the selected eccentric binaries with circumbinary disks. With the exception of the debris disk around 99 Herculis, all binaries have circumbinary disks aligned with the binary orbital plane within a few degrees. Binary eccentricities are from Kennedy et al. [2012a] (99 Herculis), Tomkin & Popper [1986] (α CrB), Pourbaix [2000] (β Tri), Czekala et al. [2016] (DQ Tau), Alencar et al. [2003] (AK Sco), and Boden et al. [2005] (HD 98800 B)

pear to have significant eccentricities [Chiang & Murray-Clay, 2004, Lacour et al., 2016].

Since planets form in gaseous circumbinary disks, planets may form with orbital planes perpendicular to the binary orbital plane if the binary is sufficiently eccentric. Such planets may be detectable in transit surveys of eclipsing binaries due to nodal precession of the planet’s orbit.

The twist and warp calculated in Section 5.3.3 is non-negligible. Further observations of (gaseous) circumbinary disks may be able to detect such warps [Juhász & Facchini, 2017], further constraining the orientation and dynamics of circumbinary disk systems.

5.7 Summary

Using semi-analytic theory, we have studied the warp and long-term evolution of circumbinary disks around eccentric binaries. Our main results and conclu-

sions are listed below.

1. For protoplanetary disks with dimensionless thickness H/r larger than the viscosity parameter α , bending wave propagation effectively couples different regions of the disk, making it precess as a quasi-rigid body. Without viscous dissipation from disk warping, the dynamics of such a disk is similar to that of a test particle around an eccentric binary (Secs. 5.2 and 5.3.2).
2. When the binary is eccentric and the disk is significantly inclined, the disk warp profile exhibits new features not seen in previous works. The disk twist [Eq. (5.34)] and warp [Eq. (5.35)] have additional contributions due to additional torques on the disk when the binary is eccentric.
3. Including the dissipative torque from warping, the disk may evolve to one of two states, depending on the initial sign of Λ [Eq. (5.4)] (Sec. 5.3.4). When Λ is initially positive, the disk angular momentum vector aligns (or anti-aligns) with the binary orbital angular momentum vector. When Λ is initially negative, the disk angular momentum vector aligns with the binary eccentricity vector (polar alignment). Note that Λ depends on both I (the disk-binary inclination) and Ω (the longitude of ascending node of the disk). Thus for a given e_b , the direction of inclination evolution depends not only on the initial $I(0)$, but also on the initial $\Omega(0)$.
4. When the disk has a non-negligible angular momentum compared to the binary, the systems fixed points are modified (Sec. 5.4). The disk may then evolve to a state of near polar alignment, with the inclination somewhat less than 90° .
5. The timescale of evolution of the disk-binary inclination angle [see Eqs. (5.52)-(5.53)] depends on various disk parameters [see Eq. (5.48)], but

is in general less than a few Myrs. This suggests that highly inclined disks and planets may exist around eccentric binaries.

Acknowledgments

JZ thanks Stephen Lubow, Rebbecca Martin, and Gongjie Li for useful conversations. We thank the anonymous referee for their comments which improved the quality of this paper. This work has been supported in part by NASA grants NNX14AG94G and NNX14AP31G, and a Simons Fellowship from the Simons Foundation. JZ is supported by a NASA Earth and Space Sciences Fellowship in Astrophysics.

Appendix: Accretion Torques

If the inner disk is not coplanar with the outer disk, accretion will change the disk angular momentum vector over time. We parameterize this accretion torque according to

$$\left(\frac{d\hat{\mathbf{L}}_d}{dt} \right)_{acc} = -\lambda \dot{M} \sqrt{GM_b r_{in}} \hat{\mathbf{l}}(r_{in}, t), \quad (5.79)$$

where \dot{M} is the accretion rate onto the binary, and $\lambda \sim 1$ parameterizes the angular momentum loss from the disk to the binary. The time evolution of \mathbf{G} , as well as the pericenter precession induced by the non-Keplarian angular frequency, warps the inner edge of the disk in the direction of the binary orbital plane [$(\mathbf{l}_1)_{warp}$; Eq. (5.35)]. Inserting $\hat{\mathbf{l}}(r, t) = \hat{\mathbf{l}}_d + (\mathbf{l}_1)_{warp}$ in equation (5.79), we obtain

$$\left(\frac{d\hat{\mathbf{L}}_d}{dt} \right)_{acc} = \gamma_a \tilde{\omega}_b \tau_b(r_{in}) \Lambda \left[(1 - e_b^2) (\hat{\mathbf{l}}_d \cdot \hat{\mathbf{l}}_b) \hat{\mathbf{l}}_d \times (\hat{\mathbf{l}}_b \times \hat{\mathbf{l}}_d) \right]$$

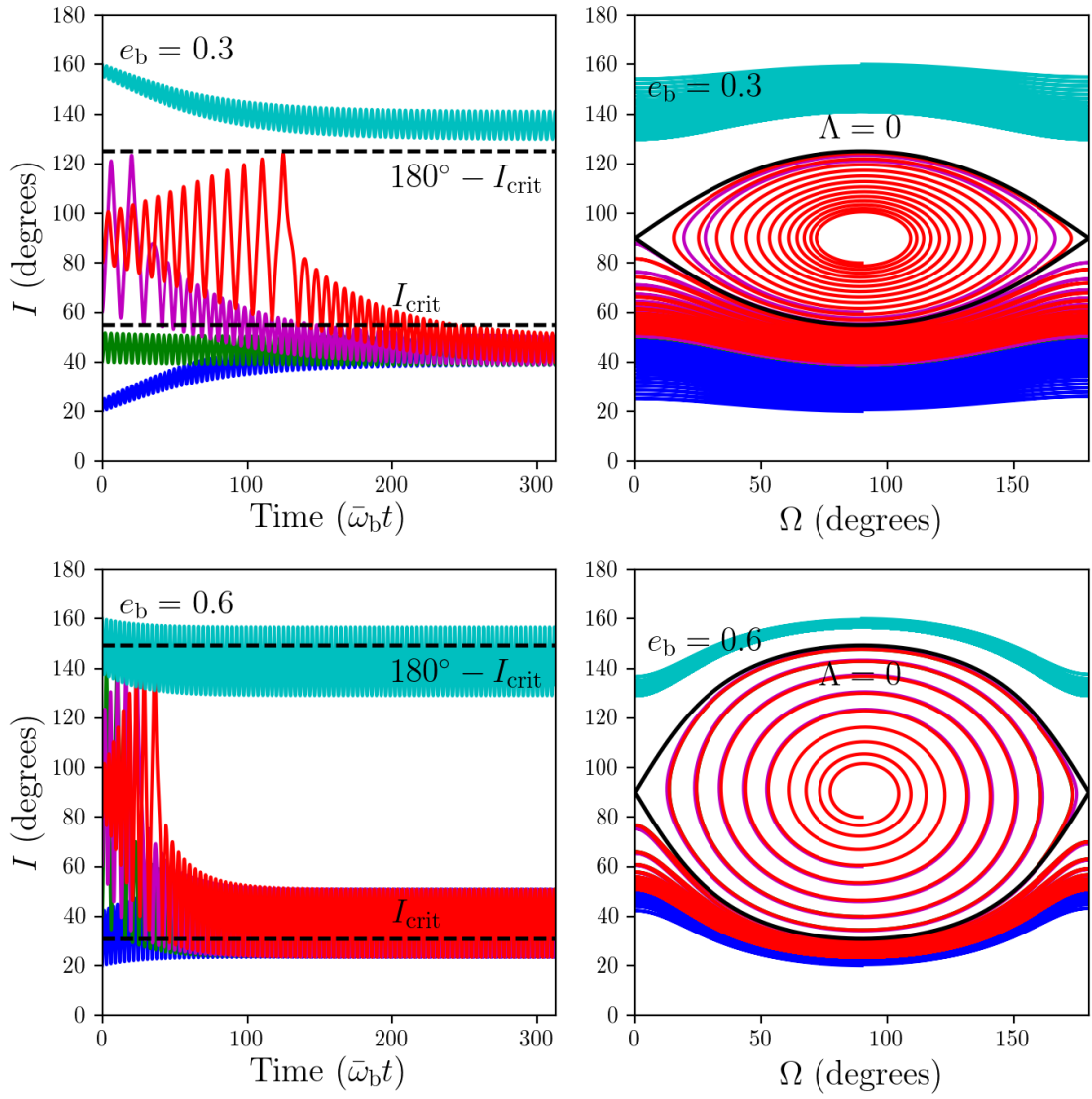


Figure 5.9: Same as Fig. 5.5, except we neglect the disk's viscous torque [Eq. (5.50)], and include the disk's accretion torque [Eq. (5.80)]. All parameter values are the same, except $\alpha = 0.2$, $h = 0.3$, and $\lambda = 1$.

$$\begin{aligned}
& - 5(\hat{\mathbf{l}}_d \cdot \mathbf{e}_b) \hat{\mathbf{l}}_d \times (\mathbf{e}_b \times \hat{\mathbf{l}}_d) \\
& + \gamma_a W_{bb}(r_{in}) f_b \left[(1 - e_b^2) (\hat{\mathbf{l}}_d \cdot \hat{\mathbf{l}}_b) \hat{\mathbf{l}}_d \times (\hat{\mathbf{l}}_b \times \hat{\mathbf{l}}_d) \right. \\
& \quad \left. - 5(\hat{\mathbf{l}}_d \cdot \mathbf{e}_b) \hat{\mathbf{l}}_d \times (\mathbf{e}_b \times \hat{\mathbf{l}}_d) \right], \tag{5.80}
\end{aligned}$$

where

$$\begin{aligned}
\gamma_a &= \frac{\lambda \dot{M} \sqrt{GM_b r_{in}}}{L_d} \simeq \frac{9}{4} \lambda a h^2 n(r_{out}) \\
&= 3.18 \times 10^{-7} \lambda \left(\frac{\alpha}{0.01} \right) \left(\frac{h}{0.1} \right)^2 \\
&\times \left(\frac{M_b}{2 M_\odot} \right)^{1/2} \left(\frac{100 \text{ AU}}{r_{out}} \right)^{3/2} \left(\frac{2\pi}{\text{yr}} \right), \tag{5.81}
\end{aligned}$$

We have assumed the disk to be in a steady state, so

$$\dot{M} \simeq 3\pi\alpha h^2 \Sigma_{in} \sqrt{GM_b r_{in}}. \tag{5.82}$$

Equation (5.80) agrees with the rough magnitude and direction of the accretion torque estimated in Equation (5.74).

Since

$$\begin{aligned}
\frac{d}{dt} (\hat{\mathbf{l}}_d \cdot \hat{\mathbf{l}}_b) \Big|_{acc} &= \gamma_a \tilde{\omega}_b \tau_b(r_{in}) \Lambda [(1 - e_b^2) - \Lambda] \\
&+ \gamma_a W_{bb}(r_{in}) f_b [(1 - e_b^2) - \Lambda] \tag{5.83}
\end{aligned}$$

$$\begin{aligned}
\frac{d}{dt} (\hat{\mathbf{l}}_d \cdot \mathbf{e}_b) \Big|_{acc} &= -\gamma_a \tilde{\omega}_b \tau_b(r_{in}) \Lambda [\Lambda + 5e_b^2] \\
&- \gamma_a W_{bb}(r_{in}) f_b [\Lambda + 5e_b^2], \tag{5.84}
\end{aligned}$$

the radial functions $\tau_b(r_{in}), W_{bb}(r_{in}) < 0$, and $f_b \sim \Lambda$, Eqs. (5.83)-(5.84) drives the disk one of two ways depending on the rough value of Λ :

1. $\Lambda \gtrsim 0$: The accretion torque (5.80) pushes $\hat{\mathbf{l}}_d$ away from $\hat{\mathbf{l}}_b$.
2. $\Lambda \lesssim 0$: The accretion torque (5.80) pushes $\hat{\mathbf{l}}_d$ away from \mathbf{e}_b .

From Eq. (5.27), it may be shown that there are no fixed points near the $\Lambda = 0$ separatrix. Therefore, the accretion torque drives the disk to a trajectory near the $\Lambda = 0$ separatrix.

Figure 5.9 plots the examples considered in Figure 5.2 with accretion torques [Eq. (5.80)]. We take h and α to be significantly higher than our canonical values of $\alpha = 0.01$ and $h = 0.1$ so that accretion torques effect the dynamical evolution of the circumbinary disk [Eq. (5.81)]. In the left panels of Figure 5.9, we plot the disk inclination with time, for the binary eccentricities indicated. The trajectories which start at $I(0) = 20^\circ, 40^\circ$, and 80° all evolve toward the prograde separatrix, which nutates around $I \sim 50^\circ$ when $e_b = 0.3$, and $I \sim 40^\circ$ when $e_b = 0.6$. The trajectories which start at $I(0) = 60^\circ$ both evolve to the retrograde separatrix, which nutates around $I \sim 130^\circ$ when $e_b = 0.3$, and $I \sim 140^\circ$ when $e_b = 0.6$. On the right panels, we plot the disk trajectories on the $I - \Omega$ plane, for the binary eccentricities indicated. All disk trajectories evolve toward the $\Lambda \approx 0$ separatrix.

The relative strength of the viscous to the accretion torques from disk warping is given by the ratio

$$\frac{|\gamma_b|}{|\gamma_a W_{bb}(r_{in})|} \approx 300\lambda^{-1} \left(\frac{0.1}{h}\right)^2. \quad (5.85)$$

As long as $|\gamma_b| \gg |\gamma_a W_{bb}(r_{in})|$, the viscous torque dominates, and \hat{l}_d aligns with either \hat{l}_b or e_b , depending on the sign of Λ (Sec. 5.3.4). When $|\gamma_b| \lesssim |\gamma_a W_{bb}(r_{in})|$, the accretion torques may dominate, and \hat{l}_d may be driven to the separatrix $\Lambda \approx 0$.

Figure 5.10 is identical to Figure 5.5, except we include viscous [Eq. (5.50)] and accretion [Eq. (5.80)] torques with $\alpha = 0.01$, $h = 0.1$, and $\lambda = 1$. Because $|\gamma_b| \gg |W_{bb}(r_{in})\gamma_a|$, the viscous torque dominates the disk's dynamics. As a result, Figure 5.10 is almost indistinguishable from Figure 5.5. Only for unrealistically

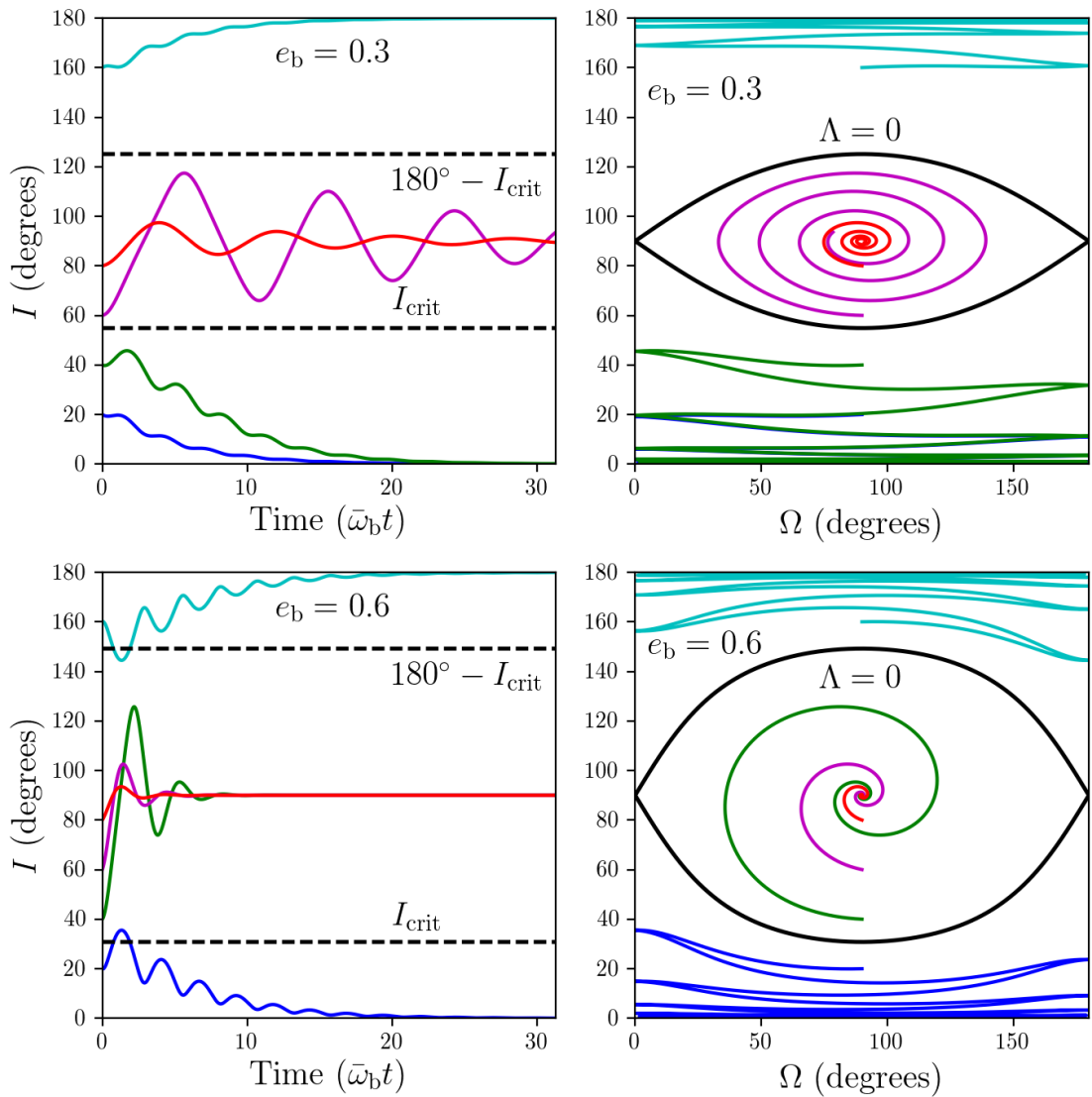


Figure 5.10: Same as Figure 5.5, except we include the disk's accretion torque [Eq. (5.80)]. All parameter values are the same, with $\lambda = 1$.

hot protoplanetary disks with $h \gtrsim 0.5$ may accretion torques significantly effect the disk evolution over viscous timescales.

CHAPTER 6

EXTENDED TRANSITING DISKS AND RINGS AROUND PLANETS AND BROWN DWARFS: THEORETICAL CONSTRAINTS

The age is nearing when direct observations of circumplanetary disks and rings become a reality through photometry. A number of studies have investigated the detectability and observational signatures of circumplanetary disks/rings [Barnes & Fortney, 2004, Ohta et al., 2009, Schlichting & Chang, 2011, Tusnski & Valio, 2011, Zuluaga et al., 2015]. Although observational searches for exo-rings have been carried out, most are inconclusive [Brown et al., 2001, Heising et al., 2015, Santos et al., 2015]. These searches focused on hot Jupiters, which have Hill radii $r_H \equiv a(M_p/3M_\star)^{1/3}$ (where a is the planetary semi-major axis, M_p is the planet mass, and M_\star is the mass of the host star) comparable to their planetary radii R_p . For this reason, these circumplanetary disks could not have outer radii r_{out} significantly larger than their respective planetary radii.

Mamajek et al. [2012] discovered that the light curve of a young (~ 16 Myr) K5 star 1 SWASP J140747-354542 (hereafter J1407) exhibited a complex series of eclipses that lasted 56 days around the month of April 2007. The central deep (> 3 mag) eclipse was surrounded by two pairs of 1 mag eclipses occurring at ± 12 and ± 26 days. They proposed that these eclipses were caused by a large ring system orbiting an unseen companion J1407b (see also van Werkhoven et al. 2014). Other explanations were considered but deemed unlikely. Follow-up observations by Kenworthy et al. [2015] constrain the companion mass to $< 80 M_J$ (where M_J is the mass of Jupiter) and semi-major axis (for circular orbits) to $a \simeq 2.2 - 5.6$ AU (3σ significance). Thus, J1407b is most likely a giant

planet or brown dwarf in a 3.5-14 year orbit around the primary star. Modeling the eclipse light curve with a series of inclined, circular optically thick rings gave a best fit outer disk radius of ~ 0.6 AU, a significant fraction of the companion's Hill radius [van Werkhoven et al., 2014, Kenworthy & Mamajek, 2015]. The disk/ring system also contains gaps, which may be cleared by exomoons orbiting around J1407b.

Currently, the ring/disk interpretation of the J1407 light curve remains uncertain, although no serious alternatives have been explored in detail. The ring/disk interpretation can be tested in the coming years if another eclipse event is detected, while a non-detection would put the model under increasing strain. In any case, the possible existence of such a ring system naturally raises questions about the formation of inclined, extended disks/rings around giant planets and brown dwarfs. In order to produce a transiting signature, the disk/ring must be inclined with respect to the orbital plane. How are such inclinations produced and maintained?

For giant planets, the inclination of the disk/ring may be tied to the obliquity of the planet due to its rotation-induced quadrupole. The obliquity may be excited through secular spin-orbit resonances, as in the case of Saturn [Hamilton & Ward, 2004, Ward & Hamilton, 2004, Vokrouhlický & Nesvorný, 2015], or through impacts with planetesimals of sufficiently large masses [Lissauer & Safronov, 1991]. In the case of brown dwarfs, which are thought to form independently of the primary, the disk could be "primordially" misaligned with respect to the binary orbit because of the turbulent motion of gas in the star forming environment [Bate, 2009, Bate et al., 2010, Tokuda et al., 2014].

In this paper, we will address the following question: Under what condi-

tions can an extended disk/ring around a planet or brown dwarf maintain its inclination with respect to the planet’s orbit in order to exhibit a transit signature? As discussed in Section 2, even when the disk is safely confined within the planet’s Hill sphere, the outer region of the disk can still suffer significant tidal torque from the host star. This tidal torque tends to induce differential precession of the disk. Without any internal forces, the disk will lose coherence in shape and inclination. In the presence of dissipation, the disk may reach a equilibrium warp profile (called “Laplace surface”) in which the outer region of the disk [beyond the Laplace radius; see Eq. (6.3) below] becomes aligned with the orbital plane.

In gaseous disks, hydrodynamic forces work to keep the disk coherent, through bending waves [Ivanov & Illarionov, 1997, Papaloizou & Lin, 1995, Lubow & Ogilvie, 2000] or viscosity [Papaloizou & Pringle, 1983, Ogilvie, 1999]. But the rapid variability in the photometric data for the inferred ring system around J1407b implies that the disk/ring system is quite thin, with a ratio of the scaleheight to radius of order $H/r \sim 10^{-3}$ [van Werkhoven et al., 2014], with significant gaps in the disk [Mamajek et al., 2012, Kenworthy & Mamajek, 2015].

It is unlikely that hydrodynamical forces are sufficiently strong to maintain the disk’s coherence (see Section 5.2).

Another plausible internal torque is self-gravity (e.g., Ward 1981; Touma et al. 2009; Ulubay-Siddiki et al 2009). This is the possibility we will focus on in this paper. Of particular relevance is the work by Ward (1981), who studied the warping of a massive self-gravitating disk in an attempt to explain the inclination of Iapetus, Saturn’s moon, with respect to the local Laplace surface. He found that self-gravity of the circumplanetary disk which formed Saturn’s

satellites could significantly modify the equilibrium inclination/warp profile.

In this paper, we re-examine the warp dynamics of self-gravitating circumplanetary disks in light of the possible detection extended transiting disks. We consider general (possibly large) planetary obliquities, and study both equilibrium disk warp and its time evolution. Our goal is to derive the conditions (in terms of disk mass and density profile) under which an extended circumplanetary disk/ring maintain its inclination with respect to the planet’s orbit. In Section 6.2, we study the equilibrium inclination/warp profile of the disk, which we will call the *Generalized Laplace Surface*, under the influences of torques from the oblate planet, the distant host star, and disk self-gravity. We show that if the disk is sufficiently massive, the outer region of the disk can maintain significant inclination relative to the planet’s orbit. In Section 4, we study the time evolution of disk warp, including the stability of the generalized Laplace surfaces, and the condition required for the disk to be capable of precessing coherently. We summarize our results and discuss their implications in Section 6.4

Although it is unknown if the object J1407b is a planet or brown dwarf, we will refer to J1407b as a “planet” throughout the rest of the paper.

6.1 External Torques and the Laplace Surface

Consider a planet (mass M_p) in a circular orbit around a central star (mass M_*) with orbital semi-major axis a . We denote the unit orbital angular momentum vector by \hat{l}_p . We take the circumplanetary disk to extend from radius $r = r_{\text{in}}$ to $r = r_{\text{out}}$, as measured from the center of the planet. We assume that the disk is circular. In general, the angular momentum unit vector at each annulus of the

disk is a function of radius and time, and is specified by $\hat{\mathbf{l}} = \hat{\mathbf{l}}(r, t)$.

The circumplanetary disk experiences two external torques, from the host star and from the planet's quadrupole. Averaging over the orbit of the planet, to leading order in the ratio r/a , the tidal torque per unit mass from the star exerted on a disk annulus with unit angular momentum $\hat{\mathbf{l}}$ is

$$\mathbf{T}_* = \frac{3GM_\star r^2}{4a^3} (\hat{\mathbf{l}} \cdot \hat{\mathbf{l}}_p) (\hat{\mathbf{l}} \times \hat{\mathbf{l}}_p). \quad (6.1)$$

The quadrupole moment of the planet is related to its J_2 parameter by $I_3 - I_1 = J_2 M_p R_p^2$, where R_p is the radius of the planet, and J_2 depends on the planet's rotation rate Ω_p via $J_2 = (k_2/3)(\Omega_p^2 R_p^3 / GM_p)$. The Love number k_2 is of order 0.4 for giant planets. The torque from the spinning planet on the disk annulus is

$$\mathbf{T}_{sp} = \frac{3GM_p R_p^2 J_2}{2r^3} (\hat{\mathbf{l}} \cdot \hat{\mathbf{s}}) (\hat{\mathbf{l}} \times \hat{\mathbf{s}}), \quad (6.2)$$

where $\hat{\mathbf{s}}$ is the unit vector along the planet's spin axis.

In general, when $\hat{\mathbf{l}}$, $\hat{\mathbf{l}}_p$, and $\hat{\mathbf{s}}$ are not parallel to each other, $|\mathbf{T}_*|$ dominates at large r while $|\mathbf{T}_{sp}|$ dominates at small r . The radius where $|\mathbf{T}_*| \sim |\mathbf{T}_{sp}|$ defines the Laplace radius

$$r_L \equiv \left(2J_2 \frac{M_p}{M_\star} R_p^2 a^3 \right)^{1/5} = \left(6J_2 R_p^2 r_H^3 \right)^{1/5}, \quad (6.3)$$

where $r_H \equiv a(M_p/3M_\star)^{1/3}$ is the Hill radius [Tremaine et al., 2009]. Tidal truncation and dynamical stability require that the outer radius of the disk be less than a fraction of r_H , i.e. $\xi \equiv r_{out}/r_H \lesssim 0.4$ (e.g. Quillen & Trilling 1998, Ayliffe & Bate 2009a, Martin & Lubow 2011, Lehébel & Tiscareno 2015). Thus the ratio of r_L to r_{out} is given by

$$\begin{aligned} \frac{r_L}{r_{out}} &= \left(\frac{6J_2 R_p^2}{\xi^3 r_{out}^2} \right)^{1/5} \\ &= 0.18 \left(\frac{J_2}{10^{-2}} \right)^{1/5} \left(\frac{r_{out}}{0.2r_H} \right)^{-3/5} \end{aligned}$$

$$\times \left(\frac{R_p}{R_{\text{Jup}}} \right)^{2/5} \left(\frac{r_{\text{out}}}{0.1 \text{ AU}} \right)^{-2/5}. \quad (6.4)$$

where we have scaled J_2 to the value appropriate to gas giants in our Solar System, and r_{out} appropriate to the claimed ring system in J1407 [van Werkhoven et al., 2014].

In the presence of dissipation in the disk, we may expect $\hat{l}(r, t)$ to evolve toward the equilibrium state, in which

$$\mathbf{T}_* + \mathbf{T}_{\text{sp}} = 0. \quad (6.5)$$

The equilibrium orientation of the disk $\hat{l}(r)$, which defines the Laplace surface [Laplace , 1805, Tremaine et al., 2009], lies in the plane spanned by the vectors \hat{s} and \hat{l}_p . Throughout this paper, we assume that the planet's spin angular momentum is much larger than the disk angular momentum, so that \hat{s} is fixed in time. Let β_p be the planetary obliquity (the angle between \hat{s} and \hat{l}_p) and $\beta(r)$ be the warp angle of the disk [the angle between $\hat{l}(r)$ and \hat{l}_p]. Equation (6.5) may be reduced to

$$0 = z^2 \cos \beta(z) \sin \beta(z) + \frac{z_L^5}{z^3} \cos [\beta(z) - \beta_p] \sin [\beta(z) - \beta_p], \quad (6.6)$$

where we have defined the dimensionless Laplace radius z_L and radial coordinate z by

$$z_L \equiv r_L / r_{\text{out}}, \quad z \equiv r / r_{\text{out}}. \quad (6.7)$$

Figure 6.1 depicts the solutions to Eq. (6.6) for $\beta_p = 30^\circ, 60^\circ$ and $z_L = 0.2, 0.5$. Clearly, in the absence of any internal torque, the outer region of the disk (beyond $\sim 2r_L$) is highly aligned with the planetary orbit, with

$$\beta(r) \simeq \left(\frac{r_L}{r} \right)^5 \cos \beta_p \sin \beta_p. \quad (6.8)$$

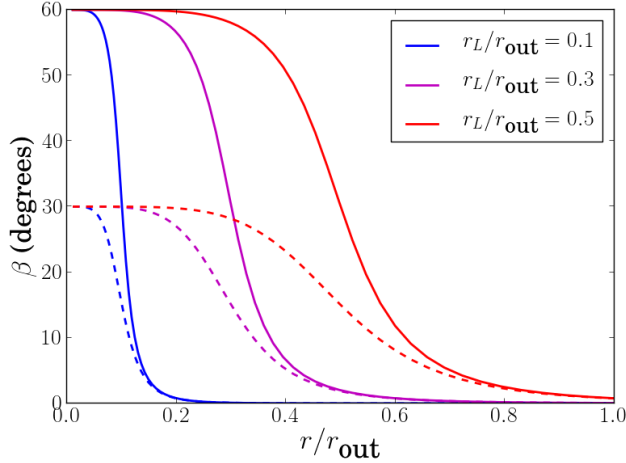


Figure 6.1: Equilibrium disk inclination profile (Laplace surface without self-gravity). The quantity β is the angle between \hat{l} and \hat{l}_p . The different lines are for $r_L/r_{\text{out}} = 0.1$ (blue), 0.3 (magenta) and 0.5 (red). The planetary obliquity β_p is assumed to be 60° (solid lines) and 30° (dotted lines).

Such an aligned outer disk would not produce the transit signal claimed in the J1407 system. To maintain significant inclination in the outer disk, some internal torques are needed. We consider the effect of self-gravity in the next section.

6.2 Generalized Laplace Surface: Equilibrium with Self-Gravity

In this section, we consider the influence of self-gravity on the equilibrium warp profile $\hat{l}(r)$ of the disk. Let the surface density of the disk be $\Sigma = \Sigma(r)$. The torque acting on the disk due to its own self-gravity is approximately given by

$$\begin{aligned} \mathbf{T}_{\text{sg}} \simeq \frac{\pi G}{2} \int_{r_{\text{in}}}^{r_{\text{out}}} dr' \frac{r' \Sigma(r')}{\max(r, r')} \chi b_{3/2}^{(1)}(\chi) \\ \times [\hat{l}(r) \cdot \hat{l}(r')] [\hat{l}(r) \times \hat{l}(r')], \end{aligned} \quad (6.9)$$

where $\chi = \min(r, r') / \max(r, r')$ and $b_{3/2}^{(1)}(\chi)$ is the Laplace coefficient

$$b_{3/2}^{(1)}(\chi) = \frac{2}{\pi} \int_0^\pi \frac{\cos \theta d\theta}{(1 - 2\chi \cos \theta + \chi^2)^{3/2}}. \quad (6.10)$$

Eq. (6.9) is an approximation which recovers two limits: When $|\hat{l}(r) \times \hat{l}(r')| \ll 1$, it reduces to Eq. (8) of Tremaine [1991] and Eq. (47) of Tremaine & Davis [2014]; when $\chi \ll 1$, $b_{3/2}^{(1)}(\chi) \simeq 3\chi$ [Murray & Dermott, 1999] and we recover the quadrupole approximation:

$$\begin{aligned} \mathbf{T}_{\text{sg}} \simeq \frac{3\pi G}{2} \int_{r_{\text{in}}}^{r_{\text{out}}} dr' \frac{r' \Sigma(r')}{\max(r, r')} \chi^2 \\ \times [\hat{l}(r) \cdot \hat{l}(r')] [\hat{l}(r) \times \hat{l}(r')]. \end{aligned} \quad (6.11)$$

The integrand of Eq. (6.9) becomes invalid when $\chi \sim 1$ and $|\hat{l}(r) \times \hat{l}(r')| \sim 1$ (i.e., when two close-by annuli have a large mutual inclination), and a different formalism is needed to calculate the torque acting on a disk from its own self-gravity (e.g. Kuijken 1991, Arnaboldi & Sparke 1994, Ulubay-Siddiki et al. 2009). In the appendix, we review the exact equations for calculating internal self-gravity torques for arbitrary χ and $|\hat{l}(r) \times \hat{l}(r')|$. Our numerical calculations based on these exact (but much more complicated) equations show that they provide only minor quantitative corrections to the disk warp profile and the inclination at the outer disk radius. For this reason, we will use the much simpler approximation (6.9) for the remainder of this paper.

For concreteness, we consider a power-law surface density profile

$$\Sigma(r) = \Sigma_{\text{out}} \left(\frac{r_{\text{out}}}{r} \right)^p. \quad (6.12)$$

Then the disk mass is (assuming $r_{\text{in}} \ll r_{\text{out}}$)

$$M_{\text{d}} \simeq \frac{2\pi}{2-p} \Sigma_{\text{out}} r_{\text{out}}^2, \quad (6.13)$$

and the total disk angular momentum is

$$L_d \simeq \frac{4\pi}{5-2p} \Sigma_{\text{out}} r_{\text{out}}^2 \sqrt{GM_p r_{\text{out}}}. \quad (6.14)$$

It is useful to compare the magnitude of $|\mathbf{T}_{\text{sg}}|$ to the external torques acting on the disk (see Fig. 6.2). Ignoring geometrical factors relating to the angles between $\hat{\mathbf{l}}$, $\hat{\mathbf{l}}_p$ and $\hat{\mathbf{s}}$, we have to an order of magnitude [see Eqs. (6.9), (6.1), and (6.2)]

$$|\mathbf{T}_{\text{sg}}| \sim \pi G \Sigma(r) r \quad (6.15)$$

$$|\mathbf{T}_*| \sim \frac{3GM_*r^2}{4a^3} \quad (6.16)$$

$$|\mathbf{T}_{\text{sp}}| \sim \frac{3GM_p R_p^2 J_2}{2r^3}. \quad (6.17)$$

Thus

$$\frac{|\mathbf{T}_{\text{sg}}|}{|\mathbf{T}_*|} \sim \frac{2(2-p)}{3} \sigma \left(\frac{r_{\text{out}}}{r} \right)^{1+p} \equiv \left(\frac{r_*}{r} \right)^{1+p}, \quad (6.18)$$

$$\frac{|\mathbf{T}_{\text{sg}}|}{|\mathbf{T}_{\text{sp}}|} \sim \frac{2(2-p)}{3} \frac{\sigma}{z_L^5} \left(\frac{r}{r_{\text{out}}} \right)^{4-p} \equiv \left(\frac{r}{r_{\text{sp}}} \right)^{4-p}, \quad (6.19)$$

where we have defined the dimensionless parameter σ (which measures $|\mathbf{T}_{\text{sg}}|/|\mathbf{T}_*|$ at $r = r_{\text{out}}$) as

$$\sigma \equiv \frac{M_d}{M_*} \left(\frac{a}{r_{\text{out}}} \right)^3 = 0.38 \left(\frac{r_{\text{out}}}{0.2 r_H} \right)^{-3} \left(\frac{M_d}{10^{-3} M_p} \right). \quad (6.20)$$

In Eqs. (6.18) and (6.19), r_* and r_{sp} are set by $|\mathbf{T}_{\text{sg}}|/|\mathbf{T}_*| \sim 1$ and $|\mathbf{T}_{\text{sg}}|/|\mathbf{T}_{\text{sp}}| \sim 1$ respectively. Recall the Laplace radius r_L is set by $|\mathbf{T}_*| \sim |\mathbf{T}_{\text{sp}}|$. For radii $r \lesssim r_{\text{sp}}$, \mathbf{T}_{sp} dominates and the disk annuli tend to be aligned with the planetary spin axis. For $r \gtrsim r_*$, \mathbf{T}_* dominates and the disk tends to be aligned with the planet's orbit. For $r_{\text{sp}} \lesssim r \lesssim r_*$, \mathbf{T}_{sg} dominates and self-gravity strongly influences the disk warp profile.

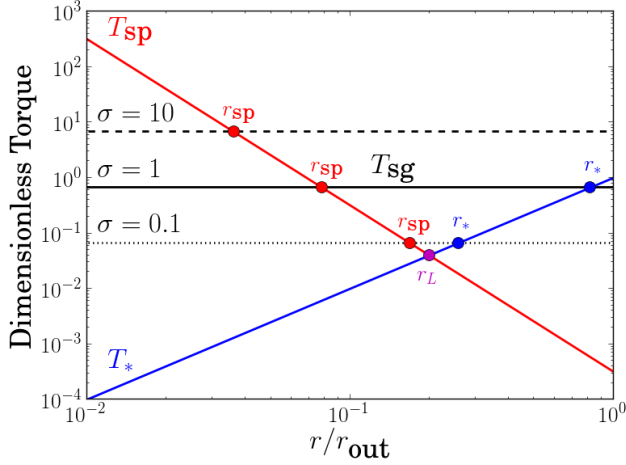


Figure 6.2: Torques on the disk based on the estimates (6.15)-(6.17) and normalized by $|T_*(r_{\text{out}})|$. The tidal torque from the star (T_*) is in blue, and the torque from the spinning planet (T_{sp}) is in red. The torque from self-gravity (T_{sg}) is in black, with three values of σ [see Eq. (6.20)] as indicated, all for $p = 1$ [see Eq. (6.12)]. The three critical radii in the disk (r_{sp}, r_L, r_*) are marked.

The equilibrium disk warp profile $\hat{l}(r)$ including the effect of self-gravity is determined by the equation

$$T_* + T_{\text{sp}} + T_{\text{sg}} = 0. \quad (6.21)$$

With $\hat{l}(r)$ lying in the plane spanned by \hat{l}_p and \hat{s} , this reduces to

$$\begin{aligned} 0 = & z^2 \cos \beta(z) \sin \beta(z) \\ & + \frac{z_L^5}{z^3} \cos [\beta(z) - \beta_p] \sin [\beta(z) - \beta_p] \\ & + \frac{2-p}{3} \sigma \int_{r_{\text{in}}/r_{\text{out}}}^1 dz' \frac{(z')^{1-p}}{\max(z, z')} \chi b_{3/2}^{(1)}(\chi) \\ & \times \cos [\beta(z) - \beta(z')] \sin [\beta(z) - \beta(z')]. \end{aligned} \quad (6.22)$$

Figure 6.3 depicts a sample of the equilibrium disk inclination profile $\beta(r)$ for $r_L/r_{\text{out}} = 0.2, 0.5$ and $p = 1, 1.5$, with various values of the disk mass parameter σ . As expected, for sufficiently large σ , self-gravity can significantly increase the outer disk's inclination.

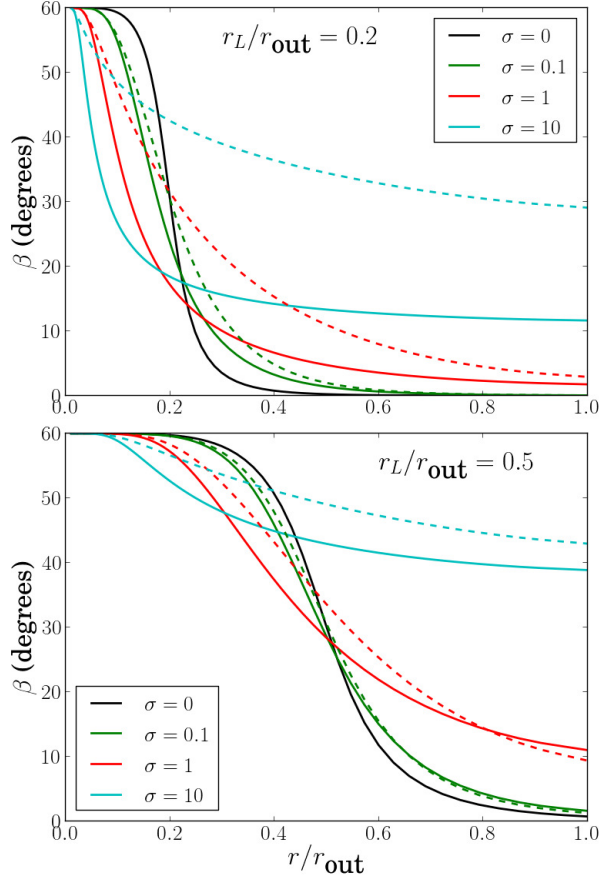


Figure 6.3: Equilibrium disk inclination profile $\beta(r)$ including the effect of self gravity (the generalized Laplace surface), for different values of r_L/r_{out} and σ [see Eq. (6.20)] as indicated. The planetary obliquity is assumed to be $\beta_p = 60^\circ$. The $\sigma = 0$ curves correspond to the standard Laplace surface (without self-gravity). The solid lines are for the surface density power-law index $p = 1$, and dashed lines for $p = 1.5$.

Figure 6.4 shows the outer disk inclination angle $\beta(r_{\text{out}})$ as a function of σ . Decreasing the parameter p or r_L/r_{out} results in a decrease of $\beta(r_{\text{out}})$. This can be understood as follows: The disk inside r_L is roughly aligned with the planet's spin. This inner disk, together with the planet's intrinsic quadrupole, act on the outer disk to resist the tidal torque from the host star and generate $\beta(r_{\text{out}})$. Reducing p leads to a smaller effective quadrupole of the inner disk, and therefore yielding a smaller $\beta(r_{\text{out}})$.

The qualitative behavior of Fig. 6.4 at low σ may be understood analytically. For $\beta(r_{\text{out}}) \ll \beta_p$, we use the approximate solution $\beta(r) \sim \beta_p \Theta[(r/r_{\text{out}}) - (r_L/r_{\text{out}})]$ in the integrand of Eq. (6.22) (Θ is the Heavyside step function). We find, to an order of magnitude,

$$\begin{aligned} \beta(r_{\text{out}}) &\sim \left[\left(\frac{r_L}{r_{\text{out}}} \right)^5 + \left(\frac{2-p}{4-p} \right) \sigma \left(\frac{r_L}{r_{\text{out}}} \right)^{4-p} \right] \\ &\quad \times \cos \beta_p \sin \beta_p. \end{aligned} \quad (6.23)$$

Comparing to Eq. (6.8), the second term in Eq. (6.23) may be understood as the correction to the planet's effective quadrupole due to inner disk's self-gravity. We see that in order to achieve significant $\beta(r_{\text{out}})$, both σ and r_L/r_{out} must be sufficiently large. We note that while Eq. (6.23) captures the correct trend of how $\beta(r_{\text{out}})$ depends on σ , r_L/r_{out} and p , it is necessary to solve Eq. (6.22) to obtain the quantitatively accurate result depicted in Fig. 6.4.

6.3 Time Evolution of Disk Warp

In this Section, we first use numerical integrations to examine the stability property of the generalized Laplace Surfaces obtained in Section 3. We then consider the possibility of coherent precession of warped self-gravitating disks.

6.3.1 Stability of Generalized Laplace Equilibria

In Tremaine et al. [2009], it was found that the solutions to Eq. (6.5) (without disk self-gravity) were unstable when $\beta_p > 90^\circ$. Although in this paper we only consider disk warp profiles with $\beta_p < 90^\circ$, it is not immediately obvious if the

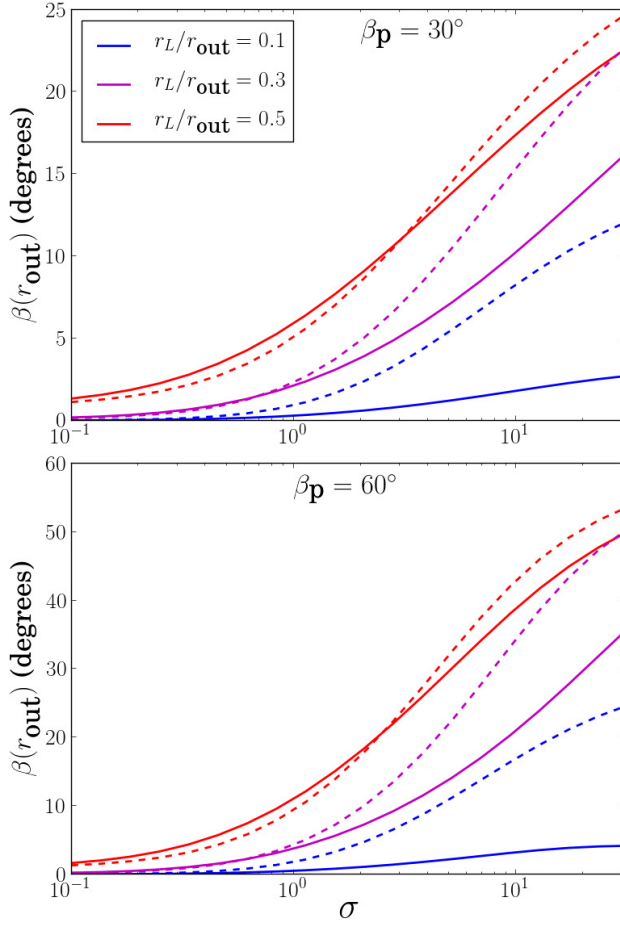


Figure 6.4: Equilibrium inclination of the disk at the outer radius [the angle between $\hat{\mathbf{l}}(r_{\text{out}})$ and $\hat{\mathbf{l}}_p$], as a function of the disk mass parameter σ [see Eq.(6.20)]. The top panel is for the planetary obliquity $\beta_p = 30^\circ$, and the lower panel for $\beta_p = 60^\circ$. Different colored curves correspond to different values of r_L/r_{out} as indicated. The solid lines are for the surface density profile of $p = 1$, while the dashed lines are for $p = 1.5$.

addition of self-gravity changes the stability of the generalized Laplace surfaces obtained by solving Eq. (6.21). A complete analysis of the Laplace equilibria [which we denote by $\hat{\mathbf{l}}_0(r)$] would require one to find the full eigenvalue spectrum of the perturbed equation of motion for $\hat{\mathbf{l}}(r, t)$. We do not carry out such an analysis here. Instead, we use numerical integrations to examine how a small deviation of $\hat{\mathbf{l}}(r, t)$ from $\hat{\mathbf{l}}_0(r)$ evolves in time.

The evolution equation for the disk warp profile $\hat{l}(r, t)$ is

$$r^2 \Omega \frac{\partial \hat{l}}{\partial t} = \mathbf{T}_* + \mathbf{T}_{\text{sp}} + \mathbf{T}_{\text{sg}}, \quad (6.24)$$

where $\Omega(r) = \sqrt{GM_p/r^3}$. The small perturbation $\mathbf{j} \equiv \hat{l}(r, t) - \hat{l}_0(r)$ satisfies

$$r^2 \Omega \frac{\partial \mathbf{j}}{\partial t} = \mathbf{T}_* + \mathbf{T}_{\text{sp}} + \mathbf{T}_{\text{sg}}. \quad (6.25)$$

We consider two independent initial perturbations:

$$\mathbf{j}(r, t = 0) = 0.02 \sin \left[\frac{\pi(r - r_{\text{in}})}{r_{\text{out}} - r_{\text{in}}} \right] \left(\frac{\hat{s} \times \hat{l}_p}{|\hat{s} \times \hat{l}_p|} \right) \quad (6.26)$$

and

$$\mathbf{j}(r, t = 0) = 0.02 \sin \left[\frac{\pi(r - r_{\text{in}})}{r_{\text{out}} - r_{\text{in}}} \right] \left(\frac{\hat{l}_0 \times (\hat{s} \times \hat{l}_p)}{|\hat{l}_0 \times (\hat{s} \times \hat{l}_p)|} \right). \quad (6.27)$$

Equation (6.26) corresponds to a perturbation perpendicular to the plane spanned by the Laplace surface, while Eq. (6.27) corresponds to a slight change in the disk inclination profile $\beta(r)$. We choose the r -dependence in Eqs. (6.26) and (6.27) such that $\mathbf{j} = 0$ at $r = r_{\text{in}}$ and $r = r_{\text{out}}$.

Figure 6.5 shows some examples of our numerical integration results. We define the quantity

$$j_{\max}(t) \equiv \max_{r \in [r_{\text{in}}, r_{\text{out}}]} (|\mathbf{j}(r, t)|), \quad (6.28)$$

and plot j_{\max} for the initial conditions (6.26) and (6.27), with parameters $\beta_p = 30^\circ, 60^\circ$ and $\sigma = 0.1, 10$. We see that j_{\max} is bounded in all cases. We have carried out calculations for other initial conditions and found similar behaviors for j_{\max} . We conclude that the equilibrium profile $\hat{l}_0(r)$ are stable (for $\beta_p < 90^\circ$).

In addition to the inclination instability, it was shown in Tremaine et al. [2009] that the Laplace surface (without self-gravity) is unstable to eccentricity growth when $\beta_p \gtrsim 69^\circ$. This “eccentricity instability” cannot be probed by our analysis, and is beyond the scope of this paper. All examples considered in this paper have planetary obliquities less than this critical angle.

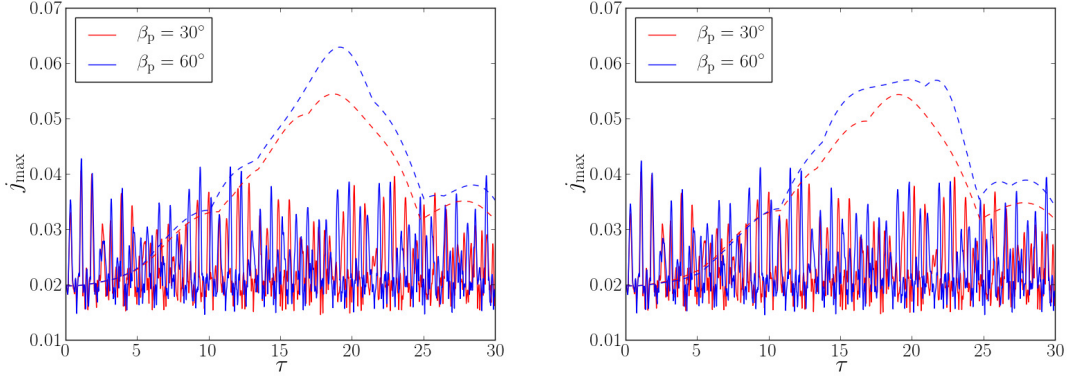


Figure 6.5: Time evolution of the quantity j_{\max} [Eq. (6.28)], with the initial condition given by (6.26) (left panel) and (6.27) (right panel). Solid lines denote $\sigma = 10$, dotted lines denote $\sigma = 0.1$. Values of β_p are as indicated.

6.3.2 Coherent Disk Precession

The generalized Laplace surfaces studied in Section 3 correspond to the disk warp equilibria that may be attained when the disk experiences sufficient internal dissipation. However, we could also imagine situations in which circumplanetary disks are formed with a warp profile that is “out of equilibrium”. It is of interest to consider the time evolution of such “out-of-equilibrium” disks. In particular, we are interested in the following scenario/question: if a disk is formed with a large inclination at r_{out} with respect to the planet’s orbit, under what condition can the disk maintain its coherence and large inclination at r_{out} ?

In general, the disk warp profile $\hat{l}(r, t)$ evolves according to Eq. (6.24). Without self-gravity, the disk will develop large incoherent warps and twists due to strong differential torques, and may eventually break. With sufficient self-gravity, coherent precession of the disk may be possible.

For concreteness, we consider an initially flat disk with \hat{l} aligned with the planet’s spin axis \hat{s} . Both \hat{s} and \hat{l}_p are assumed to be fixed in time, since the

planet's spin and orbital angular momenta are much larger than the disk angular momentum. To determine the evolution of the disk warp profile, we divide the disk into 30 rings spaced logarithmically in radius, with r_i ($i = 1, 2, \dots, 30$) ranging from $5 \times 10^{-2} r_{\text{out}}$ to r_{out} . We then integrate Eq. (6.24) to evolve the orientation of the individual ring $\hat{l}(r_i, t)$.

Figures 6.6 and 6.7 show a sample numerical result, for integration time up to $\tau = t\omega_*(r_{\text{out}}) = 30$, where

$$\omega_*(r_{\text{out}}) = \frac{3GM_\star}{4a^3\Omega(r_{\text{out}})} \quad (6.29)$$

is the (approximate) precession frequency of the outer disk annulus torqued by the central star. The planetary obliquity is fixed at $\beta_p = 40^\circ$, with $p = 1$ and $r_L/r_{\text{out}} = 0.2$. We consider three values of σ : 10, 1 and 0.1. In addition to the disk inclination angle $\beta(r, t)$ [the angle between $\hat{l}(r, t)$ and \hat{l}_p], we also show the disk twist angle $\phi(r, t)$ [the angle between $\hat{l}_p \times \hat{l}(r, t)$ and $\hat{l}_p \times \hat{s}$]. In all three cases, when $r \lesssim r_{\text{sp}}$ the disk annuli remain mostly aligned with the planetary spin, with $\beta \approx \beta_p = 40^\circ$. For the $\sigma = 10$ case, the region of the disk beyond r_{sp} precesses coherently, while for the low-mass case ($\sigma = 0.1$), the disk's self-gravity is not able to enforce coherence, since different disk annuli precess at different rates. This transition of the coherent behavior occurs at $r_\star \sim r_{\text{out}}$, or equivalently $\sigma \sim 1$. From Eq. (6.18) we have

$$\frac{r_\star}{r_{\text{out}}} = \left[\frac{2(2-p)}{3} \sigma \right]^{1/(1+p)}. \quad (6.30)$$

Thus, coherent precession of the outer disk requires $\sigma \gtrsim 1$, or in terms of disk mass,

$$M_d \gtrsim 2.67 \times 10^{-3} M_p \left(\frac{r_{\text{out}}}{0.2 r_H} \right)^3. \quad (6.31)$$

When the disk mass is high ($\sigma \gg 1$), the dynamical behavior is relatively simple. This may be understood with the model put forth in the next section.

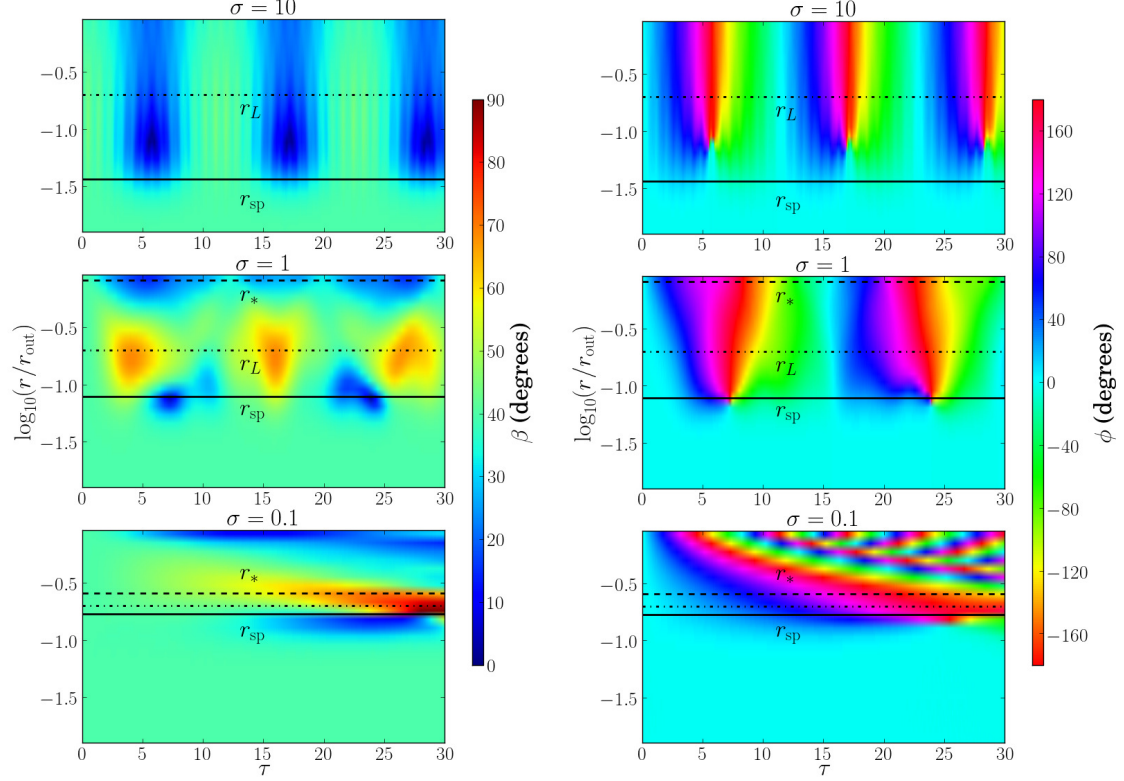


Figure 6.6: Evolution of the disk inclination $\beta(r, t)$ (left panels) and twist angle $\phi(r, t)$ (right panels) for three different disk mass parameters: $\sigma = 10$ (top), $\sigma = 1$ (middle), and $\sigma = 0.1$ (bottom). The dimensionless time is $\tau = t\omega_*(r_{\text{out}})$ [see Eq. (6.29)]. The horizontal lines mark the locations of r_{sp} (solid), r_*/r_{out} (dashed) and r_L (dot-dashed), to indicate where self-gravity and external torques dominate (see Fig. 6.2). The planetary obliquity is $\beta_p = 40^\circ$ and the Laplace radius is $r_L/r_{\text{out}} = 0.2$.

6.3.3 Model for high σ disk

We assume that for radii $r < r_{\text{sp}}$, the disk annuli stay aligned with the oblate planet, while for $r \geq r_{\text{sp}}$ the disk is a rigid plate being torqued externally by the star and the oblate planet [see Eqs. (6.1) and (6.2)]. In other words, we model the disk inclination profile as

$$\hat{\mathbf{l}}(r, t) = \begin{cases} \hat{\mathbf{s}} & r < r_{\text{sp}} \\ \hat{\mathbf{n}}(t) & r \geq r_{\text{sp}} \end{cases}, \quad (6.32)$$

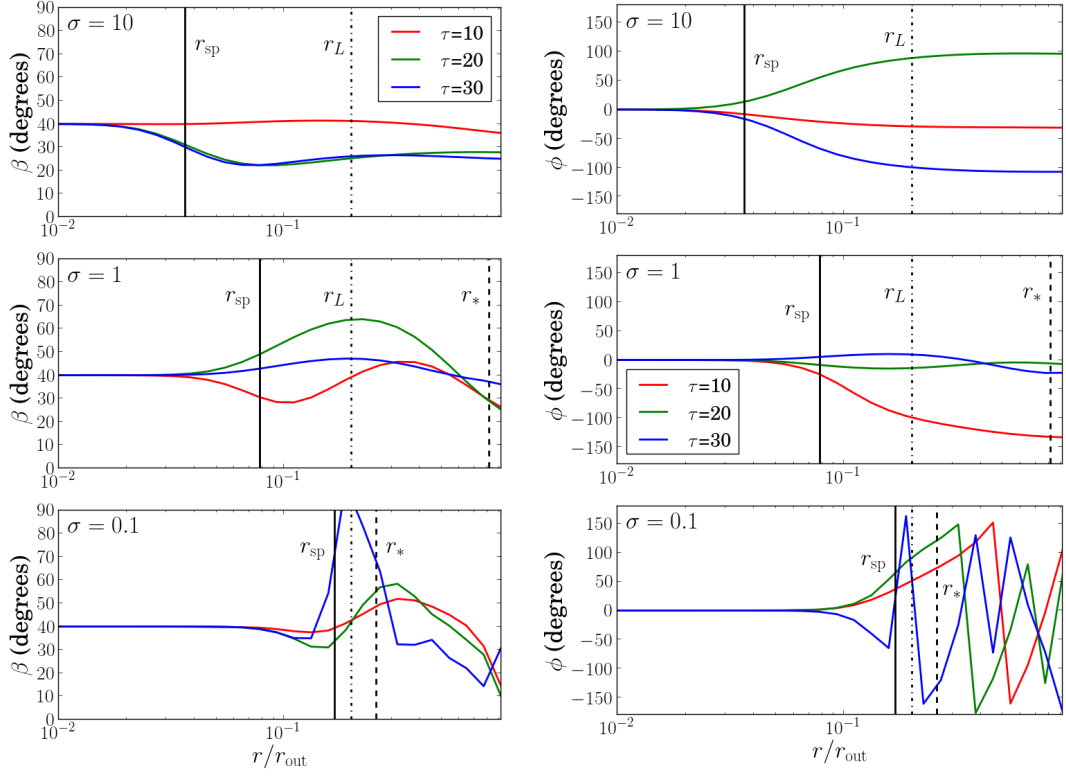


Figure 6.7: Snapshots of the disk inclination profile $\beta(r, t)$ (left) and twist profile $\phi(r, t)$ (right) at $\tau = 10$ (red), $\tau = 20$ (green) and $\tau = 30$ (blue), for the evolution depicted in Fig. 6.6. The vertical lines mark the locations r_{sp} (solid), r_* (dashed) and r_L (dot-dashed), indicating where self-gravity and external torques dominate.

with $\hat{\mathbf{n}}$ evolving in time according to

$$\frac{d\hat{\mathbf{n}}}{dt} = \bar{\omega}_*(\hat{\mathbf{n}} \cdot \hat{\mathbf{l}}_p)(\hat{\mathbf{l}}_p \times \hat{\mathbf{n}}) + (\bar{\omega}_{\text{sp}} + \bar{\omega}_{\text{d,in}})(\hat{\mathbf{n}} \cdot \hat{\mathbf{s}})(\hat{\mathbf{s}} \times \hat{\mathbf{n}}), \quad (6.33)$$

where

$$\bar{\omega}_* = \frac{2\pi}{L_{\text{d,out}}} \int_{r_{\text{sp}}}^{r_{\text{out}}} \Sigma(r) r \left(\frac{3GM_\star r^2}{4a^3} \right) dr, \quad (6.34)$$

$$\bar{\omega}_{\text{sp}} = \frac{2\pi}{L_{\text{d,out}}} \int_{r_{\text{sp}}}^{r_{\text{out}}} \Sigma(r) r \left(\frac{3GM_p R_p^2 J_2}{2r^3} \right) dr, \quad (6.35)$$

$$\bar{\omega}_{\text{d,in}} = \frac{2\pi}{L_{\text{d,out}}} \int_{r_{\text{sp}}}^{r_{\text{out}}} \Sigma(r) r \left(\int_{r_{\text{in}}}^{r_{\text{sp}}} \frac{3\pi G \Sigma(r') (r')^3}{2r^3} dr' \right) dr, \quad (6.36)$$

$$L_{\text{d,out}} = 2\pi \int_{r_{\text{sp}}}^{r_{\text{out}}} \Sigma(r) r^3 \Omega(r) dr. \quad (6.37)$$

and $\omega_*(r_{\text{out}})$ is given by Eq. (6.29). Note that r_{sp} depends on σ [see Eq. (6.19) and Fig. 6.2]. Assuming $r_{\text{in}} \ll r_{\text{sp}} \ll r_{\text{out}}$,

$$\bar{\omega}_* \simeq \omega_*(r_{\text{out}}) \frac{5 - 2p}{2(4 - p)}, \quad (6.38)$$

$$\bar{\omega}_{\text{sp}} \simeq \omega_*(r_{\text{out}}) \frac{5 - 2p}{2(1 + p)} \left(\frac{r_L}{r_{\text{out}}} \right)^5 \left(\frac{r_{\text{out}}}{r_{\text{sp}}} \right)^{1+p}, \quad (6.39)$$

$$\bar{\omega}_{\text{d,in}} \simeq \omega_*(r_{\text{out}}) \frac{(5 - 2p)(2 - p)}{2(4 - p)(1 + p)} \sigma \left(\frac{r_{\text{sp}}}{r_{\text{out}}} \right)^{3-2p}. \quad (6.40)$$

In Fig. 6.8, we show the outer disk inclination β and precession angle ϕ for \hat{n} , with $r_L/r_{\text{out}} = 0.2$ and $p = 1$. The qualitative behavior seen in Figs. 6.6 and 6.7 is reproduced. In particular, for $\sigma = 10$, the outer disk undergoes full precession in ϕ while the inclination β nutates; for $\sigma = 30$, the disk librates in ϕ around 0° , with β varying between 0° and 40° .

In our model, the behavior of ϕ switches from precession to libration at $\sigma \approx 23$.

6.4 Summary and Discussion

6.4.1 Key Results

Motivated by the recent (tentative) observational evidence for the circumplanetary disk/ring system around the young K5 star 1 SWASP J140747-354542 [Mamajek et al., 2012, van Werkhoven et al., 2014, Kenworthy et al., 2015, Kenworthy & Mamajek, 2015], we have presented a general theoretical study of the inclination (warp) profile of extended disks around giant planets (or brown dwarfs). Such a disk experiences torques from the host star and the oblate planet. In the

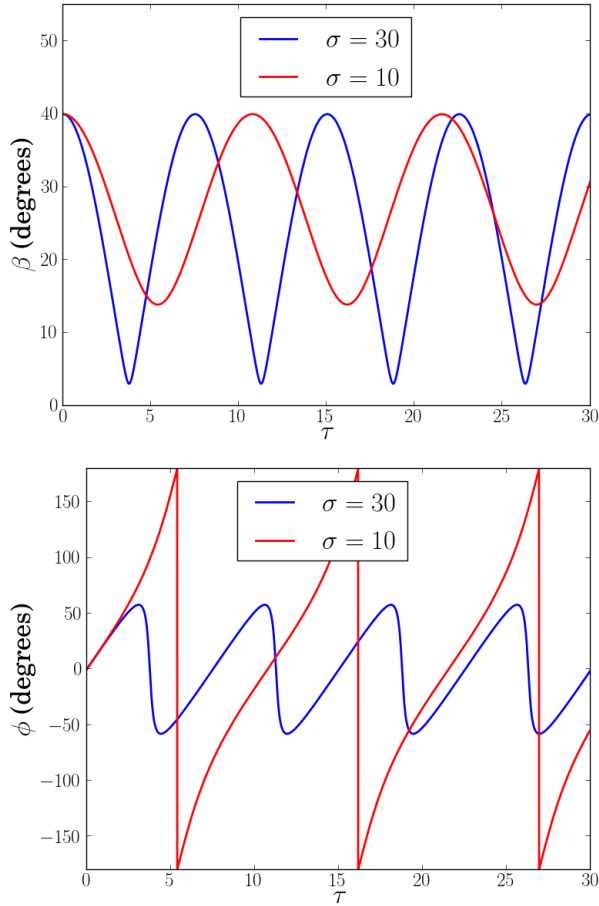


Figure 6.8: Evolution of the (flat) outer disk inclination β and twist angle ϕ for the simple model [see Eqs. (6.32)-(6.33)], with two values for the disk mass parameter σ as indicated. For $\sigma = 30$, the disk normal vector $\hat{\mathbf{n}}$ precesses around the planetary spin vector $\hat{\mathbf{s}}$, with ϕ librating around $\phi = 0^\circ$, while β varies from 0° to 40° . For $\sigma = 10$, the outer disk precesses fully around the planetary orbital angular momentum axis $\hat{\mathbf{l}}_p$, indicated by ϕ spanning the full range of -180° to 180° , while β remains more or less constant. The Laplace radius is $r_L/r_{\text{out}} = 0.2$, with $p = 1$.

absence of any internal torque, the disk may assume an equilibrium warp profile (the Laplace surface; see Section 6.1), such that the outer disk beyond the Laplace radius r_L [see Eq. (6.3)] tends to be aligned with the planet’s orbit (see Fig. 6.1). We have studied how self-gravity of the disk affects the steady-state disk inclination profile (Fig. 6.3). In general, for a given planetary obliquity β_p , the outer disk inclination can be increased due to the “rigidity” provided by the disk’s self-gravity. To produce a non-negligible outer disk misalignment requires that the combination of the disk mass and r_L/r_{out} be sufficiently large [see Fig. 6.4 and Eq. (6.23)]. The required disk mass is larger for smaller r_L/r_{out} . (Of course, if the disk lies completely inside r_L , i.e. $r_L/r_{\text{out}} \gtrsim 1$, self-gravity is not needed to achieve misalignment of the disk since $\beta \simeq \beta_p$.)

We have shown that the generalized Laplace equilibria for disk warp profiles are stable against small inclination perturbations (Section 4.1). Because a circumplanetary disk may not relax to a steady state in the absence of internal dissipation, we have also studied the dynamical evolution of a disk initially aligned with the planet’s spin (Section 6.3.2). Such a disk can attain misalignment with respect to the orbital plane if it can precess coherently and if $\beta_p \neq 0$. We showed that to achieve coherent disk precession, the disk’s self-gravity must dominate over the influence of the star’s tidal torque throughout the disk. This coherence requirement leads to a lower bound on the disk mass [Eq. (6.31)]:

$$M_d \gtrsim 2.67 \times 10^{-3} M_p \left(\frac{r_{\text{out}}}{0.2 r_H} \right)^3.$$

Of course, this mass constraint is needed only if $r_{\text{out}} > r_L$.

6.4.2 Hydrodynamical Effects

In this paper we have focused on the effect of self-gravity in maintaining the coherence and inclination of circumplanetary disks. Here we briefly comment on hydrodynamical effects internal to the disk.

As noted in Section 1, hydrodynamic forces work to keep the disk coherent through either bending waves or viscosity. If the disk viscosity parameter α satisfies $\alpha \lesssim H/r$, the warp disturbances propagate through the circumplanetary disk in the form of bending waves. In order to enforce coherence, a bending wave must propagate throughout the disk faster than a precession period from the tidal torque of the host star [Larwood et al., 1996]. The tidal precession period is of order $t_* \sim 2\pi r^2 \Omega / |\mathbf{T}_*| \sim (8\pi/\Omega)(r_H/r)^3$, while the bending-wave crossing time is $t_{\text{bend}} \simeq 2r/c_s \simeq (2/\Omega)(r/H)$ (c_s is the disk sound speed). Thus the small value of H/r ($\sim 10^{-3}$ for the inferred ring system around J1407b) makes t_* smaller than t_{bend} when the disk extends to a significant fraction of the Hill radius.

If the disk viscosity parameter satisfies $\alpha \gtrsim H/r$, hydrodynamical forces communicate through the disk in the form of viscosity. The the internal viscous torque (per unit mass) is [Papaloizou & Pringle, 1983]

$$|\mathbf{T}_{\text{visc}}| = \frac{r^2 \Omega^2}{2} \left(\frac{H}{r} \right) \left(3\alpha + \frac{1}{2\alpha} \left| \frac{\partial \hat{l}}{\partial \ln r} \right| \right) \quad (6.41)$$

Comparing this with the tidal torque $|\mathbf{T}_*|$ shows that unless the disk warp $|\partial \hat{l} / \partial \ln r|$ is significant, the viscous torque will have difficulty balancing the tidal torque from the host star; such a strongly warped disk could be subjected to breaking [Doğan et al., 2015].

In addition to the above considerations, the “observed” gaps in the J1407b disk may halt the propagation of bending waves and cut off viscous torques.

Thus, hydrodynamical effects cannot be responsible for the disk's coherence and inclination.

6.4.3 Implications

The large disk mass [Eq. (6.31)] required to enforce coherent disk precession or maintain misalignment of the outer disk may be difficult to achieve in the context of circumplanetary disk formation (e.g. Canup & Ward 2006). Moreover, a massive disk can suffer gravitational instability. Evaluating the Toomre Q parameter at the outer radius of the disk, we find

$$\begin{aligned} Q(r_{\text{out}}) &= \frac{c_s(r_{\text{out}})\kappa(r_{\text{out}})}{\pi G \Sigma(r_{\text{out}})} \\ &\simeq \frac{2}{2-p} \left(\frac{H(r_{\text{out}})}{10^{-3}r_{\text{out}}} \right) \left(\frac{10^{-3}M_p}{M_d} \right). \end{aligned} \quad (6.42)$$

where we have used $c_s \simeq H\Omega$, $\kappa \simeq \Omega \simeq \sqrt{GM_p/r^3}$ (H is the disk scale-height). Requiring $Q \gtrsim 1$ for stability puts an upper limit on M_d , and thus the size of the disk. Combining Eqs. (6.42) and (6.31), we find

$$\frac{r_{\text{out}}}{r_H} \lesssim 0.35 \left(\frac{H}{10^{-3}r_{\text{out}}} \right)^{1/3}. \quad (6.43)$$

This puts a strong constraint on the putative ring/disk system around J1407b.

Our work shows that in general, an extended circumplanetary disk is warped when in a steady state or undergoing coherent precession. This warp depends on the Laplace radius [see Eq. (6.3)] and the disk mass. Direct observations of such a warped circumplanetary disk would constrain the planet's oblateness (the J_2 parameter), complementing photometric constraints [Carter & Winn, 2010, Zhu et al., 2014].

Although our work is motivated by the putative J1407b ring system, our results can be easily adapted to circumplanetary disk/ring systems in general. We expect that the analysis developed in this paper can be a useful tool to evaluate the stability of circumplanetary disk/ring systems detected in the future.

Acknowledgments

We thank the referee for providing thorough and thoughtful comments, which have significantly improved our paper. This work has been supported in part by NSF grant AST-1211061, and NASA grants NNX14AG94G and NNX14AP31G. JZ is supported by a NASA Earth and Space Sciences Fellowship in Astrophysics.

Appendix: Exact self-gravity torque for a circular disk

As noted in Section 6.2, Eq. (6.9) is valid only when $|\hat{\mathbf{l}}(r') \times \hat{\mathbf{l}}(r)| \ll 1$ or $\chi \ll 1$. When $\chi \sim 1$ and $|\hat{\mathbf{l}}(r') \times \hat{\mathbf{l}}(r)| \sim 1$, a different formalism is needed to compute the torque acting between two circular massive rings. In terms of the warp profile $\hat{\mathbf{l}}(r, t)$ and disk surface density $\Sigma(r)$, the specific torque acting on a disk annulus at radius r from the disk's self-gravity is [Kuijken, 1991, Arnaboldi & Sparke, 1994, Ulubay-Siddiki et al., 2009]

$$\begin{aligned} \mathbf{T}_{\text{sg}} = & \int_{r_{\text{in}}}^{r_{\text{out}}} dr' \frac{4\pi G \Sigma(r') \chi I(\chi, \sin^2 \alpha)}{\max(r, r')} \frac{(1 + \chi^2)^{3/2}}{} \\ & \times [\hat{\mathbf{l}}(r, t) \cdot \hat{\mathbf{l}}(r', t)] [\hat{\mathbf{l}}(r, t) \times \hat{\mathbf{l}}(r', t)] \end{aligned} \quad (6.44)$$

where $\chi = \min(r, r') / \max(r, r')$, $\sin^2 \alpha = |\hat{\mathbf{l}}(r, t) \times \hat{\mathbf{l}}(r', t)|^2$,

$$I = \frac{4}{\pi^2} \int_0^{\pi/2} d\psi \left[\frac{E(k)(1 - k^2/2)}{(1 - k^2)} - K(k) \right] \times \frac{(1 - k^2/2)^{3/2}}{k^2} \frac{\sin^2 \psi}{\sqrt{1 - \sin^2 \alpha \sin^2 \psi}} \quad (6.45)$$

$$\begin{aligned} k^2 &= k^2(\chi, \sin^2 \psi, \sin^2 \alpha) \\ &= \frac{4\chi \sqrt{1 - \sin^2 \alpha \sin^2 \psi}}{1 + \chi^2 + 2\chi \sqrt{1 - \sin^2 \alpha \sin^2 \psi}} \end{aligned} \quad (6.46)$$

while $K(k)$ and $E(k)$ are elliptic integrals of the first and second kind, respectively. The only approximation used in the derivation of Eq. (6.44) is that the disk is infinitesimally thin; this formula is exact for arbitrary χ and mutual inclination angles α .

In the top panel of Fig. 6.9, we plot the integrand in equation (6.44),

$$\frac{8I(\chi, \sin^2 \alpha)}{(1 + \chi^2)^{3/2}}, \quad (6.47)$$

as a function of χ . We remove the dependence of $\sin \alpha \cos \alpha$, as they are already present in our approximation (6.9). We see that when $|\alpha| > 0$, the integrand (6.47) becomes large but stays finite as $\chi \rightarrow 1$. In the bottom panel of Fig. 6.9, we plot the ratio of the integrands in Eqs. (6.44) and (6.9),

$$\frac{8I(\chi, \sin^2 \alpha)}{(1 + \chi^2)^{3/2} b_{3/2}^{(1)}(\chi)}. \quad (6.48)$$

Since the quantity (6.48) is approximately unity for most of the parameter range of interest (Fig. 6.9), we do not expect significant corrections to the equilibrium disk warp profiles obtained in Section 6.2.

We have repeated the calculation of the Laplace equilibria for disk warp profiles using the exact torque expression (6.44). Figure 6.10 shows a sample of our

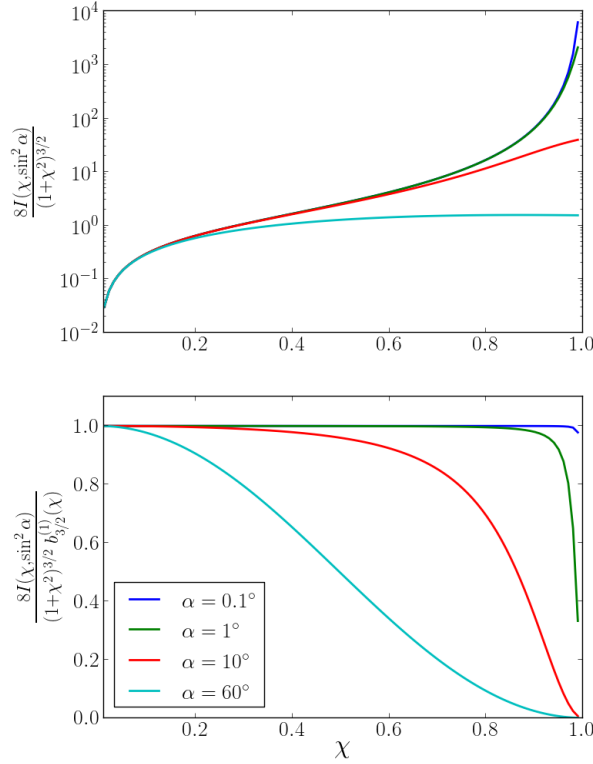


Figure 6.9: The top panel shows the integrand in Eq. (6.44) as a function of χ , with values of α as indicated. We remove the dependence on $\sin \alpha \cos \alpha$. The bottom plot shows the ratio of the integrand in (6.44) and that in (6.9).

numerical results for the disk inclination profile $\beta(r)$, with $\Sigma \propto r^{-3/2}$ and the values of σ and r_L/r_{out} as indicated. The solutions for $\beta(r)$ with the approximate torque expression (6.9) are also shown for comparison. We see that using the exact self-gravity torque (6.44) changes the solution of the equilibrium disk warp $\beta(r)$ by less than a few degrees in all cases.

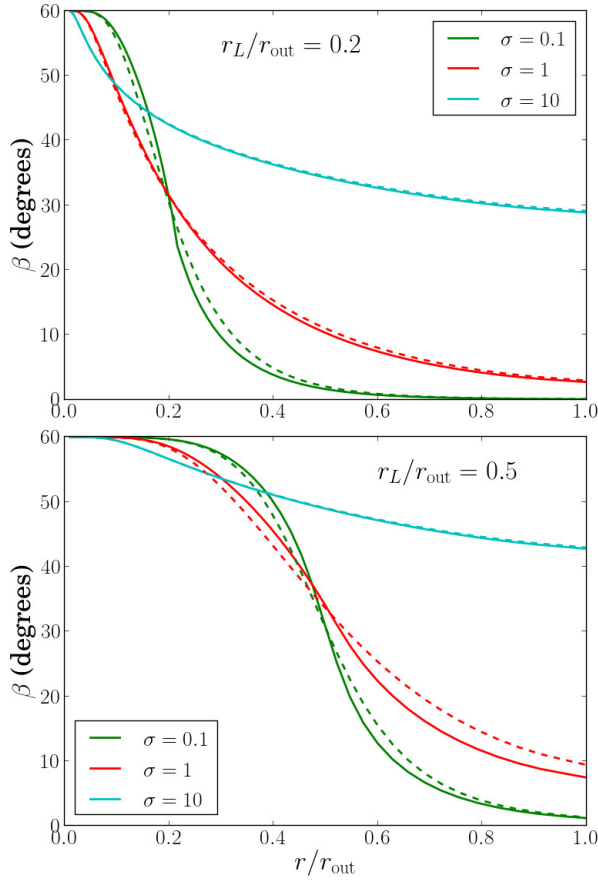


Figure 6.10: Equilibrium disk inclination profile $\beta(r)$ including the effect of self-gravity for different values of r_L/r_{out} and σ [see Eq. (6.20)] as indicated. The results obtained using the approximate self-gravity torque [Eq. (6.9)] are shown in dashed lines, while those obtained with the exact self-gravity torque [Eq. (6.44)] are shown by solid lines. We take $p = 1.5$ [Eq. (6.12)] and $\beta_p = 60^\circ$ for all solutions.

APPENDIX A

CHAPTER 1 OF APPENDIX

As mentioned in Chapter 1, an often-quoted criterion for a disk to lie in the resonant, bending wave regime is the Shakura-Sunyaev viscosity parameter α , orbital frequency $\Omega^2 = r^{-1}\partial\phi/\partial r|_{z=0}$, epicyclic frequency $\kappa^2 = (2\Omega/r)\partial(r^2\Omega)/\partial r$, and disc aspect ratio H/r satisfy

$$\alpha \lesssim \frac{H}{r} \quad \text{and} \quad \left| \frac{\Omega^2 - \kappa^2}{2\Omega^2} \right| \lesssim \frac{H}{r}. \quad (\text{A.1})$$

When condition (A.1) is met, bending waves are free to travel across the disk at half the disk's sound-speed, and the time evolution of bending disturbances in the disk are described by a wave equation [Papaloizou & Lin, 1995, Lubow & Ogilvie, 2000]. When condition (A.1) is violated, the propagation of bending waves becomes significantly affected by the disk's viscosity and/or non-Keplarian epicyclic frequency, and can no longer efficiently propagate across the disk. Bending disturbances in the non-resonant regime are then described by a diffusion equation [Papaloizou & Pringle, 1983, Ogilvie, 1999].

This appendix shows this transition may be understood from the dispersion relation for bending waves in a viscous, non-Keplarian disk. Section A.1 derives the dispersion relation of the disk in two different limiting cases. Section A.2 applies this result to bending waves, and shows bending waves travel across the disk at half the sound-speed when condition (A.1) is met.

A.1 Density Wave Dispersion Relation

We consider a viscous, non-Keplarian disk, satisfying the usual fluid equations with a gravitational potential ϕ :

$$\frac{\partial \rho}{\partial t} + \nabla \cdot (\mathbf{v}\rho) = 0 \quad (\text{A.2})$$

$$\frac{\partial \mathbf{v}}{\partial t} + (\mathbf{v} \cdot \nabla) \mathbf{v} = -\frac{1}{\rho} \nabla p - \nabla \phi + \mathbf{f}_v \quad (\text{A.3})$$

Here, ρ , p , and \mathbf{v} are the fluid density, pressure, and velocity, and

$$\mathbf{f}_v = \frac{1}{\rho} \nabla \cdot \left\{ \rho \mathbf{v} \left[(\nabla \mathbf{v}) + (\nabla \mathbf{v})^T - \frac{1}{3} \mathbf{I} (\nabla \cdot \mathbf{v}) \right] \right\} \quad (\text{A.4})$$

is the viscous force, where $\nu = \alpha c_s^2 / \Omega$ is the kinematic viscosity of the disk, \mathbf{M}^T denotes the transpose of the tensor \mathbf{M} , and \mathbf{I} is the identity tensor.

We adopt a cylindrical coordinate system (r, φ, z) centered on the central body. The un-perturbed state is taken to be axis-symmetric with $\mathbf{v} = r\Omega\hat{\varphi}$ and $\rho(r, z) = \rho(r) \exp(z^2/2H^2)$, assuming the disk is thin ($H = c_s/\Omega \ll r$). Since the disk is thin, background quantities satisfy $\partial X/\partial z \gg \partial X/\partial r \sim X/r$.

We perturb the background quantities $X(r, z)$ by perturbations $\delta X \ll X$, assumed to be high wavelength disturbances ($\partial \delta X / \partial r, \partial \delta X / \partial z \gg \delta X / r$). Taking the perturbations to be of the form

$$\delta X(r, z, \varphi, t) = \delta X(r, z) e^{i(m\varphi - \omega t)}, \quad (\text{A.5})$$

the perturbation equations become [assuming $m = O(1)$]

$$-i\varpi\delta\rho + \rho \frac{\partial}{\partial r} \delta v_r + \frac{\partial}{\partial z} (\rho \delta v_z) = 0, \quad (\text{A.6})$$

$$-i\varpi\delta v_r - 2\Omega\delta v_\varphi = -\frac{1}{\rho} \frac{\partial}{\partial r} \delta p + (\mathbf{f}_v)_r, \quad (\text{A.7})$$

$$-i\varpi\delta v_\varphi + \frac{\kappa^2}{2\Omega} \delta v_r = (\mathbf{f}_v)_\varphi, \quad (\text{A.8})$$

$$-i\varpi\delta v_z = -\frac{1}{\rho}\frac{\partial}{\partial z}\delta p + \frac{1}{\rho^2}\frac{dp}{dz}\delta\rho + (\mathbf{f}_v)_z, \quad (\text{A.9})$$

where

$$(\mathbf{f}_v)_r = \nu \left(\frac{4}{3} \frac{\partial^2}{\partial r^2} + \frac{\partial \ln \rho}{\partial z} \frac{\partial}{\partial z} + \frac{\partial^2}{\partial z^2} \right) \delta v_r \quad (\text{A.10})$$

$$+ \nu \left(-\frac{2}{3} \frac{\partial^2}{\partial r \partial z} + \frac{\partial \ln \rho}{\partial z} \frac{\partial}{\partial r} + \frac{\partial^2}{\partial r \partial z} \right) \delta v_z, \quad (\text{A.11})$$

$$(\mathbf{f}_v)_\varphi = \nu \left(\frac{\partial^2}{\partial r^2} + \frac{\partial \ln \rho}{\partial z} \frac{\partial}{\partial z} + \frac{\partial^2}{\partial z^2} \right) \delta v_\varphi, \quad (\text{A.12})$$

$$(\mathbf{f}_v)_z = \nu \left(-\frac{2}{3} \frac{\partial \ln \rho}{\partial z} \frac{\partial}{\partial r} + \frac{1}{3} \frac{\partial^2}{\partial r \partial z} \right) \delta v_r \quad (\text{A.13})$$

$$+ \nu \left(\frac{\partial^2}{\partial r^2} + \frac{4}{3} \frac{\partial \ln \rho}{\partial z} \frac{\partial}{\partial z} + \frac{4}{3} \frac{\partial^2}{\partial z^2} \right) \delta v_z, \quad (\text{A.14})$$

are the viscous force terms, and

$$\varpi = \omega - m\Omega. \quad (\text{A.15})$$

We will consider two different limits for the dispersion relation of a viscous, non-Keplarian disk. First, we examine the high vertical wavenumber limit ($|\partial\delta X/\partial z| = k_z\delta X \gg \delta X/H$). This limit allows us to examine under what conditions different viscous force terms are important. Next, we will examine the low vertical wavenumber limit ($k_z \sim H^{-1}$), neglecting specific viscous force terms. As long as the disk's α -viscosity parameter satisfies $\alpha \ll 1$, the dispersion relation derived in the following subsections applies for any density wave disturbance in viscous non-Keplarian disks.

A.1.1 High k_z limit

In this section, we assume all perturbations $\delta X \propto \exp[i(k_r r + k_z z)]$, and investigate the limit where $k_r \gg r^{-1}$ and $k_z \gg H^{-1}$. In this high wavelength limit, the viscous

force terms reduce to

$$(\mathbf{f}_v)_r \simeq -\nu(k_{rr}^2 \delta v_r + k_{rz}^2 \delta v_z), \quad (\text{A.16})$$

$$(\mathbf{f}_v)_\varphi \simeq -\nu k_{\varphi\varphi}^2 \delta v_\varphi, \quad (\text{A.17})$$

$$(\mathbf{f}_v)_z \simeq -\nu(k_{zr}^2 \delta v_r + k_{zz}^2 \delta v_z), \quad (\text{A.18})$$

where

$$k_{rr}^2 = \frac{4}{3}k_r^2 + k_z^2, \quad (\text{A.19})$$

$$k_{\varphi\varphi}^2 = k_r^2 + k_z^2, \quad (\text{A.20})$$

$$k_{zz}^2 = k_r^2 + \frac{4}{3}k_z^2, \quad (\text{A.21})$$

$$k_{rz}^2 = -\frac{2}{3}k_r k_z + k_z k_r = \frac{1}{3}k_r k_z, \quad (\text{A.22})$$

$$k_{zr}^2 = -\frac{2}{3}k_z k_r + k_r k_z = \frac{1}{3}k_r k_z. \quad (\text{A.23})$$

The perturbation equations then reduce to

$$-\mathrm{i}\varpi\delta\bar{\rho} + \mathrm{i}k_r r\Omega\delta\bar{v}_r + \mathrm{i}k_z r\Omega\delta\bar{v}_z = 0, \quad (\text{A.24})$$

$$-\mathrm{i}\varpi_r r\Omega\delta\bar{v}_r - 2r\Omega^2\delta\bar{v}_\varphi = -\mathrm{i}k_r c_s^2 \delta\bar{\rho} - \alpha r c_s^2 k_{rz}^2 \delta\bar{v}_z, \quad (\text{A.25})$$

$$-\mathrm{i}\varpi_\varphi r\Omega\delta\bar{v}_\varphi + \frac{r\kappa^2}{2}\delta\bar{v}_r = 0 \quad (\text{A.26})$$

$$-\mathrm{i}\varpi_z r\Omega\delta\bar{v}_z = -\mathrm{i}c_s^2 k_z \delta\bar{\rho} - \alpha r c_s^2 k_{zr}^2 \delta\bar{v}_r \quad (\text{A.27})$$

where $\delta\bar{\rho} = \delta\rho/\rho$, $\delta\bar{v} = \delta\mathbf{v}/r\Omega$, and

$$\varpi_r = \varpi + \mathrm{i}arc_s^2 k_{rr}, \quad (\text{A.28})$$

$$\varpi_\varphi = \varpi + \mathrm{i}arc_s^2 k_{\varphi\varphi}, \quad (\text{A.29})$$

$$\varpi_z = \varpi + \mathrm{i}arc_s^2 k_{zz}. \quad (\text{A.30})$$

These equations give the dispersion relation

$$(\varpi_r \varpi_\varphi - \kappa^2)(\Omega^2 - k_z^2 c_s^2) \Omega^2 + \alpha c_s^4 \varpi_\varphi [\alpha \varpi k_{rz}^2 k_{zr}^2 + \mathrm{i}\Omega k_r k_z (k_{rz}^2 + k_{zr}^2)]$$

$$= k_r^2 c_s^2 \varpi_z \varpi_\varphi \Omega^2. \quad (\text{A.31})$$

From this, we see the cross terms (k_{rz}^2, k_{zr}^2) only become relevant when

$$\alpha k_z^2 c_s^2 \gtrsim \Omega^2. \quad (\text{A.32})$$

For the “low” k_z values characteristic of density waves with $k_z \sim H^{-1}$, these cross terms will be negligible when $k_z \alpha \ll H^{-1}$. In the next section, we will derive a dispersion relation for high-wavelength density waves ($k_r \gg r^{-1}$), assuming $k_z \alpha \ll H^{-1}$.

A.1.2 Low k_z limit

This section derives the dispersion relation for density waves when $n\alpha \ll 1$. Because in this limit, all cross terms ($\partial^2 / \partial r \partial z$) in the viscous force of the perturbation equations have a negligible impact on the dispersion relation, the viscous forces reduce to

$$(f_v)_r \simeq \alpha H^2 \Omega \left(\frac{4}{3} \frac{\partial^2}{\partial r^2} + \frac{\partial \ln \rho}{\partial z} \frac{\partial}{\partial z} + \frac{\partial^2}{\partial z^2} \right) \delta v_r, \quad (\text{A.33})$$

$$(f_v)_\varphi \simeq \alpha H^2 \Omega \left(\frac{\partial^2}{\partial r^2} + \frac{\partial \ln \rho}{\partial z} \frac{\partial}{\partial z} + \frac{\partial^2}{\partial z^2} \right) \delta v_\varphi, \quad (\text{A.34})$$

$$(f_v)_z \simeq \alpha H^2 \Omega \left(\frac{\partial^2}{\partial r^2} + \frac{4}{3} \frac{\partial \ln \rho}{\partial z} \frac{\partial}{\partial z} + \frac{4}{3} \frac{\partial^2}{\partial z^2} \right) \delta v_z. \quad (\text{A.35})$$

Since

$$\frac{\partial \ln \rho}{\partial z} = -\frac{z}{H^2}, \quad (\text{A.36})$$

it is natural to decompose the vertical dependence of the fluid perturbations in terms of Hankel Functions $H_n(Z)$:

$$H_n(Z) \equiv (-1)^n e^{Z^2/2} \left(\frac{d}{dZ} \right)^n e^{-Z^2/2}. \quad (\text{A.37})$$

Assuming then that

$$\delta\rho = \rho\delta\bar{\rho}H_n\left(\frac{z}{H}\right)e^{ik_r r}, \quad (\text{A.38})$$

$$\delta v_r = r\Omega\delta\bar{v}_rH_n\left(\frac{z}{H}\right)e^{ik_r r}, \quad (\text{A.39})$$

$$\delta v_\varphi = r\Omega\delta\bar{v}_\varphi H_n\left(\frac{z}{H}\right)e^{ik_r r}, \quad (\text{A.40})$$

$$\delta v_z = r\Omega\delta\bar{v}_z H'_n\left(\frac{z}{H}\right)e^{ik_r r}, \quad (\text{A.41})$$

where $H'_n(Z) = dH_n/dZ$, the perturbation equations reduce to

$$-ir\Omega\varpi\delta\bar{\rho} + ik_r r^2\Omega^2\delta\bar{v}_r - k_z^2 c_s r^2\Omega\delta v_z = 0, \quad (\text{A.42})$$

$$-ir\Omega\varpi_r\delta\bar{v}_r - 2r\Omega^2\delta\bar{v}_\varphi + ic_s^2 k_r \delta\bar{\rho} = 0, \quad (\text{A.43})$$

$$-ir\Omega\varpi_\varphi\delta\bar{v}_\varphi + \frac{r\kappa^2}{2}\delta\bar{v}_r = 0, \quad (\text{A.44})$$

$$-ir\Omega\varpi_z\delta\bar{v}_z + c_s\Omega\delta\bar{\rho} = 0, \quad (\text{A.45})$$

where $k_z = \sqrt{n}/H$ and

$$\varpi_r = \varpi + i\alpha H^2 \Omega \left(\frac{4}{3} k_r^2 + k_z^2 \right), \quad (\text{A.46})$$

$$\varpi_\varphi = \varpi + i\alpha H^2 \Omega \left(k_r^2 + k_z^2 \right), \quad (\text{A.47})$$

$$\varpi_z = \varpi + i\alpha H^2 \Omega \left(k_r^2 + \frac{4(n-1)}{3n} k_z^2 \right). \quad (\text{A.48})$$

Solving, we obtain the dispersion relation

$$(\varpi\varpi_z - n\Omega^2)(\varpi_r\varpi_\varphi - \kappa^2) = c_s^2 k_r^2 \varpi_r \varpi_\varphi. \quad (\text{A.49})$$

A.2 Long-Wavelength Bending Wave Dispersion Relation

In this section, we analyze the dispersion relation for low-frequency ($\omega \ll \Omega$) bending wave disturbances ($m = n = 1$). Assuming $\alpha \ll 1$ and long-wavelengths

$(k_r \ll H^{-1})$, the dispersion relation reduces to

$$\omega^2 + \left(i\alpha + \frac{\kappa^2 - \Omega^2}{2\Omega^2} \right) \Omega\omega \simeq \frac{1}{4} k_r^2 c_s^2. \quad (\text{A.50})$$

When $|i\alpha + (\kappa^2 - \Omega^2)/2\Omega^2| \lesssim k_r H$, the phase velocity of the bending wave $v_{\text{bw}} = \omega/k_r$ becomes

$$v_{\text{bw}} \approx \pm \frac{c_s}{2}, \quad (\text{A.51})$$

while when $|i\alpha + (\Omega^2 - \kappa^2)/2\Omega^2| \gtrsim k_r H$, the bending wave velocity is modified to be

$$v_{\text{bw}} \approx \frac{k_r H c_s}{4} \left(\left| \frac{\kappa^2 - \Omega^2}{2\Omega^2} \right| + i\alpha \right)^{-1} \quad (\text{A.52})$$

or

$$v_{\text{bw}} \approx -i \frac{\alpha \Omega}{k_r} - \frac{\Omega}{2k_r} \left[\left(\frac{\kappa^2 - \Omega^2}{2\Omega^2} \right) + \left| \frac{\kappa^2 - \Omega^2}{2\Omega^2} \right| \right]. \quad (\text{A.53})$$

This analysis shows when $\alpha \gtrsim k_r H$, the bending wave can no longer propagate globally across the disk, but rather becomes diffusive and damps locally. When $|\kappa^2 - \Omega^2/2\Omega^2| \gtrsim k_r H$, the wave can still propagate globally across the disk, but outward propagating waves [$\text{Re}(v_{\text{bw}}) > 0$] become slower than $c_s/2$ by a factor $\sim k_r H/|\kappa^2/\Omega^2 - 1|$. For the long wavelength modes of a globally warped disk ($k_r \sim r^{-1}$), the approximate condition for bending waves propagating outward to travel at velocities $v_{\text{bw}} \gtrsim c_s/2$ is

$$\alpha \lesssim \frac{H}{r} \quad \text{and} \quad \left| \frac{\kappa^2 - \Omega^2}{2\Omega^2} \right| \lesssim \frac{H}{r}. \quad (\text{A.54})$$

BIBLIOGRAPHY

Chapter 1 references

- Chatterjee S., Ford E. B., Matsumura S., Rasio F. A., 2008, *ApJ*, 686, 580
- Dawson R. I., Johnson J. A., 2018, ArXiv e-prints, arXiv:1801.06117
- Ford E. B., Rasio F. A., 2008, *ApJ*, 686, 621
- Goldreich P., Lithwick Y., Sari R., 2004, *ApJ*, 614, 497
- Goldreich P., Sari R., 2003, *ApJ*, 585, 1024
- Haisch K. E., Lada E. A., Lada C. J., 2001, *ApJ*, 553, L153
- Hébrard G., et al., 2010, *A&A*, 516, A95
- Jurić M., Tremaine S., 2008, *ApJ*, 686, 603
- Lambrechts M., Johansen A., 2012, *A&A*, 544, A32
- Lin D. N. C., Bodenheimer P., Richardson D. C., 1996, *Natur*, 380, 606
- Lin D. N. C., Papaloizou J., 1986, *ApJ*, 309, 846
- Mayor M., Queloz D., 1995, *Natur*, 378, 355
- McLaughlin D. B., 1924, *ApJ*, 60, 22
- Naef D., et al., 2001, *A&A*, 375, L27
- Ogilvie G. I., Lubow S. H., 2003, *ApJ*, 587, 398
- Rasio F. A., Ford E. B., 1996, *Sci*, 274, 954

Rosotti G. P., Booth R. A., Clarke C. J., Teyssandier J., Facchini S., Mustill A. J.,
2017, MNRAS, 464, L114

Rossiter R. A., 1924, ApJ, 60, 15

Safronov V. S., 1972, epcf.book

Teyssandier J., Ogilvie G. I., 2017, MNRAS, 467, 4577

Winn J. N., Fabrycky D. C., 2015, ARA&A, 53, 409

Woolfson M. M., 1993, QJRAS, 34,

Chapter 2 references

Albrecht S., Winn J. N., Marcy G. W., Howard A. W., Isaacson H., Johnson J. A.,
2013, ApJ, 771, 11

Albrecht S., et al., 2012, ApJ, 757, 18

Bate M. R., Bonnell I. A., Bromm V., 2003, MNRAS, 339, 577

Bate M. R., Bonnell I. A., Clarke C. J., Lubow S. H., Ogilvie G. I., Pringle J. E.,
Tout C. A., 2000, MNRAS, 317, 773

Batygin K., 2012, Natur, 491, 418

Batygin K., Adams F. C., 2013, ApJ, 778, 169

Bouvier J., 2013, EAS, 62, 143

Brinch C., Jørgensen J. K., Hogerheijde M. R., Nelson R. P., Gressel O., 2016, ApJ,
830, L16

Chandrasekhar S., 1939, An introduction to the study of stellar structure, The University of Chicago press

Chakraborty C., Bhattacharyya S., 2017, MNRAS, 469, 3062

Chiang E. I., Goldreich P., 1997, ApJ, 490, 368

Demianski M., Ivanov P. B., 1997, A&A, 324, 829

Doğan S., Nixon C., King A., Price D. J., 2015, MNRAS, 449, 1251

Franchini A., Lodato G., Facchini S., 2016, MNRAS, 455, 1946

Facchini S., Lodato G., Price D. J., 2013, MNRAS, 433, 2142

Fernández-López M., Zapata L. A., Gabbasov R., 2017, ApJ, 845, 10

Foucart F., Lai D., 2014, MNRAS, 445, 1731

Foucart F., Lai D., 2013, ApJ, 764, 106

Foucart F., Lai D., 2011, MNRAS, 412, 2799

Fu W., Lubow S. H., Martin R. G., 2015, ApJ, 807, 75

Fu W., Lubow S. H., Martin R. G., 2015, ApJ, 813, 105

Gammie C. F., Goodman J., Ogilvie G. I., 2000, MNRAS, 318, 1005

Hayashi C., 1961, PASJ, 13,

Jensen E. L. N., Akeson R., 2014, Natur, 511, 567

Klessen R. S., 2011, EAS, 51, 133

Lai, D. 2014a, MNRAS, 440, 3532

Lai D., 2014b, EPJWC, 64, 01001

Lai D., Rasio F. A., Shapiro S. L., 1993, ApJS, 88, 205

Larwood J. D., Nelson R. P., Papaloizou J. C. B., Terquem C., 1996, MNRAS, 282, 597

Lee J.-E., Lee S., Dunham M. M., Tatematsu K., Choi M., Bergin E. A., Evans N. J., 2017, NatAs, 1, 0172

Li G., Winn J. N., 2016, ApJ, 818, 5

Lodato G., Facchini S., 2013, MNRAS, 433, 2157

Lubow S. H., Martin R. G., 2018, MNRAS, 473, 3733

Lubow S. H., Ogilvie G. I., 2017, MNRAS, 469, 4292

Lubow S. H., Ogilvie G. I., Pringle J. E., 2002, MNRAS, 337, 706

Lubow S. H., Ogilvie G. I., 2001, ApJ, 560, 997

Lubow S. H., Ogilvie G. I., 2000, ApJ, 538, 326

Lubow S. H., 1991, ApJ, 381, 259

Lynden-Bell D., Pringle J. E., 1974, MNRAS, 168, 603

Martin R. G., Nixon C., Lubow S. H., Armitage P. J., Price D. J., Doğan S., King A., 2014, ApJ, 792, L33

Mazeh T., Perets H. B., McQuillan A., Goldstein E. S., 2015, ApJ, 801, 3

McKee C. F., Ostriker E. C., 2007, ARA&A, 45, 565

Neuhäuser R., et al., 2009, A&A, 496, 777

- Nixon C., King A., 2016, LNP, 905, 45
- Ogilvie G. I., Latter H. N., 2013, MNRAS, 433, 2420
- Ogilvie G. I., 2006, MNRAS, 365, 977
- Ogilvie G. I., 1999, MNRAS, 304, 557
- Papaloizou J. C. B., Lin D. N. C., 1995, ApJ, 438, 841
- Rafikov R. R., 2017, ApJ, 837, 163
- Spalding, C., & Batygin, K. 2015, ApJ, 811, 82
- Spalding C., Batygin K., 2014, ApJ, 790, 42
- Stapelfeldt K. R., Ménard F., Watson A. M., Krist J. E., Dougados C., Padgett D. L., Brandner W., 2003, ApJ, 589, 410
- Stapelfeldt K. R., Krist J. E., Ménard F., Bouvier J., Padgett D. L., Burrows C. J., 1998, ApJ, 502, L65
- Tanaka H., Ward W. R., 2004, ApJ, 602, 388
- Tremaine S., Davis S. W., 2014, MNRAS, 441, 1408
- Triaud A. H. M. J., 2017, arXiv, arXiv:1709.06376
- Williams J. P., et al., 2014, ApJ, 796, 120
- Winn J. N., et al., 2017, AJ, 154, 270
- Winn J. N., Fabrycky D. C., 2015, ARA&A, 53, 409
- Winn J. N., Fabrycky D., Albrecht S., Johnson J. A., 2010, ApJ, 718, L145
- Zanazzi J. J., Lai D., 2017, MNRAS, 467, 1957

Zanazzi J. J., Lai D., 2018a, MNRAS, 473, 603

Zanazzi J. J., Lai D., 2018b, arXiv, arXiv:1711.03138

Chapter 3 references

- Albrecht S., Winn J. N., Marcy G. W., Howard A. W., Isaacson H., Johnson J. A., 2013, ApJ, 771, 11
- Albrecht, S., Winn, J. N., Johnson, J. A., et al. 2012, ApJ, 757, 18
- Alexander R., Pascucci I., Andrews S., Armitage P., Cieza L., 2014, prpl.conf, 475
- Alexander R. D., Clarke C. J., Pringle J. E., 2006, MNRAS, 369, 229
- Anderson K. R., Storch N. I., Lai D., 2016, MNRAS, 456, 3671
- Ayliffe B. A., Bate M. R., 2009, MNRAS, 393, 49
- Balbus, S. A., & Hawley, J. F. 1991, ApJ, 376, 214
- Bate M. R., Lodato G., Pringle J. E., 2010, MNRAS, 401, 1505
- Bate M. R., Bonnell I. A., Clarke C. J., Lubow S. H., Ogilvie G. I., Pringle J. E., Tout C. A., 2000, MNRAS, 317, 773
- Bayliss D. D. R., Sackett P. D., 2011, ApJ, 743, 103
- Batygin K., 2012, Natur, 491, 418
- Batygin K., Adams F. C., 2013, ApJ, 778, 169
- Batygin K., Bodenheimer P. H., Laughlin G. P., 2016, ApJ, 829, 114
- Beaugé C., Nesvorný D., 2012, ApJ, 751, 119

Becker J. C., Vanderburg A., Adams F. C., Rappaport S. A., Schwengeler H. M., 2015, *ApJ*, 812, L18

Benítez-Llambay P., Masset F., Koenigsberger G., Szulágyi J., 2015, *Natur*, 520, 63

Bitsch B., Crida A., Libert A.-S., Lega E., 2013, *A&A*, 555, A124

Boley A. C., Granados Contreras A. P., Gladman B., 2016, *ApJ*, 817, L17

Bryan M. L., Bowler B. P., Knutson H. A., Kraus A. L., Hinkley S., Mawet D., Nielsen E. L., Blunt S. C., 2016, *ApJ*, 827, 100

Chametla R. O., Sánchez-Salcedo F. J., Masset F. S., Hidalgo-Gámez A. M., 2017, *MNRAS*, 468, 4610

Chiang E., Laughlin G., 2013, *MNRAS*, 431, 3444

Clanton C., Gaudi B. S., 2016, *ApJ*, 819, 125

Clarke, C. J., Gendrin, A., & Sotomayor, M. 2001, *MNRAS*, 328, 485

Cresswell P., Dirksen G., Kley W., Nelson R. P., 2007, *A&A*, 473, 329

Cumming A., Butler R. P., Marcy G. W., Vogt S. S., Wright J. T., Fischer D. A., 2008, *PASP*, 120, 531

D'Angelo G., Lubow S. H., 2008, *ApJ*, 685, 560-583

David T. J., et al., 2016, *Natur*, 534, 658

Dawson R. I., Murray-Clay R. A., Johnson J. A., 2015, *ApJ*, 798, 66

Donati J. F., et al., 2016, *Natur*, 534, 662

- Duffell P. C., Haiman Z., MacFadyen A. I., D’Orazio D. J., Farris B. D., 2014, *ApJ*, 792, L10
- Dürmann C., Kley W., 2015, *A&A*, 574, A52
- Fabrycky D., Tremaine S., 2007, *ApJ*, 669, 1298
- Fielding D. B., McKee C. F., Socrates A., Cunningham A. J., Klein R. I., 2015, *MNRAS*, 450, 3306
- Foreman-Mackey D., Morton T. D., Hogg D. W., Agol E., Schölkopf B., 2016, *AJ*, 152, 206
- Foucart F., Lai D., 2011, *MNRAS*, 412, 2799
- Goldreich P., Tremaine S., 1979, *ApJ*, 233, 857
- Gould A., Dorsher S., Gaudi B. S., Udalski A., 2006, *AcA*, 56, 1
- Hahn J. M., 2003, *ApJ*, 595, 531
- Hamers A. S., Portegies Zwart S. F., 2016, *MNRAS*, 459, 2827
- Haworth T. J., Clarke C. J., Owen J. E., 2016, *MNRAS*, 457, 1905
- Hébrard G., et al., 2008, *A&A*, 488, 763
- Hollenbach, D., Johnstone, D., Lizano, S., & Shu, F. 1994, *ApJ*, 428, 654
- Howard A. W., et al., 2012, *ApJS*, 201, 15
- Howard A. W., et al., 2010, *Sci*, 330, 653
- Ida S., Lin D. N. C., 2004, *ApJ*, 604, 388
- Jensen E. L. N., Akeson R., 2014, *Natur*, 511, 567

Jiménez M. A., Masset F. S., 2017, MNRAS, 471, 4917

Kley W., Nelson R. P., 2012, ARA&A, 50, 211

Lai, D. 2014, MNRAS, 440, 3532

Lai, D., Foucart, F., & Lin, D. N. C. 2011, MNRAS, 412, 2790

Lai D., Rasio F. A., Shapiro S. L., 1993, ApJS, 88, 205

Li G., Winn J. N., 2016, ApJ, 818, 5

Lin D. N. C., Bodenheimer P., Richardson D. C., 1996, Natur, 380, 606

Lin D. N. C., Papaloizou J. C. B., 1993, prpl.conf, 749

Lin D. N. C., Papaloizou J., 1985, prpl.conf, 981

Lubow S. H., D'Angelo G., 2006, ApJ, 641, 526

Lubow S. H., Martin R. G., 2016, ApJ, 817, 30

Lubow S. H., Ogilvie G. I., 2001, ApJ, 560, 997

Lubow S. H., Ogilvie G. I., 2000, ApJ, 538, 326

Marcy G., Butler R. P., Fischer D., Vogt S., Wright J. T., Tinney C. G., Jones H. R. A., 2005, PThPS, 158, 24

Martin R. G., Lubow S. H., Nixon C., Armitage P. J., 2016, MNRAS, 458, 4345

Masset F. S., 2017, arXiv, arXiv:1708.09807

Masset F. S., Velasco Romero D. A., 2017, MNRAS, 465, 3175

Matsakos T., Königl A., 2017, AJ, 153, 60

- Mazeh T., Perets H. B., McQuillan A., Goldstein E. S., 2015, *ApJ*, 801, 3
- McNally C. P., Nelson R. P., Paardekooper S.-J., Gressel O., Lyra W., 2017, *MNRAS*, 472, 1565
- Muñoz D. J., Lai D., Liu B., 2016, *MNRAS*, 460, 1086
- Nagasawa M., Ida S., Bessho T., 2008, *ApJ*, 678, 498-508
- Naoz S., Farr W. M., Rasio F. A., 2012, *ApJ*, 754, L36
- Narita N., Sato B., Hirano T., Tamura M., 2009, *PASJ*, 61, L35
- Owen, J. E. 2016, *PASA*, 33, e005
- Owen J. E., Clarke C. J., Ercolano B., 2012, *MNRAS*, 422, 1880
- Owen J. E., Ercolano B., Clarke C. J., Alexander R. D., 2010, *MNRAS*, 401, 1415
- Papaloizou J. C. B., Nelson R. P., 2005, *A&A*, 433, 247
- Papaloizou J. C. B., Lin D. N. C., 1995, *ApJ*, 438, 841
- Petrovich C., 2015, *ApJ*, 805, 75
- Pollack J. B., Hubickyj O., Bodenheimer P., Lissauer J. J., Podolak M., Greenzweig Y., 1996, *Icar*, 124, 62
- Rafikov R. R., 2017, *ApJ*, 837, 163
- Rogers T. M., Lin D. N. C., Lau H. H. B., 2012, *ApJ*, 758, L6
- Russo, M., & Thompson, C. 2015, *ApJ*, 813, 81
- Russo, M., & Thompson, C. 2015, *ApJ*, 815, 38
- Sanchis-Ojeda R., et al., 2015, *ApJ*, 812, L11

- Schlaufman K. C., Winn J. N., 2016, ApJ, 825, 62
- Spalding C., Batygin K., 2017, AJ, 154, 93
- Spalding, C., & Batygin, K. 2015, ApJ, 811, 82
- Spalding C., Batygin K., 2014, ApJ, 790, 42
- Spalding C., Batygin K., Adams F. C., 2014, ApJ, 797, L29
- Stapelfeldt K. R., Krist J. E., Ménard F., Bouvier J., Padgett D. L., Burrows C. J., 1998, ApJ, 502, L65
- Storch N. I., Lai D., Anderson K. R., 2017, MNRAS, 465, 3927
- Storch N. I., Lai D., 2015, MNRAS, 448, 1821
- Storch N. I., Anderson K. R., Lai D., 2014, Sci, 345, 1317
- Tanaka H., Ward W. R., 2004, ApJ, 602, 388
- Tanaka H., Takeuchi T., Ward W. R., 2002, ApJ, 565, 1257
- Tanigawa T., Tanaka H., 2016, ApJ, 823, 48
- Thies I., Kroupa P., Goodwin S. P., Stamatellos D., Whitworth A. P., 2011, MNRAS, 417, 1817
- Triaud A. H. M. J., 2017, arXiv, arXiv:1709.06376
- Triaud A. H. M. J., et al., 2010, A&A, 524, A25
- Vigan A., et al., 2017, A&A, 603, A3
- Ward W. R., 1981, Icar, 47, 234
- Weidenschilling S. J., 1977, Ap&SS, 51, 153

- Williams J. P., Cieza L. A., 2011, *ARA&A*, 49, 67
- Winn J. N., et al., 2017, arXiv, arXiv:1710.04530
- Winn J. N., Fabrycky D. C., 2015, *ARA&A*, 53, 409
- Winn J. N., Fabrycky D., Albrecht S., Johnson J. A., 2010, *ApJ*, 718, L145
- Winn J. N., Johnson J. A., Albrecht S., Howard A. W., Marcy G. W., Crossfield I. J., Holman M. J., 2009, *ApJ*, 703, L99
- Wright J. T., Marcy G. W., Howard A. W., Johnson J. A., Morton T. D., Fischer D. A., 2012, *ApJ*, 753, 160
- Wu Y., Lithwick Y., 2011, *ApJ*, 735, 109
- Wu Y., Murray N., 2003, *ApJ*, 589, 605
- Xiang-Gruess M., Papaloizou J. C. B., 2013, *MNRAS*, 431, 1320
- Zanazzi J. J., Lai D., 2017a, *MNRAS*, 464, 3945
- Zanazzi J. J., Lai D., 2017b, arXiv, arXiv:1712.07655

Chapter 4 references

- Anderson, K. R., Lai, D., & Storch, N. I. 2016, arXiv:1610.02626
- Artymowicz, P., & Lubow, S. H. 1994, *ApJ*, 421, 651
- Batygin, K., Morbidelli, A., & Tsiganis, K. 2011, *A&A*, 533, A7
- Blaes, O., Lee, M. H., & Socrates, A. 2002, *ApJ*, 578, 775
- Carruba, V., Burns, J. A., Nicholson, P. D., & Gladman, B. J. 2002, *Icarus*, 158, 434

- Doğan, S., Nixon, C., King, A., & Price, D. J. 2015, MNRAS, 449, 1251
- Eggleton, P. P., & Kiseleva-Eggleton, L. 2001, ApJ, 562, 1012
- Fabrycky, D., & Tremaine, S. 2007, ApJ, 669, 1298
- Ford, E. B., Kozinsky, B., & Rasio, F. A. 2000, ApJ, 535, 385
- Foucart, F., & Lai, D. 2014, MNRAS, 445, 1731
- Foucart, F., & Lai, D. 2011, MNRAS, 412, 2799
- Fu, W., Lubow, S. H., & Martin, R. G. 2015a, ApJ, 807, 75
- Fu, W., Lubow, S. H., & Martin, R. G. 2015b, ApJ, 813, 105
- Goodchild, S., & Ogilvie, G. 2006, MNRAS, 368, 1123
- Holman, M., Touma, J., & Tremaine, S. 1997, Nature, 386, 254
- Katz, B., & Dong, S. 2012, arXiv:1211.4584
- Katz, B., Dong, S., & Malhotra, R. 2011, Physical Review Letters, 107, 181101
- Kozai, Y. 1962, AJ, 67, 591
- Larwood, J. D., Nelson, R. P., Papaloizou, J. C. B., & Terquem, C. 1996, MNRAS, 282, 597
- Latter, H. N., & Ogilvie, G. I. 2006, MNRAS, 372, 1829
- Lidov, M. L. 1962, Planet. Space Sci. , 9, 719
- Liu, B., Muñoz, D. J., & Lai, D. 2015, MNRAS, 447, 747
- Lodato, G., & Price, D. J. 2010, MNRAS, 405, 1212

Lodato, G., & Pringle, J. E. 2007, MNRAS, 381, 1287

Lubow, S. H. 1991, ApJ, 381, 259

Lubow, S. H., & Ogilvie, G. I. 2000, ApJ, 538, 326

Martin, R. G., Nixon, C., Lubow, S. H., et al. 2014, ApJL, 792, L33

Miranda, R., & Lai, D. 2015, MNRAS, 452, 2396

Murray, C. D., & Dermott, S. F. 1999, Solar system dynamics by Murray, C. D., 1999,

Naoz, S. 2016, ARA&A , 54, 441

Naoz, S., Farr, W. M., Lithwick, Y., Rasio, F. A., & Teyssandier, J. 2011, Nature, 473, 187

Nesvorný, D., Alvarellos, J. L. A., Dones, L., & Levison, H. F. 2003, AJ, 126, 398

Ogilvie, G. I. 1999, MNRAS, 304, 557

Ogilvie, G. I. 2001, MNRAS, 325, 231

Ogilvie, G. I. 2008, MNRAS, 388, 1372

Papaloizou, J. C. B. 2002, A & A, 388, 615

Papaloizou, J. C. B., & Lin, D. N. C. 1995, ApJ, 438, 841

Papaloizou, J. C. B., & Pringle, J. E. 1983, MNRAS, 202, 1181

Petrovich, C. 2015, ApJ, 799, 27

Picogna, G., & Marzari, F. 2015, A & A, 583, A133

Press, W. H., Teukolsky, S. A., Vetterling, W. T., & Flannery, B. P. 2002, Numerical recipes in C++ : the art of scientific computing by William H. Press. xxviii, 1,002 p. : ill. ; 26 cm.

Teyssandier, J., & Ogilvie, G. I. 2016, MNRAS, 458, 3221

Tremaine, S., Touma, J., & Namouni, F. 2009, AJ, 137, 3706

Tremaine, S., & Yavetz, T. D. 2014, American Journal of Physics, 82, 769

Wu, Y., & Murray, N. 2003, ApJ, 589, 605

Xiang-Gruess, M., & Papaloizou, J. C. B. 2014, MNRAS, 440, 1179

Chapter 5 references

Alencar S. H. P., Melo C. H. F., Dullemond C. P., Andersen J., Batalha C., Vaz L. P. R., Mathieu R. D., 2003, A&A, 409, 1037

Aly H., Dehnen W., Nixon C., King A., 2015, MNRAS, 449, 65

Anderson K. R., Lai D., Storch N. I., 2017, MNRAS, 467, 3066

Andrews S. M., Czekala I., Wilner D. J., Espaillat C., Dullemond C. P., Hughes A. M., 2010, ApJ, 710, 462

Armstrong D. J., Osborn H. P., Brown D. J. A., Faedi F., Gómez Maqueo Chew Y., Martin D. V., Pollacco D., Udry S., 2014, MNRAS, 444, 1873

Bate M. R., Lodato G., Pringle J. E., 2010, MNRAS, 401, 1505

Bate M. R., Bonnell I. A., Bromm V., 2003, MNRAS, 339, 577

Boden A. F., et al., 2005, ApJ, 635, 442

Brinch C., Jørgensen J. K., Hogerheijde M. R., Nelson R. P., Gressel O., 2016, ApJ, 830, L16

Capelo H. L., Herbst W., Leggett S. K., Hamilton C. M., Johnson J. A., 2012, ApJ, 757, L18

Casassus, S., and 12 colleagues 2015. Accretion Kinematics through the Warped Transition Disk in HD142527 from Resolved CO(6-5) Observations. The Astrophysical Journal 811, 92.

Chiang E. I., Goldreich P., 1997, ApJ, 490, 368

Chiang E., Laughlin G., 2013, MNRAS, 431, 3444

Chiang E. I., Murray-Clay R. A., 2004, ApJ, 607, 913

Corsaro E., et al., 2017, NatAs, 1, 0064

Czekala I., Andrews S. M., Jensen E. L. N., Stassun K. G., Torres G., Wilner D. J., 2015, ApJ, 806, 154

Czekala I., Andrews S. M., Torres G., Jensen E. L. N., Stassun K. G., Wilner D. J., Latham D. W., 2016, ApJ, 818, 156

Doyle L. R., et al., 2011, Sci, 333, 1602

Facchini S., Lodato G., Price D. J., 2013, MNRAS, 433, 2142

Farago F., Laskar J., 2010, MNRAS, 401, 1189

Fielding D. B., McKee C. F., Socrates A., Cunningham A. J., Klein R. I., 2015, MNRAS, 450, 3306

Foucart F., Lai D., 2013, ApJ, 764, 106

- Foucart F., Lai D., 2014, MNRAS, 445, 1731
- Gammie C. F., Goodman J., Ogilvie G. I., 2000, MNRAS, 318, 1005
- Juhász A., Facchini S., 2017, MNRAS, 466, 4053
- Kennedy G. M., et al., 2012, MNRAS, 421, 2264
- Kennedy G. M., Wyatt M. C., Sibthorpe B., Phillips N. M., Matthews B. C., Greaves J. S., 2012, MNRAS, 426, 2115
- Kostov V. B., McCullough P. R., Hinse T. C., Tsvetanov Z. I., Hébrard G., Díaz R. F., Deleuil M., Valenti J. A., 2013, ApJ, 770, 52
- Kostov V. B., et al., 2014, ApJ, 784, 14
- Kostov V. B., et al., 2016, ApJ, 827, 86
- Kozai Y., 1962, AJ, 67, 591
- Landau L. D., Lifshitz E. M., 1969, Mechanics.
- Li D., Zhou J.-L., Zhang H., 2014, MNRAS, 437, 3832
- Li G., Holman M. J., Tao M., 2016, ApJ, 831, 96
- Lacour S., et al., 2016, A&A, 590, A90
- Larwood J. D., Papaloizou J. C. B., 1997, MNRAS, 285, 288
- Lidov M. L., 1962, P&SS, 9, 719
- Liu B., Muñoz D. J., Lai D., 2015, MNRAS, 447, 747
- Lubow S. H., Ogilvie G. I., 2000, ApJ, 538, 326
- Lubow S. H., Ogilvie G. I., 2001, ApJ, 560, 997

Lubow S. H., Ogilvie G. I., Pringle J. E., 2002, MNRAS, 337, 706

Lynden-Bell D., Pringle J. E., 1974, MNRAS, 168, 603

Marino, S., Perez, S., Casassus, S. 2015. Shadows Cast by a Warp in the HD 142527 Protoplanetary Disk. The Astrophysical Journal 798, L44.

Martin D. V., Triaud A. H. M. J., 2015, MNRAS, 449, 781

Martin R. G., Lubow S. H., 2017, ApJ, 835, L28

McKee C. F., Ostriker E. C., 2007, ARA&A, 45, 565

Miranda R., Muñoz D. J., Lai D., 2017, MNRAS, 466, 1170

Miranda R., Lai D., 2015, MNRAS, 452, 2396

Naoz S., Li G., Zanardi M., de Elía G. C., Di Sisto R. P., 2017, arXiv, arXiv:1701.03795

Nixon C., King A., Price D., 2013, MNRAS, 434, 1946

Ogilvie G. I., Latter H. N., 2013, MNRAS, 433, 2420

Ogilvie G. I., 2006, MNRAS, 365, 977

Ogilvie G. I., 1999, MNRAS, 304, 557

Orosz J. A., et al., 2012, ApJ, 758, 87

Orosz J. A., et al., 2012, Sci, 337, 1511

Papaloizou J. C. B., Pringle J. E., 1983, MNRAS, 202, 1181

Papaloizou J. C. B., Lin D. N. C., 1995, ApJ, 438, 841

Petrovich C., 2015, ApJ, 799, 27

- Pourbaix D., 2000, A&AS, 145, 215
- Rafikov R. R., 2016, ApJ, 830, 8
- Rafikov R. R., 2017, ApJ, 837, 163
- Rosenfeld K. A., Andrews S. M., Wilner D. J., Stempels H. C., 2012, ApJ, 759, 119
- Schwamb M. E., et al., 2013, ApJ, 768, 127
- Tomkin J., Popper D. M., 1986, AJ, 91, 1428
- Tremaine S., Touma J., Namouni F., 2009, AJ, 137, 3706
- Tremaine S., Yavetz T. D., 2014, AmJPh, 82, 769
- Weidenschilling S. J., 1977, Ap&SS, 51, 153
- Welsh W. F., et al., 2012, Natur, 481, 475
- Welsh W. F., et al., 2015, ApJ, 809, 26
- Williams J. P., Cieza L. A., 2011, ARA&A, 49, 67
- Winn J. N., Holman M. J., Johnson J. A., Stanek K. Z., Garnavich P. M., 2004, ApJ, 603, L45

Chapter 6 references

- Arnaboldi, M., & Sparke, L. S. 1994, AJ, 107, 958
- Ayliffe, B. A., & Bate, M. R. 2009, MNRAS, 397, 657
- Barnes, J. W., & Fortney, J. J. 2004, ApJ, 616, 1193
- Bate, M. R. 2009, MNRAS, 392, 590

- Bate, M. R., Lodato, G., & Pringle, J. E. 2010, MNRAS, 401, 1505
- Brown, T. M., Charbonneau, D., Gilliland, R. L., Noyes, R. W., & Burrows, A. 2001, ApJ, 552, 699
- Canup, R. M., & Ward, W. R. 2006, Nature, 441, 834
- Carter, J. A., & Winn, J. N. 2010, ApJ, 709, 1219
- Doğan, S., Nixon, C., King, A., & Price, D. J. 2015, MNRAS, 449, 1251
- Hamilton, D. P., & Ward, W. R. 2004, AJ, 128, 2510
- Heising, M. Z., Marcy, G. W., & Schlichting, H. E. 2015, ApJ, 814, 81
- Ivanov, P. B., & Illarionov, A. F. 1997, MNRAS, 285, 394
- Kenworthy, M. A., Lacour, S., Kraus, A., et al. 2015, MNRAS, 446, 411
- Kenworthy, M. A., & Mamajek, E. E. 2015, ApJ, 800, 126
- Kuijken, K. 1991, ApJ, 376, 467
- Laplace, P. S. 1805, Mecanique C'eleste, Vol. 4 (Paris: Courcier)
- Larwood, J. D., Nelson, R. P., Papaloizou, J. C. B., & Terquem, C. 1996, MNRAS, 282, 597
- Lehébel, A., & Tiscareno, M. S. 2015, A&A, 576, A92
- Lissauer, J. J., & Safronov, V. S. 1991, Icarus, 93, 288
- Lubow, S. H., & Ogilvie, G. I. 2000, ApJ, 538, 326
- Mamajek, E. E., Quillen, A. C., Pecaut, M. J., et al. 2012, AJ, 143, 72
- Martin, R. G., & Lubow, S. H. 2011, MNRAS, 413, 1447

- Murray, C. D., & Dermott, S. F. 1999, Solar system dynamics by Murray, C. D., 1999,
- Ogilvie, G. I. 1999, MNRAS, 304, 557
- Ohta, Y., Taruya, A., & Suto, Y. 2009, ApJ, 690, 1
- Papaloizou, J. C. B., & Lin, D. N. C. 1995, ApJ, 438, 841
- Papaloizou, J. C. B., & Pringle, J. E. 1983, MNRAS, 202, 1181
- Quillen, A. C., & Trilling, D. E. 1998, ApJ, 508, 707
- Santos, N. C., Martins, J. H. C., Boué, G., et al. 2015, A&A, 583, A50
- Schlichting, H. E., & Chang, P. 2011, ApJ, 734, 117
- Tokuda, K., Onishi, T., Saigo, K., et al. 2014, ApJL, 789, L4
- Touma, J. R., Tremaine, S., & Kazandjian, M. V. 2009, MNRAS, 394, 1085
- Tremaine, S. 1991, Icarus, 89, 85
- Tremaine, S., Touma, J., & Namouni, F. 2009, AJ, 137, 3706
- Tremaine, S., & Davis, S. W. 2014, MNRAS, 441, 1408
- Tusnski, L. R. M., & Valio, A. 2011, ApJ, 743, 97
- Ulubay-Siddiki, A., Gerhard, O., & Arnaboldi, M. 2009, MNRAS, 398, 535
- Vokrouhlický, D., & Nesvorný, D. 2015, ApJ, 806, 143
- van Werkhoven, T. I. M., Kenworthy, M. A., & Mamajek, E. E. 2014, MNRAS, 441, 2845
- Ward, W. R. 1981, Icarus, 46, 97

Ward, W. R., & Hamilton, D. P. 2004, AJ, 128, 2501

Zhu, W., Huang, C. X., Zhou, G., & Lin, D. N. C. 2014, ApJ, 796, 67

Zuluaga, J. I., Kipping, D. M., Sucerquia, M., & Alvarado, J. A. 2015, ApJL, 803, L14